Refinement of connections in the absence of synaptic activity

Yumaine Chong

Integrated Program in Neuroscience
McGill University, Montreal

August 2019

A thesis submitted to McGill University in partial fulfillment
of the requirements of the degree of Doctor of Philosophy

Abstract

At the onset of early postnatal development, neural circuits are initially imprecise; axons innervate an excessive number of targets, and target neurons receive inputs from a surplus of converging axons, resulting in diffuse circuits with overlapping connections. As activity increases over time, these circuits improve their performance by refining their connections, strengthening some and eliminating others. Moreover, if there is no activity in the circuit, then the refinement of connections does not occur. It is generally thought that the increase in synaptic transmission drives refinement by stimulating the postsynaptic neuron to release retrograde signals that act locally on presynaptic inputs. However, abolishing synaptic transmission at one node of a circuit alters synaptic activity in downstream target neurons and organs. Often overlooked is the possibility that activity-dependent, target-derived factors play an essential role in mediating the refinement of connections on upstream neurons. Such long-range factors would coordinate refinement of upstream connections in a retrograde manner to establish circuits that innervate distal targets with specificity and precision. The main objective of my doctoral research was to improve our understanding of the mechanisms that underlie refinement by (i) investigating how neural circuits develop in the absence of postsynaptic activity; (ii) determining whether downstream target organs have a role in the retrograde regulation of neural development; and (iii) identifying molecular mechanisms involved in refinement.

To address these issues, I compared the development of sympathetic circuits in three mouse models. In one model, mice have a deletion in the α3 nAChR subunit gene (α3 KO), an essential gene for the assembly of postsynaptic receptors on autonomic neurons. As a result, sympathetic circuits in α3 KO mice are silenced. In a second model, 4E-BP genes

were deleted from α3 KO mice (α3/4E-BP DKO) to examine the role of cap-dependent mRNA translation. Third, to test the role of postsynaptic activity while maintaining functional innervation to sympathetic targets, I generated a novel mouse model in which sympathetic neurons with postsynaptic receptors (α3-expressing) and those without receptors (α3-negative) are randomly intermingled to generate mosaic sympathetic ganglia. In mosaic ganglia, α3-negative sympathetic neurons do not have postsynaptic activity, while neighbouring α3-expressing neurons maintain functional innervation of common targets. Using this new mouse model, I investigated (a) how preganglionic axons innervate a mosaic population of active and inactive neurons, and (b) how sympathetic neurons develop in the absence of postsynaptic activity when their targets receive functional innervation. For the experiments to address these questions, I combined electrophysiology, immunohistochemistry, retrograde labelling and proteomic profiling. In addition, to investigate, at a molecular level, the activity-dependent changes in innervation and differentiation of sympathetic neurons, I used scRNAseq to generate single cell gene expression datasets.

When sympathetic circuits are silenced as in α3 KO mice, sympathetic neurons have severe developmental defects: dendritic growth is impaired, synapses are mistargeted to the cell soma, and preganglionic axons do not refine. These results are consistent with a role for synaptic activity in refinement. On the other hand, when cap-dependent translation is enhanced, or when their targets receive functional innervation, synaptically silent neurons develop normally without postsynaptic activity; they extend elaborate dendrites and receive synapses that are appropriately targeted to the dendritic arbour. Most strikingly, preganglionic inputs onto these inactive neurons refine in the absence of

synaptic transmission. I propose that activity-dependent, target-derived factors play an essential role in the innervation and differentiation of sympathetic neurons. In support of this idea, sympathetic neurons in α3 KO mice innervate their targets poorly, whereas inactive neurons in mosaic ganglia innervate targets normally. Furthermore, I identified a number of genes whose expression levels were misregulated in synaptically inactive sympathetic neurons of α3 KO mice, and restored to normal levels in synaptically inactive sympathetic neurons of mosaic mice.

My results overturn a widely held belief that the refinement of connections and the extension of dendrites require postsynaptic activity. My experiments with α3/4E-BP DKO mice show for the first time that connections can refine and dendrites can grow normally in the absence of postsynaptic activity. These findings were firmly established by my experiments in mosaic ganglia. Insights from these mosaic experiments suggest a model in which activity-dependent, target-derived factors mediate dendritic growth, synaptic targeting and refinement, at least in part, by regulating the expression of genes involved in neuronal development and differentiation.

Résumé

Au début du développement postnatal, les circuits neuronaux sont initialement imprécis; les axones innervent trop de cellules cibles et celles-ci reçoivent un excès d'axones convergents. Par conséquent, plusieurs connexions qui se chevauchent sont formées. Après la naissance, les circuits neuronaux deviennent de plus en plus actifs et améliorent leur performance en se réorganisant : certaines connexions sont renforcées, tandis que d'autres sont éliminées. De plus, en l'absence de transmission synaptique, ce raffinement des connections n'aura pas lieu. Il est généralement accepté que ce processus est dirigé par l'activité postsynaptique en générant des signaux moléculaires qui agissent localement sur les terminaisons présynaptiques. Cependant, l'abolissement de l'activité synaptique aux connections à un niveau d'un circuit neuronal aura des répercussions sur l'activité des cellules qui suivent. La possibilité que ces cellules qui suivent pourraient générer des signaux jouant un rôle important dans le raffinement des connections précédentes est rarement considérée. Ces signaux pourraient être essentiels dans l'établissement de circuits qui innervent les cibles distantes avec spécificité et précision. L'objectif principal de ma recherche doctorale était d'améliorer notre compréhension des mécanismes qui dirigent le raffinement (i) en examinant comment les circuits neuronaux se développent en l'absence d'activité postsynaptique, (ii) en déterminant si les cibles terminales jouent un rôle dans le développement des circuits neuronaux précédents, et (iii) en identifiant les mécanismes moléculaires impliqués dans le raffinement des connexions.

Afin d'approfondir ces sujets, j'ai comparé le développement des circuits sympathiques chez trois modèles de souris. Dans le premier modèle, les souris possèdent une mutation du gène α3 (α3 KO), une sous-unité essentielle pour la formation des

récepteurs nicotiniques de l'acétylcholine postsynaptiques. Par conséquent, les circuits sympathiques des souris α3 KO ne fonctionnent pas. Pour le deuxième modèle, les gènes 4E-BPs ont été supprimés des souris α3 KO pour examiner le rôle de la traduction de l'ARNm dépendante de la coiffe (α3/4E-BP DKO). Troisièmement, afin de tester le rôle de l'activité postsynaptique tout en conservant l'innervation fonctionnelle aux cibles sympathiques, j'ai généré un nouveau modèle de souris. Dans ce modèle, les neurones sympathiques avec des récepteurs (α3-positifs) et les neurones sans récepteurs (α3-négatifs) sont aléatoirement mélangés pour générer des ganglions mosaïques. Dans ces ganglions mosaïques, les neurones sympathiques sans récepteurs n'ont pas d'activité postsynaptique, mais les neurones sympathiques avoisinants avec récepteurs maintiennent l'innervation fonctionnelle des cibles communes. Avec ces ganglions mosaïques, j'ai étudié (a) comment les axons préganglionnaires innervent une mosaïque des neurones actifs et inactifs; et (b) comment les neurones sympathiques se développent sans l'activité postsynaptique quand ces cibles reçoivent l'innervation fonctionnelle. Mon approche expérimentale impliquait une combinaison d'électrophysiologie, immunohistochimie, le traçage rétrograde et le profilage protéomique. De plus, afin d'étudier les changements dans l'innervation et différenciation des neurones sympathiques au niveau moléculaire, j'ai séquencé l'ARNm des cellules individuelles pour générer un ensemble de données d'expression des gènes.

Dans l'absence d'activité des circuits sympathiques chez les souris α3 KO, j'ai trouvé que les neurones sympathiques ont un développement altéré : l'extension des dendrites est diminuée, les synapses sont mal dirigées vers le corps cellulaire, et les axones préganglionnaires ne se raffinent pas. Ces résultats sont consistants avec le rôle de

l'activité synaptique dans le raffinement des connections. D'autre part, les neurones inactifs peuvent se développer normalement si la traduction dépendante de la coiffe est augmentée, ou si leurs cibles reçoivent de l'innervation fonctionnelle. Ces neurones inactifs forment des dendrites normales et les synapses sont distribuées correctement aux dendrites. Et, contre toute attente, les axones préganglionnaires se raffinent sans l'activité synaptique. Selon les résultats de mes expériences avec les souris à ganglions mosaïques, je propose un modèle où les cibles actives envoient, de façon rétrograde, des signaux moléculaires qui jouent un rôle essentiel dans l'innervation et la différenciation des neurones sympathiques. Pour supporter cette hypothèse, les neurones sympathiques des souris α3 KO innervent mal leurs cibles tandis que les neurones inactifs des ganglions mosaïques innervent normalement leurs cibles. De plus, j'ai identifié un ensemble de gènes qui sont déréglés avec l'absence d'activité synaptique chez les souris α3 KO, mais sont restaurés à la normale dans les neurones inactifs des ganglions mosaïques.

Mes résultats réfutent une théorie bien établie que l'activité synaptique est nécessaire pour le raffinement et l'extension des dendrites. Mes expériences avec les souris α3/4E-BP DKO démontrent, pour la première fois, que le raffinement des connections et l'extension des dendrites peuvent se produire malgré l'absence d'activité postsynaptique. Et, mes résultats avec les ganglions mosaïques supportent également cette conclusion. Collectivement, mes résultats suggèrent un modèle où l'innervation fonctionnelle des cibles génère des signaux rétrogrades qui modulent l'extension des dendrites, la distribution des synapses et le raffinement des connexions, grâce, en partie, à la régulation de l'expression des gènes impliqués dans le développement des circuits neuronaux.

Acknowledgements

First and foremost, thank you to my supervisor, Dr. Ellis Cooper, for giving me the opportunity to work on this exciting project – it's been a lot of fun, and I've learned so much from you in the process. Thank you for always encouraging me and giving me the freedom to explore my research interests, whether it be brief stints in learning to code or a lasting appreciation for all things microscopy-related. Whatever I do next, I really hope that the people I work with are as enthusiastic about science and research as you are.

Thank you to my mom and dad, who don't fully understand what I do in the lab each day, yet continue to provide endless support in every way they know how. My parents have always led by example when it comes to work ethic and have given me every single opportunity in life they could possibly provide.

Thanks as well to Brigitte and Natasha for bringing some liveliness to the lab on slow days, and for the technical help too, Brigitte. Thanks also to my supervisory committee, Dr. Keith Murai and Dr. Don van Meyel, and other members of the IPN and Physiology Department for their advice and interesting discussion over the years. Also, thank you to Arjun for your encouragement, and for giving me free rein to all of your resources and tools. A big thank you goes to Val for all of your help in translating the abstract, and for not once complaining when I made you read it over about 50 times, and thanks to Pierre as well for some final abstract touch-ups.

Lastly, thanks to all of my friends both in and out of Montreal, who have helped me retain some semblance of balance in life. A special mention goes out to the members of the cottage crew/Team Teahop for all of the adventures: Val – you get two shout outs, but you really deserve your own paragraph, thank you for all of your support and encouragement in pretty much everything I do, and also for the endless supply of Mao pics; Stuart – fellow bear enthusiast and TNRC co-lead, when should we start writing the running thesis?; Vaughn – 411 Earl OG, which city are we moving to next?; and Michel – the ring leader of the circus, the grand marshal of the parade. Get reading folks, pop quiz next week.

Contribution to original knowledge

My doctoral research challenges well-established ideas for the role of synaptic activity in refinement. My approach differed from the existing literature; rather than narrowing my focus on the mechanisms of refinement at a local level, I tested the hypothesis that long-range factors released by distal targets contribute to the synaptic refinement of upstream connections during early postnatal development. Using this approach, I discovered that many properties of neural development previously thought to depend on postsynaptic activity are in fact regulated by external signals, likely in the form of retrograde target-derived factors. Most notably, my results show for the first time that synaptic refinement can occur in the absence of postsynaptic activity when cap-dependent translation is enhanced or when downstream neuronal targets are functionally innervated.

In Chapter 3, my results demonstrate that:

- Developmental refinement of synaptic connections in the superior cervical ganglion (SCG) is dependent on postsynaptic activity; preganglionic inputs onto SCG neurons do not refine in the absence of activity.
- Postsynaptic activity is necessary for SCG neurons to maintain primary dendrites after birth, resulting in defects in dendritic outgrowth on inactive neurons.
- Silent synapses are mistargeted from the dendritic domain onto the somatic domain. This relationship between synaptic activity and targeting had not been previously reported.

In Chapter 4, my results demonstrate that:

- Random X-inactivation can be used to generate a novel mosaic mouse model to study refinement: synaptically active neurons and synaptically silent neurons are randomly intermingled in mosaic SCG, preserving the functional innervation of downstream neuronal targets.
- Postsynaptic activity is not essential for the refinement of connections; preganglionic inputs onto SCG neurons refine in the absence of synaptic transmission when neighbouring neurons are active.
- Dendritic growth and synaptic targeting on SCG neurons are regulated in a non-cell-autonomous manner, possibly by target-derived factors.

In Chapter 5, my results demonstrate that:

- Activity-dependent factors released by the iris promote their innervation and enhances arborization of sympathetic axons.

In Chapter 6, my results demonstrate that:

- Postsynaptic activity is not essential for the refinement of synaptic connections when cap-dependent translation is enhanced.
- 4E-BP plays a key role in mediating dendritic growth, synaptic targeting and refinement of connections; genetically enhancing cap-dependent translation by deleting 4E-BP in synaptically silent SCG neurons rescues defects in morphology and innervation, and preganglionic inputs refine in the absence of postsynaptic activity.

- Phosphorylation of 4E-BP in SCG neurons is decreased when sympathetic circuits are silenced.

In Chapter 7,

- Single cell RNA sequencing datasets generated from SCG neurons identified 7 subtypes of neurons in SCG.
- I compared gene expression between synaptically active SCG neurons and inactive SCG neurons, as well as neurons from mosaic SCG, and identified genes whose expression is activity-dependent, however, are not regulated directly by postsynaptic activity.
- I identified many genes that were previously not known to be expressed in sympathetic neurons.

Taken together, my doctoral research supports the idea that functional innervation of the target has an unappreciated role in governing dendritic growth, synaptic targeting, and the refinement of upstream connections. I propose a novel model for refinement, in which functional innervation of the target generates activity-dependent retrograde signals that enhance cap-dependent translation and mediate gene transcription in upstream neurons to regulate their dendritic growth, synaptic targeting and the refinement of their inputs. These findings challenge existing ideas for the cell-autonomous role of synaptic activity in neural development, and indicate that current models for synaptic refinement need to be revised.

Contribution of the author

I designed all of the experiments presented in this doctoral thesis under the guidance of my supervisor, Dr. Ellis Cooper. I wrote all of the text and prepared all of the figures presented in this thesis, which were revised with comments and edits from my supervisor. Sections of text and figures from Chapters 3 and 6 were previously published (Chong *et al*., 2018), and modified for this thesis. I performed all of the experiments and analyses presented in this thesis with two exceptions:

1. Natasha Saviuk conducted the intracellular recordings in Chapters 3 and 6, and we both analyzed the acquired data.

   I conducted all of the intracellular recordings and data analysis for Chapter 4.

2. For proteomic profiling in Chapter 6, I provided SCG samples to Nathan Basisty, Ryan Quinn and Birgit Schilling, who processed the tissue and generated the mass spectrometry data. I performed all analysis of these data.

Table of Contents

Chapter 1: Introduction and review of the relevant literature

There's a popular idea that with 10,000 hours of practice, one can master nearly any skill; this is based on the observation that performance often improves with repetition. For example, a pianist will practice the same difficult passage repeatedly until he or she is able to perform it with ease. Such improvements are generally attributed to adaptations in the neural circuits used to perform the task, starting in the central nervous system (CNS), coordinating which notes to play, down to the individual motor axons and muscle fibers responsible for fine motor control of the hands and fingers. And, the more often a circuit is used, the more precise and natural the actions become because neural circuits are remarkably plastic; with each trial, the neurons and the connections that carry out these actions undergo small adjustments that allow them to function more efficiently and with greater precision.

This ability of the nervous system to improve its function by remodelling circuits is particularly apparent during the early postnatal period and underlies the developmental refinement of connections. The immature nervous system is poorly organized and signals are often sent to diffuse targets. As a result, young animals are generally slow to react, uncoordinated and clumsy. However, as they explore their new environment, they develop their sense of balance, proprioception, and motor control. And, as they learn to process sensory stimuli such as visual and auditory cues, they grow in their capacity to interact with their surroundings. These circuits remodel in response to the neural activity generated by the highly dynamic and stimulating postnatal environment, which is a sharp contrast to the relatively stable prenatal environment that exists *in utero*. In addition to external stimuli, neonatal animals must also detect and regulate changes in body

temperature, heart rate, blood pressure, and other vital properties that were previously maintained and stabilized prenatally by the mother. The stimuli young animals are exposed to and the tasks they perform during this critical phase drive the development of circuits that underlie the complex behaviours that make them well adapted to their environment.

For refinement to occur rapidly and efficiently, one strategy is to initially overproduce an abundance of connections, and to refine these connections after birth as these neural circuits are used. When the nervous system is initially formed during embryogenesis, an assortment of attractive and repulsive guidance cues direct the general patterning of the nervous system (Kolodkin and Tessier-Lavigne, 2011; Young *et al*., 2004). At their destinations, axons branch and diverge to innervate an excessive number of targets, and simultaneously, a surplus of axons converge onto each target, generating hyper-connected networks of circuits. As the activity in these circuits increase, some axonal inputs are strengthened by increasing the number of synaptic contacts and/or by potentiating existing synapses, while other axons are weakened by depressing synaptic strength or by eliminating synaptic contacts (Cohen-Cory, 2002; Ganguly and Poo, 2013).

The process of refinement may appear to be an inefficient one: to overproduce connections, only to ultimately eliminate many of them. Yet the alternative would be to form stereotyped and predetermined circuits, which may be feasible for simple organisms such as *C. elegans*, but would not allow for complex behaviours in more complicated and larger animals. Furthermore, excess divergence and convergence of connections allows for sampling between many different combinations of axons and targets, which may be a critical step in matching axons to their appropriate targets. Therefore, although it may appear to be a disadvantage that the nervous system is initially inefficient and must

undergo considerable rearrangements after birth, this process gives rise to precise and accurate coordination between the nervous system, the body and the external environment.

Classic models of refinement include the segregation of ocular dominance columns in the visual system, elimination of motor axons at the neuromuscular junction (NMJ), preganglionic innervation of sympathetic neurons in sympathetic ganglia, and climbing fiber innervation of Purkinje cells in the cerebellum (Hong and Chen, 2011; Kano and Hashimoto, 2009; Purves and Lichtman, 1980). Across the central and peripheral nervous system and across many animal species, refinement appears to share several features, suggesting that this process is governed by a common set of rules. However, for a fundamental process that occurs ubiquitously across the nervous system and across species, we have a poor understanding of how refinement works. There is no unifying idea or model that encompasses all of the results, and the mechanisms and molecules that are involved in refining connections remain largely unknown. Popular phrases such as “use it or lose it” or “cells that fire together, wire together” have become dogma, even though there are several studies that contradict these predictions.

The idea seems simple: an axon connects to several different targets, and then retracts from the incorrect ones. However, circuits consist of more than just one level of connections. For example, touch receptors at the tip of the finger may generate signals in sensory neurons that are destined for specific neurons in the primary somatosensory cortex. However, signals are integrated and filtered as they pass through nuclei in the spinal cord and again in the thalamus before it reaches the appropriate neurons in the cortex. How do sensory neurons refine their connections to converge onto the particular

second or third order neurons that will ultimately project to the correct neurons in the cortex?

To date, most experiments were designed to study refinement at the level of axon terminals and individual postsynaptic neurons, with little consideration for the overall circuit. My doctoral research addressed this gap and focused on how connections refine within the context of a complete neural circuit. In this introductory chapter, I will pose some of the key questions regarding how refinement is regulated, and discuss what we know about these issues, with a particular focus on several key experiments that have led to significant advances in our understanding of the refinement process. I will also evaluate proposed mechanisms for refinement, and discuss how experimental outcomes often contradict these models. After this, I will compile a list of key questions that remain unanswered, and describe the experimental approach I used to address some of these questions.

The terms "synapse elimination", "pruning", and "refinement" are often used interchangeably in spite of their differences. "Synapse elimination" and "pruning" generally refer to a reduction in the number of synaptic contacts between an axon and one of its targets, and does not take into consideration how the axon innervates other targets or how the target is innervated by other axons. For example, a retinal ganglion cell (RGC) axon can retract its branches and withdraw its synaptic connections from neuron A in the lateral geniculate nucleus (LGN). However, the RGC axon can simultaneously strengthen its connections onto LGN neurons B and C by forming additional synapses. Similarly, neuron A may be receiving additional synaptic contacts from other RGC axons. Therefore, although "refinement" occurs partially through "synapse elimination" and "pruning," it also

encompasses the strengthening of other connections that remain, such that there can be a decrease in the number of axonal inputs, but a net increase in the number of synapses.

1.1 Part A: How does activity mediate refinement?

Hubel and Wiesel were among the first to probe the role of activity in refinement, and in the 1960s, performed a series of key experiments to investigate the role of external sensory activity in the formation and development of the visual pathway in young cats (Wiesel and Hubel, 1963a, 1963b, 1965). In the mammalian visual system, RGCs project to the LGN, where their axons segregate into ipsilateral and contralateral layers. The LGN then sends their axons to the primary visual cortex, where cortical neurons initially receive overlapping inputs from both ipsilateral and contralateral layers of the LGN. Over the next few developmental weeks, LGN projections from each eye segregate, such that cortical neurons become more responsive to one eye over the other, forming ocular dominance columns.

Hubel and Wiesel eliminated visual input in neonatal cats during the first three postnatal months and examined the visual circuits for physiological and anatomical changes. When both eyes were deprived of visual input, ocular dominance columns were poorly formed, eye-specific inputs overlapped, and cortical neurons continued to respond to stimuli in both eyes (Wiesel and Hubel, 1965). On the other hand, when Hubel and Wiesel eliminated visual input to one eye in neonatal cats for three months by suturing the eye shut prior to eye opening, cortical neurons were more responsive to visual stimuli from the open eye, and anatomically, the projections from the open eye occupied a much larger area in the cortex than the deprived eye. These results suggest that active connections from

the open eye were preferentially maintained over inactive connections from the deprived eye (Le Vay *et al*., 1980; Wiesel and Hubel, 1963b, 1965).

Since these experiments from the 1960s, many others have demonstrated a role for activity in refinement through a variety of different animals, model systems and techniques. Like Hubel and Wiesel's experiments, many of these experiments did not identify the site(s) along the neural pathway at which activity may be acting. And, despite decades of research, it is still not entirely clear where or how activity exerts its influence.

1.1.1 Competition I: Do axons compete to innervate the same targets?

Hubel and Wiesel's deprivation studies showed that sensory activity has a strong influence on the development of a circuit, particularly in young cats that had not previously experienced visual stimulation. The preferential maintenance of active inputs over inactive ones suggests that axons might compete via activity to innervate a target. Other models have shown that silencing presynaptic activity from all inputs, for example, with tetrodotoxin to inhibit action potentials, prevents axons from refining, and targets remain hyperinnervated (Thompson *et al*., 1979).

If refinement is a competitive process mediated by activity, then stronger or more active inputs are more likely to persist over weaker or less active ones. Consistent with this idea, the selective strengthening of the persisting axon and the near simultaneous weakening of those that are eliminated has been described in several systems, including the NMJ and the cerebellum (Colman *et al*., 1997; Hashimoto *et al*., 2009). To test this idea, one could set up a scenario in which a target is innervated by one active axon and one inactive axon. If axons compete, then we would expect that in every scenario, the active

axon would persist and the inactive axon would be eliminated. On the other hand, if the activity of the axon is independent of its fate, then one would expect on average, 50% of the time the inactive axon would persist, and the other half of the time, the active axon would persist.

In 2003, Buffelli *et al*. performed an experiment similar to this by using a genetic approach to inhibit the release of acetylcholine from a subset of motor axons innervating muscle fibers. The rate-limiting enzyme to synthesize acetylcholine in motor neurons is choline acetyl transferase (ChAT). By crossing a floxed ChAT mouse line to a Cre-ER mouse line, and using low doses of tamoxifen, Buffelli *et al*. eliminated ChAT expression from a subset of motor neurons, and consequently these motor neurons were unable to release acetylcholine. They then examined input elimination during the early postnatal period. By postnatal day 14 (P14), axons that expressed ChAT persisted, whereas ChAT-negative axons were eliminated. Therefore, refinement is unlikely to be a random elimination of axonal inputs. These results provide strong support for the idea that refinement is driven by activity-dependent competition between inputs. However, this experiment did not identify the properties of neural activity that mediate competition. Namely, are the strongest axons that release the greatest amount of neurotransmitter more likely to persist, or is the frequency or pattern of firing more important in determining which axons are strengthened or eliminated?

1.1.2 Competition II: Is patterned activity important for refinement?

The visual system is an attractive model for studying refinement for several reasons, one being that each eye offers an independent input of activity, presenting a simple way to

manipulate the relative timing of activity between inputs. Zhang *et al*., (2011) exploited this feature to test whether the level of activity or the relative patterns of activity has a greater influence on refinement. In these experiments, they expressed channelrhodopsin in a subset of mouse RGCs, and stimulated RGCs in each eye to fire synchronously, or asynchronously, alternating between the left and right eyes. As the output, they examined how RGCs innervated the superior colliculus, where RGC axons normally segregate into eye-specific layers in an activity-dependent process.

As one would expect, alternating RGC activity between the left and right eyes led their axons to segregate. However, when RGCs from both eyes fired synchronously, their axons did not segregate and maintained a high degree of overlap (Zhang *et al*., 2011), reminiscent of Hubel and Wiesel's visual deprivation experiments. This result indicates that activity alone does not guarantee refinement, and that a differential signal between competing inputs is necessary for them to refine.

In the experiments performed by Zhang *et al*., neuronal activity was driven by channelrhodopsin, and the segregation of visual inputs was based on changes observed at a gross anatomical level. Munz *et al*. (2014) tested similar ideas using visual stimuli and investigated changes in connectivity at a much higher resolution by electrophysiologically recording and then comparing the amplitude of postsynaptic currents before and after synchronous or asynchronous stimulation of RGCs. Generally, RGC axons project to the contralateral optic tectum in *Xenopus laevis* tadpoles. However, Munz *et al*. took advantage of an intriguing phenomenon, in which random pathfinding errors result in aberrant projections of individual RGC axons to the ipsilateral optic tectum. In this model, the ipsilateral axon can be manipulated in an independent manner to either fire in synchrony

with neighbouring axons by simultaneously stimulating both eyes, or be forced to fire asynchronously by alternating stimuli delivered to each eye. Asynchronous stimulation, but not synchronous stimulation, led to a rapid weakening of the ipsilateral input onto tectal neurons (Munz *et al*., 2014). These results provide further evidence that differential, asynchronous activity between competing axons is necessary for refinement.

However, I think it would be more interesting to examine these connections at a circuit level. The visual pathway has been examined in depth and the segregation of ipsilateral and contralateral inputs is remarkably consistent. So consistent in fact, that it almost appears to be predetermined: in mice, contralateral projections always terminate in the most superficial layer of the superior colliculus, whereas ipsilateral projections reliably form distinct clusters inferior to the contralateral layer. Although molecular guidance cues are involved (Huberman *et al*., 2005; Pfeiffenberger *et al*., 2005), activity is still necessary to aid in the formation of these and other eye-specific structures. And, it is not clear why or how layers in the LGN and superior colliculus, or ocular dominance columns in the primary visual cortex are formed. In the experiments in which competing RGCs from different eyes fire asynchronously, they do so at relatively equal strength and frequency, and yet their axons segregate, indicating that persisting axons are not necessarily the stronger ones. Whether an axon persists is determined by something more complex, related to the patterns of firing, and appears as if each region of neurons in the superior colliculus has an intrinsic preference for inputs from one eye over the other. Presumably, RGC activity in one eye is more cohesive with one another than with the other eye. This type of patterning can be used by neurons in the superior colliculus to determine which inputs belong to the same

eye. However, this does not explain how superior colliculus neurons within a layer coordinate to select inputs from the same eye.

Although the visual system offers several attractive features, there are also complexities that make it challenging to interpret these results. The visual system generates spontaneous activity in the form of cholinergic and glutamatergic retinal waves, both of which are present and sufficient to drive eye-specific inputs to segregate prior to eye opening (Huberman *et al*., 2008). Furthermore, refinement in the visual system is often examined at a relatively superficial level, often quantified by the territory occupied by axons, where a larger territory is interpreted as an active axon that has outcompeted weaker axons. However, the territory they occupy doesn't necessarily correlate with the number of synaptic contacts they form, whether the synapses are functional, nor do they distinguish between strong connections (i.e. many synapses) with few cells or weak connections (i.e. few synapses) with many cells. Additionally, refinement in the visual system is often focused on presynaptic activity, without considering any potential contribution of postsynaptic activity. Nevertheless, the findings described above from Zhang *et al*. and Munz *et al*., as well as similar results from other labs, provide clear evidence that activity on its own is not sufficient to drive refinement; differential, asynchronous activity is required to mediate competition (Andjus *et al*., 2003; Favero *et al*., 2012).

1.1.3 Competition III: Is postsynaptic activity necessary to mediate competition?

The experiments described above indicate that asynchronous presynaptic activity is necessary for axons to compete, however the mechanisms involved are not clear. One

possibility is that axons release molecular signals locally at the terminal to cause nearby competing axons to retract, which would occur independently of any postsynaptic response. On the other hand, if refinement is a Hebbian mechanism, then the connections that cause postsynaptic neurons to fire should be stabilized and strengthened, whereas those that do not should be eliminated. In this scenario, a postsynaptic response would be necessary to mediate presynaptic competition.

Balice-Gordon and Lichtman (1994) published one of the most frequently cited experiments as evidence for the role of postsynaptic activity in refinement. To study the contribution of postsynaptic activity, Balice-Gordon and Lichtman applied alpha-bungarotoxin at the mouse NMJ to irreversibly block postsynaptic acetylcholine receptors (AChRs). When the blocker saturated the entire NMJ, no changes were detected at either the presynaptic terminals or the postsynaptic endplates. On the other hand, focal application of alpha-bungarotoxin to an isolated region of the NMJ led to a gradual and permanent loss of postsynaptic AChRs at the blocked region, followed by the subsequent retraction of presynaptic motor nerve terminals (Balice-Gordon and Lichtman, 1994).

Since synapses appeared to disassemble only when in the presence of active ones, Balice-Gordon and Lichtman claimed that the active synapses destabilized silent ones, which they suggested to be the driving force for competition and refinement. However, there are alternative interpretations. It is important to note that these experiments were performed in adult mice, when motor axons had already refined, and only a single axon terminal innervated each motor endplate. In the focal blockade experiments, it is possible that the axon simply received feedback that some terminal regions were more effective at generating an endplate potential than others and therefore retracted the ineffective ones

through a reparative or maintenance program that is entirely independent of competition or refinement. One might argue that postsynaptic disassembly appeared to precede any presynaptic change, providing support for the idea that the postsynaptic side selectively maintained active terminal regions and initiated the withdrawal of others. This observation was based on a mitochondrial dye used to label presynaptic terminals. In 2003, Walsh and Lichtman used improved labelling methods in which motor axons expressed a fluorescent protein and showed that motor axon terminals were first to retract, without any observable changes on the postsynaptic side, contradicting these earlier results.

Had the experiments been performed in younger mice, when motor axons at the NMJ were in the process of refining, the results would have been considerably more impactful. Despite how frequently this paper is cited as evidence that postsynaptic activity is important for refinement, upon close review, it does not adequately address this issue. Furthermore, it is difficult to apply these results from the NMJ to neuronal connections, in large part because it is not clear whether a single NMJ is analogous to one individual synapse or to a cluster of adjacent synapses in close proximity. While each muscle fiber has only one single site for innervation, neurons receive up to 100s of distinct synaptic contacts that are distributed across their dendrites. Similarly, axons often form multiple synapses onto the 3-dimensional (3-D) surface of each postsynaptic neuron, in which their spatial location on the dendrites may have significant impacts on their function. Due to these differences, it is unclear what the equivalent of focal blockade at the NMJ would be at a neuronal synapse.

Hashimoto *et al*. (2011) used an alternative approach to investigate the role of postsynaptic activity by limiting calcium influx downstream of receptor activation. They

examined the refinement of climbing fiber inputs onto Purkinje cells using a Purkinje cell-specific P/Q-type voltage-dependent calcium channel ($Ca_v2.1$) knockout (KO) mouse. In these $Ca_v2.1$ KO mice, calcium influx in response to burst firing of climbing fibers was significantly reduced. In the immature cerebellum, virtually all Purkinje cells are innervated by at least 4 climbing fiber inputs. Gradually, one climbing fiber input is selectively strengthened and translocates up the Purkinje cell dendritic arbour, while the remaining inputs withdraw. In two-week-old mice, over half of the Purkinje cells are mono-innervated and very few remain innervated by more than 4 inputs. In contrast, when $Ca_v2.1$ was deleted, very few Purkinje cells were mono-innervated, and ~30% remained hyperinnervated by at least 4 climbing fiber inputs (Hashimoto *et al*., 2011).

Although there was a clear difference between wildtype (WT) control and KO mice, there was a gradual elimination of inputs that took place in the first three postnatal weeks, and I would have liked to see the authors extend these experiments to later time points, as the number of inputs onto $Ca_v2.1$ KO neurons had not yet plateaued. Furthermore, rather than the selective strengthening of a single climbing fiber observed in WT mice, multiple climbing fibers onto $Ca_v2.1$ KO neurons strengthened equally, resulting in a much lower disparity in strength than in control mice. One possibility is that the similarity in strength between inputs led to defects in refinement, consistent with the idea that a differential signal between inputs is necessary to generate competition. However, it remains unclear whether the selective strengthening of an axon allows it to outcompete other inputs and persist, or whether the strengthening occurs after it has already been determined which axons will persist. And, from a circuit-level perspective, it is not known how the reduction in calcium influx affected the output of the Purkinje cells. Nevertheless, Hashimoto *et al*.

demonstrated that limiting calcium influx downstream of postsynaptic receptor activation led to defects in the refinement of presynaptic inputs. Similar manipulations to dampen the effects of postsynaptic activity also disrupted refinement (Kawata *et al*., 2014; Lorenzetto *et al*., 2009). Collectively, these experiments suggest that synaptic activity initiates processes downstream of receptor activation that mediate presynaptic competition in a retrograde manner.

Taken together, these experiments in which activity was manipulated in several different ways provide strong evidence that asynchronous activity between axons drives competition through a retrograde signal generated by the postsynaptic neuron in order to remodel neuronal connections and to establish precise and efficient circuits. However, there are key questions that remain, mostly concerning the signalling pathways downstream of synaptic activity, and the identity of the elusive signal(s) that determines which inputs persist and which are eliminated is unclear.

1.2 Part B: What are the molecular mechanisms downstream of activity?

Our ability to produce a complete and accurate model that explains how activity regulates downstream pathways to mediate refinement is a good reflection of how well we understand this process. To date, there is no molecular model that successfully illustrates how activity coordinates synapse elimination and strengthening. Here, I will discuss two of the currently prevailing ideas, and identify the deficiencies that limit the ability of these models to describe fully how connections refine.

1.2.1 Model I: The neurotrophic factor hypothesis

The neurotrophic factor hypothesis was first proposed in a review article written by Changeux and Danchin in 1976. The overall idea behind this model is that presynaptic nerve terminals compete for a retrograde trophic factor, or a "reward" signal, that is secreted locally at synaptic sites in limited quantities by the postsynaptic target cell. And, presynaptic activity confers a competitive advantage, either by promoting increased release of the factor from the postsynaptic cell or by enhancing the receptiveness of the presynaptic terminal to the factor. Ultimately, terminals that are more active receive a greater quantity of the trophic factor and become stabilized, whereas weaker terminals receive an insufficient amount of the trophic factor and retract (Katz and Shatz, 1996; Purves and Lichtman, 1980). This "reward" model has since been extended with the addition of a "punishment" factor that is released by presynaptic nerve terminals of active, stronger axons and diffuses to nearby synapses to destabilize competing, less active inputs (Jennings, 1994; Lichtman and Colman, 2000).

The most commonly proposed candidate for the trophic factor is brain-derived neurotrophic factor (BDNF), which has well-established roles in synaptogenesis and neurite outgrowth (Cohen-Cory *et al*., 2010). As well, transcription of the BDNF gene is enhanced by activity, and theoretically, BDNF could act as either the reward signal or the punishment factor, depending on which neurotrophin receptor it acts on (Tao *et al*., 2002). Moreover, Je *et al*. (2012, 2013) proposed that immature proBDNF binds to the p75 neurotrophin receptor ($p75^{NTR}$) to induce axon degeneration and retraction, whereas activity promotes the release of metalloproteinases that cleave proBDNF into its mature form (mBDNF), which binds to TrkB receptors to maintain and stabilize synapses.

The model proposed by Je *et al*. is based primarily on evidence from co-cultures of nerve and muscle (Je *et al*., 2012), and according to this idea, one would expect that deleting either BDNF or $p75^{NTR}$ would prevent synapse elimination and result in hyperinnervation. Yet, when tested *in vivo*, both BDNF KO and $p75^{NTR}$ KO mouse models showed normal refinement at the NMJ (Je *et al*., 2013). To test TrkB-mediated synapse stabilization, Je *et al*. (2013) mimicked a gain-of-function by infusing exogenous mBDNF. However, it is difficult to draw strong conclusions from this approach because BDNF is well documented to promote synaptogenesis and axon growth (Cohen-Cory *et al*., 2010). Any effects on synapse maintenance or any aberrant formation of synapses does not indicate that BDNF has a role in stabilizing connections during refinement, and would be no different than elevating any other synaptogenic factor. Therefore, although treatment with mBDNF caused a portion of NMJs to remain multiply innervated when control NMJs had refined, this result does not definitively point to a role for BDNF in refinement.

In order for BDNF to function as either a reward signal or punishment factor, it would need to be secreted locally at synaptic sites, and its secretion should be controlled independently at each individual synapse. Indeed, bursts of backpropagating action potentials from the soma are capable of inducing BDNF release at synapses (Kuczewski *et al*., 2008), however, it remains unclear whether BDNF can be released in a synapse-specific manner. Hypothetically, the effects of BDNF could be mediated through a presynaptic mechanism, in which only those nerve terminals that were recently active are temporarily protected from proBDNF or receptive to mBDNF, and may explain why active presynaptic neurons must fire asynchronously in order for some inputs to be eliminated (Andjus *et al*., 2003; Favero *et al*., 2012).

Furthermore, whether BDNF is secreted as an immature propeptide or in its cleaved, mature form is controversial (Lu *et al*., 2005; Matsumoto *et al*., 2008). This model operates on the assumption that BDNF is secreted in its propeptide form, and that activity promotes conversion from proBDNF to mBDNF. Consequently, in a default state without synaptic activity, BDNF would be present at low levels, with the ratio heavily favouring the propeptide form, which would activate $p75^{NTR}$ and result in massive synapse elimination. This prediction contradicts numerous experimental outcomes, particularly those described above, indicating that synapses persist and refinement is attenuated in the absence of activity.

Based on a similar idea, Singh *et al*. (2008) proposed that presynaptic nerve terminals secrete proBDNF in an activity-dependent manner, which binds to $p75^{NTR}$ on neighbouring competing axons to promote axon degeneration and retraction. Unlike the previous model, the prediction and the experimental outcome when activity is absent do not conflict: low levels of proBDNF secretion would be insufficient to cause axon degeneration and retraction, and as a result, refinement would not occur. However, in this model, competing axons are acting directly on each other, without any involvement from the postsynaptic cell, which contradicts the evidence that postsynaptic activity and calcium influx are important for refinement.

Several other variations of the neurotrophic factor hypothesis have been proposed, and experimental manipulations of trophic factors such as BDNF or their receptors can lead to defects in the development of circuits (Cao *et al*., 2007; Deppmann *et al*., 2008). While some aspects of these models are interesting and hold potential, it remains a challenge to

determine whether trophic factors are involved in refinement outside of their well-established roles in neurite outgrowth and synaptic plasticity.

1.2.2 Model II: The classical complement cascade

Large-scale screening technologies, such as gene-expression arrays, have often been used in an attempt to identify key molecular players that regulate refinement. One candidate, C1q, which activates the classical complement cascade, has recently gained traction for its proposed role in refinement. The complement cascade is known primarily for its role in initiating an immune response to remove pathogens, foreign cells or debris. C1q recognizes, binds and coats foreign material, and forms a complex with other complement proteins to cleave C3 into an activated form. Activated C3 fragments are recognized by phagocytes, macrophages and microglia expressing the C3 receptor (CR3), which engulf the tagged material through phagocytosis (Stephan *et al*., 2012).

The classical activation pathway of the complement cascade was first implicated in synapse elimination in the retinogeniculate projection by Stevens *et al*., (2007). They proposed that C1q activates the complement cascade to tag synapses for elimination by microglia (Schafer *et al*., 2012; Stevens *et al*., 2007). As evidence, the authors showed that C1q and C3 expression were upregulated during the developmental period when RGC projections to the LGN refine, and there appeared to be some colocalization between C1q and synaptic markers. In mice with deletions in C1q or C3, RGC axons did not completely segregate into eye-specific layers and did not fully refine at the LGN; LGN neurons, which normally receive 1–2 inputs, were innervated by over 4 inputs. And, microglia preferentially engulfed presynaptic terminals from TTX-treated RGCs in a C3/CR3-

dependent manner (Schafer *et al*., 2012). Despite the defects in elimination, the selective strengthening of one input over the others remained intact.

Based on these results, it is premature to consider the complement cascade a mechanism of refinement because the model is incomplete. Most importantly, there is no evidence to show that activity acts on the complement cascade to determine which synapses are eliminated and which are maintained. As it stands, other mechanisms more directly downstream of activity are responsible for selecting specific synapses for elimination, and the complement cascade is recruited (possibly via TGF-β, Bialas and Stevens, 2013) merely as a method to disassemble a synapse or to remove the cellular debris that is generated in the process. In addition, the evidence that C1q tags synapses for disassembly is weak. Although C1q colocalized with synaptic markers, the synapses were not tracked, and the fates of these C1q-positive synapses is not known. There is no evidence to indicate that synapses tagged by C1q are subsequently disassembled. Furthermore, the complement cascade does not appear to have any role in stabilizing synapses; the proposed mechanism only describes removal of synaptic components, and C1q KO or C3 KO mice continue to exhibit selective strengthening of inputs. Therefore, if the complement cascade were involved in refinement, then several other mechanisms would be necessary to link its recruitment to neural activity and to stabilize and strengthen the persisting axons.

Here, I have focused on BDNF and C1q as candidate molecules involved in refinement. Several other candidates, such as semaphorin 3A and caspase-3, have been identified through large-scale screens, and when inhibited or deleted, led to defects in refinement (Uesaka *et al*., 2014; Wang *et al*., 2014). While initial results often seemed

interesting and appeared to hold potential, they were usually not revisited after one or two publications. Although these candidates have each been shown to individually disrupt refinement, it appears that no effort has been made to unify them under the same model. An understanding of how they interact with each other, and whether they function in the same pathways, may help us develop new models for the mechanisms that underlie refinement.

To date, the identity of the molecules that activity acts on to coordinate the strengthening of some inputs and the elimination of others remain unknown. In developing these current molecular models for refinement, the primary focus remained narrowly at the level of synapses and individual neurons. However, refinement is much more complex than merely maintaining the strongest connections and eliminating the weakest. The approaches described above cannot explain how specificity between neurons and their targets is developed in the context of a circuit, where signals are integrated and filtered through several neurons before they reach their intended distal targets. There must be long-range, activity-dependent anterograde and retrograde signals that travel across synapses, which help to determine which connections are appropriate and should be maintained and to identify inappropriate connections for elimination. Developing and testing a model from this new perspective would improve our understanding of the molecular players and the mechanisms that regulate refinement.

1.3 Part C: What morphological changes correlate with refinement?

During early postnatal development, as connections refine, axons and dendrites undergo a considerable amount of growth and remodelling: dendrites branch and extend to

form elaborate arbours as axons expand their innervation on some targets, and withdraw from others. Just as activity is important for refinement, it is regarded to be essential for dendritic growth as well, and maximal dendrite extension tends to coincide with peak synapse formation during the early postnatal period (Redmond and Ghosh, 2005). It is well accepted that afferent synaptic activity elevates intracellular calcium levels postsynaptically, activating several signalling pathways that collectively regulate dendritic growth (Redmond, 2008). The molecular mechanisms that underlie these pathways have been described in detail in many review articles, and the idea that synaptic activity is necessary for dendritic growth has remained mostly unchallenged.

The relationship between afferent activity and dendritic growth has also been demonstrated *in vivo*. Increasing sensory experience enhances dendritic extension and retraction, whereas sensory deprivation or pharmacological block of receptors lead to defects in dendritic growth (Sin *et al*., 2002; Wong and Ghosh, 2002). Naturally, these results are often interpreted as direct, anterograde effects. Yet, increasing activity in one population of neurons also increases activity in the rest of the circuit. And, when activity is globally blocked, overall circuit activity is depressed, making it difficult to attribute changes in morphology solely to anterograde effects. Furthermore, reducing activity may also result in the unintended elimination of their axon projections. For example, when Hubel and Wiesel performed their monocular deprivation experiments, they examined the visual pathway for anatomical changes. They discovered that LGN neurons in the layers receiving RGC inputs from the deprived eye were smaller in size (Wiesel and Hubel, 1963a). Initially, this atrophy of LGN neurons was attributed to the loss of afferent synaptic stimulation as a result of sensory deprivation. However, an equally plausible explanation is that these LGN

neurons had fewer terminals in the primary visual cortex than those innervated by RGCs from the open eye, and therefore received lower quantities of retrograde target-derived trophic support from cortical neurons (Guillery, 1972; Wiesel and Hubel, 1963b).

Despite these cautionary results, the impact of manipulating activity on downstream targets, and the possibility that some of these activity-dependent effects may be mediated indirectly in a retrograde manner is often overlooked. To circumvent this issue, Lu *et al*. (2013) developed an approach to eliminate excitatory input onto individual CA1 pyramidal neurons while neighbouring neurons remained active, thereby leaving circuit activity intact. To generate this model, Lu *et al*. used a quadruple conditional KO mouse, in which the genes encoding AMPAR subunits GluA1-3 and NMDAR subunit GluN1 were floxed, and at P0, delivered a low concentration of an adeno-associated virus expressing GFP-Cre. This approach allowed Lu *et al*. to eliminate excitatory synaptic transmission from a sparse population of CA1 neurons. Three to five weeks later, these neurons were examined morphologically. Given the evidence that neural activity is necessary for dendritic growth, one would expect that in the absence of excitatory inputs, Cre-expressing neurons would show severe defects in dendritic morphology. However, these neurons were morphologically identical to control neurons in all observable aspects, including dendritic length and number of branch points (Lu *et al*., 2013).

These results contradict an abundance of literature indicating that neuronal activity plays essential roles in the development of the nervous system. Dendritic growth appears to be regulated, at least in part, by signals secreted either by active neighbouring neurons and/or by retrograde signals originating from downstream targets. Indeed, in the sympathetic nervous system, target size is correlated to dendrite size (Voyvodic, 1989),

suggesting that afferent activity and target-derived retrograde signals have shared roles in dendritic regulation.

These unexpected results indicate that our understanding of how activity influences early postnatal development of the nervous system needs to be revisited. Recent advancements in genetic tools have enhanced our ability to develop new mouse models that will allow us to manipulate activity in novel ways. These approaches will generate opportunities to further dissect these issues by isolating local, synaptically-mediated effects from global, circuit-wide ones.

1.4 Summary and unresolved questions

Divergence of presynaptic axons and convergence of inputs onto the same target generates an overproduction of connections at birth, which results in diffuse and imprecise circuits. To improve function, circuits refine as they become active during early postnatal development: asynchronous activity between competing axons drives a competitive process that requires postsynaptic activity and eliminates excess inputs. Meanwhile, persisting axons strengthen their connections by forming additional synapses as dendrites branch and extend. Through refinement, circuits function more efficiently and with greater precision. The current molecular models of refinement do not fully explain this process, and many unresolved questions remain:

1. Is refinement mediated locally at each individual synapse or by long-range anterograde and retrograde signals that are integrated and processed at a circuit level?

2. What is the "default" state of refinement? Do all connections persist until activity triggers elimination or are all connections destined to be eliminated while some are stabilized by activity?
3. Is the disassembly of a synapse initiated by the postsynaptic neuron, causing presynaptic axon terminals to retract? Or do competing axons use an activity-dependent retrograde signal generated by the postsynaptic neuron to determine which branches to withdraw and which to strengthen?
4. Why does presynaptic activity need to be asynchronous in order to drive competition?
5. Is the source of activity important? Is synaptic activity essential or would depolarizing the neuron (ex. via channelrhodopsin expression and stimulation) be sufficient to cause inputs to refine?
6. Is the strengthening of one input necessary to drive elimination of competing inputs? Can elimination take place without the strengthening of persisting inputs?
7. Can neurons maintain dendrites that do not receive functional innervation?
8. Do axons grow and form synapses if they do not receive an activity-dependent retrograde signal from the postsynaptic target?
9. How is wiring specificity within a circuit generated?
10. What are the short and long-range anterograde and retrograde molecular signals that mediate refinement?

1.5 Objectives and rationales

The main objective of my doctoral research was to improve our understanding of the mechanisms that underlie refinement by addressing some of the unresolved questions listed above. In particular, my goal was to investigate how activity governs the reorganization of neural connections with a focus on testing how local synaptic activity and circuit-wide activity interact to coordinate refinement. Specifically, my aims were to:

1. Establish how circuits develop in the absence of activity by examining their function and morphology.

   Rationale: This will serve as a baseline for subsequent experiments (aims 2 and 3), in which I will evaluate how manipulating activity or signalling pathways will influence or possibly rescue the development of inactive circuits. Given the ample evidence that activity is important for competition and elimination, I expect circuits that develop without activity to have severe functional and morphological defects: connections should not refine, and dendritic growth will be stunted.

2. Differentiate between the contributions of local synaptic activity and overall circuit activity on refinement by generating and examining a novel mouse model in which silent synapses are intermingled with active synaptic connections.

   Rationale: When overall circuit activity is abolished, it is difficult to interpret the results because the precise cause of the developmental defects is ambiguous. However, we can circumvent this issue by examining how silent connections develop while in the presence of active ones to learn more about the specific roles of presynaptic activity, postsynaptic activity and downstream targets. For example, if an axon encountered two intermingled populations of neurons: some active and

others inactive, i) would they form silent synapses on inactive neurons? If so, ii) would the silent synapses persist or would they be eliminated during refinement? From the perspective of the axon, one reasonable expectation would be to withdraw connections from silent neurons and consolidate those on active neurons. On the other hand, if postsynaptic activity is necessary to mediate competition between axons, then connections onto silent neurons may not refine.

3. Identify signalling pathways downstream of activity that mediate synaptic refinement, and test their involvement by examining whether enhancing the pathway in the absence of activity can rescue defects in development.

   Rationale: Presumably, activity must be acting on several downstream pathways in the postsynaptic neuron to regulate refinement. While transcription factors and post-translational modifications are known to be upregulated in response to neural activity, the regulation of cap-dependent translation by activity has not yet been explored. Several pathways, including those mediated by intracellular calcium or neurotrophin binding, converge to enhance cap-dependent translation by promoting phosphorylation of 4E-BP, which enhances cap-dependent translation (Ma and Blenis, 2009). However, whether 4E-BP has a role in mediating refinement has not been tested.

1.6 The sympathetic nervous system as a model for circuit refinement

For my research, I examined how connections develop and refine during the early postnatal period in sympathetic circuits. Specifically, I focused on the superior cervical ganglion (SCG), which offers several advantages for my experiments. The SCG is the largest

of the three cervical ganglia, and is easily accessible for many different types of experiments. Its structure is well suited for circuit tracing and electrophysiology experiments, and its inputs and outputs are clearly mapped out, allowing me to probe connections in the circuit beyond those in the SCG. However, the most appealing property, particularly for studying activity-dependent refinement, is that sympathetic neurons only receive one type of excitatory input and no inhibitory inputs. Therefore, by manipulating the expression of postsynaptic receptors we can alter the activity of the circuits.

The sympathetic branch of the autonomic nervous system is best known for its role in generating a rapid and involuntary "fight-or-flight" reaction in response to stress. When activated, sympathetic neurons prepare the body for action by releasing epinephrine; effects include a rise in heart rate and blood pressure, pupil dilation, and increased perspiration (Glebova and Ginty, 2005). Because most of these functions are unnecessary in the stable prenatal environment maintained by the mother, sympathetic activity is low during prenatal development. After birth, sympathetic circuits become a lot more active in order to cope with dynamically changing external environments. Therefore, I can study circuits at birth when there has been minimal activity, and also study them as they become active during postnatal development and as their connections refine.

1.6.1 Embryonic development of the superior cervical ganglion (SCG)

During embryogenesis, between embryonic day 12 (E12)–E14, precursor cells from the neural crest migrate and accumulate next to cervical segments C1-5 to form a primitive SCG. As the cells proliferate via mitosis and mature into sympathetic neurons, they begin to extend processes that resemble axons and immature dendrites (Rubin, 1985a).

Simultaneously, preganglionic axons originating from C8-T4 segments of the spinal cord arrive through the caudal end of the SCG and rapidly begin to form functional synapses (Rubin, 1985b). Synapses are initially formed on the cell soma because few dendrites have developed. As sympathetic neurons begin to extend dendrites, synapses become preferentially targeted to the dendrites, such that by birth, ~85% of synapses reside on the dendritic arbour (Rubin, 1985c). The axons of sympathetic neurons exit the SCG at the rostral end, and innervate targets in the head and neck, including the pineal gland, blood vessels such as the circle of Willis, and the iris.

1.6.2 Specificity of connections in the sympathetic circuit

The distinct isolation of the preganglionic "input" and postganglionic "output" nerves at opposite ends of the SCG facilitates circuit tracing and labelling experiments as well as electrophysiological experiments. Through these types of experiments and a combination of anterograde and retrograde labelling, it has been shown that there is no topographic relationship between spinal segment and end location of axon terminals within the ganglion, and groups of sympathetic neurons that innervate the same target are not clustered within the SCG (Rubin, 1985b). However, in adult SCG, preganglionic axons originating from the same spinal segment tend to innervate a corresponding population of sympathetic neurons scattered in the SCG that all project to the same target, and how this specificity is established is unknown (Nja and Purves, 1977; Rubin, 1985b).

1.6.3 Developmental refinement in the SCG

The SCG is a classic model for refinement, and the elimination of inputs during postnatal development has been described in detail. At birth, each preganglionic axon branches to innervate ~100 sympathetic neurons, whereas in the adult, many branches have retracted, and a single preganglionic axon innervates only ~20–30 sympathetic neurons. This elimination of connections is reflected in the number of inputs innervating a sympathetic neuron. At birth, each sympathetic neuron is innervated by ~7–9 preganglionic inputs, whereas sympathetic neurons in the adult receive inputs from ~2–4 preganglionic axons. In total, an estimated 700–800 preganglionic axons innervate 10,000–12,000 sympathetic neurons in the adult mouse SCG (Deppmann *et al*., 2008; Purves *et al*., 1986).

1.6.4 Manipulating activity in the SCG through two genetic mouse models

All synaptic transmission in sympathetic ganglia is mediated by nicotinic cholinergic synapses; sympathetic neurons do not receive any other type of excitatory or inhibitory inputs. Postsynaptic nicotinic acetylcholine receptors (nAChRs) are pentamers composed of two α3 subunits and three β4 subunits. When the α3 subunit gene is deleted, the receptors do not form, and synaptic transmission is abolished (Rassadi *et al*., 2005; Xu *et al*., 1999). For my experiments, I used two mouse models: in one model (α3 KO), all sympathetic neurons lack nAChRs and all connections in the SCG are electrophysiologically silent; and in the second model, we randomly intermingled sympathetic neurons with postsynaptic receptors and those without receptors in equal proportions, creating mosaic ganglia. In this model, the incoming axons have a choice between making functional

synapses on neurons with receptors, or silent synapses on neurons without receptors. Together, these two mouse models allow me to compare how inactive circuits develop when in the complete absence of circuit activity (α3 KO) and when neighbouring neurons are active and circuit activity is intact.

Chapter 2: Experimental models and methods

2.1 Mouse models

The data described in Chapters 3–7 were collected from five mouse models: WT, α3 KO, $X^{\alpha 3}X^{RFP}$ mosaic, 4E-BP KO, and α3/4E-BP DKO. All genotyping was performed by PCR, and primer sequences can be found in Figure 2.1D. Experiments were conducted on both male and female mice and all procedures for animal handling were carried out according to the guidelines of the Canadian Council on Animal Care.

2.1.1 α3 KO model

Mice with a deletion in the α3 nAChR subunit gene (Figure 2.1A) were maintained on an outcrossed background because inbred C57BL/6J α3 KO mice die during the first week after birth (Krishnaswamy and Cooper, 2009; Xu *et al*., 1999). Briefly, inbred C57BL/6J α3+/– mice were mated to CD-1 WT mice and F1 α3+/– heterozygotes were used as breeders to produce α3 KO mice and WT littermates on a mixed C57BL/6J x CD-1 background.

2.1.2 $X^{\alpha 3}X^{RFP}$ mosaic model

α3 rat cDNA was ligated into a previously modified Gateway entry vector pENTR1a between the human ubiquitin C promoter (UbiC) and bovine growth hormone polyA site (Yurchenko *et al*., 2007). The pENTR1a entry vector was then recombined *in vitro* into the HPRT gateway destination vector, which contained homology arms for the HPRT locus on the X chromosome (Figure 4.1C). The recombined vector was electroporated into BK4 embryonic stem (ES) cells, which have a partial deletion in the HPRT gene (promoter and exons 1 and 2). Successful homologous recombination inserts the UbiC-α3 construct upstream (5') of the HPRT gene and restores HPRT expression, which confers resistance to

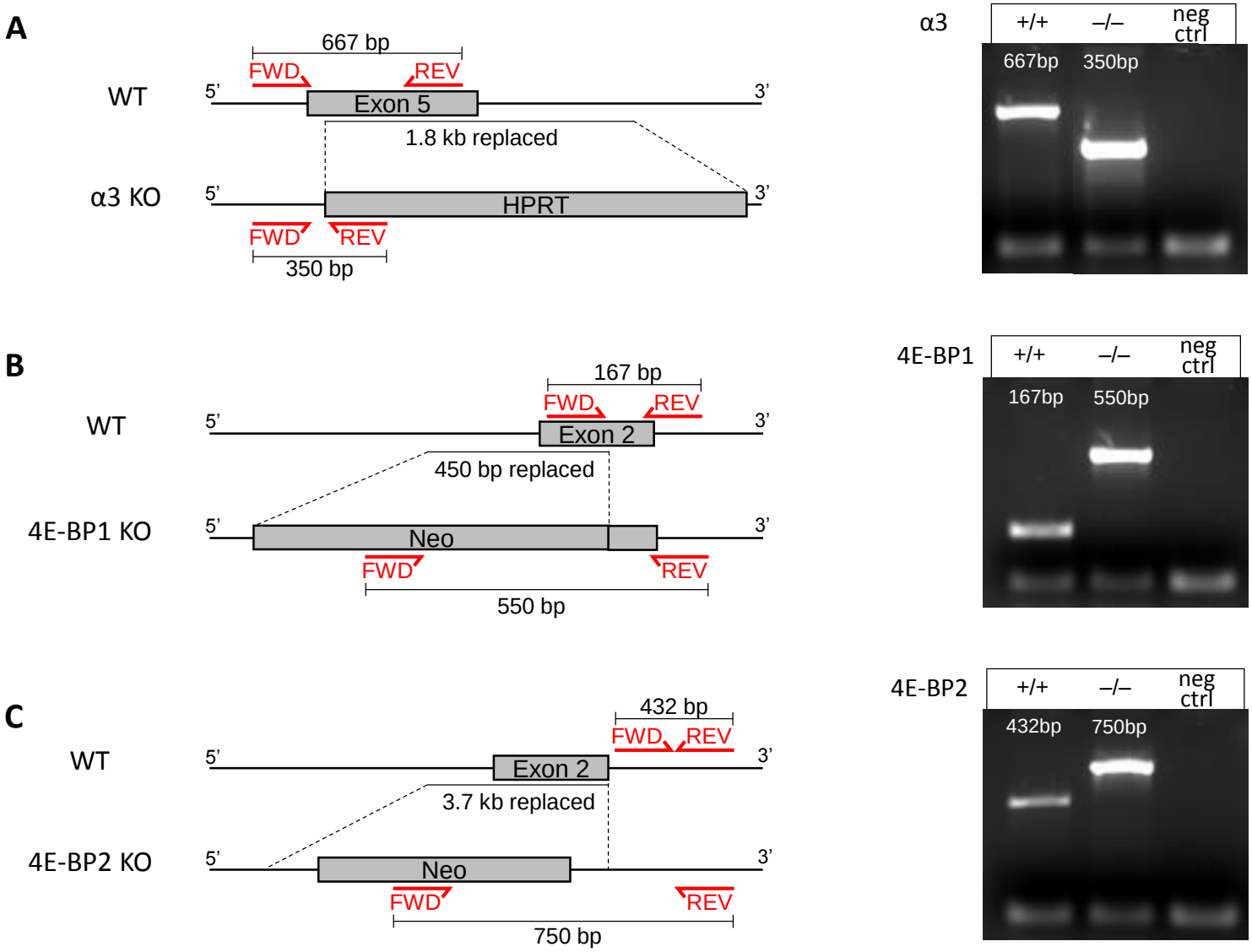

D

Gene		Primer sequence (5' – 3')
α3	WT	FWD: GTT ATG CAC GGG AAG CCA GGC TGG REV: GAC TGT GAT GAC GAT GGA CAA GGT GAC
	KO	FWD: GTT ATG CAC GGG AAG CCA GGC TGG REV: TGG CGC GAA GGG ACC ACC AAA GAA CGG
4E-BP1	WT	FWD: GAT GGA GTG TCG GAA CTC ACC REV: GAC CTG GAC AGG ACT CAC CGC
	KO	FWD: GCA TCG AGC GAG CAC GTA CTC REV: GAC CTG GAC AGG ACT CAC CGC
4E-BP2	WT	FWD: GGG TGG ACT GTC GGT CTT CTG REV: CAG CAC CTG GTC ATA GCC GTG
	KO	FWD: GCA TCG AGC GAG CAC GTA CTC REV: CAG CAC CTG GTC ATA GCC GTG
$X^{\alpha 3}$		FWD: GCA GTG CAC CCG TAC CTT TGG GAG REV: CTT AAA GAT GGC CGG CGG GAT CC
X^{RFP}		FWD: GCA GTG CAC CCG TAC CTT TGG GAG REV: CGT AGG CCT TGG AGC CGT ACT GG

Figure 2.1

Figure 2.1 Experimental mouse models: α3, 4E-BP1 and 4E-BP2 genes.

(**A**-**C**) Genotyping of (**A**) α3, (**B**) 4E-BP1 and (**C**) 4E-BP2 KO mice were performed by PCR.

Left: Diagrams show WT and KO alleles for α3, 4E-BP1 and 4E-BP2. The binding locations of the forward (FWD) and reverse (REV) primers used for genotyping are indicated in red.

Right: PCR amplicons run on an agarose gel; the numbers above each band correspond to expected amplicon sizes.

(**D**) Primer sequences from A-C and for $X^{\alpha 3}$ and X^{RFP} alleles in the mosaic mouse model.

0.1mM hypoxanthine, 0.0004mM aminopterin, 0.016mM thymidine (HAT). HAT-resistant ES cells were injected into blastocysts that were transplanted into recipient females. Chimeric progeny that had germline expression of UbiC-α3 from the X chromosome were crossed with α3 KO mice and with X^{RFP} mice (Yurchenko *et al*., 2007) to generate the α3 KO; $X^{\alpha 3}X^{RFP}$ mouse model (Figure 4.1D).

2.1.3 4E-BP KO and α3/4E-BP DKO models

4E-BP1/4E-BP2 double knockout (DKO) mice (Figures 2.1B, C; (Banko *et al*., 2005; Tsukiyama-Kohara *et al*., 2001) were provided by Dr. Nahum Sonenberg, McGill University, and are referred to as 4E-BP KO mice. 4E-BP KO mice were crossed with α3+/– mice to generate 4E-BP1/2 KO; α3 KO mice, which are referred to as α3/4E-BP DKO mice.

2.2 Electrophysiological recordings

SCG were acutely dissected in oxygenated Tyrode's solution (pH 7.4) supplemented with glucose (5.6mM) and choline (0.01mM), and pinned down securely with minutia pins on a Sylgard-coated petri dish. To record nerve-evoked postganglionic compound action potentials (CAPs), a suction electrode connected the preganglionic nerve to a stimulator (Stimulus Isolator, model A365; World Precision Instruments, Sarasota, FL) and CAPs were recorded from the postganglionic nerve with a suction electrode connected to differential amplifier (DP-301; Warner Instruments); the signals were amplified 1000X, filtered at 300Hz and 10kHz, and digitized at 10kHz.

To record intracellularly from ganglion cells, 80–120mΩ glass microelectrodes (G150F-4; Warner Instruments, Hamden, CT) were made with a DMZ universal puller (Zeitz Instruments, Munich, Germany). Stable intracellular recordings were achieved with a

high inertial precision microdrive (Inchworm 8200; EXFO, Quebec, Canada) attached to a micromanipulator (SM11; Narshige, Tokyo, Japan or MPC-200/ROE-200; Sutter Instruments, Novato, CA) that drove the electrode through the ganglion at 4μm steps. The recording electrode was filled with 1M KAc. To measure dendrites and synaptic targeting on Ad-α3 infected neurons in P60 α3 KO rescue mice or to confirm the identity of neurons in mosaic SCG of $X^{\alpha3}X^{RFP}$ mice, intracellular electrodes were filled with 10mM Alexa Fluor 488 hydrazide (Thermo Fisher Scientific, Waltham, MA) in 200mM KCl. The recording electrode was connected with a silver chlorided wire to the head stage of an Axoclamp 2A amplifier (Axon Instruments, Union City, CA) used in current-clamp mode to deliver depolarizing or hyperpolarizing current pulses through the recording electrode. Ionic currents were filtered at 3kHz (low-pass cutoff) and 1Hz (high-pass cutoff) and digitized at 50kHz. Stimulation and data acquisition were performed with N-Clamp (Neuromatic, UK) and offline data analysis was performed using Igor Pro (WaveMetrics, Lake Oswego, OR).

2.2.1 Estimating the number of inputs converging onto a neuron

To measure the convergence of preganglionic axons innervating a sympathetic neuron, the preganglionic nerve was stimulated with voltages of increasing strength while holding the neuron at approximately –90mV to prevent EPSPs from triggering action potentials. In some experiments, the sodium channel blocker QX314 was also included in the recording electrode to prevent action potentials. At maximal stimulus strength, the $EPSP_{max}$ is the sum of the EPSPs evoked by each of the axons innervating that neuron (Eq. 1). Increasing the strength of the stimulus to the preganglionic nerve activates axons of different threshold, which results in discrete jumps in the amplitude of the EPSPs. I used these discrete jumps as a measure of the number of axons innervating the neuron. To isolate the

EPSP evoked by individual axons, I averaged at least 10 traces for each discrete jump to obtain the average EPSP evoked by that axon and all axons of lower threshold, and subtracted from it the average EPSP evoked only by axons of lower threshold (Eq. 2).

For N axons innervating a neuron,

Eq.1

$$EPSP_{max} = \sum_{n=1}^{N} EPSP_n$$

To isolate the $EPSP_n$ evoked by axon n,

Eq. 2

$$EPSP_n = \sum_{n=1}^{n} EPSP_n - \sum_{n=1}^{n-1} EPSP_{n-1}$$

2.2.2 Calculating the disparity index (DI)

To calculate the disparity index (DI) for each neuron, I divided the standard deviation (SD) of the EPSPs by the mean (M) EPSP (Eq.3; Hashimoto and Kano, 2003).

Eq. 3

$$DI = SD/M$$

where

$$SD = \sqrt{\frac{\sum_{n=1}^{N}(EPSP_n - M)^2}{N-1}}$$

$$M = EPSP_{max}/N$$

2.3 Adenoviruses

Full-length α3 neuronal nAChR subunit cDNA was ligated into pAdTrack-synapsin 1 (Ad-α3/Syn), and replication-deficient viral vectors were generated (He *et al*., 1998) and titered in duplicate with Adeno-X Rapid Titer Kit, (Clontech Lab, Mountain View, CA) (Krishnaswamy and Cooper, 2009). The synapsin promoter was only active in SCG neurons for ~2 weeks; to express α3 for longer times, the human ubiquitin C promoter was used (Ad-α3/Ubi; Schorpp *et al*., 1996).

I infected mice with either Ad-α3/Syn or Ad-α3/Ubi adenovirus at a concentration of $\sim 10^7$pfu/mL diluted in sterile 1X PBS. For P0–P1 pups, I injected ~50μL into the temporal vein, for pups up to P21, I injected 100–150μL into the intraperitoneal cavity (IP), and for P21 mice or older, I injected 200–300μL into the tail vein (IV). Injections were performed using a 29G x 1/2" 1mL insulin syringe (Bencton Dickinson, Franklin Lakes, NJ).

2.4 Confocal imaging

Images were acquired on an upright confocal microscope (BX-61W, Olympus) with a 60X, N.A. 1.42 PlanApo N oil-immersion objective at a scan speed of 8μs/pixel and an image depth of 12 bits. Laser lines were activated sequentially to avoid bleed-through of signals. All image analysis was performed with FIJI/ImageJ (NIH, Bethesda, MD).

2.5 Lipophilic tracer labelling for dendrite morphology and axonal targeting

I used lipophilic tracers 1,1'-Dioctadecyl-3,3,3',3'-tetramethylindocarbocyanine perchlorate (DiI) and 3,3'-Dioctadecyloxacarbocyanine perchlorate (DiO) (Thermo Fisher Scientific) to sparsely label a random subset of preganglionic axons and postsynaptic neurons in the

SCG. When used to quantify dendritic morphologies, this method is preferable to labelling with intracellular dye injection because it avoids selection bias for neurons with large cell bodies. Briefly, freshly dissected ganglia with intact pre- and postganglionic nerves were fixed in 1% PFA (pH 7.4) in 0.1M PB for 2 hours at room temperature, rinsed with 1X PBS, and embedded in 3% agarose Type I-B (Sigma-Aldrich, St. Louis, MO) dissolved in 1X PBS. A scalpel blade was used to slice through the pre- and postganglionic nerves to expose a cross-sectional area of the nerve. Platinum wires were used to gently apply fine crystals of DiI to the preganglionic nerve to label preganglionic axons, and DiO to the postganglionic nerve to label sympathetic neurons and their dendritic structures. After labelling, ganglia were kept in the dark in 1X PBS for 5–6 days to allow for tracers to diffuse along lipid membranes. Excess DiI and DiO were removed and ganglia were sliced into 100μm sections with the Compresstome VF-200 (Precisionary Instruments Inc., Greenville, NC) using a solid zirconia ceramic injector blade (Cadence Inc., Staunton, VA). Sections were either mounted with Vectashield (Vector Laboratories, Burlingame, CA) and immediately imaged, or first processed with immunohistochemistry before mounting and imaging.

Dendrite analysis: Images of DiO-labelled neurons were acquired at a pixel size of 0.172μm/pixel and an optical thickness of 0.37μm/slice. Only neurons with complete dendritic arbours and an identifiable axon were analyzed. For neurons with a dendritic arbour that extended beyond one field of view, neighbouring z-stacks were acquired and stitched together with XuvTools (Emmenlauer *et al*., 2009). To quantify the length and number of dendritic branches, I reconstructed neurons in 3-D and used the Simple Neurite Tracer plugin (Longair *et al*., 2011) to trace dendrites. Primary dendrites were categorized as those directly leaving the cell body, while secondary branches extended off primary

dendrites. Thin protrusions shorter than 5μm were considered dendritic filopodia and not counted as branches.

For representative images, I removed DiO-labelled neurites of other neurons from the field of view for clarity. On each plane of the z-stack, I eliminated all DiO-labelled neurites that were not connected to the dendritic arbour of the neuron of interest, as determined by 3-D reconstruction and dendritic tracing. After removing non-connected neurites, the z-stack was used to produce a maximum intensity z-projection of the neuron. For illustration purposes, figures show the maximum intensity z-projections.

Preganglionic axonal targeting: Images were acquired at a pixel size of 0.188μm/pixel and an optical thickness of 0.4μm/slice. To estimate the percentage of the cell body surface covered by an axon, I measured the circumference of the cell body (DiO-labelled from postganglionic nerve), and the proportion of the cell body circumference occupied by an axon (DiI-labelled from preganglionic nerve) on each plane of the cell body. The total surface area was calculated from the circumference of the cell body on each plane multiplied by the optical thickness. Figures show 3-D reconstructions of DiO-labelled neurons innervated by a DiI-labelled preganglionic axon(s).

2.6 Immunohistochemistry

For immunohistochemical staining experiments, the fixation, permeabilization, incubation times, and antibody concentrations were optimized for each antibody and tissue type; detailed descriptions for these steps are provided in the sections below. Briefly, tissue samples were fixed with PFA, rinsed with 1X PBS after fixation, and incubated in blocking solution for 1–2 hours at room temperature. Samples were transferred directly from

blocking solution to the primary antibody solution. Primary antibodies were diluted in blocking solution, and samples were incubated on a shaker for 24–48 hours at 4°C. After rinsing with 1X PBS, samples were incubated in secondary antibodies, which were diluted in 10% donkey serum (Millipore, Billerica, MA) in 1X PBS, for 1–2 hours at room temperature. Samples were rinsed with 1X PBS and mounted onto slides with Vectashield for imaging.

2.6.1 VAChT staining on DiO-labelled SCG neurons for synaptic targeting

SCG were fixed and the postganglionic nerve was labelled with DiO and incubated in the dark for 5–6 days as described above. Labelled SCG were sliced into 100μm sections, and incubated in blocking solution for 2 hours at room temperature [Blocking solution: 10% normal donkey serum and 0.3% Tween 20 (Fisher Scientific, Waltham, MA) in 1X PBS], in the primary antibody for 48 hours at 4°C [Primary antibody: Rabbit anti-VAChT (1:3000; Synaptic Systems)], and in secondary antibody for 2 hours at room temperature [Secondary antibody: Alexa Fluor 647 goat anti-rabbit (1:500; Thermo Fisher Scientific)]. This method was also used on Alexa Fluor 488 hydrazide-filled Ad-α3 infected neurons in P60 α3 KO rescue mice.

Synaptic targeting analysis: Images were acquired at a pixel size of 0.22μm/pixel and an optical thickness of 0.45μm/slice. To examine synaptic targeting, I identified VAChT puncta located on a neuron of interest on each plane of a z stack. To be counted as a synapse, VAChT puncta must (i) colocalize with the DiO membrane label, (ii) be at least 0.5μm in diameter, and (iii) span at least two optical slices. Synapses were categorized as being on the cell body or on the dendritic arbour. The density of synapses on the cell body was calculated by dividing the number of synapses on the cell body by the total surface area of

the cell body. To estimate the surface area of the cell body, I measured the circumference of the cell body on each plane and multiplied the circumference by the thickness of the optical slice. To calculate the density of synapses on the dendrites, I divided the number of synapses on the dendrites by the total dendritic outgrowth (TDO). TDO was measured using 3-D reconstructed neurons and the Simple Neurite Tracer plugin as described above. For representative images, VAChT puncta that were not located on the neuron of interest were eliminated for clarity. To clearly illustrate the location of VAChT puncta, maximum intensity z-projections of DiO-labelled SCG neurons were thresholded and skeletonized, and the locations of VAChT puncta were clearly identified with a red circle.

2.6.2 VAChT and PSD-93 staining

SCG were dissected and immediately sliced into 100μm sections. Sections were fixed in 2% PFA (pH 6.0) in 0.1M PB for 10 minutes at room temperature. Sections were incubated in blocking solution for 1 hour at room temperature [Blocking solution: 10% normal donkey serum, 0.3% Tween 20 in 1X PBS], in primary antibodies for 48 hours at 4°C [Primary antibody: Rabbit anti-VAChT (1:3000; Synaptic Systems) and Mouse anti-PSD-93, clone N18/30 (1:300; NeuroMab, Davis, CA)], and in secondary antibodies for 1 hour at room temperature [Secondary antibody: Alexa Fluor 647 goat anti-rabbit (1:500; Thermo Fisher Scientific) and Alexa Fluor 568 goat anti-mouse IgG1 (1:500; Thermo Fisher Scientific)].

Colocalization analysis: Images were acquired at a pixel size of 0.22μm/pixel and an optical thickness of 0.47μm/slice. Images were split into separate channels for VAChT puncta and PSD-93 puncta, and thresholded. For each optical slice, regions of interest (ROI) representing puncta were generated for each channel, and those with an area greater than

0.2μm^2 were counted. Overlapping ROIs on each optical slice were considered colocalized puncta.

2.6.3 P-4E-BP, NP-4E-BP and MAP-1A staining

Staining on WT and α3 KO SCG were performed in parallel. SCG were dissected and immediately fixed in 2% PFA (pH 7.4) in 0.1M PB with 5mM EGTA (to chelate Ca^{2+} ions released from intracellular stores by fixation) for 1 hour at room temperature. After fixation, ganglia were sliced into 100μm sections and incubated in blocking solution for 1 hour at room temperature [Blocking solution: 10% normal donkey serum, 0.3% Tween 20, and 0.05% Triton X-100 (Fisher Scientific) in 1X PBS], in primary antibodies (P-4E-BP with MAP-1A or NP-4E-BP with MAP-1A) for 48 hours at 4°C [Rabbit anti-P-4E-BP (1:600; Cell Signaling, Danvers, MA), rabbit anti-NP-4E-BP (1:600; Cell Signaling), goat anti-MAP-1A (1:360; Santa Cruz Biotechnology, Dallas, TX)], and in secondary antibodies for 1 hour at room temperature [Secondary antibodies: TRITC donkey anti-rabbit (1:500; Jackson ImmunoResearch Laboratories) or Alexa Fluor 488 donkey anti-rabbit (1:500; Thermo Fisher Scientific) and Alexa Fluor 647 donkey anti-goat (1:500; Thermo Fisher Scientific)].

Fluorescence intensity analysis: A z-stack of 20 images were acquired at a pixel size of 0.22μm/pixel and an optical thickness of 0.45μm/slice. All image acquisition parameters (HV, gain, offset, laser power) were kept constant between samples. For intensity analysis, each stack was used to generate a summed z-projection. Regions of interest (ROI), each consisting of one neuronal cell body, excluding the nucleus, were selected from the MAP-1A channel. Average fluorescence intensity for each ROI was measured from the MAP-1A channel, and ROI were transferred to the P-4E-BP1 channel or

the 4E-BP1 channel to measure the corresponding fluorescence intensity. Figures show maximum intensity z-projections.

2.6.4 Sympathetic innervation of the iris

Irises were dissected from albino mice and fixed with 2% PFA (pH 6.0) in 0.1M PB for 10 minutes at room temperature. To achieve a consistent state of contraction between samples, carbachol was added to the fixative at a final concentration of 500μM. During fixation, irises were left attached to the cornea to maintain the structure, and carefully separated from the cornea with a scalpel blade after fixation. Irises were incubated in blocking solution for 1 hour at room temperature [Blocking solution: 10% normal donkey serum, 0.3% Tween 20, and 0.1% Triton X-100 in 1X PBS], in primary antibodies for 24 hours at 4°C [Primary antibodies: Mouse anti-tyrosine hydroxylase (TH) clone LNC1 (1:500; Millipore) and rabbit anti-vesicular monoamine transporter 2 (1:1000; Phoenix Pharmaceuticals, Burlingame, CA)], and in secondary antibodies for 1 hour at room temperature [Secondary antibodies: Alexa Fluor 405 goat anti-rabbit (1:500; Thermo Fisher Scientific) and Alexa Fluor 647 goat anti-mouse IgG1 (1:500; Thermo Fisher Scientific)].

Iris innervation analysis: Images were acquired at a pixel size of 0.22μm/pixel and an optical thickness of 0.44μm/slice. All image acquisition parameters (HV, gain, offset, laser power) were kept constant between samples. Images were taken at the radial muscles halfway between the inner (pupil) and outer (attachment to sclera) edge of the iris. Z-stacks were split into separate channels for TH and VMAT2, and the same threshold values for each channel were applied to both WT and α3 KO samples. On each channel, I recorded the mean fluorescence intensity of the pixels above threshold. Innervation

density was expressed in two ways: (1) TH-positive area over a given area, and (2) number of VMAT2 puncta in a given area. To calculate the TH innervation density, a maximum intensity z-projection was generated from the TH channel, thresholded, and the TH area was divided by the total area. To calculate the VMAT2 innervation density, a maximum intensity z-projection was generated from the VMAT2 channel, single pixel noise was removed with "Despeckle" and "Find maxima…" was used to automatically count puncta (noise=700), the number of puncta was then divided by the total area. To calculate the density of VMAT2 puncta on TH-positive fibers, a maximum intensity z-projection of the TH channel was thresholded, skeletonized, and total length was measured. Figures show a maximum intensity z-projection for each channel.

To determine the ratio between $X^{\alpha 3}$ axons and X^{RFP} axons in mosaic mice, subsets of 3 slices were summed through a maximum intensity z-projection and individual axon fibers were identified on the TH channel. The lengths and areas of the axons were measured, and the number of VMAT2 puncta along the axon was counted. Each axon was then overlaid onto the RFP channel, and categorized as either RFP-positive, RFP-negative, or undetermined.

2.7 Primary neuronal culture and immunocytochemistry

SCG were dissected from P4 mice under sterile conditions. Ganglia were dissociated in trypsin (1mg/mL; Worthington, Freehold, NJ) dissolved in 1X HBSS pH 7.4 at 37°C, washed with 1X HBSS, and plated on laminin-coated coverslips in growth media. The growth media consisted of L15 media supplemented with vitamins, cofactors, penicillin-streptomycin, 5% rat serum, and NGF (50ng/ml). Cultures were treated with cytosine arabinoside (10μm;

Sigma Millipore, St. Louis, MO) from days *in vitro* 2 to 4 to eliminate non-neuronal cells, and growth media was changed every 3 days.

To stain for dendrites, cultures were rinsed with 1X PBS, fixed and permeabilized with cold methanol for 10 minutes at –20°C. Cultures were blocked for 1 hour at room temperature [Blocking solution: 10% donkey serum in 1X PBS], incubated in primary antibody for 24 hours at 4°C [Primary antibody: Mouse anti-MAP2 (1:1000; Sigma-Aldrich)], and in secondary antibody for 1 hour at room temperature [Secondary antibody: Alexa Fluor 568 goat anti-mouse IgG1 (1:1000; Thermo Fisher Scientific)].

2.8 Retrograde labelling with cholera toxin subunit B (CTB)

Mice were anaesthetized with isoflorane, and the cornea was punctured with a 29G hypodermic needle (Bencton Dickinson) to allow for outflow of aqueous humour. Using the same puncture site, ~2µL of cholera toxin subunit B conjugated to Alexa Fluor 488 (CTB-488; Thermo Fisher Scientific) was injected into the anterior chamber of the eye using a 33G x 1/2" TSK SteriJect hypodermic needle (Air-Tite Products, Virginia Beach, VA) fitted onto a 25µL Gastight Hamilton syringe (Hamilton Company, Reno, NV). SCG were dissected after ~4 days, fixed in 1% PFA in 0.1M PB for 1 hour at room temperature and sliced into 100µm sections for imaging.

Retrograde labelling analysis: Each section was imaged at a pixel size of 0.207µm/pixel and an optical thickness of 0.42µm/slice. All labelled neurons were intensely fluorescent and easily identified; mean intensity fluorescence (excluding the nucleus) was at least 10X greater than background fluorescence intensity. For mosaic SCG, labelled neurons were superimposed on the RFP channel and categorized as RFP-positive or RFP-negative. Low

magnification figures for illustration purposes were obtained using a 10X air objective (N.A. 0.3).

2.9 Ultrastructural studies

SCG were dissected and fixed in 2% PFA/2% glutaraldehyde in 0.1M PB for 1 hour at room temperature, cut into smaller sections, and fixed for an additional 30 minutes. For mosaic SCG, after dissection, SCG were fixed in 4% PFA (pH 7.4) in 0.1M PB for 1 hour at room temperature, sliced into 100μm sections, and fixed for an additional 10 minutes at room temperature. Sections were rinsed with 0.1M PB, imaged with a 40X water-immersion objective (N.A. 0.8) on an upright confocal microscope. After imaging, sections were fixed again in 2% PFA/2% glutaraldehyde for 30 minutes at room temperature. After fixation, SCG were rinsed with 0.1M PB for 30 minutes, and incubated in 1% osmium tetroxide/1.5% potassium ferricyanide in H_2O for 1 hour at room temperature. Ganglia were rinsed briefly with H_2O to remove osmium tetroxide, and dehydrated in a graded series of ethanol concentrations from 30–100%, where each interval lasted 10 minutes, with the 100% ethanol step repeated 3 times. After dehydration, ganglia were incubated in 100% propylene oxide for 15 minutes twice, and incubated in a propylene oxide:EMbed812 mixture at a ratio of 1:1, 1:2, 1:3 and pure EMbed812 for 1 hour each, and polymerized in EMbed812 at 60°C for 24 hours. Thin sections of ganglia were cut on an ultramicrotome, stained with 2% aqueous uranyl acetate and 3% lead citrate, and viewed with a Tecnai Spirit 120kV transmission electron microscope with Gatan Ultrascan 4000 4k x 4k CCD Camera System Model 895.

2.10 Quantitative PCR (qPCR)

RNA extraction and quantitative PCR (qPCR) were optimized, validated and performed in accordance with the MIQE guidelines (Bustin *et al*., 2009; Taylor *et al*., 2010).

RNA extraction and reverse transcription: All dissection tools were cleaned with RNase Away (Thermo Fisher Scientific). SCG from P28 WT mice were dissected and immediately flash frozen in liquid nitrogen. For cerebellum, P28 WT mice were perfused with oxygenated aCSF made with DEPC-treated H_2O, cerebella were quickly dissected, and ~200µm of the dorsal surface (lobes ~VI–IX) was isolated to minimize contribution of granule cell layer, and immediately flash frozen in liquid nitrogen. Total RNA was extracted using the RNeasy Mini Kit (Qiagen, Hilden, Germany). Frozen tissue was homogenized (Polytron PT 2100, Kinematica, Luzern, Switzerland) in buffer RLT with β-mercaptoethanol. Homogenates were processed according to the RNeasy Mini Kit protocol, and included a DNase I (Qiagen) treatment step to avoid contamination from genomic DNA. RNA quantity and purity was assessed with a NanoDrop2000c (NanoDrop, Wilmington, DE), and RNA integrity was assessed by running 400ng on a gel. 260/230 and 260/280 values were consistently >2.0, and 28S and 18S rRNA bands were consistently clear and sharp, with the 28S band approximately twice as intense as the 18S band. Reverse transcription (iScript Reverse Transcription Supermix for RT-qPCR, Bio-Rad, Hercules, CA) was performed immediately after RNA extraction, and used 200ng of RNA per reaction volume of 20µL. No reverse transcriptase controls were included for each reaction to test for contamination from genomic DNA. cDNA was stored at –20°C.

qPCR: qPCR reactions were performed using SsoFast EvaGreen (Bio-Rad, Hercules, CA) on the Eco Real-Time PCR System (Illumina, San Diego, CA). Cycling parameters were as

follows: UDG incubation 2mins at 50°C; Polymerase activation 30s at 95°C; PCR cycling (5s at 95°C, 15s at 60°C) for 40 cycles. All primers were 90–100% efficient at an annealing temperature of 60°C. Samples were run in duplicates, and no-reverse transcriptase and no template controls consistently showed no amplification.

2.10.1 α3 mRNA expression

In α3 KO mice and in mosaic mice, the endogenous α3 nAChR subunit gene on chromosome 9 has a deletion in exon 5. Even though this deletion prevents the formation of functional α3 subunit protein, it is possible that partial mRNA is produced. To ensure that I only quantified the α3 mRNA that would generate a functional protein, I designed the reverse primer to bind to a sequence in exon 5, and therefore would not recognize any potential mRNA generated from the KO allele. In addition, intron-spanning primer pairs reduce amplification of residual genomic DNA. Standard curves were generated from an 8-point 4X serial dilution of cDNA to determine primer efficiencies. α3 mRNA levels were normalized to GAPDH expression.

α3 FWD: 5' – GTG GAG TTC ATG CGA GTC CCT G – 3' (in exon 4)

α3 REV: 5' – TAA AGA TGG CCG GAG GGA TCC – 3' (in exon 5)

GAPDH FWD: 5' – CTG GCA TGG CCT TCC GTG TT – 3'

GAPDH REV: 5' – TAC TTG GCA GGT TTC TCC AGG CG – 3'

2.10.2 4E-BP1 and 4E-BP2 mRNA expression

To compare 4E-BP1 and 4E-BP2 mRNA expression between SCG and cerebella, all steps from RNA extraction to qPCR were carried out in parallel. Standard curves were generated from an 8-point 4X serial dilution of a mixed sample of SCG and cerebellar cDNA to determine primer efficiencies. mRNA expression levels were normalized to the geometric

mean of the reference genes GAPDH and 18S. The stability value determined by NormFinder (Andersen *et al*., 2004) for the combination of GAPDH and 18S was 0.351. To estimate a ratio between 4E-BP1 and 4E-BP2 mRNA levels, I first generated standard curves from a 6-point serial dilution of 26 known copy numbers of 4E-BP1 and 4E-BP2 cDNA to ensure that both primer pairs and respective amplicons respond in a near-identical manner (Figure 6.2A).

4E-BP1 FWD: 5' – AGC CAT TCC TGG GGT CAC TA – 3'

4E-BP1 REV: 5' – ATC ATT GCG TCC TAC GGC TG– 3'

4E-BP2 FWD: 5' – CTG CCC TCT GCC CAG TTA AG – 3'

4E-BP2 REV: 5' – TGC TTG GAG ACT GCC CTA GA – 3'

GAPDH FWD: 5' – CTG GCA TGG CCT TCC GTG TT – 3'

GAPDH REV: 5' – TAC TTG GCA GGT TTC TCC AGG CG – 3'

18S FWD: 5' – GCA ATT ATT CCC CAT GAA CG– 3'

18S REV: 5' – GGG ACT TAA TCA ACG CAA GC – 3'

2.11 Proteomic analysis

Chemicals: Acetonitrile and water were obtained from Burdick & Jackson (Muskegon, MI). Reagents for protein chemistry including iodoacetamide, dithiothreitol (DTT), ammonium bicarbonate, formic acid, and urea were purchased from Sigma-Aldrich. Sequencing grade trypsin was purchased from Promega (Madison, WI). HLB Oasis SPE cartridges were purchased from Waters (Milford, MA).

SCG digestion: For mass spectrometric analysis, isolated frozen SCG tissue pellets in 1X PBS from P28 WT, α3 KO, 4E-BP KO, and α3/4E-BP DKO mice were processed. 6 SCG were

pooled into one sample, with a total of 3 biological replicates per mouse strain. SCG were re-suspended in 1X PBS containing 1X Roche protease and phosphatase inhibitor cocktail and lysed using a bead-beater and sonication. Samples were concentrated using 3kDa centrifugal filters and transferred into a solution of 8M urea/100mM Tris (pH 8), and protein quantitation was performed using a BCA Protein Assay Kit (Pierce). An aliquot of 10-20µg from each sample was then brought to equal volume with 100mM Tris buffer (pH 8). The protein mixtures were reduced with 20mM DTT (37°C for 1 hour), and subsequently alkylated with 40mM iodoacetamide (30 minutes at room temperature in the dark). Samples were diluted 10-fold with 100mM Tris (pH 8) and incubated overnight at 37°C with sequencing grade trypsin (Promega) added at a 1:50 enzyme:substrate ratio (wt/wt). The peptide supernatants were collected and desalted with Oasis HLB 30mg Sorbent Cartridges (Waters), concentrated and re-suspended in a solution containing mass spectrometric 'Hyper Reaction Monitoring' peptide standards (Biognosys, Switzerland) and 0.2% formic acid in water.

Mass Spectrometry: Samples were analyzed by reverse-phase HPLC-ESI-MS/MS using the Eksigent Ultra Plus nano-LC 2D HPLC system (Dublin, CA) combined with a cHiPLC System, which was directly connected to a quadrupole time-of-flight SCIEX TripleTOF 6600 mass spectrometer (SCIEX, Redwood City, CA). Typically, mass resolution in precursor scans was ~45,000 (TripleTOF 6600), while fragment ion resolution was ~15,000 in 'high sensitivity' product ion scan mode. After injection, peptide mixtures were transferred onto a C18 pre-column chip (200µm x 6mm ChromXP C18-CL chip, 3µm, 300Å; SCIEX) and washed at 2µl/min for 10 min with the loading solvent (H_2O/0.1% formic acid) for desalting. Subsequently, peptides were transferred to the 75µm x 15cm ChromXP C18-CL chip, 3µm,

300Å (SCIEX), and eluted at a flow rate of 300nL/min with a 3h gradient using aqueous and acetonitrile solvent buffers.

For spectral library building, initial data-dependent acquisitions (DDA) were carried out to obtain MS/MS spectra for the 30 most abundant precursor ions (100ms per MS/MS) following each survey MS1 scan (250ms), yielding a total cycle time of 3.3s. For collision induced dissociation tandem mass spectrometry (CID-MS/MS), the mass window for precursor ion selection of the quadrupole mass analyzer was set to ±1m/z using the Analyst 1.7 (build 96) software. Subsequently, for label-free relative quantification, all study samples were analyzed by data-independent acquisitions (DIA), or specifically variable window SWATH acquisitions. In these SWATH acquisitions, instead of the Q1 quadrupole transmitting a narrow mass range through to the collision cell, windows of variable width (5–90m/z) are passed in incremental steps over the full mass range (400–1250m/z). The cycle time of 3.2s includes a 250ms precursor ion scan followed by 45ms accumulation time for each of the 64 SWATH segments. The variable windows were determined according to the complexity of the typical MS1 ion current observed within a certain m/z range using a SCIEX "variable window calculator" algorithm (i.e. more narrow windows were chosen in 'busy' m/z ranges, wide windows in m/z ranges with few eluting precursor ions) (Schilling *et al*., 2017). SWATH MS2 produces complex MS/MS spectra, which are a composite of all the analytes within each selected Q1 m/z window.

Data processing and bioinformatics: Mass spectrometric data from data dependent acquisitions was analyzed using the database search engine ProteinPilot (SCIEX 5.0) using the Paragon algorithm (Shilov *et al*., 2007). The following sample parameters were used: trypsin digestion, cysteine alkylation set to iodoacetamide, urea denaturation, and species

Mus musculus. Trypsin specificity was assumed as C-terminal cleavage at lysine and arginine. Processing parameters were set to "Biological modification" and a thorough ID search effort was used. All DDA data files were searched using the SwissProt 2016_07 database (species: *M. musculus*). For Protein Pilot searches, to assess and restrict rates of false positive peptide/protein identifications, we used the (PSPEP) tool available in ProteinPilot 5.0, which automatically creates a concatenated forward and reverse decoy database. For database searches, a cut-off peptide confidence value of 99 was chosen. The Protein Pilot false discovery rate (FDR) analysis tool PSPEP provided a global FDR of 1% and a local FDR at 1% in all cases. SWATH acquisitions were quantitatively processed using the proprietary Spectronaut v11 (11.0.15038.2.22948) software (Bruderer *et al*., 2016) from Biognosys. Quantitative SWATH MS2 data analysis was based on extracted ion chromatograms (XICs) of 6–10 of the most abundant fragment ions in the identified spectra. Relative quantification was performed comparing different conditions and assessing fold changes for proteins from the investigated mouse lines. Significance was assessed using FDR corrected q-values<0.05.

Figures: To generate the heatmap, I first identified proteins that were expressed at significantly different levels between WT and α3 KO SCG (±1.25X at q-value <0.05). For each of the 83 proteins identified to be differentially expressed, the $\log_2$ z-score ratio between the expression level in α3 KO SCG and the corresponding level in WT SCG, and between α3/4E-BP DKO SCG and WT SCG were plotted using the gplots package in RStudio (R Core Team, 2013; RStudio team, 2015). To generate pie charts, proteins were classified according to Gene Ontology terms and PANTHER protein classes (Ashburner *et al*., 2000; The Gene Ontology Consortium, 2017).

2.12 Single cell RNA sequencing (scRNAseq)

Single cell RNA libraries were generated using 10X Genomics droplet-based technology at the Genome Québec Innovation Centre (Montréal, Canada).

2.12.1 Sample preparation

SCG from 5–7 P28 mice were pooled for each genotype (WT, α3 KO and $X^{\alpha 3}X^{RFP}$ mosaic mice). Freshly dissected SCG were incubated on a shaker in 1mg/mL collagenase (Sigma-Aldrich) and 5mg/mL bovine serum albumin (BSA; Sigma-Aldrich) in 1X HBSS (pH 7.4) for 30 minutes at 37°C, followed by 1mg/mL trypsin (Worthington) in 1X HBSS (pH 7.4) for 1 hour at 37°C. To dissociate ganglia into a single cell suspension, SCG were gently titurated with a fire-polished pipette, washed with 10% horse serum and 1X HBSS and filtered through a 30µm cell strainer (Miltenyi Biotec, Bergisch Gladbach, Germany). Cells were reconstituted in calcium- and magnesium-free 1X PBS containing 400µg/mL non-acetylated BSA at concentration of ~1000 cells/µL in 2mL LoBind Eppendorf tubes (Thermo Fisher Scientific). Cell viability was determined with a 0.4% trypan blue solution (Thermo Fisher Scientific) and was consistently >90%. Cell suspensions were kept on ice, and loaded onto the 10X Loading Single Cell Chip within 30 minutes to 1 hour after preparation. For all samples, ~9,000–10,000 cells were loaded and ~6,000–7,000 cells were recovered for a recovery rate of ~60–70%, consistent with this technology (Zhang *et al*., 2019). During this process, RNA molecules were captured and tagged with a cellular barcode and a unique molecular identifier barcode. RNA molecules were then reversed transcribed to generate cDNA libraries.

2.12.2 Sequencing and alignment

cDNA libraries were amplified, and multiplexed for sequencing with the Illumina HiSeq 4000 to generate read data. Read data were grouped based on barcodes and aligned using Cell Ranger software to a custom reference package consisting of the mouse genome version GRCm38/mm10 with the addition of rat α3 and mRFP1 cDNA.

2.12.3 Data analysis

Count matrices were analyzed using the Seurat package (Butler *et al*., 2018; Stuart *et al*., 2019) in Rstudio (R Core Team, 2013; RStudio team, 2015). I filtered out cells that had fewer than 200 transcripts, and genes that were expressed in fewer than 3 cells. To be considered a neuron, cells must express Dbh, Ntrk1, Slc6a2, either Scn3a or Scn9a (or both), and either Cacna1a or Cacna1b (or both), and not Notch1, 2 or 3. The fraction of mitochondrial counts per cell was consistently <0.2, and there were no outliers with high transcript counts that may represent doublets. The neuronal subset was normalized to the count depth per cell, and transformed via a natural log-plus-one transformation (ln(x+1)). For clustering analysis, WT, α3 KO and mosaic datasets were either integrated into one population or the WT dataset was clustered, and used as a classifier (prediction score > 0.5) to sort α3 KO neurons, $X^{\alpha 3}$ neurons and X^{RFP} neurons into the same clusters identified in the WT population. Data were scaled to have zero mean and variance of 1. Scaled expression equally weighs high- and low-expressing genes for clustering analysis. The top 2000 highly variable genes were identified, and used for preprocessing with principal components analysis (PCA). Clusters were visualized using a uniform approximation and projection method (UMAP; Becht *et al*., 2019). To test for differential expression, a Wilcoxon rank sum test was used. Genes were considered to be differentially

expressed if their average ln(x+1) fold change was ±0.25, with a Bonferroni adjusted p-value <0.05.

2.13 Statistical analysis

Values of n and p-values are reported in the figures and corresponding figure legends. In all figures, error bars represent ± SEM, *p<0.05, ***p<0.001. To test for statistical differences between two samples, I used unpaired two-tailed t tests assuming equal variance. To test for statistical differences between three or more samples, I used a one-way ANOVA to determine if one or more samples were significantly different. If the p-value calculated from the F-statistic was less than 0.05, I used a post-hoc Tukey HSD test to identify which pairs of samples were significantly different from each other.

2.14 CRISPR-Cas9-mediated homology directed repair

To restrict RFP expression to adrenergic neurons in mosaic mice, my strategy was to insert a sequence containing three SV40 transcriptional stop sequences flanked by loxP (loxP-SV40 x3-loxP; LSL) between the UbiC promoter and mRFP1 coding region on the X chromosome (Figure 2.2A). The $X^{LSL\text{-}RFP}$ mice that are generated would then be mated to a dopamine beta-hydroxylase (Dbh)-Cre driver line to remove the SV40 transcriptional stop sequences and allow RFP expression specifically in adrenergic neurons.

For these experiments, the Alt-R CRISPR-Cas9 System from IDT (Coralville, IA) was used. I designed the guide RNA (gRNA; more specifically, I designed the crRNA that is linked with a predetermined sequence called the tracrRNA to produce the gRNA), repair template, prepared superovulated female mice, collected oviducts from pregnant females,

and performed all genotyping. Dr. Mitra Cowan and her team at the Transgenic Facility at McGill University (Montreal, Canada) performed microinjections and implantations into recipient females.

gRNA design and testing: There were a total of 25 basepairs (bp) that spanned the region between the end of the UbiC promoter and the start codon of mRFP1 (Figure 2.2B). Within these 25bp, I found 4 possible gRNAs using the crispr.mit.edu Guide Design Tool from the Zhang lab. I selected 3 gRNAs with the fewest predicted off-target sites, of which 2 targeted the sense strand and 1 targeted the antisense strand, and determined their targeting efficiencies by testing them on $X^{RFP}X^{RFP}$ or $X^{RFP}Y$ embryos. Cultured blastocysts were lysed, the targeted region was amplified by PCR (X^{RFP} primer sequences from Figure 2.1D), and PCR products were submitted for Sanger sequencing at the Genome Québec Innovation Center (Montreal, Canada). Because DNA repair mechanisms are imperfect, at least one nucleotide is often either inserted or deleted (indels), and indicates that a double stranded break had been created by the gRNA. All 3 gRNAs had efficiencies >50%, and I proceeded with the gRNA that cut with the greatest efficiency (80–90%).

Repair template design: For homology directed repair, I designed a construct composed of three SV40 transcriptional stop sequences (~800bp) flanked by two loxP sites (34bp each) with a HindIII restriction enzyme site at the 5' end and BamHI site at the 3' end. This sequence was synthesized by GenScript (Nanjing, China) and ligated (using the HindIII and BamHI sites) into a modified pENTR1A-mRFP1 vector (Yurchenko *et al*., 2007) that contains the UbiC promoter and mRFP1 sequences that would serve as homology arms (Figure 2.2C).

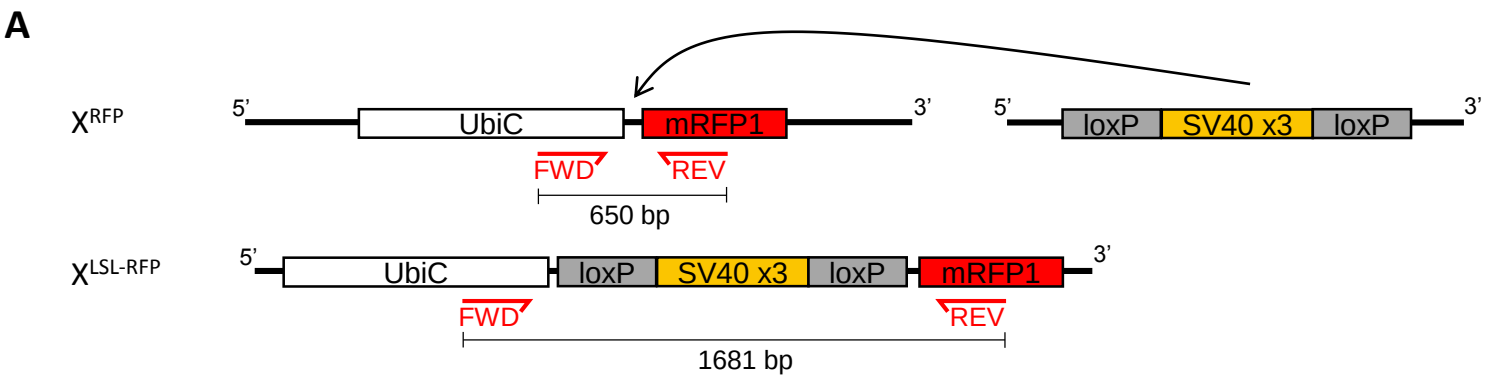
A
X^RFP
5'
UbiC
mRFP1
3'
FWD
REV
650 bp
X^LSL-RFP
loxP
SV40 x3
1681 bp

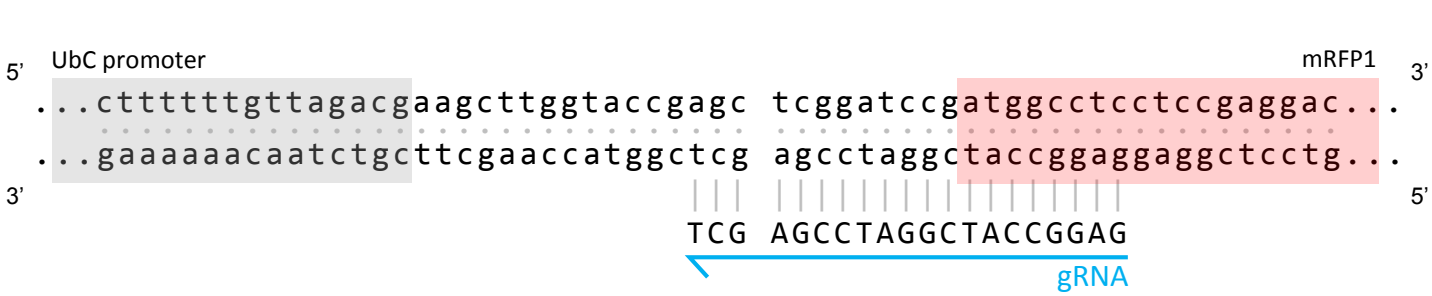
B
UbC promoter
mRFP1
...ctttttttgttagacgaagcttggtaccgagc tcggatccgatggcctcctccgaggac...
...gaaaaaacaatctgcttcgaaccatggctcg agcctaggctaccggaggaggctcctg...
TCG AGCCTAGGCTACCGGAG
gRNA


C
5' homology
...TGGCTTTTTTGTTAGACGAAGCTTTACCGCGGGCCCCTCGAGTAAGAAGTTCCTATTCTCT
AGAAAGTATAGGAACTTCGTCGACATTTAAATCATTTAAATATAACTTCGTATAATGTATGC
loxP
TATACGAAGTTATTCGCGATGAATAAATGAACCGGTGCAGATCTGCGACTCTAGAGGATCTG
CGACTCTAGAGGATCATAATCAGCCATACCACATTTGTAGAGGTTTTACTTGCTTTAAAAAA
CCTCCCACACCTCCCCCTGAACCTGAAACATAAAATGAATGCAATTGTTGTTGTTAACTTGT
TTATTGCAGCTTATAATGGTTACAAATAAAGCAATAGCATCACAAATTTCACAAATAAAGCA
TTTTTTTCACTGCATTCTAGTTGTGGTTTGTCCAAACTCATCAATGTATCTTATCATGTCTG
GATCTGCGACTCTAGAGGATCATAATCAGCCATACCACATTTGTAGAGGTTTTACTTGCTTT
SV40 x3
AAAAAACCTCCCACACCTCCCCCTGAACCTGAAACATAAAATGAATGCAATTGTTGTTGTTA
ACTTGTTTATTGCAGCTTATAATGGTTACAAATAAAGCAATAGCATCACAAATTTCACAAAT
AAAGCATTTTTTTCACTGCATTCTAGTTGTGGTTTGTCCAAACTCATCAATGTATCTTATCA
TGTCTGGATCTGCGACTCTAGAGGATCATAATCAGCCATACCACATTTGTAGAGGTTTTACT
TGCTTTAAAAAACCTCCCACACCTCCCCCTGAACCTGAAACATAAAATGAATGCAATTGTTG
TTGTTAACTTGTTTATTGCAGCTTATAATGGTTACAAATAAAGCAATAGCATCACAAATTTC
ACAAATAAAGCATTTTTTTCACTGCATTCTAGTTGTGGTTTGTCCAAACTCATCAATGTATC
TTATCATGTCTAGATCTCCATCAAGCTGATCCGGAACCCTTAATATAACTTCGTATAATGTA
loxP
TGCTATACGAAGTTATTAGGTCCCTCGACCTGCAGCCCAAGCTAGATCGAATTCGGCCGGCC
TTCGAACAGGATCGATCCGATGGCCTCCTCC...
3' homology

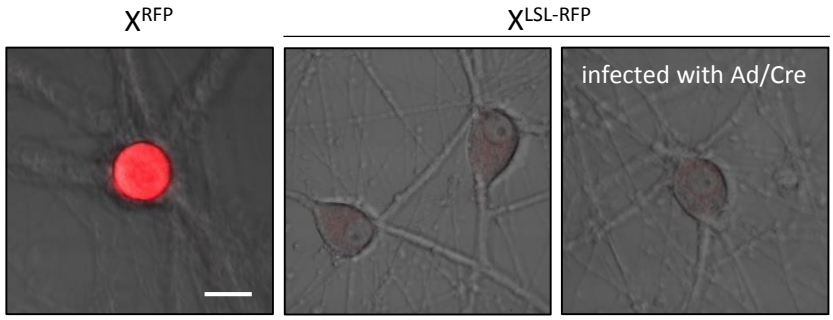
D
X^RFP
X^LSL-RFP
infected with Ad/Cre

Figure 2.2

Figure 2.2 CRISPR-Cas9-mediated homology directed repair to insert LSL.

(**A**) Diagram demonstrating the strategy to insert a sequence containing three SV40 transcriptional stop sequences flanked by loxP (loxP-SV40 x3-loxP; LSL) between the UbiC promoter and mRFP1 coding region on the X chromosome. Indicated in red are the forward (FWD) and reverse (REV) primer binding sites used for genotyping.

(**B**) gRNA (blue) used create a double-stranded break in the region between the UbiC promoter (grey) and mRFP1 gene (red).

(**C**) The repair template used to insert three SV40 transcriptional stop sequences (yellow) flanked by loxP (grey) into the mouse genome via homologous recombination. The underlined sequences refer to the homology arms.

(**D**) Cultured P4 neurons (7 days *in vitro*) from X^{RFP} SCG (left) and $X^{LSL\text{-}RFP}$ SCG (middle). $X^{LSL\text{-}RFP}$ SCG neurons were infected with Ad-Cre/Syn (right). Scale bar, 20μm.

The functions of the SV40 transcriptional stop sequences and the loxP sites in the LSL construct were tested *in vitro* prior to microinjections into embryos. The repair template was transfected into HEK cells, and screened for RFP expression before and after Cre-mediated excision of the three SV40 transcriptional stop sequences. There was no detectable RFP expression prior to Cre transfection, suggesting that there was no leaky expression from the RFP gene. After Cre transfection, several HEK cells were RFP-positive, indicating successful Cre-mediated removal of the SV40 transcriptional stop sequences.

Collection of embryos: 4 to 5-week-old $X^{RFP}X^{RFP}$ females were superovulated with IP injections of pregnant mare serum and 48 hours later, with human chorionic gonadotropin, and mated to $X^{RFP}Y$ male mice. I checked for plugged female mice the next morning after mating (day 1) and plugged mice were sacrificed on the next morning (day 2) to collect embryos at the 2-cell stage. Usually, oviducts were collected from 5–10 plugged mice, for an average yield of ~80–100 healthy embryos for microinjection.

Microinjections: gRNA (crRNA:tracrRNA duplex) were complexed to Cas9 protein *in vitro* to form a ribonucleoprotein (RNP) complex prior to microinjection. The RNP complex and the repair template were microinjected into the cytoplasm of embryos at the 2-cell stage, and healthy embryos post-microinjection were implanted into pseudo pregnant females on the same day.

Screening: Tail clippings were collected from 3-week-old mice, and first viewed under a microscope for RFP fluorescence before being lysed for genotyping. The region spanning the targeted site was amplified by PCR (using X^{RFP} primer sequences from Figure 2.1D). The forward primer was in the UbiC promoter and the reverse primer was in mRFP1. In X^{RFP} mice, the PCR product is 656bp, whereas successful insertion of the LSL sequence would

increase the expected band size to 1681bp. PCR products were also sequenced, and indels were often observed, indicating that the sgRNA had cut the DNA but homologous recombination did not occur. Several times, sequencing revealed that the start codon of RFP had been deleted, and correspondingly, the tail clipping did not express RFP.

In the third round of microinjections, two mice expressed low levels of RFP, and PCR amplification showed a large band, suggesting insertion of the LSL sequence into the genome, which was confirmed by sequencing the PCR product. These mice were mated to WT mice, and showed germline expression of $X^{LSL\text{-}RFP}$. To test whether Cre expression would restore RFP expression, I (1) cultured SCG neurons from $X^{LSL\text{-}RFP}$ mice, and infected cultures with an adenovirus expressing Cre (Ad-Cre/Syn) under the synapsin promoter (Figure 2.2D); and (2) crossed $X^{LSL\text{-}RFP}$ mice with Dbh-CreER mice to generate progeny with both genes, and administered IP injections of tamoxifen for 5 days. As positive controls, I infected cultured SCG neurons from LSL-ChR2-YFP mice with a Cre adenovirus under the synapsin promoter, and administered tamoxifen to LSL-ChR2-YFP; Dbh-CreER mice, and observed strong expression of YFP in both controls.

Unfortunately, I was unable to restore RFP expression with either approach. Also puzzling is that the insertion of the LSL sequence did not completely eliminate RFP expression; RFP expression was still present albeit at faint levels that were barely detectable but remained above autofluorescence when compared to WT controls (Figure 2.2D). One possibility is that the LSL sequence was inserted into another region of the genome, and RFP expression was disrupted in a separate, independent event. PCR only indicates insertion of LSL in the genome, but does not indicate where it is located. However, this seems unlikely because several algorithms and models produced a specificity score

>90 (out of 100) for this sgRNA. Generally, specificity scores >50 are acceptable, and a greater score indicates a high specificity with a low risk of off-target matches (predicted: 2 off-target sites with 3bp mismatches and 44 off-target sites with 4bp mismatches).

Chapter 3: How do SCG neurons develop in the absence of postsynaptic activity?

3.1 Introduction

To learn more about how activity governs the development of neural circuits, my first task was to establish how neural circuits develop in the absence of synaptic transmission. For these experiments, I investigated the innervation of sympathetic neurons in the SCG of α3 KO mice that have a deletion in the α3 nAChR subunit gene (Xu *et al*., 1999). α3-containing nAChRs are the major postsynaptic receptors in autonomic ganglia (Listerud *et al*., 1991). In α3 KO mice, sympathetic neurons do not form postsynaptic nAChRs, however, preganglionic axons establish morphologically normal but electrophysiologically silent synapses on sympathetic neurons even though the postsynaptic receptors are absent (Krishnaswamy and Cooper, 2009). Specifically, I tested the hypothesis that postsynaptic activity is necessary for preganglionic axons to refine and for the growth of dendrites.

I examined silent sympathetic circuits in α3 KO mice of different postnatal ages and compared them to active circuits in age-matched wild type (WT) mice. I found that SCG neurons in α3 KO mice remain innervated by multiple preganglionic axons and have defects in the growth of dendrites and in the targeting of synapses by preganglionic axon terminals. Restoring synaptic transmission by virally expressing α3 led to a redistribution of synapses on the postsynaptic neuron and enabled preganglionic axons to refine.

3.2 Methods

To carry out my experiments, I used a combination of methods including electrophysiological recordings, lipophilic dye labelling and immunohistochemistry. All

experimental models and methods used this chapter and the following four chapters are described in full detail in Chapter 2. For this chapter, they include: α3 KO mouse model (2.1.1), intracellular recording (2.2), adenoviruses (2.3), confocal imaging (2.4), lipophilic dye tracing (2.5), VAChT and PSD-93 immunohistochemistry (2.6.1-2.6.2), primary neuronal culture and immunocytochemistry (2.7), ultrastructural studies (2.9), and statistical analysis (2.13).

3.3 Results

3.3.1 Preganglionic axons innervating SCG neurons in α3 KO mice do not refine

To estimate the number of preganglionic synaptic inputs onto sympathetic neurons in WT SCG, we recorded the discrete jumps in the evoked excitatory postsynaptic potentials (EPSPs) while gradually increasing the stimulus to the preganglionic nerve to recruit innervating axons. In postnatal day 1–3 (P1–P3) mice, approximately 7–8 preganglionic axons converged onto postsynaptic sympathetic neurons, each axon evoking a small EPSP and all inputs were approximately equal in strength (Figure 3.1A). Over the first postnatal month, activity in the autonomic nervous system increases as neonatal pups begin to regulate internal organs to maintain homeostasis, and most preganglionic axons innervating sympathetic neurons are gradually eliminated. By P8–P9, sympathetic neurons were innervated by approximately 5–6 axons, and, by P28, only 2–3 axons innervated SCG neurons (Figures 3.1B, F). At P60, the neurons remained innervated by 2–3 axons (Figure 3.1F).

As preganglionic inputs were eliminated, the strength of the persisting inputs increased markedly. I quantified the disparity in strength of the EPSPs on each neuron in

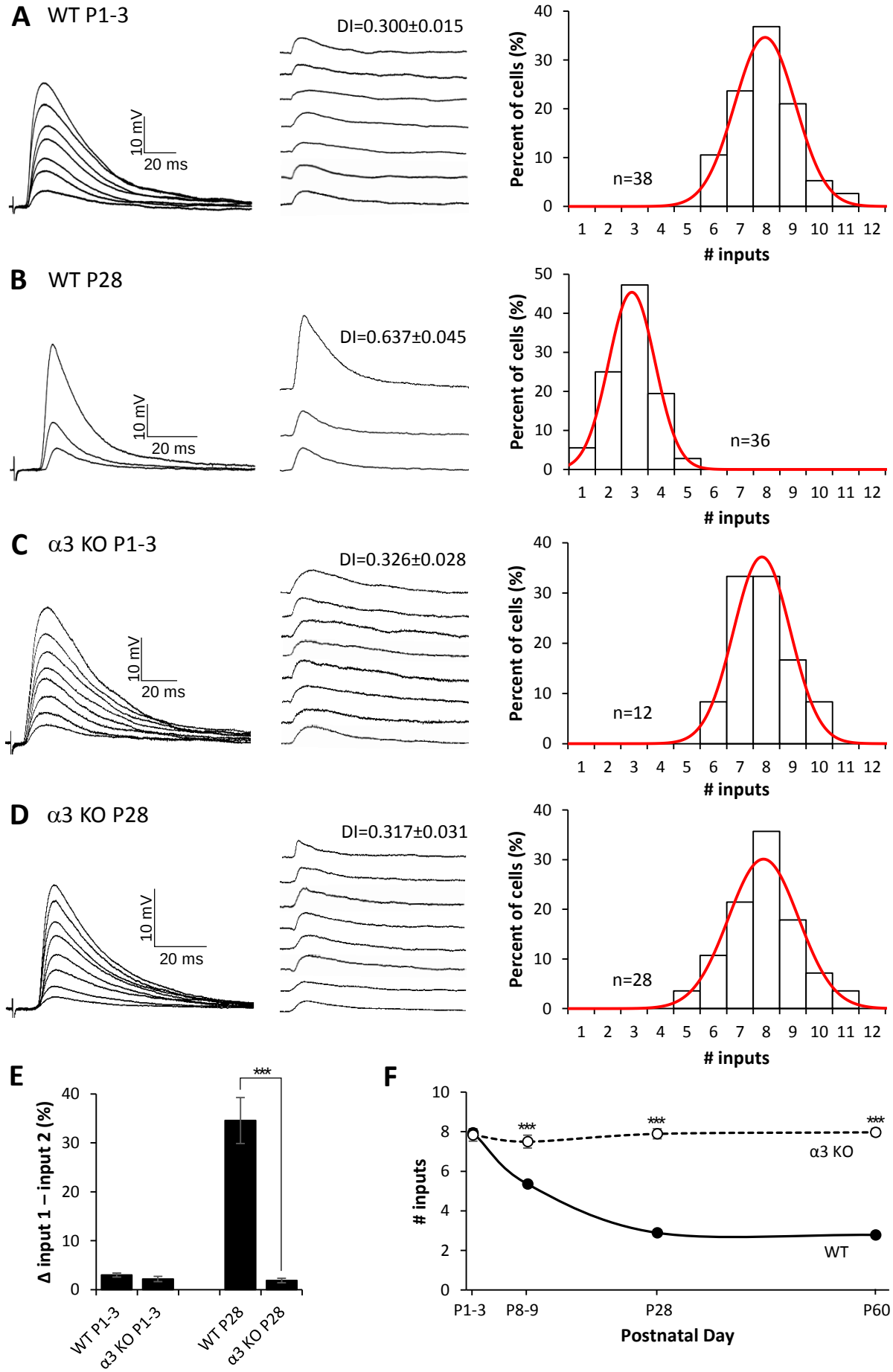
A WT P1-3
DI=0.300±0.015
10 mV
20 ms
Percent of cells (%)
n=38
# inputs
B WT P28
DI=0.637±0.045
10 mV
20 ms
Percent of cells (%)
n=36
# inputs
C α3 KO P1-3
DI=0.326±0.028
10 mV
20 ms
Percent of cells (%)
n=12
# inputs
D α3 KO P28
DI=0.317±0.031
10 mV
20 ms
Percent of cells (%)
n=28
# inputs
E
Δ input 1 – input 2 (%)
***
WT P1-3
α3 KO P1-3
WT P28
α3 KO P28
F
inputs
***
α3 KO
WT
P1-3
P8-9
P28
P60
Postnatal Day

Figure 3.1

Figure 3.1 Preganglionic axons innervating neurons in α3 KO SCG do not refine.

(**A**-**D**) Left: Representative compound EPSPs in a SCG neuron from (**A**) P1-3 WT, (**B**) P28 WT, (**C**) P1-3 α3 KO, and (**D**) P28 α3 KO mice evoked by increasing stimuli to the preganglionic nerve.

Middle: The EPSPs evoked by individual preganglionic axons. DI indicates disparity index.

Right: Distribution of SCG neurons innervated by the number of inputs, fit with a Gaussian function. The distribution for P28 α3 KO is not significantly different from P1-3 WT or α3 KO ($p>0.2$), but significantly different from P28 WT ($p<0.001$). Each distribution in A-D contains data from at least 4 mice; n refers to the number of neurons.

(**E**) The average difference in strength between the strongest and second strongest inputs, expressed as a percentage of the maximum compound EPSP.

(**F**) The average number of axons innervating a SCG neuron in WT (solid line) and α3 KO (dotted line) mice at P1, P4, P28 and P60.

For E, F, error bars represent ± SEM; ***$p<0.001$.

two ways. In one, I calculated a disparity index (DI), defined as the ratio of the standard deviation of the EPSPs evoked by each axon divided by the mean (SD/M) (Hashimoto and Kano, 2003; see Chapter 2.2.2). From P1–P3 to P28, I observed a significant increase in the mean DI, reflecting the increase in strength of 1 or more inputs (Figures 3.1A, B). In the second method, I computed the difference in strength between the strongest and second strongest input, expressed as a percentage of the maximum compound EPSP. At P1–P3, the difference between the strongest and the next strongest input was <5%, whereas at P28, the difference was ~35% (Figure 3.1E). These results establish that, over the first postnatal month, preganglionic inputs innervating sympathetic neurons refine their connections by eliminating some axons and strengthening others.

To test whether refinement is dependent on synaptic activity, as it is elsewhere in the nervous system, we examined preganglionic innervation in the SCG of α3 KO mice. Although preganglionic axons establish morphological synapses in the SCG when α3-containing nAChRs are absent, synapses are electrophysiologically silent (Krishnaswamy and Cooper, 2009). To measure the convergence of preganglionic axons on SCG neurons in α3 KO mice, I first infected these mice for 1–2 days with α3-encoding adenoviral vectors (Ad-α3) to make synapses functional. At P1–P3, approximately 7–8 preganglionic axons converged onto α3 KO sympathetic neurons, with each axon evoking a small EPSP of approximately equal strength, comparable to that of WT at P1–P3 (Figure 3.1C). In contrast to WT, preganglionic axons innervating SCG neurons showed no refinement, and α3 KO neurons continued to be innervated by 7–8 axons over the next 2 months of postnatal life (Figures 3.1D, F). Moreover, EPSPs measured from α3 KO neurons showed little disparity during the same period of time (Figures 3.1C, D, E). These results suggest that postsynaptic

activity during the first postnatal month is necessary both for the elimination of preganglionic axons and the selective strengthening of persisting inputs.

3.3.2 Preganglionic axons refine when synaptic activity is restored in α3 KO SCG

To examine whether preganglionic axons in α3 KO mice are capable of refining when postsynaptic activity is restored, I infected mice with Ad-α3 at P30, and we examined functional innervation of SCG neurons 1 month later (at P60). We found that SCG neurons from rescued α3 KO mice were innervated by only 2–3 preganglionic axons (Figure 3.2A), similar to that of WT neurons at P60 (Figure 3.2C), whereas α3 KO SCG neurons (not rescued) at P60 continued to be innervated by 7–8 axons (Figure 3.2B). In addition to the shift in convergence, the EPSPs evoked by 1–2 preganglionic axons on rescued neurons strengthened considerably, increasing the disparity among EPSPs to levels in WT SCG (Figures 3.2A, C, D). From these data, I conclude that, to refine and strengthen, synapses made by preganglionic axons require retrograde signals downstream of postsynaptic activity. Furthermore, these findings demonstrate that presynaptic inputs onto postsynaptic sympathetic neurons maintain their ability to refine in an activity-dependent manner, well beyond the early postnatal period.

3.3.3 The extension of dendrites and targeting of synapses are defective in the absence of postsynaptic activity

In addition to the convergence of preganglionic axons, I asked whether the absence of postsynaptic activity modifies the organization of pre- and postsynaptic structures,

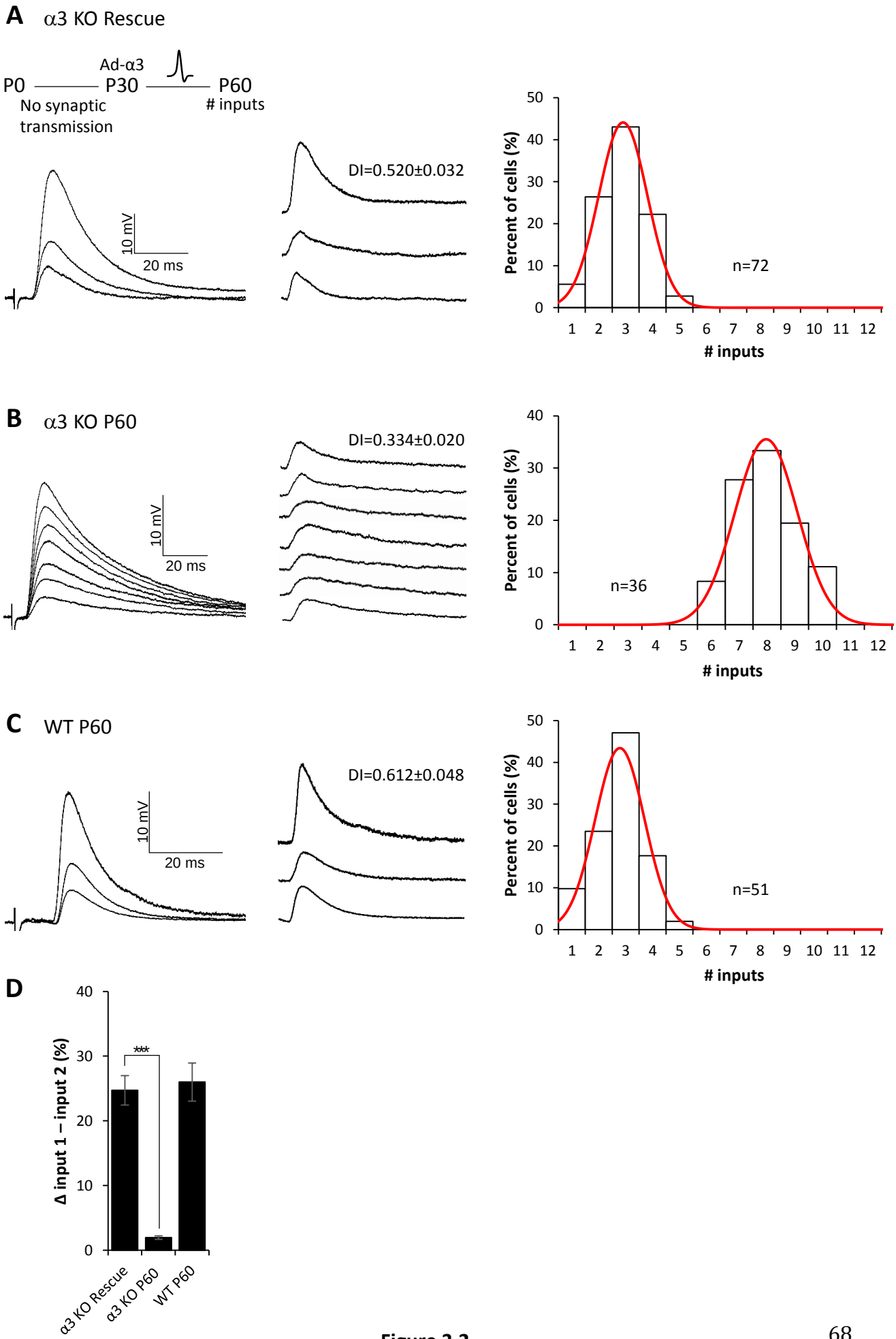
A
α3 KO Rescue
Ad-α3
P0
P30
P60
No synaptic transmission
inputs
10 mV
20 ms
DI=0.520±0.032
Percent of cells (%)
n=72
# inputs
B
α3 KO P60
10 mV
20 ms
DI=0.334±0.020
Percent of cells (%)
n=36
# inputs
C
WT P60
10 mV
20 ms
DI=0.612±0.048
Percent of cells (%)
n=51
# inputs
D
Δ input 1 – input 2 (%)
***
α3 KO Rescue
α3 KO P60
WT P60

Figure 3.2

Figure 3.2 Refinement of preganglionic axons requires postsynaptic activity.

(**A**-**C**) Left: Representative compound EPSPs evoked in a SCG neuron from (**A**) α3 KO mice 1 month after rescue, (**B**) P60 α3 KO, and (**C**) P60 WT mice.

Middle: The EPSPs evoked by individual preganglionic axons. DI indicates disparity index.

Right: Distribution of SCG neurons innervated by the number of inputs, fit with a Gaussian function. The distribution for α3 KO rescue neurons is not significantly different from P60 WT ($p>0.2$), but significantly different from P60 α3 KO ($p<0.001$). Each distribution in A-C contains data from at least 4 mice; n refers to the number of neurons.

(**D**) The average difference in strength between the strongest and second strongest inputs, expressed as a percentage of the maximum compound EPSP. Error bars represent ± SEM; ***$p<0.001$.

including the growth of dendrites, or the manner in which preganglionic axons target their synapses onto SCG neurons.

To quantify dendritic growth, I sparsely labelled SCG neurons with the lipophilic dye 3,3'-Dioctadecyloxacarbocyanine perchlorate (DiO). At P1, total dendritic outgrowth (TDO) on WT and α3 KO neurons was similar; however, by as early as P4, TDO on WT neurons was significantly greater than that on α3 KO neurons, and, by P28, TDO on WT neurons was twice that of α3 KO neurons (Figures 3.3A, B, C). These results are consistent with a role for activity in promoting dendritic growth (Cline, 2001; Haas *et al*., 2006; Niell *et al*., 2004; Wong and Ghosh, 2002). The main defect in dendritic growth on sympathetic neurons developing without excitatory synaptic transmission was that they could not maintain primary branches: the number of primary dendrites on α3 KO neurons decreased from 5–6 at P1–P4 to 2–3 at P28 (Figure 3.3D). On the other hand, I found no significant difference in the length of the dendritic branches on α3 KO neurons when compared to neurons in WT SCG (Figures 3.3E, F, G), nor did I find differences in the number of secondary or higher-order branches, once normalized for primary branch number (Figures 3.3H, I). These results suggest that, apart from maintaining primary dendrites, most aspects of dendritic growth on sympathetic neurons do not depend on synaptic activity. The defects in dendritic growth are unlikely caused by some unanticipated role of the α3 nAChR subunit because when neurons develop *in vitro* for 2-3 weeks, I detected no difference in TDO between WT and α3 KO sympathetic neurons (Figures 3.3J, K).

Preganglionic axons mainly target their synapses to the dendrites of sympathetic neurons (Forehand, 1985). Given the decrease in primary dendrites when synaptic transmission is absent, I asked whether preganglionic axons targeted their synapses

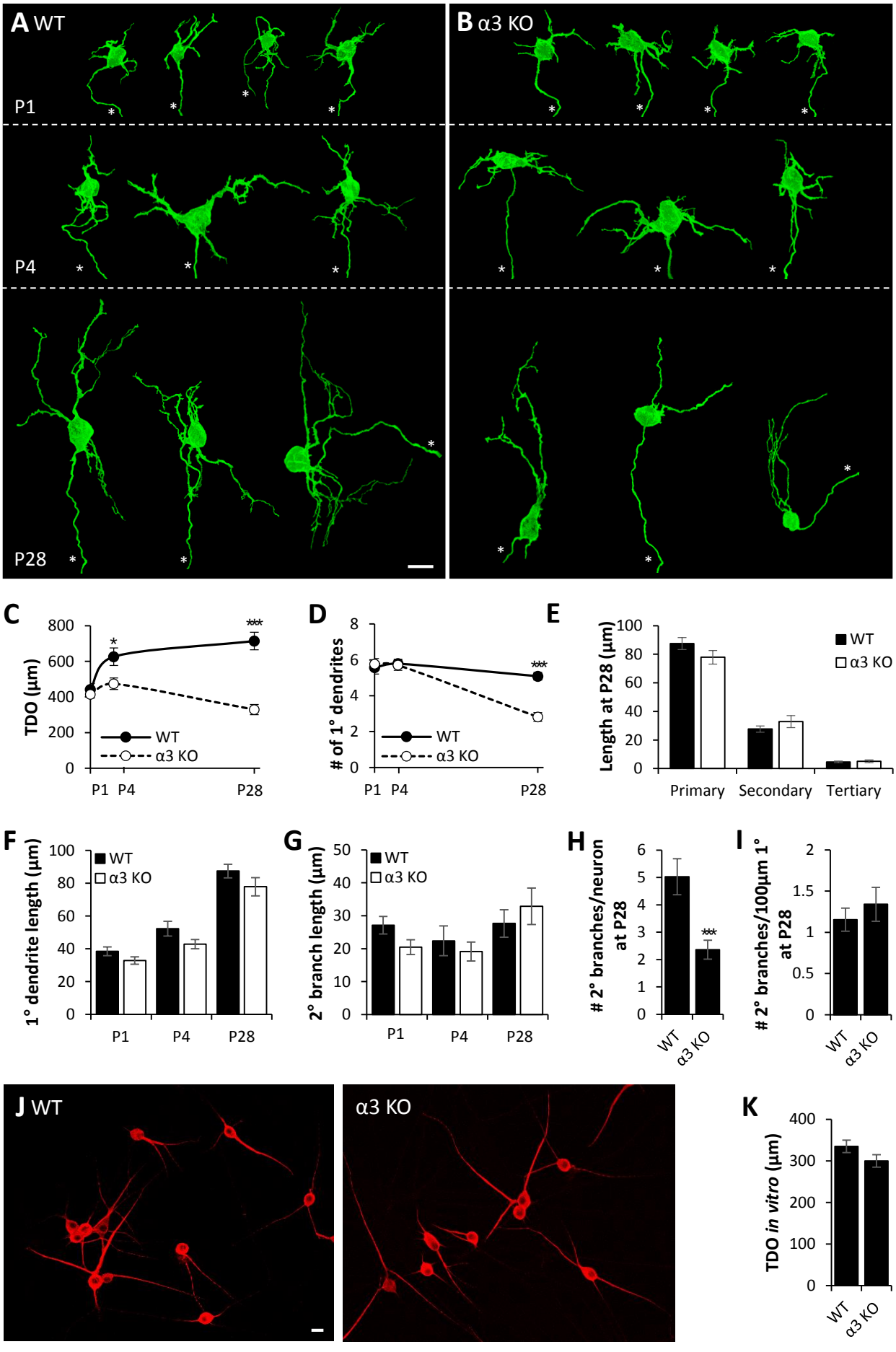
A WT
B α3 KO
P1
P4
P28
C
TDO (µm)
WT
α3 KO
P1 P4 P28
D
# of 1° dendrites
E
Length at P28 (µm)
Primary
Secondary
Tertiary
F
1° dendrite length (µm)
G
2° branch length (µm)
H
2° branches/neuron at P28
I
2° branches/100µm 1° at P28
J WT
α3 KO
K
TDO in vitro (µm)

Figure 3.3

Figure 3.3 Primary dendrites are not maintained in the absence of postsynaptic activity.

(**A**-**B**) Maximum intensity projections of DiO-labelled SCG neurons from (**A**) WT and (**B**) α3 KO mice labelled at P1 (top), P4 (middle) and at P28 (bottom). All neurons are shown at the same scale; axons are marked by an asterisk. Scale bar, 20μm. In each panel, neurons are from different ganglia and have been tiled for comparison.

(**C**) Average total dendritic outgrowth per neuron at P1, P4 and P28; filled circles represent WT, open circles represent α3 KO in this panel and D.

(**D**) Average number of primary dendrites per neuron at P1, P4 and P28.

(**E**) Average length of primary dendrites, secondary branches and tertiary branches at P28; filled columns represent WT, open columns represent α3 KO in this panel and F, G.

(**F**) Average length of primary dendrites at P1, P4, and P28.

(**G**) Average length of secondary dendrites at P1, P4, and P28.

(**H**) Average number of secondary branches per SCG neuron at P28.

(**I**) Average number of secondary branches normalized to 100μm length of primary dendrite at P28.

(**J**) Immunostaining for MAP-2 labels dendrites of cultured P4 neurons (14 days *in vitro*) from WT SCG (left) and α3 KO SCG (right). Scale bar, 20μm.

(**K**) Average total dendritic outgrowth per cultured SCG neuron after 14 days *in vitro*.

For C-I, K, error bars represent ± SEM; *$p<0.05$, ***$p<0.001$. WT: For P1, n=23 neurons (10 mice); for P4, n= 28 neurons (10 mice); and for P28, n= 34 neurons (12 mice). α3 KO: For P1, n=21 neurons (10 mice); for P4, n= 24 neurons (10 mice); and for P28, n=36 neurons (14 mice).

differently onto WT and α3 KO SCG neurons. To address this, I sparsely labelled preganglionic axons in WT and α3 KO SCG at P28 with 1,1'-Dioctadecyl-3,3,3',3'-tetramethylindocarbocyanine perchlorate (DiI) while also labelling sympathetic neurons with DiO. I found a striking difference in how presynaptic axons converged onto SCG neurons. In α3 KO SCG, the preganglionic axons grew extensively over the cell soma of sympathetic neurons; the proportion of the neuronal cell soma covered by preganglionic axons in α3 KO SCG was at least 50% on average, likely an underestimation because the preganglionic axons were sparsely labelled in these experiments (Figures 3.4B, C). In contrast, in WT SCG, the average proportion of the soma covered by preganglionic axons was less than 5% (Figures 3.4A, C). My ultrastructural studies support these results: comparing random sections from WT and α3 KO SCG, I detected 6 times as many varicosities bordering neuronal cell bodies in α3 KO SCG (Figures 3.5A, B). These results indicate that, in the absence of synaptic activity, preganglionic axons more readily contact the cell bodies of sympathetic neurons.

This prominent growth of preganglionic axons over SCG neuronal cell bodies in 1-month-old α3 KO mice suggests that, without synaptic activity, the axons target silent synapses onto the soma instead of preferentially onto dendrites. To determine whether this mistargeting of synapses in α3 KO SCG is already present at birth or whether it evolves during the first postnatal month as preganglionic innervation increases without activity, I stained varicosities of preganglionic axons at P1, P4, and P28 for vesicular acetylcholine transporter protein (VAChT). VAChT is highly localized in cholinergic presynaptic terminals, and over 90% of these VAChT-positive varicosities colocalized with

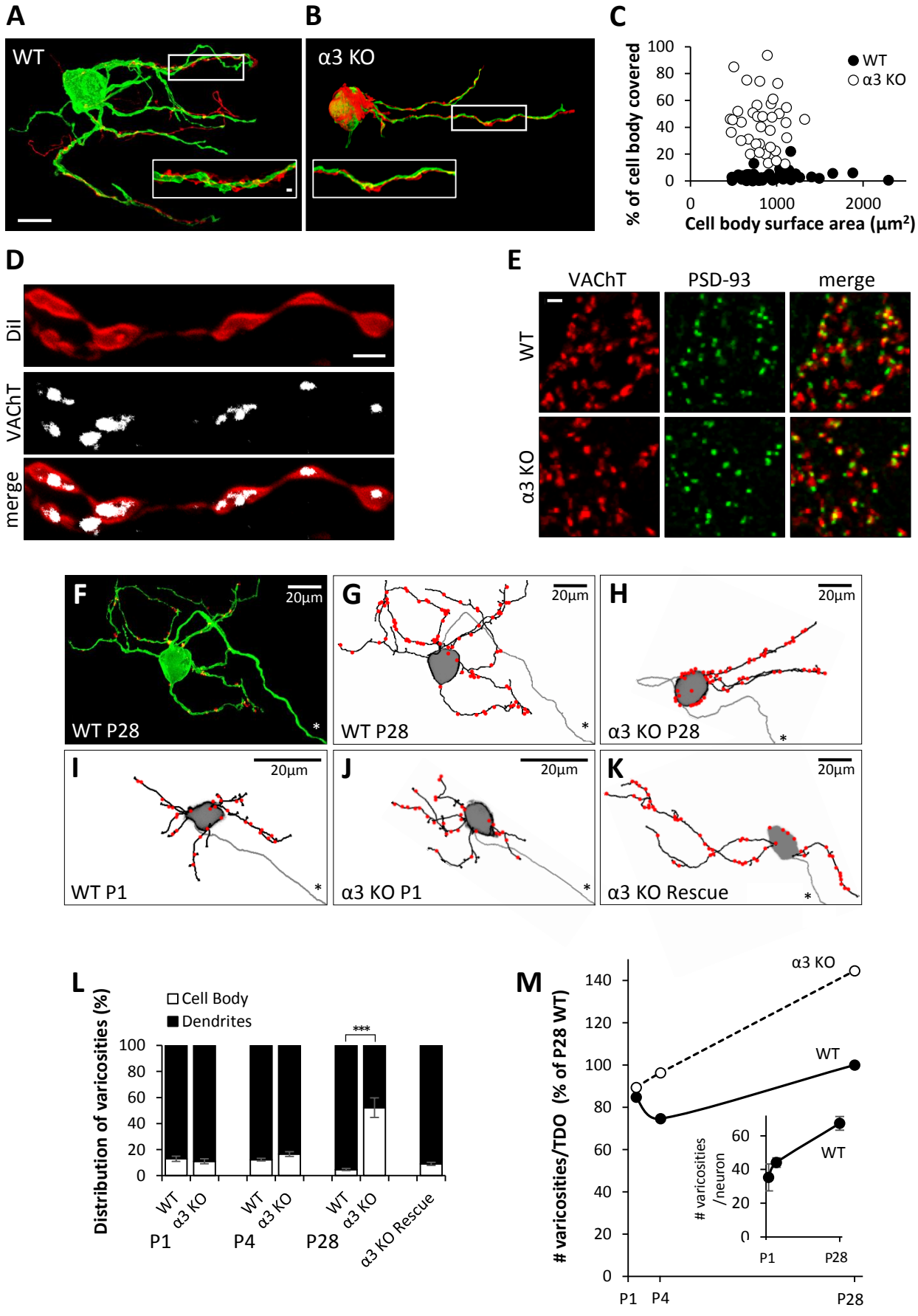
A
WT
B
α3 KO
C
% of cell body covered
100
80
60
40
20
0
0
1000
2000
Cell body surface area (μm²)
WT
α3 KO
D
DiI
VAChT
merge
E
VAChT
PSD-93
merge
WT
α3 KO
F
20μm
WT P28
G
20μm
WT P28
H
20μm
α3 KO P28
I
20μm
WT P1
J
20μm
α3 KO P1
K
20μm
α3 KO Rescue
L
Distribution of varicosities (%)
Cell Body
Dendrites
***
100
80
60
40
20
0
WT
α3 KO
P1
P4
P28
α3 KO Rescue
M
varicosities/TDO (% of P28 WT)
α3 KO
WT
140
120
100
80
60
40
20
0
P1
P4
P28
varicosities /neuron
60
40
20
0
WT
P1
P28

Figure 3.4

Figure 3.4 Silent synapses are targeted to the cell soma.

(**A**-**B**) Maximum intensity projections of DiO-labelled P28 SCG neurons (green) innervated by DiI-labelled preganglionic axons (red) in (**A**) WT and (**B**) α3 KO SCG. Scale bar, 20μm. Inset: The boxed region at higher magnification shows preganglionic axons (red) with varicosities along a segment of dendrite (green). Scale bar, 2μm.

(**C**) Percentage of neuronal cell body covered by preganglionic axons for P28 SCG neurons of different sizes. (WT, filled circles, n=50 neurons (16 mice), α3 KO, open circles, n=38 neurons (13 mice)).

(**D**) DiI-labelled axon (red) immunostained for VAChT (white), indicating varicosities. Scale bar, 2μm.

(**E**) SCG sections immunostained for VAChT (red) and PSD-93 (green). Scale bar, 2μm. Images were selected from the neuropil area between cell bodies where synapse concentration is highest.

(**F**) DiO-labelled WT SCG neuron (green) at P28 immunostained for VAChT (red); axon is marked by an asterisk. VAChT puncta not touching the neuron were removed for clarity.

(**G**-**K**) Skeletonized reconstructions showing dendritic arbors (black), axon (grey, marked by an asterisk), and preganglionic axon varicosities (red) determined by VAChT staining, as in F. Neurons in F-H, K are shown at the same scale, neurons in I, J are magnified for clarity. Scale bar, 20μm.
(**G**) WT neuron shown in F, (**H**) α3 KO neuron at P28, (**I**) WT neuron at P1, (**J**) α3 KO neuron at P1, (**K**) α3 KO neuron 1 month after rescue with Ad-α3.

(**L**) Average distribution of varicosities on the cell body (open) and dendrites (filled) in WT and α3 KO SCG at P1, P4 and P28, and on α3 KO neurons 1 month after rescue with Ad-α3. Error bars represent ± SEM; ***p<0.001. WT: For P1, n=6 neurons (3 mice); for P4, n=9 neurons (5 mice); and for P28, n=10 neurons (4 mice). α3 KO: For P1 n=6 (5 mice); for P4, n=10 neurons (4 mice); and for P28, n=11 neurons (4 mice). For α3 KO Rescue, n=12 neurons (8 mice).

(**M**) Number of varicosities normalized to total dendritic outgrowth for WT neurons and α3 KO neurons at P1, P4 and P28. Inset shows the number of varicosities for WT SCG neurons, which increases over 2-fold from P1 to P28. For P1, n=6 neurons (3 mice); for P4, n=9 neurons (5 mice); and for P28, n=10 neurons (4 mice).

A WT

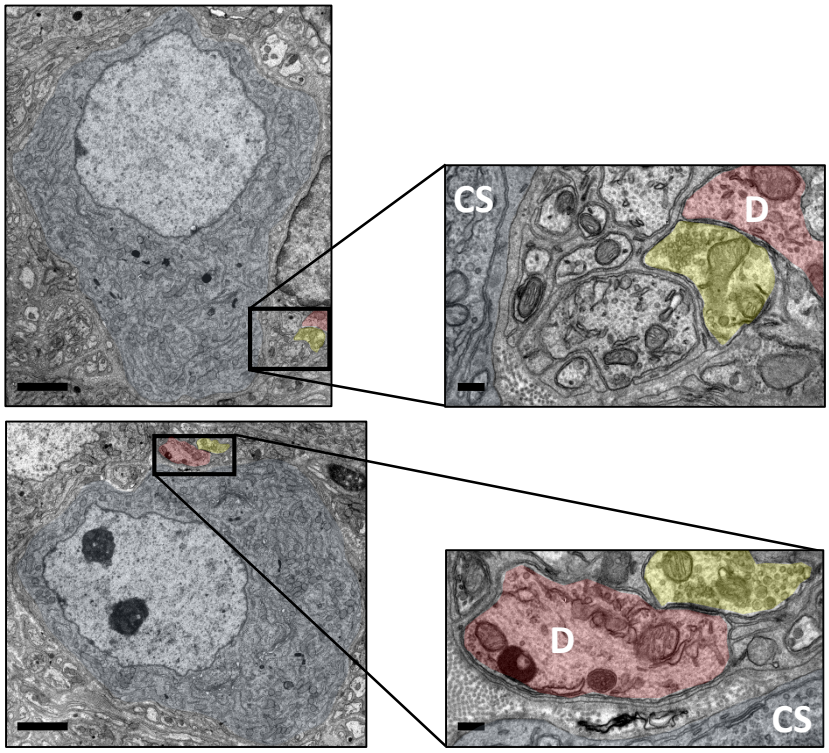

B α3 KO

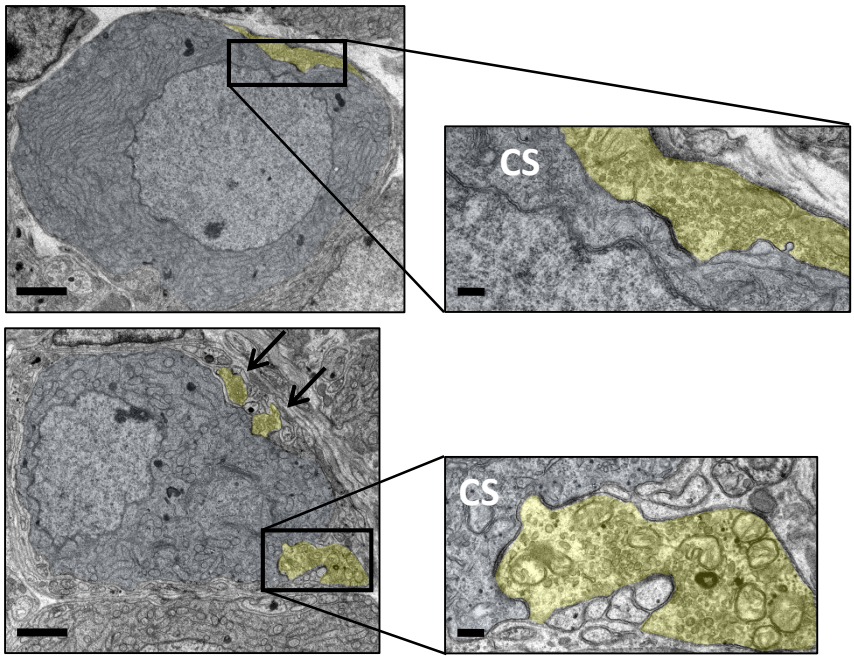

Figure 3.5 Varicosities in α3 KO SCG border the cell soma more frequently than in WT SCG.

(**A**-**B**) Electron micrographs showing cell somas (blue), varicosities (yellow) and dendrites (red) in (**A**) WT SCG and (**B**) α3 KO SCG. Low power images (left) show the cell soma in its entirety; scale bar, 2μm. Arrows in the lower α3 KO micrograph point to two additional varicosities on the cell soma. Boxed regions are magnified on the right; scale bar, 0.2μm.

postsynaptic density-93 (PSD-93) puncta (Figures 3.4D, E), suggesting that these are sites of synaptic contact.

Over the first postnatal month, the number of synapses on WT SCG neurons increased ~2-fold. In α3 KO mice, preganglionic axons continued to establish synapses on SCG neurons during the first postnatal month, even when synaptic transmission was absent and synapses were electrophysiologically silent. When normalized to the size of the dendritic tree, the number of synapses per α3 KO neuron at P28 was ~40% greater than the number for age-matched WT controls (Figure 3.4M).

Preganglionic axons target their synapses mainly to dendrites of sympathetic neurons in WT SCG. I found that over 90% of the VAChT-positive varicosities on P1 and P4 SCG neurons were located on dendrites, and, by P28, this proportion increased to ~95% (Figures 3.4F, G, I, L). As well, in α3 KO SCG at P1–P4, synapses were mainly distributed on dendrites and not statistically different from those on age-matched WT neurons (Figures 3.4J, L). In contrast, at P28, when the preganglionic axons converged on the soma in α3 KO neurons, over 50% of the VAChT-positive varicosities were located on the cell body (Figures 3.4H, L). Moreover, rescuing synaptic activity in the SCG of α3 KO mice at P28 with Ad-α3 resulted in a shift in the distribution of presynaptic varicosities from the soma to the dendrites at P60, without any effect on the size of the dendritic tree (Figures 3.4K, L). These findings indicate that synaptic activity reorganizes preganglionic synapses and targets them to dendrites of sympathetic neurons.

3.4 Discussion

During the first postnatal month, connections between preganglionic inputs and postsynaptic sympathetic neurons in the mouse SCG undergo robust refinement and dendritic remodeling. In this study, I demonstrated that this developmental reorganization is mediated by postsynaptic activity. In α3 KO mice lacking fast nicotinic transmission in SCG because of a deletion in the α3 nAChR subunit gene, dendritic growth is stunted and the reorganization of synaptic connections is severely disrupted: the targeting of synapses on postsynaptic neurons is impaired, and preganglionic axons fail to refine. Virally introducing the missing α3 subunit and establishing synaptic transmission in α3 KO SCG restored synaptic targeting and refinement to match that of WT mice. These results clearly establish that postsynaptic activity is necessary for the reorganization and refinement of synaptic connections in the mouse SCG. My results in this chapter are consistent with a role for postsynaptic activity in generating retrograde factors that mediate presynaptic competition between preganglionic inputs.

3.4.1 Adenoviral rescue of α3 expression

To record EPSPs and estimate the number of inputs converging onto inactive neurons in α3 KO mice, I first restored synaptic transmission by infecting SCG neurons with an adenovirus to express the missing α3 nAChR subunit, and recorded EPSPs 1–2 days post-infection. It is unlikely that two days of rescued activity generated changes in refinement in α3 KO mice for two reasons. First is the slow time course at which refinement occurs, usually taking place gradually over the first several postnatal weeks. For example, by the second postnatal week, SCG neurons in WT mice remain innervated by 5-6

inputs. Second, viral expression for two days does not necessarily equate to two days of postsynaptic activity because the appearance of functional postsynaptic nAChRs takes time. In addition to the transcription and translation of the α3 subunit, nAChRs must be assembled and inserted into the postsynaptic membrane for synapses to function. After 24 hours of expression, infected neurons only generate small and subthreshold EPSPs that are too weak to evoke action potentials.

On the other hand, we clearly show that restoring synaptic transmission for one month significantly reorganized connections in the SCG of one-month-old α3 KO mice. This activity-induced reorganization suggests that the defects in refinement and in synaptic targeting were caused by the absence of synaptic transmission and not a result of an unanticipated but essential role of the α3 subunit during development. In addition, these rescue experiments clearly indicate that in SCG, refinement mediated by postsynaptic activity is not confined to a critical period, and the plasticity of inputs to refine persists for at least the first several postnatal months.

3.4.2 Refinement of preganglionic axons

To estimate the number of preganglionic axons converging onto individual SCG neurons, we used intracellular sharp electrode recordings in current clamp. At the resting potential, stimulating the preganglionic nerve often evoked suprathreshold EPSPs, which may have occluded additional preganglionic inputs. However, to avoid this issue, we hyperpolarized the neuron prior to stimulating preganglionic inputs or used a sodium channel blocker, QX314, to prevent action potentials.

Whole-cell patch clamp may have offered the option of holding the membrane potential at a more negative potential to avoid activating voltage-gated sodium channels and would allow direct measurement of the excitatory postsynaptic currents (EPSCs). However, these experiments were not possible because patch electrodes are unable to penetrate the fibrous tissue that encapsulates the SCG. Conceivably, one might circumvent this issue by preparing healthy vibratome slices of the SCG to expose the neurons, though this method risks severing many of the axons that run throughout the SCG, and would therefore underestimate the number of preganglionic inputs onto each neuron. With fine-tipped sharp electrodes, we could easily penetrate the capsule, allowing us to record directly from intact SCG. Fine-tipped electrodes also minimized dialysis of intracellular contents, reducing the likelihood of disrupting secondary messenger pathways, and missing a potential non-nAChR-mediated synaptic response.

One concern of intracellular sharp electrode recordings is the variability in EPSP amplitude between neurons. This is not an issue when calculating the disparity index because I compared the relative strength of inputs on the same individual neuron, which was then either normalized to the mean EPSP (Hashimoto and Kano, 2003) or the maximum EPSP. The conventional method to measure disparity was adopted from Hashimoto and Kano (2003), in which the standard deviation of the inputs is divided by the mean. However, I observed that in the case of SCG neurons, when the contribution of each individual input was isolated by subtracting one EPSP from another, one input was often much stronger than the remaining inputs, such that the greatest difference in strength is between the strongest input and the second strongest. For example, for a neuron with 4 inputs, the EPSP amplitude of one input is much greater than each of the remaining 3,

which are relatively equal in strength. Therefore, in addition to calculating the conventional disparity index according to Hashimoto and Kano (2003), I also calculated the disparity in a second method by computing the difference in strength between the strongest and second strongest input, expressed as a percentage of the maximum compound EPSP. The conventional calculation takes into consideration the relative strength between all the inputs onto a neuron, whereas the second method effectively measures the greatest difference in relative input strength onto a neuron. Both measurements indicate that the disparity in strength increases as inputs refine.

While it is difficult to directly compare the strength of inputs between P1–3 and P28 mice using current clamp, my immunohistochemistry experiments suggest that those preganglionic axons that persist strengthen their inputs by increasing the number of synaptic contacts on sympathetic neurons. The overall number of synapses on SCG neurons doubles from the first postnatal week to P28, consistent with other studies (Smolen and Raisman, 1980). This increase in the disparity in strength between inputs is consistent with the idea that axons compete for a trophic factor secreted by the postsynaptic cell (Lichtman and Colman, 2000), likely operating by promoting more active axons to form synapses, further increasing their strength.

Synaptic contacts in α3 KO SCG continue to increase over the first postnatal month in an activity-independent manner, and their disparity in strength does not change significantly, indicating that inputs strengthen equally. Therefore, while postsynaptic activity does not appear to be necessary for synapse formation, it may play a role in the selective strengthening of one input over others. However, although these results are consistent with a model in which the selective strengthening of one or more inputs drives

refinement by outcompeting others, the results also do not rule out the possibility that persisting inputs are strengthened through a more passive process that takes place after other inputs withdraw.

3.4.3 Distribution of silent synapses

Postsynaptic activity plays a crucial role in determining how preganglionic axons target their synapses onto sympathetic neurons during early postnatal development. At birth, most synapses are targeted to dendrites in both WT and α3 KO SCG. Yet, over the first postnatal month, as synapses are continually formed, the preganglionic axons in WT SCG continue to target their synapses to dendrites, while most synapses in α3 KO SCG at P28 are targeted to and hyperinnervate the soma of synaptically inactive neurons.

My measurements on the distribution of synapses are based primarily on using VAChT as a synaptic marker and are consistent with ultrastructural studies, as well as DiI and DiO labelling of preganglionic axons on SCG neurons. However, one caveat is that VAChT only indicates the presence of presynaptic cholinergic varicosities, and does not necessarily represent a fully formed synapse, therefore I verified through colocalization experiments that over 90% of VAChT puncta corresponded to PSD-93 puncta, which is present at postsynaptic densities (Parker *et al*., 2004). It can still be argued that to truly identify neuronal synapses, the resolution of confocal microscopy is insufficient. Ideally, the synapses would be identified at the electron microscopy level. However, the amount of data required to reconstruct the entire dendritic arbour from even one single neuron using high-resolution serial section electron microscopy (ssEM) would be enormous. Given this limitation, my use of light microscopy was more practical, particularly for the purpose of

obtaining an overview of the distribution of synapses across the surface of the postsynaptic neuron, and also provides the opportunity to sample many more neurons than would have been possible by ssEM.

Why synapses are mistargeted to the cell soma in the absence of postsynaptic activity is unclear. One possibility is that in response to the lack of functional innervation, inactive neurons upregulate the release of attractive cues that are released from the cell soma to promote their innervation. Alternatively, because SCG neurons in α3 KO mice have a reduced TDO, and preganglionic axons continue to establish synapses, it is tempting to think that synapses become mistargeted to the cell soma after the dendritic arbour becomes saturated. However, this seems unlikely because restoring postsynaptic activity to α3 KO SCG neurons resulted in a shift in the distribution of synapses from the soma to the dendrites without a significant increase in TDO. This shift in synapse distribution indicates that the targeting of synapses remains plastic and likely occurred through one of two possible scenarios: (1) axons that innervated the cell soma were preferentially eliminated when inputs refined; or (2) persistent axons disassembled synapses from the cell soma and reassembled them on the dendritic arbour. To distinguish between these two possibilities would require *in vivo* imaging over a one-month period, however the inaccessibility of the SCG and the extended length of time makes this experiment technically challenging.

3.4.4 Dendritic growth

Dendrites on SCG neurons in α3 KO mice grow poorly over the first postnatal month. This is consistent with several studies demonstrating that disrupting synaptic activity influences the growth of dendrites (Cline and Haas, 2008; Lefebvre *et al*., 2015; Wong and

Ghosh, 2002). Most studies attribute the reduction in dendritic growth to defects in branching. Here, I find that in the absence of postsynaptic activity, the frequency of branching and the lengths of higher order branches on SCG neurons is not statistically different between WT and α3 KO neurons, rather, synaptically inactive SCG neurons are unable to maintain their primary dendrites. There may also be differences in the dynamics of dendrite extension and retraction than can only be captured through *in vivo* time-lapse imaging.

Interestingly, rescuing activity in one-month-old mice did not have any effect on dendritic growth: the number of primary dendrites remained the same, indicating that primary dendrites are formed only during embryogenesis, and when they are not maintained during postnatal development, neurons cannot extend additional primary dendrites, even when postsynaptic activity is restored.

My findings are at odds with previous work showing that cutting the preganglionic nerve at birth had no effect on the growth of dendrites on denervated SCG neurons over the first postnatal month (Voyvodic, 1987). It is not clear why inactivity produced by the deletion of α3 had a different effect on dendritic growth than inactivity produced by cutting the preganglionic nerve. The α3 subunit does not appear to have some unanticipated role in dendritic growth and stabilization apart from its role in forming functional nAChRs and mediating fast synaptic transmission because, when placed in culture, WT and α3 KO SCG neurons extended dendrites that were statistically similar.

Neurons in SCG receive cholinergic-nicotinic synaptic transmission before birth (Rubin, 1985c), raising the possibility that a reduction in synaptic activity in α3 KO SCG *in utero* might have influenced the growth of dendrites. However, this seems unlikely

because: (1) activity is low in the sympathetic nervous system prenatally, as the mother maintains the pups' homeostasis; and (2) at birth, dendrites on α3 KO SCG are not statistically different from control WT neurons.

A clear distinction between α3 KO neurons and denervated neurons is that α3 KO neurons receive morphological synapses. Conceivably, the difference in dendritic growth between α3 KO SCG neurons and denervated WT neurons is that α3 KO SCG neurons have electrophysiologically silent synapses. If silent synapses signal inappropriately to molecules downstream of the postsynaptic complex to perturb dendritic growth (Quach *et al*., 2013), it might account for the difference in dendritic growth between inactive α3 KO SCG neurons and denervated neurons. Or, along a similar principle, the presynaptic terminals that are present on α3 KO neurons and not on denervated neurons may release factors that destabilize dendrites, whose impact are overridden by postsynaptic activity.

The discrepancy may also be explained by differences in experimental models and techniques. In the experiments detailed by Voyvodic, dendrites were measured from rat SCG, whereas my experiments were performed in mice. It is possible that the molecular pathways that underlie dendritic growth are more stable in the rat than in mice, allowing dendrites to grow and persist for a longer period in the absence of postsynaptic activity. As such, there is evidence that dendritic arbours of SCG neurons are more complex in larger animals (Purves *et al*., 1986). In addition, the labelling and imaging techniques used to estimate dendritic outgrowth were different. In Voyvodic's experiments, neurons were impaled with a sharp electrode and filled with horseradish peroxidase by iontophoresis, whereas in my experiments, neurons were randomly labelled with a lipophilic dye. In our experience, labelling neurons with a sharp electrode biases the selection towards larger

neurons because they are more likely than smaller neurons to be impaled when performed blindly, and also because larger neurons are more stable and therefore more amenable for longer recordings required to optimize the quality of the labelling. Conceivably, larger neurons are more resistant to changes in dendritic growth caused by denervation. Furthermore, Voyvodic quantified dendritic growth from 2-D *camera lucida* images of HRP-filled neurons, and I used confocal z-stacks that were reconstructed in 3-D, then rotated and examined to account for dendrites that grew perpendicular to the field of view. Any or all of these issues, including those listed in the paragraphs above, may explain why denervating neurons at birth and eliminating synaptic transmission had different effects on the growth of dendrites in the SCG.

3.4.5 Conclusion

In summary, my findings from α3 KO mice are consistent with the evidence that postsynaptic activity is important for connections to refine. In the absence of postsynaptic activity, preganglionic inputs onto SCG neurons fail to refine, and SCG neurons in α3 KO mice remain hyperinnervated into adulthood. Unsilencing synapses by virally restoring α3 expression and establishing synaptic transmission for one month induced preganglionic axons to refine. My results further demonstrated that synaptic transmission is necessary for the maintenance of primary dendrites, and as a consequence, SCG neurons in α3 KO mice have a reduced TDO. Additionally, although preganglionic axons continue to establish electrophysiologically silent synapses onto inactive SCG neurons in α3 KO mice during postnatal development, these synapses are mistargeted to the cell soma rather than to the dendritic arbour, where most synapses are located in WT mice.

Chapter 4: How do axons innervate a mixed population of active and inactive neurons?

4.1 Introduction

In the previous chapter, my results from the α3 KO mouse model demonstrated that in the absence of postsynaptic activity, preganglionic axons onto SCG neurons do not refine. This suggests that postsynaptic activity promotes downstream pathways to generate a retrograde signal(s) that is necessary for connections to refine. How this retrograde signal mediates the elimination of preganglionic inputs is unclear. Specifically, I asked: do presynaptic neurons receive retrograde feedback from the targets they innervate and compare them to determine which connections to maintain and which targets to withdraw from? Or, do postsynaptic neurons compare the inputs they receive and through a competitive process, selectively retain some inputs while eliminating others?

To address this issue, we generated a novel mosaic mouse model, in which two populations of sympathetic neurons of approximately equal proportions are randomly intermingled in the SCG: one population expresses the α3 subunit and forms postsynaptic nAChRs, while the other population does not express α3 and does not form functional postsynaptic receptors (Figure 4.1A). In these mosaic ganglia, preganglionic axons have a choice between innervating active and inactive SCG neurons. Since only the active neurons generate activity-dependent retrograde signals, and inactive neurons do not, one might predict that preganglionic axons will only maintain connections on active neurons and withdraw their connections from inactive neurons. On the other hand, if refinement is mediated locally and regulated by the postsynaptic neuron, then neighbouring active neurons would not have any influence on the refinement of connections on inactive

neurons in mosaic ganglia, and based on my results from α3 KO mice, connections would not refine.

In this study, I compared preganglionic innervation and the morphological development of neurons with functional postsynaptic receptors (α3-containing) to those without receptors (α3 KO neurons) in mosaic SCG. I found that α3 KO neurons in mosaic SCG develop remarkably like α3-containing neurons: preganglionic axons refine their connections, and axon terminals are appropriately targeted to the dendrites, which are complex and elaborate, and resemble those extended by active neurons. My results indicate that postsynaptic activity is not essential for dendritic growth nor is it necessary to mediate synaptic targeting. And, in surprising contrast to the results from the previous chapter, preganglionic inputs onto α3 KO neurons in mosaic SCG refine in the absence of postsynaptic activity. Taken together, I conclude that activity regulates the development of circuits in a non-cell-autonomous manner.

4.2 Methods

The experimental model and methods used to investigate the development of sympathetic circuits in this chapter are similar to those used in the previous chapter: mosaic mouse model (2.1.2), intracellular recordings (2.2), adenoviruses (2.3), confocal imaging (2.4), lipophilic dye tracing (2.5), VAChT immunohistochemistry (2.6.1), ultrastructural studies (2.9), quantitative PCR (2.10), and statistical analysis (2.13).

4.3 Results

4.3.1 Expressing the α3 nAChR subunit gene on the X chromosome generates mosaic ganglia

To achieve a random distribution of active and inactive sympathetic neurons in the SCG, we generated female mice that express the α3 nAChR subunit gene under the human ubiquitin C (UbiC) promoter (Schorpp *et al*., 1996) on one X chromosome (see Chapter 2.1.2; Figure 4.1C), and on the other X chromosome, UbiC driving the expression of red fluorescent protein (RFP) (Figure 4.1D). This strategy generates mosaicism because of random X-inactivation, which causes each cell to either express α3 (referred to as $X^{\alpha3}$ neurons) or to express RFP (referred to as X^{RFP} neurons). Then, I mated these mice to α3 KO mice that have a deletion in the endogenous α3 subunit gene on chromosome 9 to generate an α3 KO; $X^{\alpha3}X^{RFP}$ mosaic mouse model. $X^{\alpha3}$ neurons are able to form functional nAChRs, whereas X^{RFP} neurons are essentially α3 KO neurons in that they cannot form functional nAChRs.

Phenotypically, mosaic mice are healthy and fertile, and do not show any signs of dysautonomia such as those observed in α3 KO mice, including the loss of pupillary responses, and enlarged kidneys and bladders (Xu *et al*., 1999). Confocal images of live and fixed SCG show strong expression of RFP in X^{RFP} neurons allowing for easy visual differentiation between active and inactive populations. In addition, X^{RFP} neurons and non-fluorescent $X^{\alpha3}$ neurons are distributed randomly in roughly equal proportions (Figure 4.1B, E).

To estimate the level of α3 expression driven by the UbiC promoter on the X chromosome, I used quantitative PCR (qPCR) to measure relative α3 mRNA expression in

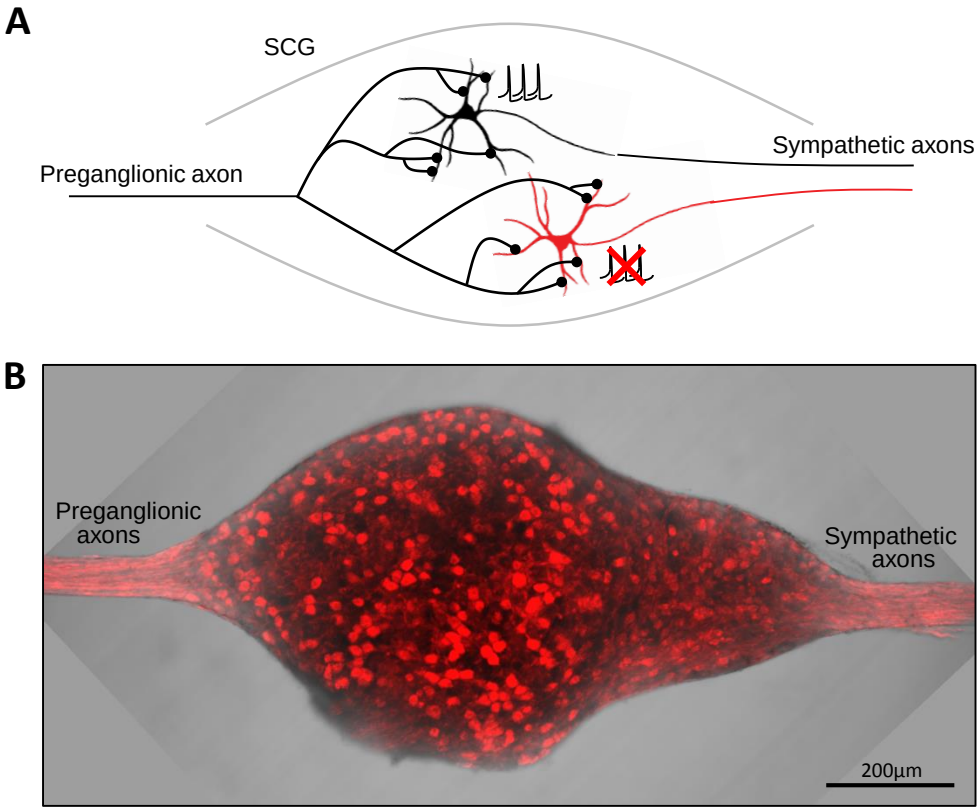
A
SCG
Preganglionic axon
Sympathetic axons
B
Preganglionic axons
Sympathetic axons
200µm

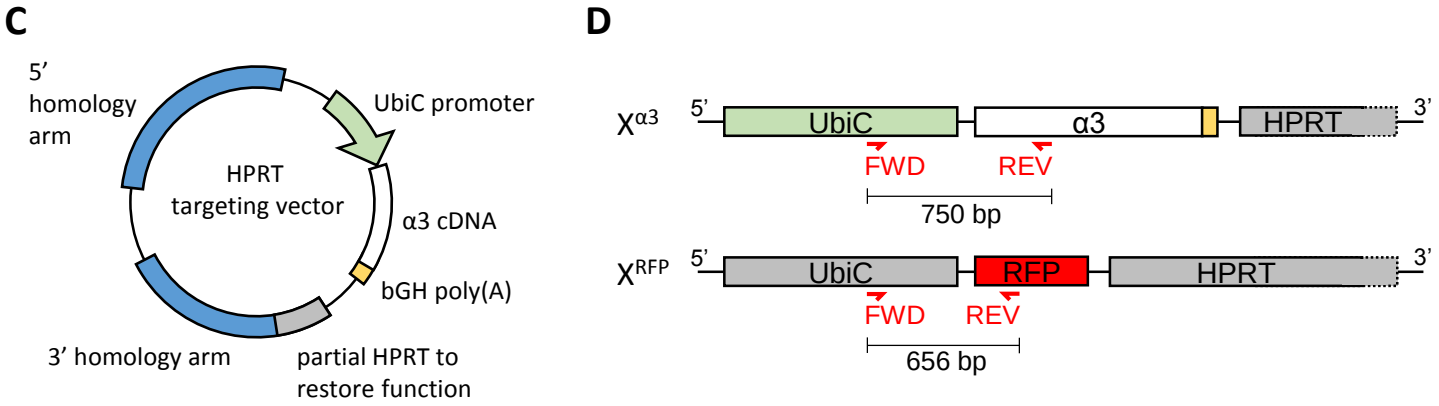
C
5' homology arm
UbiC promoter
HPRT targeting vector
α3 cDNA
bGH poly(A)
3' homology arm
partial HPRT to restore function
D
Xα3
5'
UbiC
α3
HPRT
3'
FWD
REV
750 bp
XRFP
5'
UbiC
RFP
HPRT
3'
FWD
REV
656 bp

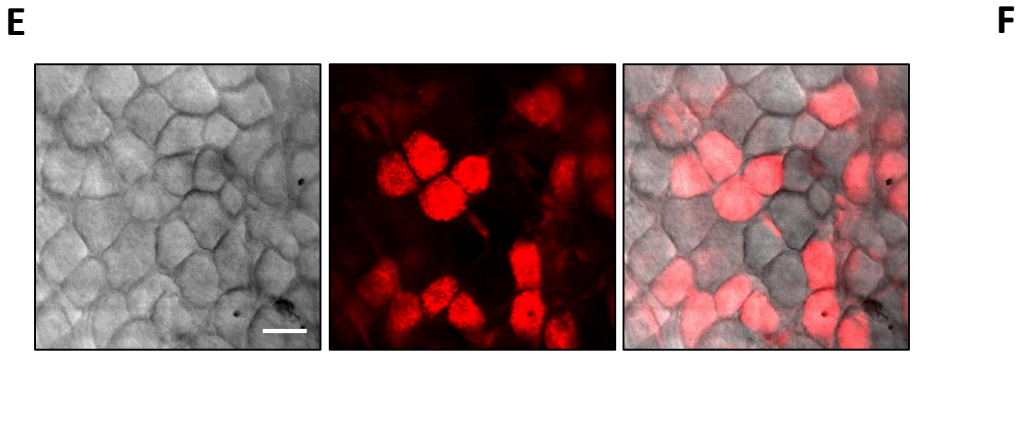
E
F
Relative α3 mRNA expression normalized to α3+/- (%)
200
180
160
140
120
100
80
60
40
20
0
Xα3
WT
α3 +/-
α3 -/-

Figure 4.1

Figure 4.1 Expressing the α3 nAChR gene on the X chromosome generates mosaic SCG.

(**A**) Illustration demonstrating preganglionic innervation of active and inactive neurons in mosaic SCG. Some neurons (black) have α3-containing nAChRs and other neurons (red) do not form nAChRs and have no postsynaptic activity.

(**B**) DIC and confocal images were superimposed to show an intact mosaic SCG composed of non-fluorescent $X^{\alpha 3}$ neurons and RFP-expressing X^{RFP} neurons.

(**C**) α3 rat cDNA (white) was ligated into a previously modified vector in between the human ubiquitin C promoter (UbiC; green) and bovine growth hormone polyA site (bGH poly(A); yellow), and recombined *in vitro* into the HPRT gateway destination vector to generate the targeting vector. Homology arms (blue) direct homologous recombination into the HPRT locus, and partial HPRT (grey) restores HPRT function in HPRT-deficient ES cells for resistance to HAT media (see Chapter 2.1.2).

(**D**) Diagram shows locations of α3 and mRFP1 genes between the human ubiquitin C promoter (UbiC) and HPRT gene on the X chromosome. Forward (FWD) and reverse (REV) primers used for genotyping are indicated in red with expected amplicon sizes, primer sequences can be found in Figure 2.1D.

(**E**) DIC (left) and confocal images (middle) of non-fluorescent $X^{\alpha 3}$ neurons and RFP-expressing X^{RFP} neurons in a section of mosaic ganglia. Scale bar, 20μm.

(**F**) Relative α3 mRNA expression in SCG normalized to α3+/– SCG. For $X^{\alpha 3}$, n=22 mice; for WT, n=3 mice, for α3+/–, n=3 mice; and for α3 KO, n=2 mice.

the SCG. For these experiments, I extracted RNA from P28 $X^{\alpha3}X^{\alpha3}$ female mice or $X^{\alpha3}Y$ male mice, so that each neuron contained one active $X^{\alpha3}$ allele. Since SCG neurons in α3+/– heterozygous mice also have one allele for α3, while SCG neurons in WT controls have two alleles, I compared $X^{\alpha3}$ expression to α3+/– heterozygous mice. SCG from WT mice contained approximately double the quantity of α3 mRNA than SCG from α3+/– heterozygous mice, whereas SCG from α3 KO mice contained virtually no α3 mRNA (Figure 4.1F). The expression of α3 in SCG from $X^{\alpha3}X^{\alpha3}$ or $X^{\alpha3}Y$ mice was lower than anticipated. $X^{\alpha3}$ mRNA was ~20% of α3+/– heterozygous mice (Figure 4.1F), indicating that the expression of α3 from the UbiC promoter on the X chromosome was approximately 5-fold lower than when expressed from its endogenous location on chromosome 9.

4.3.2 $X^{\alpha3}$ neurons generate suprathreshold EPSPs in response to preganglionic nerve stimulation

Despite low expression, mosaic mice are phenotypically normal and the autonomic nervous system appears to function normally, suggesting that α3 expressed from the X chromosome can form nAChRs and mediate synaptic transmission. Nonetheless, it was important to verify this by recording intracellularly from $X^{\alpha3}$ neurons in SCG of $X^{\alpha3}X^{\alpha3}$ female mice, $X^{\alpha3}Y$ male mice, and $X^{\alpha3}X^{RFP}$ mosaic mice. Stimulating the preganglionic nerve evoked large, suprathreshold EPSPs (Figure 4.2A) that were not different from those elicited in WT controls. However, at P1–P3, approximately half of the $X^{\alpha3}$ neurons did not have detectable EPSPs, whereas at P7–P8, the nerve-evoked EPSPs were comparable to those observed in WT neurons, indicating that α3 from the X chromosome appears to be expressed with a minor developmental delay.

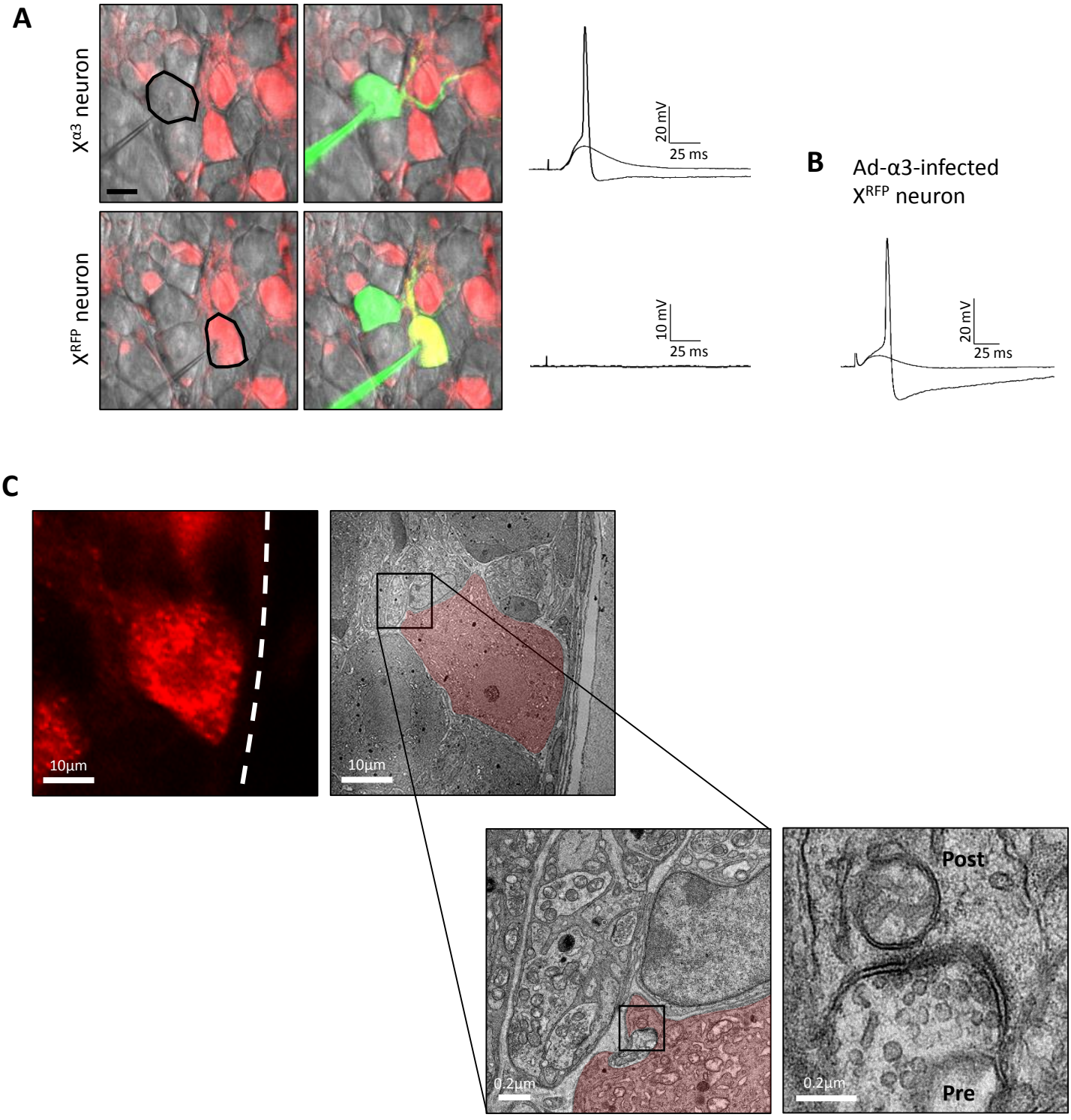
A
Xα3 neuron
XRFP neuron
20 mV
25 ms
10 mV
25 ms
B
Ad-α3-infected
XRFP neuron
20 mV
25 ms
C
10µm
10µm
0.2µm
0.2µm
Post
Pre

Figure 4.2

Figure 4.2 X^{RFP} neurons in mosaic SCG are innervated by preganglionic axons.

(**A**) Left: DIC and confocal images were superimposed to show a sharp electrode filled with Alexa Fluor 488 hydrazide (green) recording intracellularly from a $X^{\alpha 3}$ neuron (top) and a neighbouring X^{RFP} neuron (bottom). Scale bar, 20μm.

Right: Representative suprathreshold EPSPs evoked in a $X^{\alpha 3}$ neuron (top). Preganglionic nerve stimulation does not generate responses in X^{RFP} neurons (bottom).

(**B**) Mosaic mice were infected with Ad-α3 and intracellular recordings were performed 24–48 hours post-infection. After restoring synaptic transmission, preganglionic nerve stimulation evoked EPSPs in X^{RFP} neurons.

(**C**) Corresponding images of a X^{RFP} neuron viewed at the light microscopy level and at the ultrastructural level (red). Boxed areas were magnified to show presynaptic vesicles and postsynaptic densities of one synaptic input.

To establish that X^{RFP} neurons in mosaic SCG do not form postsynaptic nAChRs and do not have postsynaptic activity, I recorded from several hundred X^{RFP} SCG neurons in mosaic mice whose ages varied between P1 and P60, and never detected any EPSPs in response to preganglionic nerve stimulation (Figure 4.2A). Nonetheless, all X^{RFP} neurons were capable of generating overshooting action potentials with current injection.

4.3.3 Preganglionic axons form and maintain electrophysiologically silent synapses on X^{RFP} neurons in mosaic SCG

In mosaic SCG, preganglionic axons have a choice between innervating active neurons and inactive neurons. Possibly, preganglionic axons will distinguish immediately between active neurons and inactive neurons when circuits form during embryogenesis, and avoid establishing connections onto neurons without functional nAChRs. My results from α3 KO mice suggest that the initial innervation of SCG neurons occurs in an activity-independent manner because WT and α3 KO circuits were similar at birth. Therefore, it is reasonable to expect that during embryogenesis, preganglionic axons will form connections onto both active neurons and inactive neurons. However, it is conceivable that preganglionic axons will only maintain connections onto active $X^{\alpha 3}$ neurons, and selectively withdraw from X^{RFP} neurons as they refine their connections.

I investigated whether X^{RFP} neurons in mosaic SCG from P28 mice are innervated in two ways: electrophysiologically and ultrastructurally. I infected P28 mosaic mice with Ad-α3, and 1–2 days later, recorded intracellularly from X^{RFP} neurons to determine whether they are innervated. For these experiments, mosaic SCG were viewed under a confocal laser-scanning microscope equipped with an electrophysiological set-up to identify RFP-

expressing neurons. In addition, neurons were filled with an Alexa Fluor 488 hydrazide dye during the recordings to confirm their identities. I found that X^{RFP} neurons produced EPSPs when the preganglionic nerve was stimulated (Figure 4.2B), indicating that inactive neurons in mosaic SCG retain synaptic innervation during postnatal development.

I further established that X^{RFP} neurons in P28 mosaic mice receive synaptic connections by examining mosaic SCG at the ultrastructural level. In order to identify X^{RFP} neurons in electron micrographs, fixed sections of mosaic SCG were first imaged with confocal microscopy to obtain a map of RFP-expressing neurons, which was later used to match RFP-expressing neurons to the corresponding neuron at the ultrastructural level. Although most synapses were found in the neuropil region between cell somas, it was challenging to clearly distinguish between dendrites extended by $X^{\alpha 3}$ neurons and those from X^{RFP} neurons. Therefore, I focused on the regions adjacent to the cell soma and proximal dendrites of X^{RFP} neurons, and where I established the presence of morphological synapses (Figure 4.2C).

My results from intracellular recordings and ultrastructural studies demonstrate that X^{RFP} neurons in mosaic mice maintained their synaptic inputs during postnatal development even in the absence of postsynaptic activity. This suggests that preganglionic axons did not withdraw their connections from inactive neurons. Given that X^{RFP} neurons remain innervated in the absence of synaptic transmission, I investigated the refinement of preganglionic inputs on these neurons, as well as their dendritic growth and synaptic targeting.

4.3.4 Preganglionic axons innervating X^{RFP} neurons refine without postsynaptic activity

To estimate the number of inputs converging onto sympathetic neurons in mosaic ganglia, I first infected mosaic mice with Ad-α3, and 1–2 days post infection, recorded intracellularly from $X^{\alpha3}$ neurons and X^{RFP} neurons in the same mosaic ganglia. Due to the delay in α3 expression, P7–P8 was the earliest time point at which I could reliably record EPSPs and measure the number of inputs. In P7–P8 mosaic mice, $X^{\alpha3}$ neurons and X^{RFP} neurons were innervated by ~7 preganglionic axons (Figures 4.3A, B). This pattern is similar to the innervation of SCG neurons in WT mice during the first postnatal week (Figure 4.3E), indicating that connections in mosaic SCG, particularly those on inactive X^{RFP} neurons, had formed normally, and provides further evidence that synapse formation occurs independently of activity.

At P25–P28, $X^{\alpha3}$ neurons were innervated by ~3 inputs, indicating that preganglionic axons had refined over this postnatal period, following a similar time course as WT SCG neurons (Figures 4.3C, E). On the other hand, in surprising contrast to SCG neurons in α3 KO mice, X^{RFP} neurons at P25–P28 were only innervated by ~3 preganglionic inputs, indicating that preganglionic axons refined even though X^{RFP} neurons were synaptically silent (Figures 4.3D, E).

As described in the previous chapter, I quantified the disparity in strength between inputs. Preganglionic inputs innervating $X^{\alpha3}$ neurons followed a similar pattern as observed in WT SCG: at P7, inputs were approximately equal in strength, and by P25–P28, one axon had strengthened considerably over the remaining inputs (Figures 4.3A, C, F). Inputs innervating X^{RFP} neurons were also similar in strength at P7 (Figures 4.3B, F), and by P25–

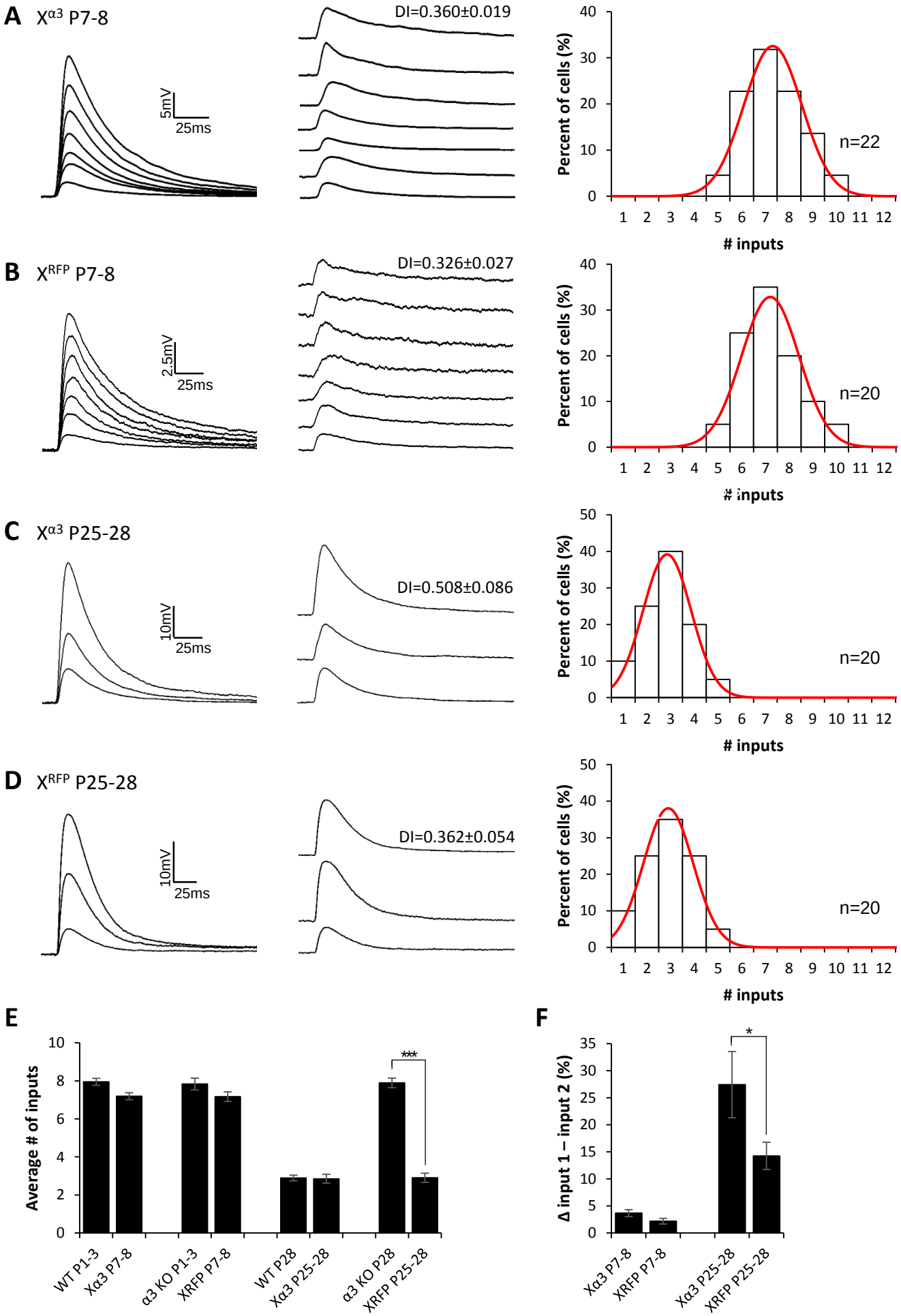
A Xα3 P7-8
5mV
25ms
DI=0.360±0.019
Percent of cells (%)
n=22
# inputs
B XRFP P7-8
2.5mV
25ms
DI=0.326±0.027
Percent of cells (%)
n=20
# inputs
C Xα3 P25-28
10mV
25ms
DI=0.508±0.086
Percent of cells (%)
n=20
# inputs
D XRFP P25-28
10mV
25ms
DI=0.362±0.054
Percent of cells (%)
n=20
# inputs
E
Average # of inputs
***
WT P1-3
Xα3 P7-8
α3 KO P1-3
XRFP P7-8
WT P28
Xα3 P25-28
α3 KO P28
XRFP P25-28
F
Δ input 1 – input 2 (%)
*
Xα3 P7-8
XRFP P7-8
Xα3 P25-28
XRFP P25-28

Figure 4.3

Figure 4.3 Preganglionic axons innervating X^{RFP} neurons refine in the absence of postsynaptic activity.

(**A**-**D**) Left: Representative compound EPSPs in a (**A**) P7-8 $X^{\alpha 3}$ neuron, (**B**) P7-8 X^{RFP} neuron, (**C**) P25-28 $X^{\alpha 3}$ neuron, and (**D**) P25-28 X^{RFP} neuron in mosaic SCG evoked by increasing stimuli to the preganglionic nerve.

Middle: The EPSPs evoked by individual preganglionic axons. DI indicates disparity index.

Right: Distribution of SCG neurons innervated by the number of inputs, fit with a Gaussian function. Each distribution in A-D contains data from at least 8 mice; n refers to the number of neurons.

(**E**) The average number of axons innervating WT neurons, α3 KO neurons, $X^{\alpha 3}$ neuron, and X^{RFP} neurons at different postnatal ages. WT and α3 KO data are from Figure 3.1.

(**F**) The average difference in strength between the strongest and second strongest inputs, expressed as a percentage of the maximum compound EPSP.

For E, F, error bars represent ± SEM; *$p<0.05$, ***$p<0.001$.

28, 1–2 inputs increased in strength (Figures 4.3D, F), however, the disparity in strength between inputs was not as large as that of WT and $X^{\alpha 3}$ neurons.

4.3.5 X^{RFP} neurons form elaborate dendritic arbours without postsynaptic activity

I previously showed that synaptically silent SCG neurons in α3 KO mice are defective in their ability to maintain primary dendrites, and therefore have a reduced TDO when compared to active SCG neurons in WT mice. These findings are consistent with the well-established idea in the literature that afferent synaptic activity is necessary for dendritic growth and maintenance (Cline, 2001; Haas *et al*., 2006; Niell *et al*., 2004; Wong and Ghosh, 2002).

To examine dendritic morphology, I sparsely labelled neurons with the lipophilic dye DiO in mosaic SCG from P28 mice. The synaptically active $X^{\alpha 3}$ neurons formed elaborate dendritic arbours, and when quantified, the average TDO and the number of primary dendrites were not significantly different from that of WT neurons (Figures 4.4A, C, D). Surprisingly, the dendritic arbours formed by inactive X^{RFP} neurons closely matched the morphology of active $X^{\alpha 3}$ neurons and WT neurons, and the TDO as well as the number of primary dendrites was significantly greater than that of α3 KO neurons (Figures 4.4B, C, D).

4.3.6 Silent synapses onto X^{RFP} neurons are appropriately targeted to the dendritic arbour

In WT mice, preganglionic axons target their synapses to the dendrites of sympathetic neurons, however, in the absence of postsynaptic activity in α3 KO mice, silent synapses become mistargeted to the cell soma of SCG neurons. Given that inputs onto X^{RFP}

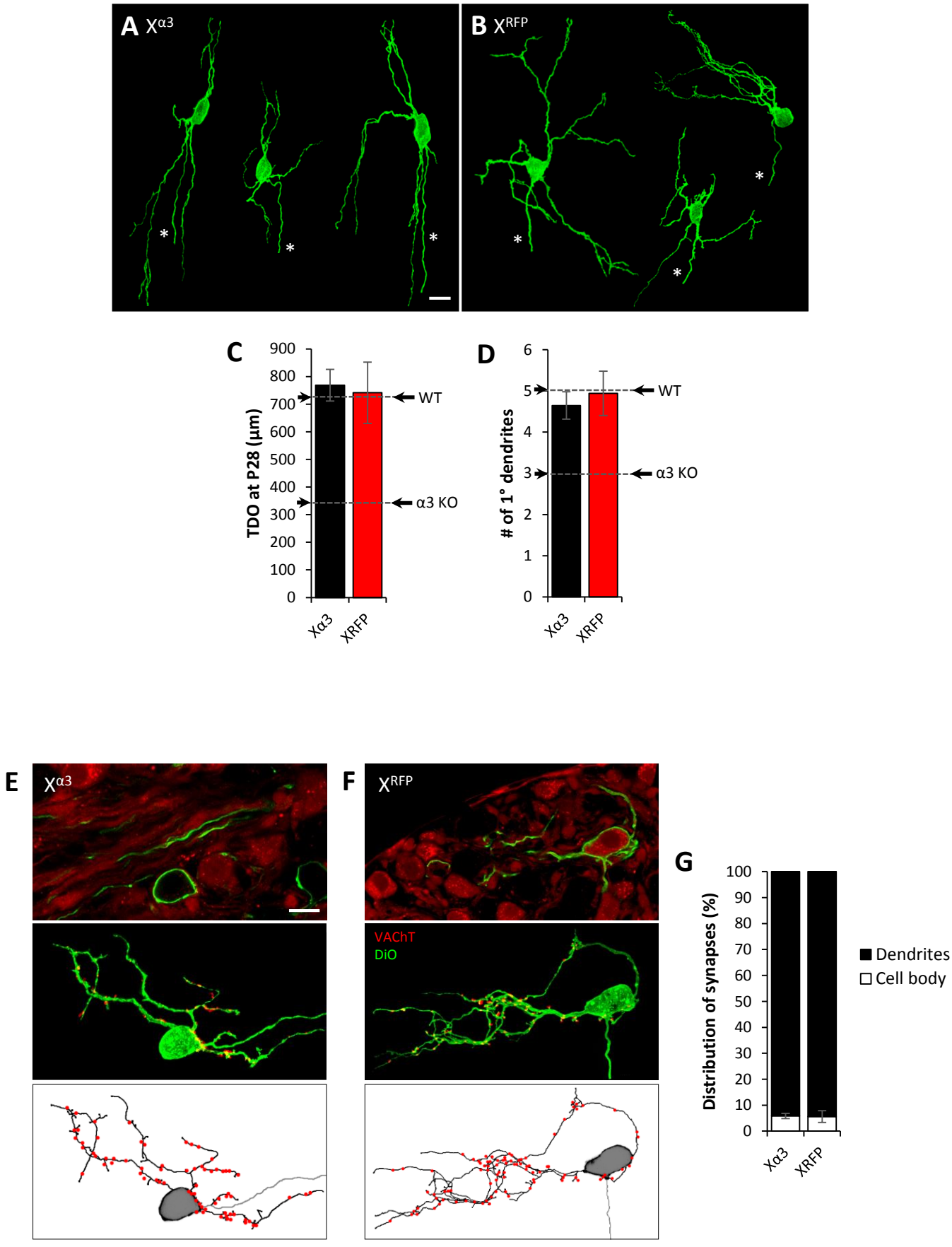
A Xα3
B XRFP
C
TDO at P28 (µm)
900
800
700
600
500
400
300
200
100
0
WT
α3 KO
Xα3
XRFP
D
# of 1° dendrites
6
5
4
3
2
1
0
WT
α3 KO
Xα3
XRFP
E
Xα3
F
XRFP
VAChT
DiO
G
Distribution of synapses (%)
100
90
80
70
60
50
40
30
20
10
0
Dendrites
Cell body
Xα3
XRFP

Figure 4.4

Figure 4.4 Dendritic growth and synaptic targeting on X^{RFP} neurons develop normally.

(**A**-**B**) Maximum intensity projections of DiO-labelled (**A**) $X^{\alpha 3}$ neurons and (**B**) X^{RFP} neurons from mosaic SCG labelled at P28. All neurons are shown at the same scale; axons are marked by an asterisk. Scale bar, 20μm. In each panel, neurons are from different ganglia and have been tiled for comparison.

(**C**-**D**) Quantification of (**C**) average total dendritic outgrowth per neuron at P28, and (**D**) average number of primary dendrites per neuron at P28. Black columns represent $X^{\alpha 3}$ neurons and red columns represent X^{RFP} neurons. For comparison, arrows indicate average values from P28 WT and α3 KO neurons, WT and α3 KO data are from Figure 3.3.

(**E**-**F**) Top: Single optical plane of a DiO-labelled (green) (**E**) $X^{\alpha 3}$ neuron and (**F**) X^{RFP} neuron in mosaic SCG (RFP expression in red) at P28. Scale bar, 20μm.

Middle: Maximum intensity z-projection of the same DiO-labelled SCG neuron as above, immunostained for VAChT (red); axon is marked by an asterisk. VAChT puncta not touching the neuron were removed for clarity. Scale bar, 20μm.

Bottom: Skeletonized reconstructions showing dendritic arbors (black), axon (grey, marked by an asterisk), and preganglionic axon varicosities (red) determined by VAChT staining.

(**G**) Average distribution of varicosities on the cell body (open) and dendrites (filled) of $X^{\alpha 3}$ neurons and X^{RFP} neurons in mosaic SCG at P28.

For C, D, G, error bars represent ± SEM. For $X^{\alpha 3}$, n=10 neurons, and for X^{RFP}, n=10 neurons (8 mice).

neurons refined and the dendrites were morphologically normal in the absence of activity, I asked how synapses are targeted on X^{RFP} neurons. I sparsely labelled neurons with DiO in mosaic SCG from P28 mice and stained for the presynaptic marker VAChT to localize synapses. For $X^{\alpha 3}$ neurons, approximately 95% of the VAChT-positive varicosities were located on the dendrites (Figures 4.4E, G). Similarly, >90% of VAChT puncta were located on the dendritic arbour of X^{RFP} neurons, which is significantly different from the distribution on α3 KO SCG neurons, even though the synapses on X^{RFP} neurons are also silent (Figures 4.4F, G).

4.4 Discussion

To learn more about how pre- and postsynaptic neurons govern the development of neural circuits, we developed a unique mouse model in which preganglionic axons have a choice between innervating active neurons that form functional synapses and inactive neurons that form silent synapses. To my knowledge, the strategy of using X-inactivation to investigate how silent connections develop in the presence of active ones has not been carried out before. My results showed that silent connections on inactive X^{RFP} neurons persist and refine in the absence of postsynaptic activity. Additionally, X^{RFP} neurons extend elaborate dendrites that are not statistically different from WT neurons and synapses are primarily distributed on the dendritic arbour even though the neurons do not receive any functional innervation. These findings contradict those from the α3 KO model in the previous chapter, and indicate that postsynaptic activity is not essential for the normal development of neural circuits. During early postnatal development, the refinement of

preganglionic axons, dendritic growth, and synaptic targeting appear to be regulated in a non-cell-autonomous manner.

An alternative approach to generate mosaicism was described in Lu *et al*. (2013), in which a low concentration of Cre-expressing adeno-associated virus was used to eliminate glutamatergic synaptic transmission in a subset of CA1 pyramidal neurons. In their experiments, most cellular properties that were examined, including neuronal morphology, were similar between active and inactive neurons, consistent with the results in this chapter. However, Lu *et al*. did not investigate the refinement of converging inputs onto these pyramidal neurons.

4.4.1 Mosaic expression of the α3 nAChR subunit gene on the X chromosome

To generate mosaic expression of the α3 subunit, we used a targeting vector to insert rat α3 subunit cDNA into the HPRT locus on the X chromosome. Quantifying relative mRNA expression with qPCR indicated that expression of α3 from the X chromosome was 5-fold lower than the expression from a single WT α3 allele on chromosome 9. In addition, approximately half of the $X^{\alpha 3}$ neurons from P1–P3 mice did not have detectable EPSPs, and appeared to require a few postnatal days for the α3 subunit to accumulate in order to reach levels that were sufficient to effectively mediate synaptic transmission. This is somewhat perplexing because the human UbiC promoter is active prenatally, and at birth, RFP expression driven by the same promoter is strong and intensely fluorescent in X^{RFP} neurons. Conceivably, many more α3 subunit proteins are necessary for synaptic transmission than the number of RFP molecules required to reach detectable levels of fluorescence.

One possible explanation for the low levels of α3 mRNA expression is that the mRNA generated from rat cDNA is less stable than endogenous mouse α3 mRNA. This seems unlikely because the sequences between rat and mouse are ~95% similar. A more likely explanation for reduced levels of α3 mRNA is that the gene was removed from its endogenous location on chromosome 9, where it is part of an α5/α3/β4 gene cluster and the regulation of this gene cluster is complex (McDonough and Deneris, 1997). On the X chromosome, α3 is expressed under a foreign promoter, and therefore is not regulated by its endogenous promoter or by the enhancer present in the 3' end of the β4 gene. Why α3 mRNA is present at such abundant levels in WT mice is not clear. Possibly, nAChRs in WT neurons turnover at a high frequency, and it would be interesting to investigate whether nAChRs in $X^{\alpha 3}$ neurons turnover at the same rate as in WT neurons. Nonetheless, expression of α3 from the X chromosome is clearly sufficient to mediate synaptic transmission by P7–P8 because stimulating the preganglionic nerve evoked suprathreshold EPSPs in $X^{\alpha 3}$ neurons.

4.4.2 Refinement of preganglionic axons

I initially anticipated one of two likely outcomes in the innervation of X^{RFP} neurons in adult mosaic mice. In one scenario, I expected preganglionic axons to differentiate between active synapses and inactive synapses, and to withdraw their connections from X^{RFP} neurons, leaving them without innervation. On the other hand, my previous results from α3 KO mice suggest that preganglionic axons require postsynaptic activity for refinement, and therefore X^{RFP} neurons would remain hyperinnervated. Surprisingly,

neither scenario transpired; preganglionic inputs onto X^{RFP} neurons refine as if their connections were active.

The disparity in strength between inputs on X^{RFP} neurons is lower than the disparity of active connections innervating $X^{\alpha 3}$ neurons or WT neurons. An often-cited model is that presynaptic axons compete for trophic factors, which drives the refinement process (Lichtman and Colman, 2000). And, several studies suggest that the strength and timing of presynaptic activity generates postsynaptic retrograde signals that allow some inputs to outcompete other inputs. My results contradict these models because inputs onto X^{RFP} neurons do not generate postsynaptic responses, yet inputs refine. Therefore, it is not clear what factors determine which inputs are maintained and which ones are eliminated. Possibly, the inputs that remain are those that had formed more synapses than other inputs, which would indicate that morphological synapses, even though they are electrophysiologically silent, play a role in stabilizing axons and mediating refinement, possibly through cell adhesion molecules or other cell surface proteins.

The mechanisms that underlie refinement are likely to involve anterograde and retrograde signals that cross synapses and coordinate how connections are reorganized during postnatal development. However, it is unclear whether these signals operate locally by acting directly on individual synapses, or on a global, circuit-wide scale, whereby signals from a collection of synapses are integrated and compared to determine which connections to maintain and which to eliminate.

Whether refinement is regulated locally or globally is difficult to address because neural activity in animal models has generally been manipulated in a global manner, in which all synapses are rendered inactive through common strategies such as abolishing

presynaptic release, antagonizing postsynaptic receptors, or sensory deprivation. Unfortunately, eliminating activity at one "node" of the pathway has an unintended effect of silencing the entire circuit, which may occlude the specific effects of local synaptic activity on circuit development. Although the resulting developmental defects are often attributed to the absence of anterograde synaptic activity, in reality, it is difficult to precisely identify the cause of these defects. For example, my results from α3 KO mice indicated that when synaptic transmission is abolished, connections do not refine, dendritic growth is stunted, and synapses are mistargeted to the cell soma. However, as a consequence of eliminating synaptic transmission in the SCG, all downstream activity to target organs was also silenced. Any activity-dependent retrograde signals such as those generated by sympathetic targets were likely to have been disrupted, and it is possible that the defects I observed in α3 KO mice may have been secondary to the effects of eliminating circuit activity. On the other hand, inactive neurons in the mosaic mouse model do not form postsynaptic nAChRs and do not receive functional innervation, however, circuit activity remains intact. My results from this chapter provide strong support for a role of circuit activity in regulating the development of neural circuits.

4.4.3 Dendritic growth and distribution of silent synapses in mosaic SCG

In the previous chapter, I described morphological defects observed in the SCG of α3 KO mice: neurons could not maintain all of their primary dendrites and therefore have a reduced TDO, and silent synapses were mistargeted to the cell soma. Since SCG neurons in α3 KO mice do not express postsynaptic nAChRs, it is instinctive to assume that these defects were directly caused by the absence of anterograde synaptic activity. Similar

defects in morphology are often attributed to loss of synaptic activity in the literature, and these ideas have become well established. Therefore, I was surprised to discover that the postnatal development of X^{RFP} neurons in mosaic SCG more closely resemble active neurons than inactive ones, even though X^{RFP} neurons do not form functional nAChRs and have no postsynaptic activity.

In the absence of postsynaptic activity, X^{RFP} neurons formed complex and elaborate dendritic arbours that matched those of active $X^{\alpha3}$ neurons and WT neurons, clearly indicating that extracellular signals can promote dendritic growth and maintenance through signalling pathways that do not depend on the influx of extracellular calcium induced by postsynaptic activity. The identity of these pathways are not clear, however, there is evidence that trophic factors released by targets, such as NGF, enhance dendritic arborization of SCG neurons (Purves *et al*., 1988; Snider, 1988). One cannot rule out the influence of local interactions with neighbouring $X^{\alpha3}$ neurons or glial cells. However, this seems unlikely because SCG neurons are not connected by gap junctions, and satellite glial cells in the SCG do not envelop more than one neuron, although it remains possible that $X^{\alpha3}$ neurons release molecular signals that diffuse locally to act on neighbouring X^{RFP} neurons.

As was previously observed in α3 KO mice, preganglionic axons in mosaic SCG continue to strengthen their connections by establishing synapses onto the postsynaptic neuron in an activity-independent manner. While synapses on SCG neurons in α3 KO mice are mistargeted to the cell soma, synapses onto X^{RFP} neurons are appropriately targeted to the dendrites even though they are silent. I previously speculated that synapses are targeted to the cell soma of SCG neurons in α3 KO mice because inactive neurons compensate by secreting attractive molecular cues to actively seek innervation. However,

given that synaptic targeting onto X^{RFP} neurons is normal, even though they are also inactive and do not receive functional innervation, this idea now seems unlikely.

X^{RFP} neurons have a significantly greater TDO than neurons from α3 KO. Considering that the density of synapses on SCG neurons in WT and α3 KO mice is not significantly different, it is conceivable that dendrites regulate the density of their synaptic inputs. As a result, a reduced TDO in α3 KO mice can only support a limited number of synaptic sites, and once saturated, direct all additional synapses to be formed on the cell soma. In contrast, X^{RFP} neurons extend elaborate dendrites, which are capable of supporting large numbers of synapses. This interpretation would suggest that the defects in synaptic targeting in α3 KO mice are secondary to their defects in dendrite morphology.

4.4.4 Conclusion

On one level, X^{RFP} neurons are equal to sympathetic neurons in α3 KO mice. Both types of neurons do not express postsynaptic receptors and remain inactive throughout embryonic and postnatal development. This being the case, one might expect X^{RFP} neurons and α3 KO neurons to develop in similar ways. On the other hand, there is a clear difference in the environment between X^{RFP} neurons and α3 KO neurons. In α3 KO mice, all SCG neurons are inactive, whereas in mosaic SCG, X^{RFP} neurons are surrounded by neighbouring $X^{\alpha 3}$ neurons that express postsynaptic receptors and function normally. This activity generated by $X^{\alpha 3}$ neurons appears to be responsible for the normal development of X^{RFP} neurons in a non-cell-autonomous manner by signalling through unknown pathways. I speculate that there are two possible mechanisms: (1) $X^{\alpha 3}$ neurons generate activity-dependent molecular signals that diffuse locally within the SCG; or (2) $X^{\alpha 3}$ neurons

stimulate downstream targets and promote the release of activity-dependent retrograde signals that are taken up at the axon terminals of X^{RFP} neurons and transported to the cell body to mediate their growth. In the next chapter, I explore this possibility by investigating whether inactive neurons have defects in the innervation of their targets, which would consequently limit the retrograde trophic support they receive. Indeed, it is possible that both mechanisms operate in parallel and contribute to the normal development of X^{RFP} neurons in mosaic mice.

Chapter 5: Does neuronal activity influence target innervation?

5.1 Introduction

Neurons in the SCG innervate several downstream targets including the iris, circle of Willis, pineal gland, bone marrow, and various other glands and blood vessels in the head and neck to regulate their function. These targets secrete retrograde trophic factors, such as nerve growth factor (NGF), which are necessary for the growth and survival of sympathetic neurons (Levi-Montalcini, 1987). Since SCG neurons in α3 KO mice exhibit severe developmental defects in refinement, dendritic growth and synaptic targeting, I considered the possibility that target innervation by inactive neurons may be defective and consequently limit the quantity of retrograde trophic factors received. In this chapter, I investigated (1) whether inactive neurons in α3 KO mice have defects in the innervation of their targets; and (2) whether synaptic activity gives active neurons a competitive advantage over less active neurons when innervating common targets.

To learn more about how the activity of SCG neurons influences target innervation, I focused my experiments on the iris. The iris is easily accessible and I can observe its function in awake behaving mice without invasive surgeries and with minimal stress to the animal. In addition, because of its thin structure, the iris is an ideal tissue to investigate sympathetic innervation with whole-mount immunostaining and confocal imaging. The iris is made up of smooth muscle organized into two structures: (1) sphincter muscles that form the inner ring of the iris, which are innervated primarily by parasympathetic fibers that release acetylcholine and cause the pupil to constrict; and (2) radial muscles that are innervated primarily by sympathetic fibers, which release noradrenaline to stimulate the pupil to dilate.

I found that a similar number of SCG neurons project to the iris in WT and α3 KO mice, indicating that neurons do not need to be active for their axons to innervate the iris. However, the innervation density of the iris is significantly lower in α3 KO mice than in WT controls, suggesting that neural activity is necessary for sympathetic neurons to innervate their targets effectively. In mosaic mice, the total number of SCG neurons that project to the iris is similar to the numbers in WT and α3 KO mice. And, the innervation density of the iris in mosaic mice is similar to that of irises in WT mice. In mosaic mice, active $X^{\alpha 3}$ neurons do not outcompete synaptically silent X^{RFP} neurons; the contribution of $X^{\alpha 3}$ and X^{RFP} axons at the level of the iris reflected the ratio of neurons that project to the iris. This suggests that synaptically active neurons do not have a major competitive advantage over synaptically silent neurons when innervating common targets.

5.2 Methods

For this chapter, experimental models and methods included: α3 KO and mosaic mouse models (2.1.1-2.1.2), confocal imaging (2.4), immunohistochemistry of the iris (2.6.4), retrograde labelling with cholera toxin subunit B (2.8), and statistical analysis (2.13).

5.3 Results

5.3.1 Axons of SCG neurons in α3 KO mice innervate the iris and are maintained in the absence of activity

Considerable evidence indicates that inactive connections are often eliminated during postnatal development (Buffelli *et al*., 2003; Katz and Shatz, 1996; Wiesel and

Hubel, 1965). Therefore, I first addressed whether inactive axons of SCG neurons in α3 KO mice reach the iris and whether these silent connections are maintained in adult mice. To determine the number of neurons that project to the iris in WT and α3 KO mice at P28, I injected the retrograde tracer cholera toxin subunit B conjugated to Alexa Fluor 488 (CTB-488) into the anterior chamber of one eye. If axons of SCG neurons were present at the iris, the fluorescent label would be endocytosed at axon terminals and transported retrogradely to cell bodies in the SCG. In WT mice, an average of 34.75 ± 3.56 SCG neurons were retrogradely labelled with CTB-488 and most were distributed in the rostral end of the SCG (Figures 5.1A, C), consistent with previous work (Luebke and Wright, 1992). Interestingly, the number of labelled neurons in the SCG of α3 KO mice (36.8 ± 1.11) and their spatial distribution was not significantly different from WT (Figures 5.1B, C). No labelling was observed in the contralateral SCG in either WT or α3 KO mice. These results indicate that synaptic activity is not necessary for sympathetic axons to reach their targets or for this innervation to persist.

5.3.2 SCG neurons in α3 KO mice innervate the iris at a lower density than in WT mice

To further investigate the role of neuronal activity in target innervation, I examined whether activity influences axon arborization and the innervation density of the iris. In order to visualize the innervation of the iris, I performed whole-mount immunohistochemistry on irises from P28 WT and α3 KO mice, and used tyrosine hydroxylase (TH) as a marker of sympathetic axons, and the vesicular monoamine transporter 2 (VMAT2) to identify presynaptic varicosities. TH-positive fibers and VMAT2

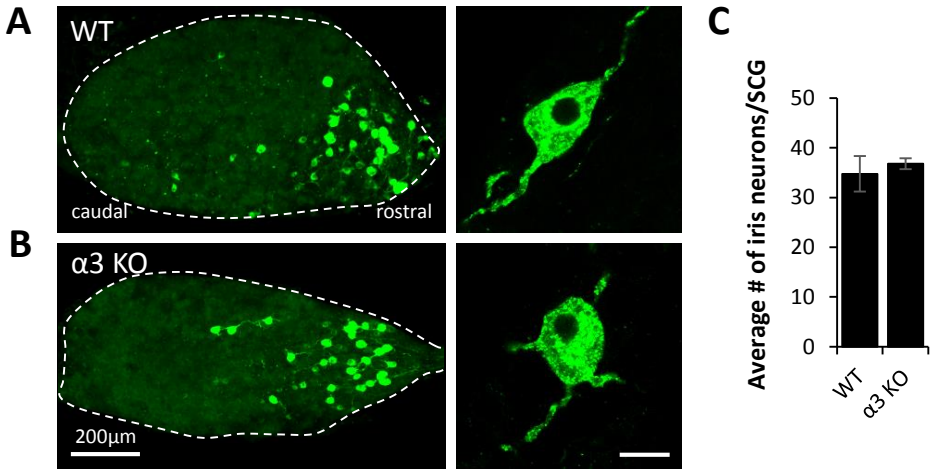

Figure 5.1 Similar numbers of SCG neurons project to the iris in WT and α3 KO mice.

(**A**-**B**) Left: Maximum intensity projection of CTB-488-labelled neurons (green) in intact SCG. Neurons were retrogradely labelled from the iris in (**A**) WT and (**B**) α3 KO mice at P28.

Right: CTB-488-labelled neurons (green) at higher magnification. Scale bar, 20µm.

(**C**) Average number of neurons innervating the iris per WT and α3 KO SCG at P28. Error bars represent ± SEM. For WT, n=8 SCG (8 mice), and for α3 KO, n=7 SCG (7 mice).

puncta were found in irises of both WT and α3 KO mice (Figure 5.2A), confirming my retrograde labelling results.

The fluorescence intensity of TH-positive axons was significantly lower in α3 KO mice than in WT mice (Figure 5.2B), consistent with previous work showing that the regulation of TH expression is activity-dependent (Kumer and Vrana, 1996). This was not the case for VMAT2 (Figure 5.2D). Therefore, I used TH and VMAT2 signals to quantify the density of innervation at the iris in two independent ways: (1) I calculated the proportion of the area occupied by TH-positive fibers; and (2) I measured the number of VMAT2 puncta within a given area. Both measurements indicated that the density of innervation in α3 KO mice was approximately half that of WT mice (Figures 5.2C, E). In addition, I quantified the density of varicosities (VMAT2 puncta) along a sympathetic axon and found that there was no statistical difference between the density of varicosities along WT and α3 KO axons (Figure 5.2F); these data suggest that presynaptic differentiation does not require activity.

5.3.3 $X^{\alpha 3}$ neurons and X^{RFP} neurons from mosaic SCG both innervate common targets

The results from α3 KO mice indicate that synaptic activity is not necessary for sympathetic axons to reach their targets or for this innervation to persist, but activity does increase the density of innervation of the target. Therefore, one might predict that synaptically active neurons have a competitive advantage over inactive neurons in target innervation.

To test this prediction, I investigated iris innervation in the mosaic mouse model. Specifically, I asked whether active $X^{\alpha 3}$ neurons outcompete synaptically silent X^{RFP}

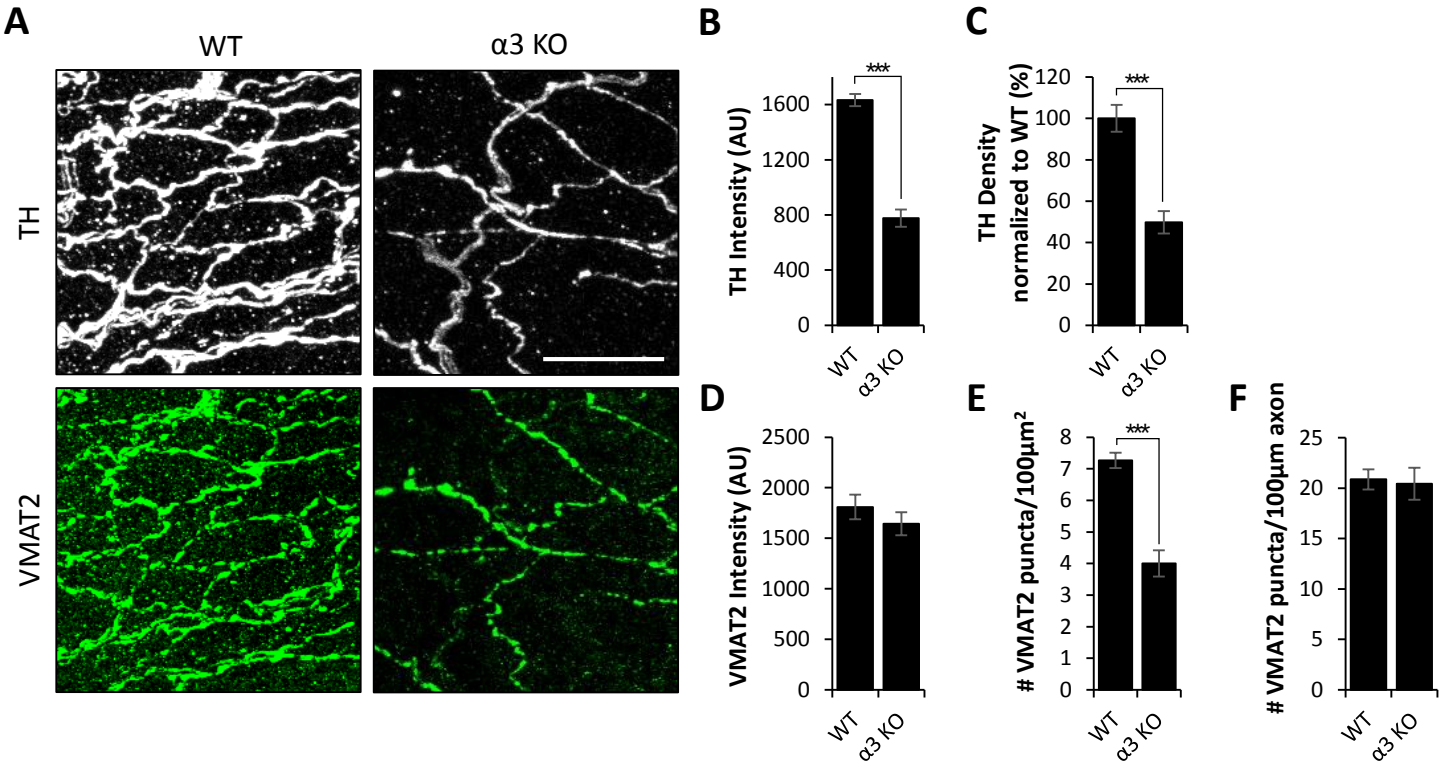

Figure 5.2 Innervation density of the iris is lower in α3 KO mice than in WT mice.

(**A**) Maximum intensity projections of immunostaining for TH (white; top) and VMAT2 (green; bottom) in iris of (left) WT and (right) α3 KO mice at P28. Scale bar, 20μm.

(**B**) TH mean fluorescence intensity for axon fibers innervating the iris of WT and α3 KO mice at P28.

(**C**) Average area of the iris innervated by TH-positive axons in WT and α3 KO mice at P28, normalized to WT.

(**D**) VMAT2 mean fluorescence intensity of VMAT2 puncta on the iris of WT and α3 KO mice at P28.

(**E**) Average number of VMAT2 puncta per 100μm^2 square area of iris in WT and α3 KO mice at P28.

(**F**) Average number of VMAT2 puncta per 100μm length of skeletonized TH-positive axons innervating the iris in WT and α3 KO mice at P28.

For B, C, D, E, F, error bars ± SEM; ***p<0.001. For WT, n=10 irises (5 mice), and for α3 KO, n=10 irises (5 mice).

neurons to innervate the iris, a shared target. To determine the ratio of $X^{\alpha 3}$ neurons and X^{RFP} neurons that innervate the iris in P28 mosaic mice, I repeated the CTB-488 retrograde labelling experiments described above. I found that the total number of SCG neurons that projected to the iris in mosaic mice was 35 ± 4.23, and not significantly different from either WT mice or α3 KO mice (Figures 5.3A, B). Similarly, the labelled neurons were localized at the rostral end of the SCG (Figure 5.3A), and only projected to the ipsilateral eye. However, within the labelled population of neurons in mosaic SCG, the ratio between labelled $X^{\alpha 3}$ neurons and X^{RFP} neurons was not equal. Of the SCG neurons that innervated the iris, approximately 60% were $X^{\alpha 3}$ neurons and 40% were X^{RFP} neurons (Figure 5.3C). Based on these results, I concluded that although axons of X^{RFP} neurons innervate the iris, $X^{\alpha 3}$ neurons appear to have a slight competitive advantage.

5.3.4 $X^{\alpha 3}$ neurons and X^{RFP} neurons in mosaic mice innervate the iris at similar densities

Since the density of sympathetic axons innervating the iris in α3 KO mice was approximately 50% of the density of synaptically active axons in WT mice, one might expect that if there is no competition among axons, then the innervation density would be at an intermediate level between WT mice and α3 KO mice. To test this idea, I quantified the density of innervation from active axons of $X^{\alpha 3}$ neurons and inactive axons of X^{RFP} neurons innervating the iris.

As above, I stained for TH to visualize sympathetic axons and VMAT2 to label presynaptic varicosities and calculated the total innervation density of both $X^{\alpha 3}$ and X^{RFP} sympathetic axons at the iris of mosaic mice. Together, the total density of sympathetic

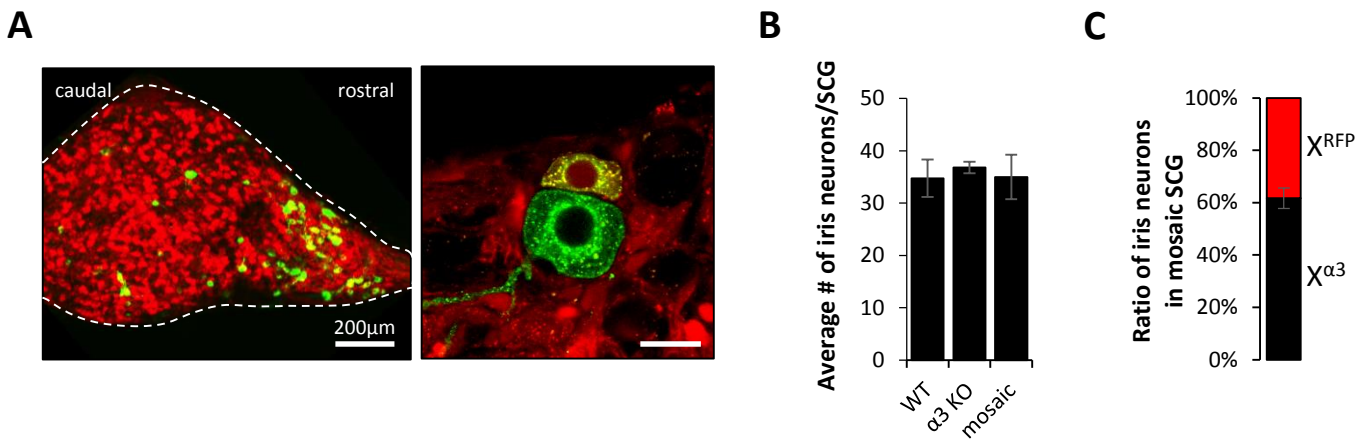

Figure 5.3 $X^{\alpha 3}$ neurons and X^{RFP} neurons in mosaic SCG innervate the iris at roughly similar proportions.

(**A**) Left: Maximum intensity projections of CTB-488-labelled neurons (green) in intact mosaic SCG (X^{RFP} neurons in red). Neurons were retrogradely labelled from the iris in mosaic mice at P28.

Right: CTB-488-labelled (green) $X^{\alpha 3}$ neuron and X^{RFP} neuron (red) at higher magnification. Scale bar, 20µm.

(**B**) Average number of neurons innervating the iris per SCG in WT, α3 KO, and mosaic mice at P28. WT and α3 KO data are from Figure 5.1.

(**C**) Average ratio of CTB-488-labelled $X^{\alpha 3}$ neurons (black) and X^{RFP} neurons (red) per SCG innervating the iris in mosaic mice at P28.

For B, C, error bars represent ± SEM, n=9 SCG (9 mice).

innervation was not significantly different from WT mice (Figures 5.4A, B, C). However the question is whether most of these axons belong to $X^{\alpha 3}$ neurons.

To address this, I measured the ratio of axon fibers belonging to $X^{\alpha 3}$ neurons and X^{RFP} neurons at the iris of P28 mosaic mice. I found that the proportion of axons from $X^{\alpha 3}$ neurons and axons from X^{RFP} neurons roughly mirrored the 60:40 ratio of $X^{\alpha 3}$ neurons to X^{RFP} neurons that projected to the iris. Of the TH-positive fibers innervating the iris, approximately 56% were extended by $X^{\alpha 3}$ neurons, and 44% belonged to X^{RFP} neurons (Figure 5.4D). Additionally, the density of synaptic nerve terminals, identified by VMAT2 labelling, along the length of an axon fiber, was not different between $X^{\alpha 3}$ neurons and X^{RFP} neurons (Figure 5.4E).

5.4 Discussion

SCG neurons are dependent on retrograde factors generated by target organs for growth and survival (Levi-Montalcini, 1987). Since retrograde factors are endocytosed at nerve terminals and transported back to the cell body (Ginty and Segal, 2002), I investigated whether the activity of the SCG neurons influences how they innervate targets and consequently regulate the quantity of retrograde signals they receive. I found that a relatively constant number of SCG neurons project to the iris between WT, α3 KO, and mosaic mice, regardless of their activity. Presumably, the guidance cues that direct axonal projections from SCG neurons to their appropriate targets operate independently of activity. However, after reaching the target, the innervation density in α3 KO mice was significantly lower than that of WT and mosaic mice, and could have downstream

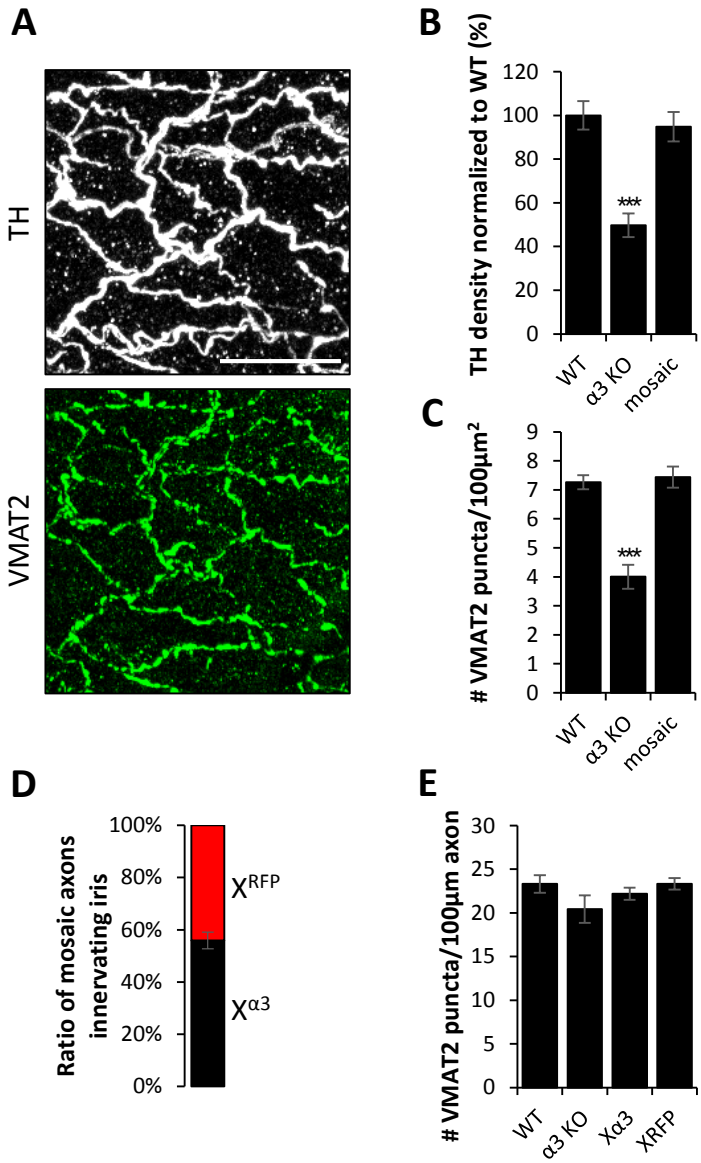

Figure 5.4 Innervation density of the iris in mosaic mice is similar to WT mice and higher than in α3 KO mice.

(**A**) Maximum intensity projections of immunostaining for TH (white; top) and VMAT2 (green; bottom) in the iris of mosaic mice at P28. Scale bar, 20μm.

(**B**) Average area of the iris innervated by TH-positive axons in mosaic mice at P28, normalized to WT. WT and α3 KO data are from Figure 5.2.

(**C**) Average number of VMAT2 puncta per 100μm^2 square area of iris from mosaic mice at P28.

(**D**) Average ratio of TH-positive axons from $X^{\alpha3}$ neurons (black) and X^{RFP} neurons (red) per iris in mosaic mice at P28.

(**E**) Average number of VMAT2 puncta per 100μm length of skeletonized TH-positive axons from WT, α3 KO, $X^{\alpha3}$ or X^{RFP} SCG neurons innervating the iris at P28. WT and α3 KO data are from Figure 5.2.

For B, C, D, E, error bars ± SEM; ***p<0.001; n=8 irises (4 mice).

consequences for the uptake of retrograde signals that mediate dendritic growth and innervation.

5.4.1 Retrograde regulation of axon arborization

To quantify nerve fiber density, I stained for TH and VMAT2. TH expression is activity-dependent (Kumer and Vrana, 1996), and consistent with this, I showed that the TH signal was less intense in α3 KO axons than in WT. It is unlikely that the lower expression of TH in α3 KO axons biased these measurements because all image acquisition parameters and threshold values were maintained constant between WT and α3 KO mice. And, in addition, I generated skeletonized representations of the fluorescent images. When used to calculate innervation density, skeletonized networks and thresholded fluorescent signals both indicated a similar difference between WT and α3 KO mice. These results were further substantiated by quantification with VMAT2.

Based on my results from α3 KO mice alone, defective innervation of the iris is likely caused by one of two mechanisms: either neuronal activity promotes axonal branching and growth, or in the absence of stimulation, the targets do not release sufficient levels of activity-dependent retrograde signals to enhance innervation.

In mosaic mice, X^{RFP} neurons are also inactive and yet axons branched normally, indicating that it is unlikely that axon arborization is dependent on neuronal activity. While X^{RFP} neurons themselves are inactive, they share the innervation of sympathetic targets with active $X^{\alpha 3}$ neurons and targets are functionally innervated by $X^{\alpha 3}$ neurons. Therefore, it is likely that axon arborization is not regulated by neuronal activity in a cell-autonomous manner, but rather, through retrograde signalling pathways that are mediated by the

functional stimulation of target organs. That postsynaptic activation of the targets can modulate presynaptic axon branch stability is consistent with several studies (Munz *et al*., 2014; Zou and Cline, 1996).

My results suggest that target-derived molecules that stabilize axon arbours are not limited only to active axons. Rather, the signals involved appear to be diffusible, stabilizing active and inactive axons alike so long as the target is functionally innervated. My findings on sympathetic axon-iris innervation differ from *Xenopus* RGC axons innervating tectal neurons (Munz *et al*., 2014). In those studies, RGC axons that fire out-of-sync from neighbouring axons are not stabilized, indicating that retrograde regulation of presynaptic axons can be restricted to specific axons. One possible explanation is the different time course of the experiments: in experiments performed by Munz *et al*., axonal dynamics were measured *in vivo* at frequent (10 minute or daily) intervals, whereas my results were quantified at a fixed time point (P28). Conceivably, inactive X^{RFP} axons innervating the iris show a high degree of branch additions and retractions that is only detectable through *in vivo* live-imaging experiments.

5.4.2 Target-derived retrograde growth factors

It is well established that sympathetic neurons are critically dependent on NGF for growth and survival (Levi-Montalcini, 1987). However, NGF has also been investigated as a candidate that mediates neuronal competition during development (Deppmann *et al*., 2008). Deppmann *et al*., proposed a model in which target-derived NGF binds to TrkA on sympathetic nerve terminals and are transported retrogradely to the cell soma where they have at least two roles: (1) Promote the release of BDNF and/or NT4, which bind to $p75^{NTR}$

on neighbouring neurons and activate signalling pathways downstream of $p75^{NTR}$ that result in cell death; and (2) enhance neuroprotective mechanisms against $p75^{NTR}$-mediated apoptosis. This model for neuronal competition proposed by Deppmann *et al*. is based on the idea that NGF production by the target and its uptake at nerve terminals differ in concentration and duration between neurons, conferring a competitive advantage to a subset of neurons. However, one difficulty with this model is that the authors do not offer any explanation for how the production of NGF is regulated. Instead, they assume that axons receiving higher quantities of NGF are selected randomly and become more competitive by chance. When measured *in vivo*, neither surgical nor pharmacological denervation of the iris resulted in any changes in NGF mRNA levels (Shelton and Reichardt, 1986). Therefore, it is unlikely that NGF is the retrograde factor that mediates refinement of sympathetic neurons in the SCG.

BDNF has also been proposed as a key mediator of competition. In this model, BDNF synthesis is enhanced in more active neurons and promotes axon degeneration of competing neurons by binding to $p75^{NTR}$, which is enriched in less active axons (Singh *et al*., 2008). However, because inactive axons of X^{RFP} neurons in mosaic mice do not show massive amounts of degeneration, and largely innervate the iris at a similar degree to $X^{\alpha 3}$ neurons, one can confidently rule out the possibility that this BDNF-driven mechanism mediates competition between SCG neurons.

5.4.3 Competition between active and inactive axons

Evidence from the NMJ suggest that active axons outcompete inactive axons (Buffelli *et al*., 2003). Therefore, it was somewhat surprising that X^{RFP} neurons innervate the iris to a

similar degree as active $X^{\alpha 3}$ neurons. To gain a better understanding of target innervation in mosaic mice, ideally, one would map out the individual territories of active and inactive axons, and examine whether they share territories that overlap or whether there are clear boundaries between them. Such measurements are challenging to obtain in mosaic mice because half the muscle cells also express RFP, making it difficult to distinguish between axons that express RFP from those that do not.

I considered several approaches to address this issue, and one strategy was to confine RFP expression only to sympathetic neurons. The concept was to use CRISPR-Cas9 technology and homology-directed repair (HDR) to insert three SV40 transcriptional stop sequences flanked by loxP sites (lox-STOP-lox; LSL) immediately in front of the RFP gene, and to mate these mice to a dopamine beta-hydroxylase (Dbh)-Cre driver line.

After designing and generating the LSL construct and an appropriate guide RNA, I collaborated with Dr. Mitra Cowan of the McGill Transgenic Facility, whose team performed the microinjections that delivered the LSL construct and CRISPR-Cas9 components into fertilized mouse embryos of X^{RFP} mice. All technical details are described in the Experimental models and methods section (Chapter 2.14). Briefly, after I screened and genotyped the progeny, I established a mouse line that appeared to have incorporated the LSL sequence into its genome.

While RFP expression was disrupted in these LSL mice, I was unable to restore RFP expression with Cre, either through mating with a Dbh-Cre driver line or when placed in culture and treated with a Cre-expressing adenovirus. I speculate that the LSL construct was not inserted into the anticipated location in the genome, and that the RFP gene was disrupted in an independent event. However, I cannot rule out the possibility that the loxP

sites may be occluded by secondary DNA structures *in vivo* and inaccessible for Cre to excise the SV40 transcription stop sequences.

5.4.4 Conclusion

My results on the target innervation of the iris by SCG neurons demonstrated several key findings. I showed that neuronal activity is not necessary for pathfinding of axonal projections from the SCG to their appropriate target, nor is activity necessary for silent connections to persist at their target organs. Furthermore, although activity has a role in mediating axon arborization and innervation density, I find that the mechanisms involved likely operate in a non-cell-autonomous manner. I speculate that functional stimulation of the target generates retrograde growth factors that regulate refinement, dendritic growth and synaptic targeting of SCG neurons.

Chapter 6: Does cap-dependent translation downstream of postsynaptic activity regulate refinement?

6.1 Introduction

Several signalling pathways that mediate gene transcription, mRNA translation and post-translational modifications likely converge to regulate dendritic targeting, synaptic targeting and the refinement of preganglionic axons in sympathetic ganglia. In preliminary screening of potential signalling pathways that may be involved, I identified the regulation of cap-dependent translation as a candidate pathway, and therefore I focused on whether it has a role in reorganizing neural connections during early postnatal development.

A growing body of evidence points to a link among regulated mRNA translation, neuronal development, and synaptic plasticity. Activity-dependent mechanisms promote cap-dependent mRNA translation in developing dendrites and axons, and play essential roles in forming neural circuits (Bramham and Wells, 2007; Jung *et al*., 2012; Lin *et al*., 2016; Wang *et al*., 2010). Briefly, a critical step in regulating cap-dependent translation is the binding of the eukaryotic translation initiation factor 4E (eIF4E) to the 5' cap structure of mRNAs (Gingras *et al*., 1999; Sonenberg and Hinnebusch, 2009). The availability of eIF4E is controlled by 4E-binding proteins (4E-BP), important regulators of cap-dependent mRNA translation and major downstream targets of the mechanistic target of rapamycin complex 1 (mTORC1), a serine-threonine kinase (Richter and Sonenberg, 2005; Thoreen *et al*., 2012). Hypophosphorylated 4E-BP represses the initiation of cap-dependent translation by sequestering eIF4E, whereas hyperphosphorylated 4E-BP releases eIF4E and allows eIF4E to bind to eIF4G, a molecular interaction that is required to initiate cap-

dependent translation and *de novo* protein synthesis (Figure 6.1A; Gingras *et al*., 1999; Sonenberg and Hinnebusch, 2009).

To determine whether cap-dependent translational mechanisms have a role in synaptic refinement during postnatal development, I manipulated cap-dependent translation in α3 KO mice by crossing them to mice with deletions in 4E-BP1 and 4E-BP2 genes. Since 4E-BPs function as a repressor of translation, the genetic removal of 4E-BP is expected to enhance cap-dependent translation, independent of synaptic transmission. If cap-dependent translation is enhanced by synaptic activity (or by target activation downstream of synaptic activity), then elevating cap-dependent translation in α3 KO mice may rescue the developmental defects in innervation of synaptically silent neurons in the SCG.

In α3 KO sympathetic neurons, levels of phosphorylated 4E-BP1 are lower than levels found in WT controls. On the other hand, levels of phosphorylated 4E-BP1 do not differ between $X^{\alpha 3}$ neurons and X^{RFP} neurons in mosaic SCG. Furthermore, I showed that removing 4E-BP from α3 KO mice reversed the defects both in dendritic growth on SCG neurons and in the targeting of synapses, and, remarkably, the preganglionic inputs refine in the absence of postsynaptic activity. In addition, in proteomic experiments, I observed activity-dependent changes in levels for a large number of proteins in the SCG of α3 KO mice. Interestingly, genetically removing 4E-BP from α3 KO mice largely restored these protein levels toward those in WT mice, even though the SCG has no synaptic transmission. Taken together, my findings indicate that cap-dependent translation plays a key role in reorganizing connections.

6.2 Methods

Many of the techniques used in this chapter are similar to those used to investigate the development of neural circuits in Chapters 3 and 4. For this chapter specifically, the experimental models and methods include: mosaic and α3/4E-BP DKO mouse models (2.1.2-2.1.3), intracellular recording (2.2), adenoviruses (2.3), confocal imaging (2.4), lipophilic dye tracing (2.5), 4E-BP and VAChT immunohistochemistry (2.6.1, 2.6.3), proteomic profiling (2.11) and statistical analysis (2.13).

6.3 Results

6.3.1 Levels of phosphorylated 4E-BP are higher in WT SCG than in α3 KO SCG

Since the phosphorylation status of 4E-BP regulates the availability of eIF4E and therefore the initiation of translation (Gingras *et al.*, 1999; Ma and Blenis, 2009; Sonenberg and Hinnebusch, 2007), I examined the levels of phosphorylated 4E-BP1 in WT and α3 KO SCG. At birth, there was no significant difference in the levels of phosphorylated 4E-BP1 in α3 KO SCG neurons when compared to age-matched WT neurons; however, at P28, phosphorylated 4E-BP1 in α3 KO SCG was ~25–30% less than in WT SCG, while total 4E-BP1 was at comparable levels (Figures 6.1B, C, D, E). This finding raised the intriguing possibility that the phosphorylation of 4E-BP and the regulation of translation in SCG neurons are mediated by mechanisms downstream of postsynaptic activity.

6.3.2 X^{RFP} neurons in mosaic SCG have normal levels of phosphorylated 4E-BP

Next, I examined the levels of phosphorylated 4E-BP1 in mosaic SCG. At P28, the levels of phosphorylated 4E-BP1 between $X^{\alpha 3}$ neurons and X^{RFP} neurons were not

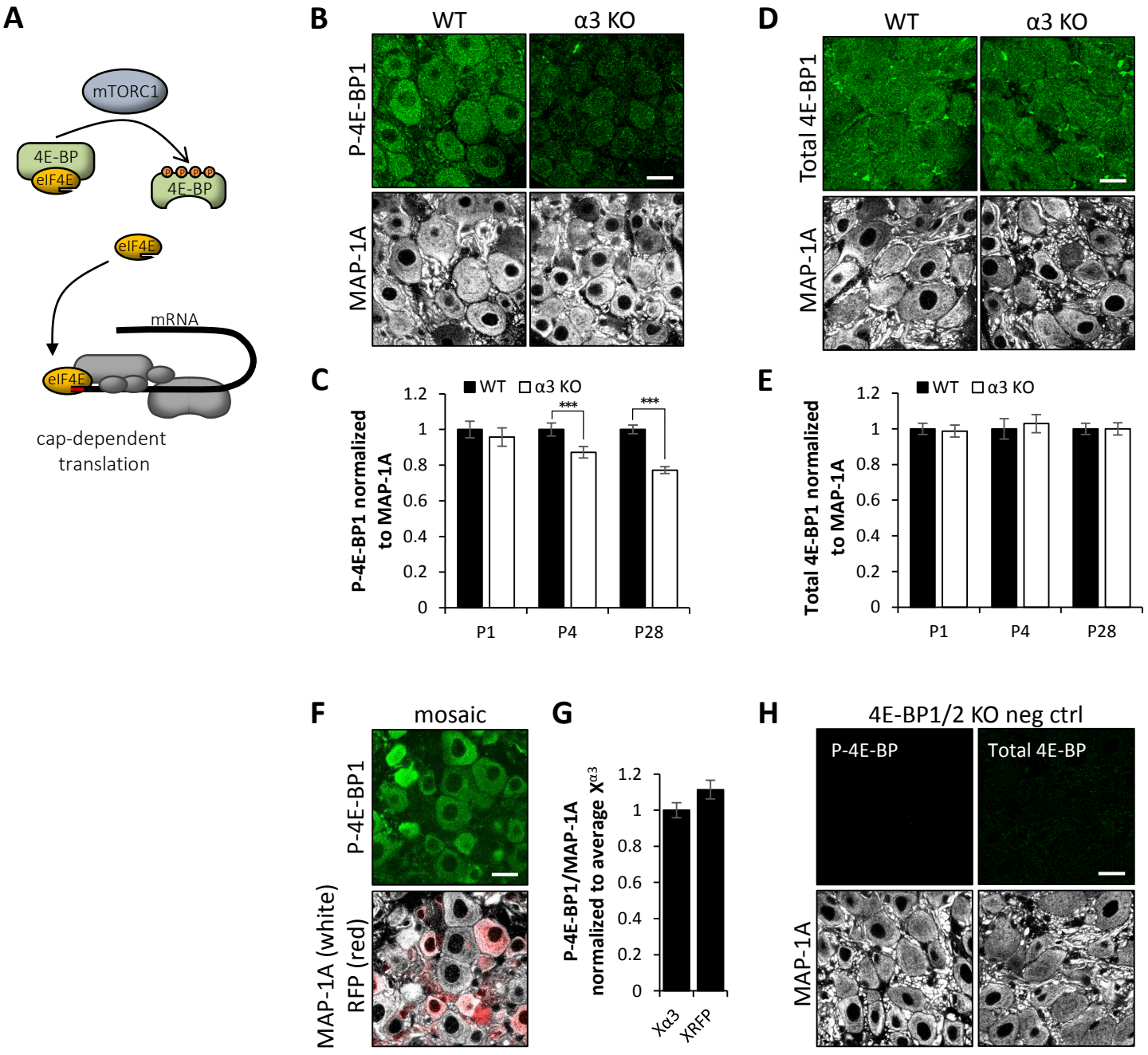
A
mTORC1
4E-BP
eIF4E
4E-BP
eIF4E
mRNA
eIF4E
cap-dependent
translation
B
WT
α3 KO
P-4E-BP1
MAP-1A
D
WT
α3 KO
Total 4E-BP1
MAP-1A
C
WT
α3 KO
P-4E-BP1 normalized to MAP-1A
1.2
1
0.8
0.6
0.4
0.2
0
***
***
P1
P4
P28
E
WT
α3 KO
Total 4E-BP1 normalized to MAP-1A
1.2
1
0.8
0.6
0.4
0.2
0
P1
P4
P28
F
mosaic
P-4E-BP1
MAP-1A (white)
RFP (red)
G
P-4E-BP1/MAP-1A normalized to average Xα3
1.2
1
0.8
0.6
0.4
0.2
0
Xα3
XRFP
H
4E-BP1/2 KO neg ctrl
P-4E-BP
Total 4E-BP
MAP-1A

Figure 6.1

Figure 6.1 Levels of phosphorylated 4E-BP are higher in WT SCG than in α3 KO SCG.

(**A**) Illustration showing cap-dependent translation, governed by the availability of eIF4E, which is regulated by 4E-BP, a major downstream target of the mTORC1 complex. Hypophosphorylated 4E-BP represses the initiation of cap-dependent translation by sequestering eIF4E. When hyperphosphorylated, 4E-BP releases eIF4E, which interacts with eIF4G and other initiation factors to initiate cap-dependent translation.

(**B**) Confocal images showing immunostaining for P-4E-BP1 (green) and MAP-1A (white) in WT and α3 KO SCG at P28. Scale bar, 20μm.

(**C**) P-4E-BP1 mean fluorescence intensity per neuron normalized to MAP-1A in WT and α3 KO neurons at P1, P4 and P28. Filled columns represent WT, open columns represent α3 KO.

(**D**) Confocal images showing immunostaining for total 4E-BP1 (green) and MAP-1A (white) in WT and α3 KO SCG at P28. Scale bar, 20μm.

(**E**) Total 4E-BP1 mean fluorescence intensity per neuron normalized to MAP-1A in WT and α3 KO neurons at P1, P4 and P28. Filled columns represent WT, open columns represent α3 KO.

(**F**) Confocal images showing immunostaining for P-4E-BP1 (green) and MAP-1A (white) in mosaic SCG (RFP expression in red) at P28. Scale bar, 20μm.

(**G**) P-4E-BP1 mean fluorescence intensity per neuron normalized to MAP-1A in $X^{\alpha 3}$ and X^{RFP} neurons at P1, P4 and P28.

(**H**) SCG from P28 4E-BP KO mice were immunostained for P-4E-BP1 (green), total 4E-BP1 (green) and MAP-1A (white) to test for non-specific binding of antibodies. Scale bar, 20 μm.

For C, E, G, error bars represent ± SEM; ***$p<0.001$. For WT in C and E, n=90 neurons (4 mice) for P1, n=90 neurons (4 mice) for P4, n=300 neurons (4 mice) for P28; and for α3 KO, n=90 neurons (4 mice) for P1, n=90 neurons (4 mice) for P4, and n=300 neurons (4 mice) for P28. For G, n=100 $X^{\alpha 3}$ neurons and 100 X^{RFP} neurons (4 mice).

statistically different (Figures 6.1F, G). This indicates that 4E-BP1 can be phosphorylated through non-cell-autonomous pathways activated by external cues such as those involving retrograde signals from sympathetic targets.

6.3.3 Deletion of 4E-BP genes when synaptic transmission is intact does not affect neuronal development

Since 4E-BP functions as a repressor of translation, one would expect the genetic removal of 4E-BP to enhance cap-dependent translation, independent of activity. To test this idea, I examined SCG neurons in mice with a deletion in 4E-BP genes. SCG neurons express both 4E-BP1 and 4E-BP2 at comparable levels (in contrast to CNS neurons, which primarily express 4E-BP2, Figures 6.2A, B); therefore, I used mice with a deletion in both genes (4E-BP1/2 KO; referred to simply as 4E-BP KO).

To determine whether deleting 4E-BP genes has any effect on the development of sympathetic neurons in the SCG when synaptic transmission is intact, I examined dendritic growth, synaptic targeting and refinement in SCG from 4E-BP KO mice. I observed no significant difference in dendritic growth on SCG neurons during the first postnatal month compared to that on age-matched SCG neurons in WT mice (Figures 6.3A, B, C, D, E, F). In addition, I did not detect any significant difference in the targeting of preganglionic axons compared to that in SCG of age-matched WT mice (Figure 6.3G). Moreover, at P1–P3, sympathetic neurons in the SCG of 4E-BP-KO mice were innervated by 7–8 axons, similar to WT SCG neurons. By P8–P9, there was a mild acceleration in the elimination of preganglionic axons (average of ~5 axons in WT vs. average of ~4 axons in 4E-BP KO);

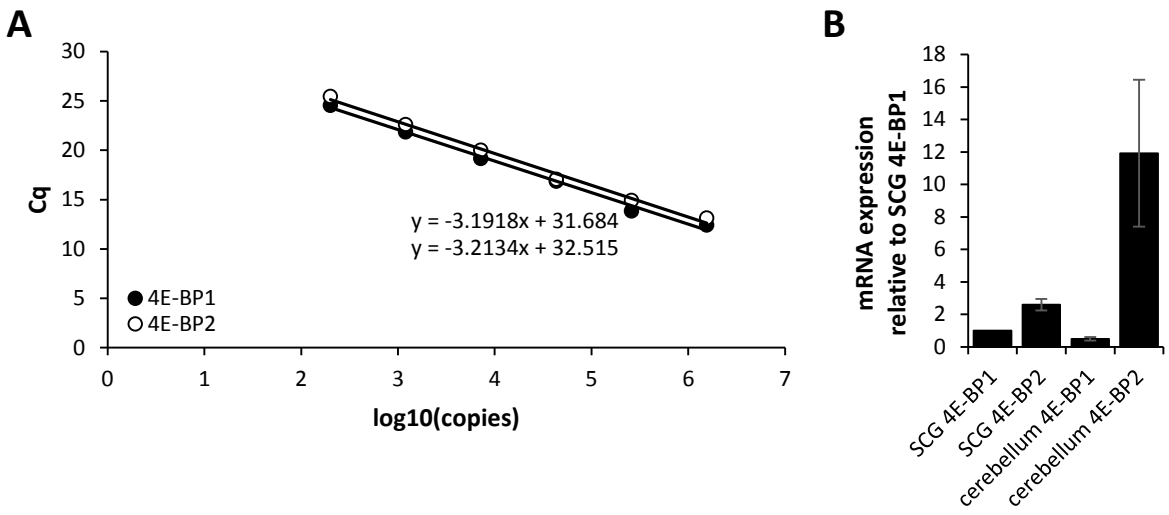

Figure 6.2 4E-BP1 and 4E-BP2 are both expressed in SCG neurons.

(**A**) Standard curves were generated from a 6-point serial dilution of known copy numbers of 4E-BP1 and 4E-BP2 cDNA. Primer pairs for each transcript have near-identical amplification efficiency. Overlapping standard curves indicate that both primer pairs function in a comparable manner.

(**B**) Average 4E-BP1 and 4E-BP2 mRNA levels expressed in SCG and cerebellum. The ratios of 4E-BP1:4E-BP2 mRNA levels are ~1/2.6 in SCG and ~1/24 in cerebellum. For SCG, n=16 (8 mice) and for cerebellum n=8 mice.

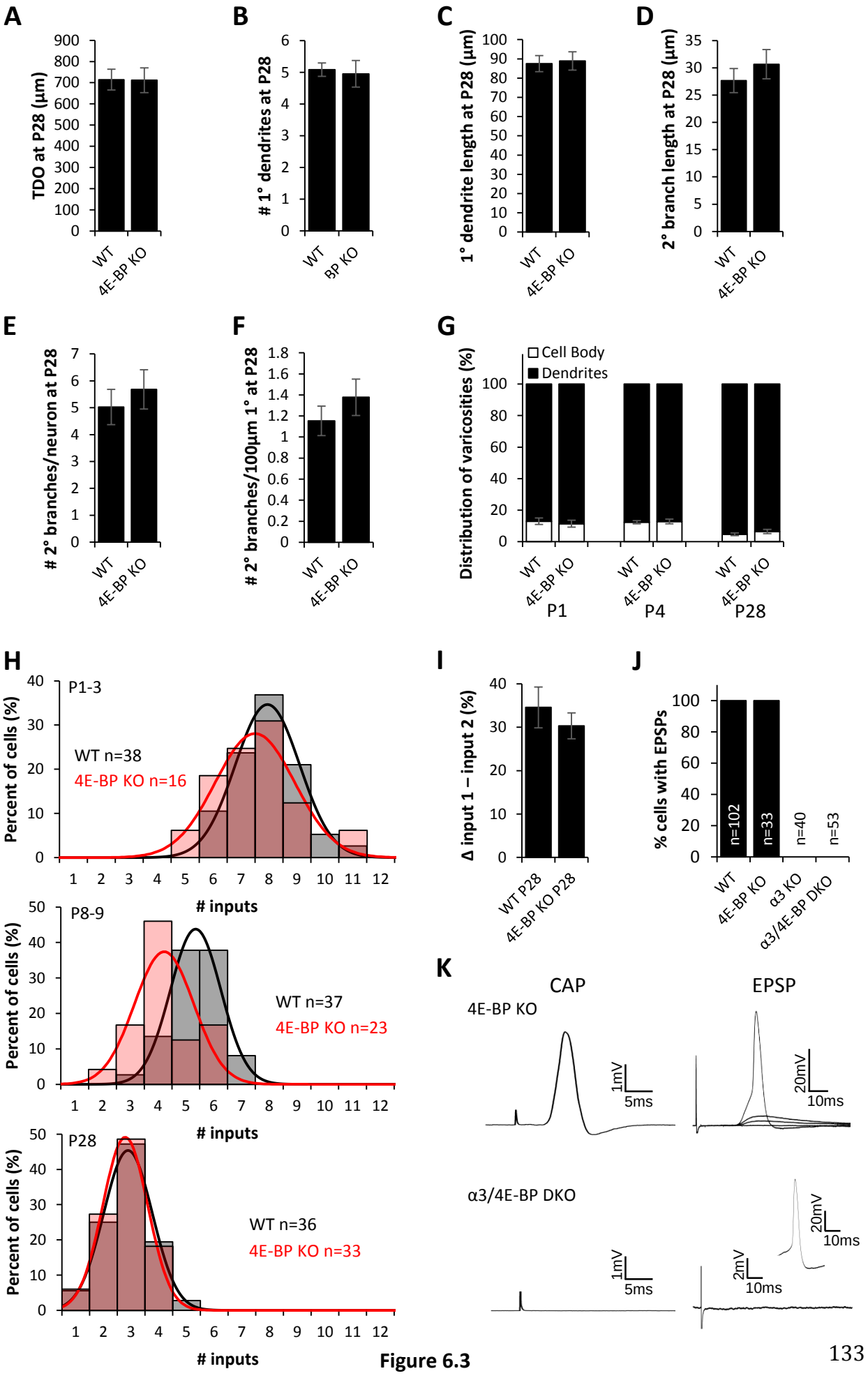
A
TDO at P28 (µm)
WT
4E-BP KO
B
1° dendrites at P28
WT
BP KO
C
1° dendrite length at P28 (µm)
WT
4E-BP KO
D
2° branch length at P28 (µm)
WT
4E-BP KO
E
2° branches/neuron at P28
WT
4E-BP KO
F
2° branches/100µm 1° at P28
WT
4E-BP KO
G
Cell Body
Dendrites
Distribution of varicosities (%)
WT
4E-BP KO
P1
P4
P28
H
P1-3
WT n=38
4E-BP KO n=16
Percent of cells (%)
inputs
P8-9
WT n=37
4E-BP KO n=23
P28
WT n=36
4E-BP KO n=33
I
Δ input 1 – input 2 (%)
WT P28
4E-BP KO P28
J
% cells with EPSPs
n=102
n=33
n=40
n=53
WT
4E-BP KO
α3 KO
α3/4E-BP DKO
K
CAP
EPSP
4E-BP KO
1mV
5ms
20mV
10ms
α3/4E-BP DKO
1mV
5ms
20mV
10ms
2mV
10ms

Figure 6.3

Figure 6.3 The morphology and innervation of 4E-BP KO SCG neurons are similar to WT.

(**A**) Average total dendritic outgrowth per neuron at P28.

(**B**) Average number of primary dendrites per neuron at P28.

(**C**) Average length of primary dendrites per neuron at P28.

(**D**) Average length of secondary dendrites per neuron at P28.

(**E**) Average number of secondary branches per neuron at P28.

(**F**) Average number of secondary branches normalized to 100μm length of primary dendrite per neuron at P28 from WT and 4E-BP KO SCG

For A, B, C, D, E, F, WT data are from Figure 3.3. For 4E-BP KO, n=22 neurons (8 mice).

(**G**) Average distribution of varicosities on the cell body (open) and dendrites (filled) in WT and 4E-BP KO SCG at P1, P4 and P28. WT data are from Figure 3.4. For 4E-BP: for P1 n=6 neurons (3 mice); for P4, n=7 neurons (5 mice); and for P28, n=10 neurons (4 mice).

(**H**) Distribution of SCG neurons innervated by the number of inputs in WT (grey) and 4E-BP KO (red) mice at P1-3, P8-9, and P28. Each distribution was fit with a Gaussian function. The distributions at P1-3 and at P28 are not significantly different ($p>0.2$), whereas at P8-9, $p<0.05$. Each distribution contains data from at least 4 mice; n refers to the number of neurons. DI is the disparity index. WT P1-3 and P28 data are from Figure 3.1.

(**I**) The average difference in strength between the strongest and second strongest inputs in WT and 4E-BP KO SCG at P28, expressed as a percentage of the maximum compound EPSP.

(**J**) Graph shows percent of SCG neurons that had EPSPs in response to supramaximal stimulation of the presganglionic nerve. For WT, n=8 mice; for 4E-BP KO, n=6 mice; for α3 KO, n=4 mice; and for α3/4E-BP DKO, n=8 mice.

(**K**) Left: Extracellular recordings from the SCG postganglionic nerve at P28 in response to supramaximal stimulation of the preganglionic axons. Compound action potentials were evoked in 4E-BP KO SCG, but not in α3/4E-BP DKO SCG.

Right: Intracellular recordings from a SCG neuron in response to stimulation of the preganglionic axons. EPSPs and action potentials were recorded in SCG neurons from P28 4E-BP KO mice, but not detected in SCG neurons from α3/4E-BP DKO mice; inset shows that SCG neurons are capable of firing action potentials.

Error bars represent ± SEM; ***$p<0.001$.

however, at P28, the preganglionic innervation of the SCG neurons in 4E-BP mutant mice was indistinguishable from that of WT SCG neurons (Figures 6.3H, I).

6.3.4 Loss of 4E-BP restores synaptic refinement and remodelling in the absence of activity

To determine whether removing 4E-BP from α3 KO mice restores the synaptic organization in the SCG, I crossed 4E-BP KO mice with α3 KO mice to generate α3/4E-BP double KO (DKO) mice; the SCG in these mice had no 4E-BP or synaptic transmission (Figures 6.3J, K).

I found that at P28, TDO on SCG neurons in α3/4E-BP DKO mice was approximately twice that of age-matched α3 KO neurons (Figures 6.4A, B) and not statistically different from WT neurons. Also, α3/4E-BP-DKO SCG neurons at 1 month maintained 5 primary dendrites, in contrast to 3 primary dendrites maintained on age-matched neurons in the SCG in α3 KO mice (Figure 6.4C). These results show that the genetic removal of 4E-BP largely restores normal dendritic growth, even though the SCG had no synaptic transmission.

In addition, the removal of 4E-BP from α3 KO mice influenced the targeting of synapses by preganglionic axons. At the end of the first postnatal month, the distribution of synapses on sympathetic neurons in the SCG of α3/4E-BP DKO mice was similar to that on WT neurons, and it was significantly different from that on α3 KO SCG. Over 95% of synapses on the SCG neurons in α3/4E-BP-DKO mice were located on dendrites, in contrast to that on α3 KO SCG, where over 50% were located to the soma (Figures 6.4D, E). These results show that genetic removal of 4E-BP largely restores dendritic targeting of presynaptic innervation on SCG neurons that are synaptically silent during development.

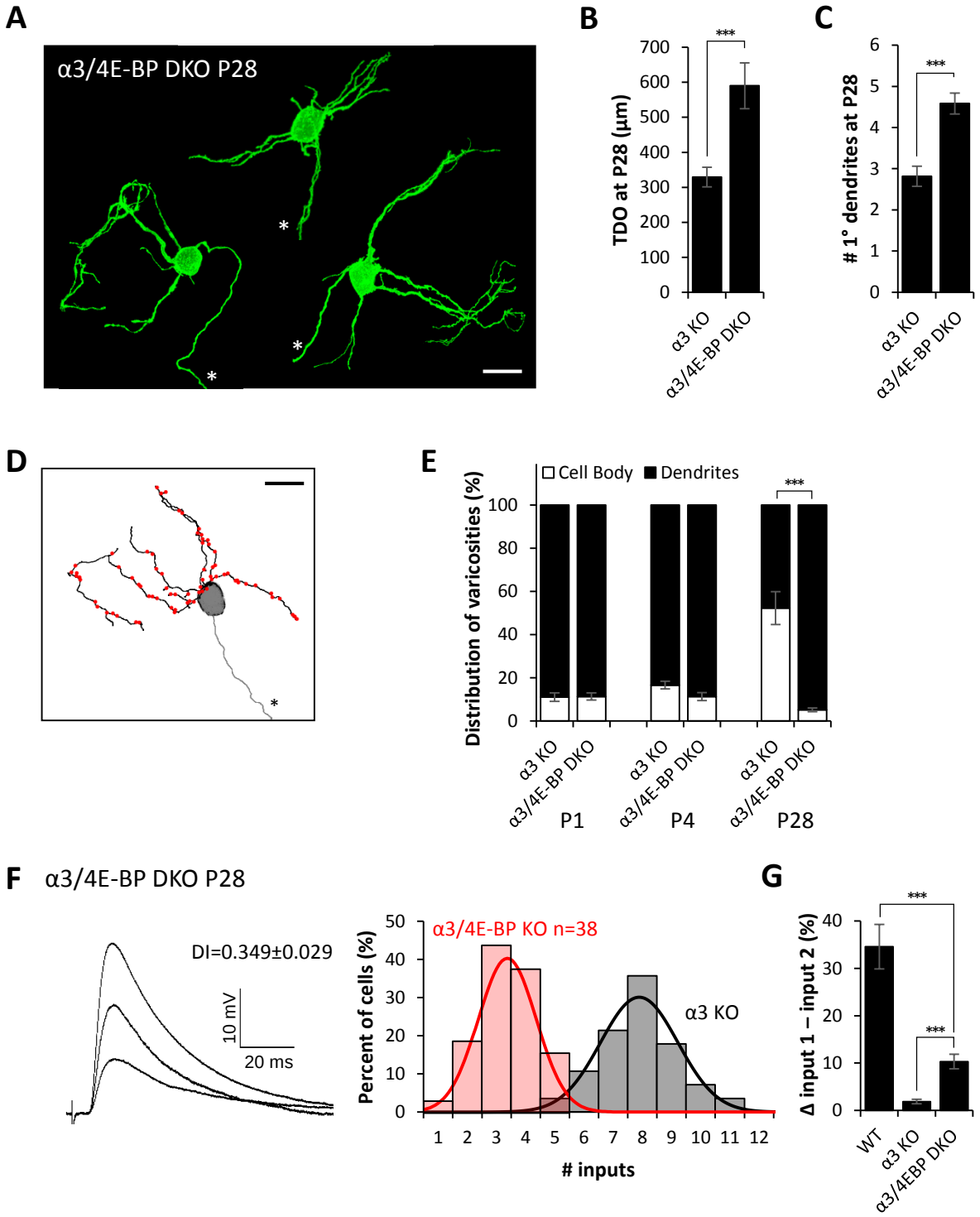
A
α3/4E-BP DKO P28
B
TDO at P28 (µm)
***
α3 KO
α3/4E-BP DKO
C
1° dendrites at P28
***
α3 KO
α3/4E-BP DKO
D
E
Cell Body
Dendrites
Distribution of varicosities (%)
***
α3 KO
α3/4E-BP DKO
P1
P4
P28
F
α3/4E-BP DKO P28
DI=0.349±0.029
10 mV
20 ms
α3/4E-BP KO n=38
α3 KO
Percent of cells (%)
inputs
G
Δ input 1 – input 2 (%)
***
***
WT
α3 KO
α3/4EBP DKO

Figure 6.4

Figure 6.4 Genetic removal of 4E-BP restores dendritic morphology, synaptic targeting and refinement of inputs in α3/4E-BP DKO mice.

(**A**) Maximum intensity projections of DiO-labelled P28 SCG neurons from α3/4E-BP DKO mice. All neurons are shown at the same scale; axons are marked by an asterisk. Scale bar, 20 μm. Neurons are from different ganglia and have been tiled for comparison.

(**B**) Average total dendritic outgrowth per neuron at P28 in α3 KO and α3/4E-BP DKO SCG.

(**C**) Average number of primary dendrites per neuron at P28 in α3 KO and α3/4E-BP DKO SCG.

For B, C, α3 KO data are from Figure 3.3, for α3/4E-BP DKO n=24 neurons (10 mice).

(**D**) Skeletonized reconstruction of a P28 neuron in α3/4E-BP DKO SCG showing dendritic arbors (black), axon (grey, marked by an asterisk), and the locations of preganglionic axon varicosities (red), determined by VAChT staining. Scale bar, 20 μm.

(**E**) Average distribution of varicosities on the cell body (open) and dendrites (filled) in α3 KO and α3/4E-BP DKO SCG at P1, P4 and P28. α3 KO data are from Figure 3.4, for α3/4E-BP DKO at P1 n=6 (3 mice); at P4, n=7 neurons (4 mice); and at P28, n=10 neurons (4 mice).

(**F**) Left: Representative compound EPSPs evoked on a P28 SCG neuron from α3/4E-BP DKO mice. DI indicates disparity index.

Right: Distribution of P28 SCG neurons in α3/4E-BP DKO (red) and α3 KO (grey) mice innervated by the number of inputs. The distribution was fit with a Gaussian function, and contains data from at least 4 mice.

(**G**) The average difference in strength between the strongest and second strongest inputs, expressed as a percentage of the maximum compound EPSP in WT, α3 KO, and α3/4E-BP DKO SCG. Error bars represent ± SEM; ***p<0.001.

For F, G, WT and α3 KO data are from Figure 3.1.

Error bars represent ± SEM; ***p<0.001.

Since removing 4E-BP from α3 KO neurons restored the targeting of synapses to dendrites and increased dendritic growth, I asked whether synaptic refinement would be restored in α3/4E-BP-DKO mice even in the absence of postsynaptic activity. To address this possibility, we compared the number of preganglionic inputs that converged onto SCG neurons in α3/4E-BP DKO mice at P28 to the number that converged onto SCG neurons in α3 KO mice.

Remarkably, SCG neurons in 1-month-old α3/4E-BP DKO mice were innervated by only ~3 preganglionic axons, significantly fewer than the 7–8 on age-matched α3 KO neurons, but not statistically different from the 2–3 axons innervating SCG neurons in 4E-BP-KO or WT mice (Figure 6.4F). These results indicate that removal of 4E-BP from α3 KO mice restores the ability of preganglionic axons to refine, even though synaptic transmission is absent and synapses remain silent.

The persistent preganglionic inputs to SCG neurons in α3/4E-BP-DKO mice increased in strength, but unlike WT SCG, the disparity among these inputs was small, but greater than that in α3 KO; this is reflected both by the disparity index and by the difference in strength between the strongest input and second strongest input (Figures 6.4F, G). These results suggest that activity-dependent mechanisms controlling axon elimination are distinct from those that control the differential strengthening of refined connections.

6.3.5 The proteomic profile of SCG neurons is significantly changed in the absence of synaptic activity and largely restored by the removal of 4E-BP

Next, we conducted a proteomic profiling of SCG from 1-month-old WT, α3 KO,

4E-BP KO, and α3/4E-BP DKO mice to determine whether removing 4E-BP influences the profile of SCG when synaptic transmission is absent.

Using a data-independent acquisition SWATH workflow (Gillet *et al*., 2012), we quantified over 2,100 proteins expressed in the SCG, including representatives from all the major molecular function and protein classes (Figures 6.5A, B). Between WT and α3 KO SCG, at least 83 proteins were expressed at significantly different levels (greater than ±1.25-fold change at a q-value<0.05). Figure 6.6 shows a heatmap for these 83 proteins (log_2 z-score ratios), and indicates that loss of synaptic activity led to significant changes in the SCG proteome. To determine the impact of removing 4E-BP on translation in the SCG when synaptic activity is absent, we examined the proteome of α3/4E-BP DKO SCG. Of the 83 proteins whose levels were altered in α3 KO SCG, over 60% (51/83) were reversed and closer to levels in WT SCG (Figure 6.6, Table 1). On the other hand, a similar comparison between WT and 4E-BP KO SCG revealed insignificant differences for >99% of all proteins between the two groups, suggesting that, when fast synaptic transmission was intact, loss of 4E-BP had little effect on the proteome in the SCG.

6.4 Discussion

In α3 KO sympathetic neurons, I found lower levels of phosphorylated 4E-BP1 compared to that of WT controls. Additionally, in proteomic experiments, I observed changes in levels for a large number of proteins in the SCG of α3 KO mice. Interestingly, genetically removing 4E-BP from α3 KO mice largely restored these protein levels toward those in WT, even though the SCG had no synaptic transmission. Furthermore, I showed

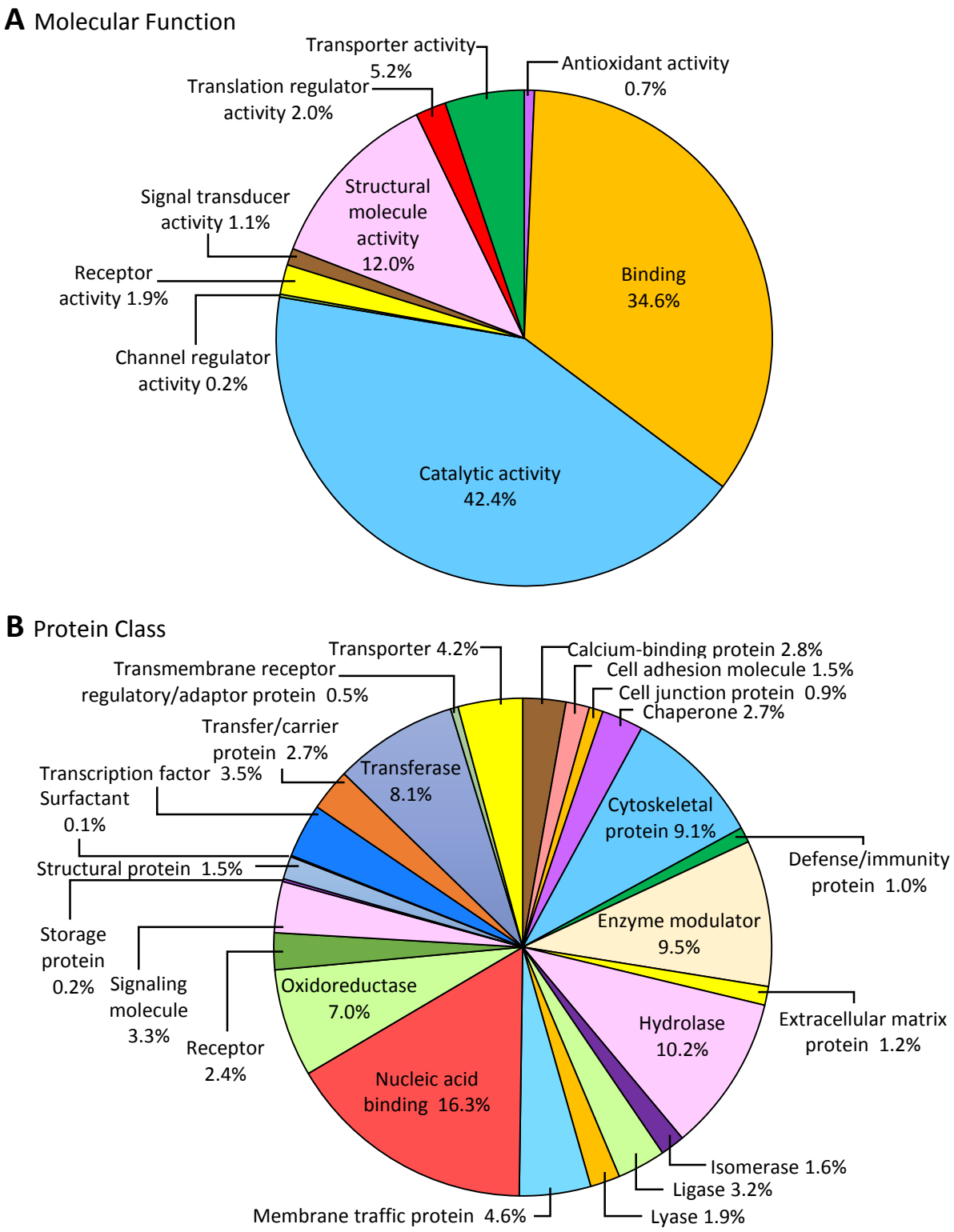

Figure 6.5 The classification of 2100 proteins identified in P28 WT SCG.

(**A**-**B**) Pie charts showing the classification of 2100 proteins identified in P28 WT SCG into (**A**) molecular functions, and (**B**) protein classes according to according to Gene Ontology terms and PANTHER protein classes.

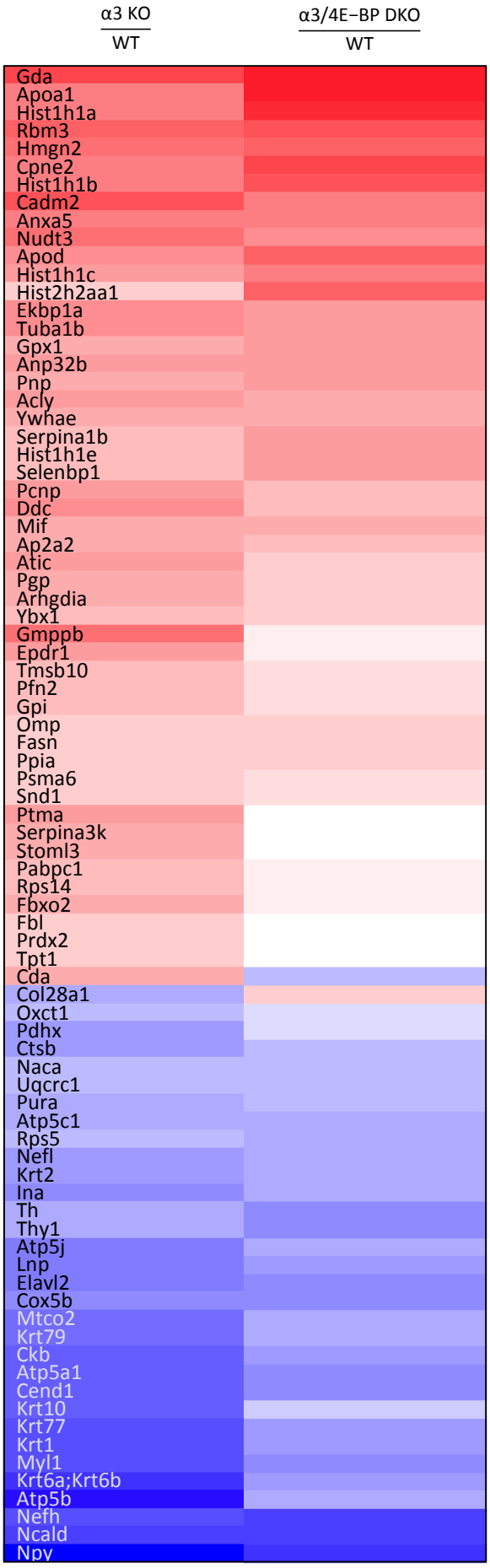

Figure 6.6 The classification of 2100 proteins identified in P28 WT SCG.

Heatmap showing the $\log_2$ z-score ratios of protein levels in α3 KO SCG to WT SCG (left column) and in α3/4E-BP DKO SCG to WT SCG (right column) for 83 proteins whose levels were significantly different (± 1.25x, q-value<0.05) between α3 KO and WT SCG. Of these 83 proteins, 51 were restored in the direction of WT levels in the α3/4E-BP DKO SCG proteome. See Table 1 for values.

Table 1. Z-scores, z-score ratios, and q-values used to generate the heatmap in Figure 6.6.

Gene	z-score			α3 KO : WT		α3/4E-BP DKO : WT	
	WT	α3 KO	α3/4E-BP DKO	Ratio	q-value	Ratio	q-value
Acly	1250.5	1942.25	1874.97	1.55	1.08E-07	1.5	1.81E-06
Anp32b	399.8	610.7	617.01	1.53	0.048	1.54	0.018
Anxa5	2915.33	5223.19	5387.85	1.79	1.16E-15	1.85	2.49E-14
Ap2a2	247.34	358.36	340.03	1.45	0.021	1.37	0.278
Apoa1	2924.02	5262.45	8421.88	1.8	1.77E-04	2.88	4.41E-09
Apod	127.19	210.8	257.8	1.66	0.037	2.03	0.157
Arhgdia	1602.77	2313.65	2066.32	1.44	3.34E-04	1.29	0.008
Atic	872.33	1324.71	1120.78	1.52	0.007	1.28	0.002
Atp5a1	3152.5	1567.74	1882.91	0.5	0.007	0.6	2.78E-08
Atp5b	182.91	62.09	121.81	0.34	0.028	0.67	0.238
Atp5c1	413.57	288	293.54	0.7	0.008	0.71	0.305
Atp5j	362.61	208.97	240.97	0.58	0.026	0.66	0.229
Cadm2	149.53	332.15	264.36	2.22	0.006	1.77	0.319
Cda	246.78	369.41	184.57	1.5	0.016	0.75	0.028
Cend1	212.73	101.83	123.41	0.48	0.002	0.58	0.001
Ckb	2518.17	1231.73	1622.96	0.49	0.002	0.64	0.024
Col28a1	1191.56	824.37	1487.35	0.69	0.002	1.25	0.087
Cox5b	967.24	593.47	559.63	0.61	0.033	0.58	0.013
Cpne2	49.04	89.34	112.22	1.82	0.024	2.29	0.277
Ctsb	1064.6	673.32	805.34	0.63	3.00E-05	0.76	0.002
Ddc	943.57	1525.27	1254.44	1.62	1.48E-04	1.33	0.422
Elavl2	640.62	350.58	379.97	0.55	0.005	0.59	0.002
Epdr1	487.08	774.35	549.25	1.59	0.01	1.13	0.571
Fasn	1719.25	2196.54	2206.74	1.28	2.30E-09	1.28	2.3E-06
Fbl	283.6	359.22	301.55	1.27	0.021	1.06	0.532
Fbxo2	451.87	639.45	484.52	1.42	0.01	1.07	0.311
Fkbp1a	1219.7	2053.61	1936.77	1.68	0.001	1.59	2.02E-04
Gda	403.7	980.37	1204.14	2.43	0.002	2.98	6.62E-11
Gmppb	411.7	771.64	458.94	1.87	0.006	1.11	0.346
Gpi	523.14	694.22	619.6	1.33	0.004	1.18	0.515
Gpx1	838.91	1226.97	1345.89	1.46	0.029	1.6	0.097
Hist1h1a	300.51	550.38	807.74	1.83	0.008	2.69	0.007
Hist1h1b	324.5	563.9	723.3	1.74	0.044	2.23	3.50E-05
Hist1h1c	2075.08	3307.83	3830.5	1.59	0.044	1.85	0.001
Hist1h1e	2120.81	2958.81	3303.83	1.4	0.006	1.56	0.007
Hist2h2aa1	225.09	295.46	455.17	1.31	0.029	2.02	0.204
Hmgn2	50.61	98.82	106.94	1.95	2.00E-05	2.11	0.054
Ina	1663.29	1026.06	1130.21	0.62	4.31E-04	0.68	0.079
Krt1	1236.6	548.35	811.24	0.44	1.74E-08	0.66	1.23E-04
Krt10	1498.45	724.91	1171.19	0.48	0.02	0.78	0.116
Krt2	632.05	394.83	448.31	0.62	0.014	0.71	0.187
Krt6a/6b	1032.29	415.01	666.1	0.4	0.005	0.65	0.355
Krt77	1285.23	588.03	838.06	0.46	4.48E-04	0.65	0.003
Krt79	378.5	197.18	252.02	0.52	0.001	0.67	8.00E-06
Lnp	137.96	76.22	85.59	0.55	0.012	0.62	0.186
Mif	1907.87	2727.7	2745.68	1.43	0.008	1.44	0.034
Mtco2	439.93	227.52	296.75	0.52	0.03	0.67	0.343
Myl1	615.39	275.81	371.95	0.45	0.001	0.6	0.003

Table 1. (continued)

Gene	z-score			α3 KO : WT		α3/4E-BP DKO : WT	
	WT	α3 KO	α3/4E-BP DKO	Ratio	q-value	Ratio	q-value
Naca	751.28	557.81	556.84	0.74	0.01	0.74	0.062
Ncald	229.29	97.49	96.16	0.43	3.66E-05	0.42	0.005
Nefh	950.5	432.24	414.24	0.45	8.20E-08	0.44	1.43E-08
Nefl	3029.67	1977.93	2040.21	0.65	9.35E-11	0.67	1.33E-09
Npy	129.9	33.06	50.79	0.25	0.039	0.39	0.413
Nudt3	105.6	202.96	179.44	1.92	0.023	1.70	0.427
Omp	594.07	761.61	763.64	1.28	0.028	1.29	0.127
Oxct1	1116.11	814.54	920.08	0.73	0.001	0.82	0.044
Pabpc1	898.41	1240.42	993.25	1.38	0.038	1.11	0.066
Pcnp	237.34	373.99	333.01	1.58	0.041	1.40	0.602
Pdhx	255.47	162.62	208.66	0.64	0.033	0.82	0.349
Pfn2	240.89	327.03	286.13	1.36	0.011	1.19	0.241
Pgp	128.23	190.64	164.13	1.49	0.034	1.28	0.289
Pnp	329.19	495.64	507.25	1.51	0.007	1.54	0.004
Ppia	2699.2	3405.2	3383.34	1.26	5.79E-05	1.25	2.00E-05
Prdx2	6025.87	7602.19	6347.94	1.26	8.33E-05	1.05	0.648
Psma6	581.44	735.78	694.06	1.27	0.014	1.19	0.248
Ptma	232.69	362.75	233.55	1.56	4.45E-04	1.00	0.386
Pura	1701.36	1194.41	1250.4	0.70	1.92E-04	0.73	0.007
Rbm3	259.32	519.76	567.58	2.00	0.039	2.19	0.099
Rps14	659.08	897.3	733.44	1.36	0.013	1.11	0.626
Rps5	762.55	561.21	515.19	0.74	0.015	0.68	1.08E-05
Selenbp1	260.2	353.64	394.6	1.36	0.013	1.52	1.70E-05
Serpina1b	377.23	511.03	604.04	1.35	1.20E-05	1.60	0.001
Serpina3k	621.93	927.09	629.82	1.49	0.034	1.01	0.011
Snd1	677.49	856.72	780.93	1.26	0.004	1.15	0.068
Stoml3	268.68	403.21	251.51	1.50	0.039	0.94	0.442
Th	1267.48	896.7	778.87	0.71	0.031	0.61	0.007
Thy1	816	573	489.42	0.70	0.005	0.60	2.02E-04
Tmsb10	3240.45	4483.99	3968.66	1.38	0.008	1.22	0.652
Tpt1	403.12	507.3	394.21	1.26	0.036	0.98	0.403
Tuba1b	1513.21	2513.96	2299.94	1.66	8.81E-08	1.52	5.98E-07
Uqcrc1	666.74	483.92	488.96	0.73	0.007	0.73	0.049
Ybx1	81.76	112.96	107.04	1.38	0.049	1.31	0.062
Ywhae	732.18	1075.49	1099.8	1.47	4.79E-09	1.50	6.02E-06

that removing 4E-BP from α3 KO mice reversed the defects both in dendritic growth on SCG neurons and in targeting of synapses, and, remarkably, the preganglionic inputs refine in the absence of postsynaptic activity.

6.4.1 Regulation of cap-dependent translation

In its basal state, hypophosphorylated 4E-BP suppresses cap-dependent translation by sequestering eIF4E and preventing the formation of the 5′ cap. Several signals converge to phosphorylate 4E-BP and release eIF4E to initiate cap-dependent translation. I show that, in SCG neurons, signals downstream of synaptic transmission lead to increased 4E-BP phosphorylation and, by extension, cap-dependent translation.

In SCG neurons from α3 KO mice, levels of P-4E-BP are significantly lower than in those in WT neurons. However, X^{RFP} neurons have similar levels of P-4E-BP to $X^{\alpha 3}$ neurons. These differences are not due to a decreased level in overall 4E-BP protein because staining for total 4E-BP did not show any changes between WT neurons and α3 KO neurons. Ideally, the P-4E-BP signal would be normalized to total 4E-BP, however, because both antibodies were generated in rabbit, P-4E-BP signals were normalized against MAP-1A levels, which are consistent between WT and α3 KO SCG neurons. In α3 KO mice, SCG neurons do not have postsynaptic activity, and their targets do not receive functional innervation. On the other hand, while X^{RFP} neurons also do not have postsynaptic activity, their targets are functionally innervated. Therefore, cap-dependent translation in SCG neurons is likely regulated, at least in part, by synaptic transmission through an indirect mechanism that likely involves retrograde target-derived factors.

X^{RFP} neurons and neurons in α3/4E-BP DKO mice are similar in several ways: functionally, both neurons develop in the absence of postsynaptic activity; and phenotypically, X^{RFP} neurons and α3/4E-BP DKO neurons extend normal dendritic arbours, silent synapses are targeted appropriately to the cell soma, and preganglionic axons refine without synaptic transmission. Molecularly, X^{RFP} neurons have elevated levels of P-4E-BP and therefore cap-dependent translation is enhanced, whereas cap-dependent translation is increased in α3/4E-BP DKO neurons because 4E-BP genes are deleted. Given their similarities, it is conceivable that cap-dependent translation plays a role in the normal growth of dendrites, synaptic targeting and in the refinement of connections in X^{RFP} neurons.

A main regulator of 4E-BP phosphorylation is mTOR, and there are many signalling pathways that converge to influence mTOR activity. My results point to a role for an activity-dependent retrograde factor that is released by sympathetic targets, taken up at nerve terminals of SCG neurons and transported to the cell soma, where they act to promote phosphorylation of 4E-BP. In support of this idea, the binding of extracellular growth factors to receptor tyrosine kinases and G-protein coupled receptors (GPCR) have been shown to activate signal transduction pathways that promote mTOR activity (Jung *et al*., 2012; Ma and Blenis, 2009). However, my results do not rule out the possibility that there are also intracellular signalling pathways that are activated by calcium influx induced by postsynaptic activity that mediate cap-dependent translation in a conventional, cell-autonomous manner.

6.4.2 The effects of activity and removing 4E-BP on protein levels

Deletion of 4E-BP has a similar effect as phosphorylation in that it removes the sequestration of eIF4E, and leads to enhanced cap-dependent translation and altered protein levels. Unexpectedly, I found that deletion of 4E-BP had little effect on the development and innervation of SCG neurons or on the global proteomic profile of SCG neurons when synaptic transmission was intact; of the 2,100 specific proteins identified in the SCG, only a few showed differential expression as a result of the loss of 4E-BP. Recent discoveries suggest that specific mRNAs and, therefore, specific pathways rather than overall maintenance of proteins are affected as a result of these manipulations (Gkogkas *et al*., 2013; Truitt *et al*., 2015). Additionally, the identification of proteins is limited by the peptide spectral library. Therefore, it is possible that there are differentially expressed proteins that were not identified.

In contrast, the absence of excitatory synaptic transmission had a significant effect on the proteomic profile: the levels of at least 83 proteins were significantly altered in α3 KO SCG, indicating that these proteins are regulated either directly by postsynaptic activity or indirectly through target-derived signals. Relevantly, deleting 4E-BP from α3 KO mice largely restores the proteome and shifted the levels of more than half of these proteins toward values found in WT SCG. Several of these proteins that are restored in α3/4E-BP DKO are likely involved in the refinement of presynaptic inputs, the stability of primary dendritic branches, and the targeting of synapses by preganglionic axons.

Interestingly, the levels of a large number of proteins were not statistically different between WT and α3 KO SCG, suggesting that the translation of these mRNAs are not regulated by synaptic transmission. Of particular interest are proteins that have previously

been implicated in synapse elimination elsewhere in the nervous system. For example, the major histocompatibility complex class 1 molecules H2-Db and H2-Kb appear to be involved in refinement of retinal ganglion cell axons innervating the lateral geniculate nucleus (LGN) through a mechanism that regulates the expression of postsynaptic AMPA receptors (Lee *et al*., 2014). I found no difference in the levels of major histocompatibility complex class 1 molecule H2-Db between WT and α3 KO SCG, and did not detect H2-Kb. Moreover, I detected no statistical difference in the level of the complement proteins C1q and C3, molecules required for the elimination of retinal ganglion cell synapses in the LGN (Stephan *et al*., 2012; Stevens *et al*., 2007). These results suggest that other molecules and pathways are involved in synapse elimination in the SCG.

My proteomic analysis provides a comprehensive profile of activity-dependent protein expression in mouse SCG, not only revealing that synaptic activity and target-derived factors during the first postnatal month have profound effects on cap-dependent translation in the SCG but also confirms that the removal of 4E-BP can largely normalize the proteome in the absence of synaptic transmission.

6.4.3 Conclusion

In summary, my findings demonstrate that 4E-BP-regulated mechanisms are involved in the growth of dendrites, the targeting of synapses, and the refinement of preganglionic axons. Genetic removal of 4E-BP can compensate for the loss of synaptic transmission, presumably by upregulating the signals that direct the reorganization of neural circuits and the refinement of preganglionic inputs. Presumably, cap-dependent

translation operates in parallel with mechanisms that regulate gene transcription and post-translational modification, and collectively, mediate the development of neural circuits.

Chapter 7: Does circuit activity influence transcriptional regulation of gene expression?

7.1 Introduction

In α3 KO mice, SCG neurons have defects in dendritic growth, synaptic targeting, and in the refinement of preganglionic axons. In these mice, postsynaptic activity of sympathetic neurons and the activity of targets innervated by sympathetic neurons are both absent. To determine how much of the defects in the morphology and innervation of sympathetic neurons were caused by the absence of postsynaptic activity and how much were due to the absence of activity-dependent, target-derived signals, I investigated mosaic SCG composed of X^{RFP} neurons that are synaptically silent, and neighbouring $X^{\alpha 3}$ neurons that functionally innervate targets. If the defects in differentiation and innervation were due to the absence of postsynaptic activity, then one would expect X^{RFP} neurons to be similar to α3 KO neurons. In contrast, I showed that X^{RFP} neurons are similar to $X^{\alpha 3}$ neurons and WT neurons, suggesting that $X^{\alpha 3}$ neurons evoke the release of activity-dependent, target-derived factors that act on X^{RFP} neurons to regulate their development. In this chapter, I investigated gene expression in WT and α3 KO neurons to identify genes that are regulated by postsynaptic activity. In addition, I compared the gene expression profiles of α3 KO and X^{RFP} neurons to determine whether the expression of any genes is restored to WT levels, which would suggest that these genes are not directly regulated by synaptic activity. Moreover, these genes may play important roles in the differentiation and innervation of sympathetic neurons during postnatal development.

In general, sympathetic ganglia are thought to consist of a homogenous population of neurons, although there are some indications that they contain several different

neuronal subtypes based on peptide expression or firing properties (Benarroch, 1994; Masliukov *et al*., 2012). How this diversity comes about is poorly understood. Conceivably, it may be generated by activity patterns of the neurons, or by the targets they innervate (Landis, 1990; Luebke and Wright, 1992). I was particularly interested to determine, at the molecular level, whether some sympathetic neuronal subtypes are more sensitive to changes in postsynaptic activity than others.

To gain insight into the organization and development of neurons in the SCG, and to investigate how postsynaptic activity influences gene expression in different subtypes, I conducted single cell RNA sequencing (scRNAseq) studies on SCG neurons. This technology captures gene expression profiles from individual cells, allowing us to examine the previously underappreciated cellular heterogeneity at high resolution.

Surprisingly, SCG contain 7 neuronal subtypes based on gene expression profiles. For each subtype, I compared WT and α3 KO SCG neurons for activity-dependent changes in gene expression. I identified ~250 unique genes that were differentially expressed between WT and α3 KO neurons for at least one subtype. These data suggest that the expression of these genes is regulated downstream of synaptic activity. On the other hand, I found that ~90 of these differentially expressed genes were restored to WT levels in X^{RFP} neurons, indicating that this subset of genes is not directly regulated by synaptic activity but through some indirect pathway. Equally interesting, the proportion of cholinergic neurons was significantly greater in the α3 KO and X^{RFP} neuronal populations than in the WT neuronal population, as was their expression levels of cholinergic genes. This indicates that postsynaptic activity has an important role in maintaining an adrenergic profile.

7.2 Methods

Detailed descriptions of the experimental procedures and analysis can be found in Chapter 2. In this chapter, they include: α3 KO and mosaic mouse models (2.1.1-2.1.2) and scRNAseq sample preparation (2.12.1), sequencing and alignment (2.12.2) and data analysis (2.12.3).

7.3 Results

7.3.1 Single cell droplet-based technology was used to generate gene expression datasets

Briefly, to generate single cell gene expression datasets, SCG were pooled from 5–7 P28 WT, α3 KO or mosaic mice, and dissociated into a single cell suspension. For each sample, ~9,000–10,000 cells were loaded and ~6,000–7,000 cells were recovered for a recovery rate of ~60–70%, which is consistent with droplet-based technology (Zhang *et al*., 2019). For each recovered cell, RNA molecules were captured; all RNA molecules from the same cell were tagged with the same cellular barcode, and each individual RNA molecule in that cell was tagged with its own unique molecular identifier barcode. Captured and tagged RNA molecules were reverse transcribed to generate cDNA libraries, which were then amplified and multiplexed for sequencing to generate read data.

Each sequence (representing one RNA molecule) in the read data was sorted according to their cellular barcodes. Then, for each cell, the number of unique RNA molecules per gene was counted to generate count matrices. To identify genes, sequences were aligned to a reference genome. RNA count matrices were imported and analyzed with R in RStudio using the Seurat package (Butler *et al.*, 2018; R Core Team, 2013; RStudio Team, 2015; Stuart *et al*., 2019). Cells that had fewer than 200 transcripts were filtered, as

were genes that were not expressed in more than 3 cells because they were unlikely to be informative to the overall cellular population of 6000–7000 cells per dataset. Count data were normalized based on count depth per cell and natural-log transformed via a log-plus-one transformation.

7.3.2 Selection markers were used to generate a neuronal subset

The single cell suspension from dissociated SCG contained a heterogeneous population comprised of both sympathetic neurons and non-neuronal cells. Therefore, to isolate the neuronal population, I used a set of selection markers. In the preliminary subset, adrenergic neurons were considered as cells that expressed Dbh (dopamine beta hydroxylase, an enzyme involved in noradrenaline synthesis), Ntrk1 (receptor for NGF, TrkA), and Slc6a2 (noradrenaline transporter), and not Notch1, 2 or 3. In addition, because all SCG neurons generate action potentials and therefore express voltage-gated Na^+ (Na_v) and Ca^{2+} (Ca_v) channels, I included Na_v and Ca_v genes as selection markers for sympathetic neurons.

There are 9 different genes that encode isoforms of the Na_v α subunit ($Na_v1.1$–1.9), and 10 different genes that encode isoforms of the Ca_v α_1 subunit ($Ca_v1.1$–1.4, $Ca_v2.1$–2.3, and $Ca_v3.1$–3.3). In the subset of cells that expressed Dbh, Ntrk1, Slc6a2, and not Notch1, 2, or 3, approximately 50% of the WT subset and ~45% of the α3 KO subset expressed at least one Ca_v α_1 subunit gene and at least one Na_v α subunit. I found that the predominant Ca_v α_1 subunit genes expressed in WT and α3 KO subsets were Cacna1a ($Ca_v2.1$) and Cacna1b ($Ca_v2.2$), genes that code for the α_1 subunit of P/Q and N-type calcium channels, respectively. Only ~4–6% expressed one of the other remaining 8 Ca_v α_1 subunit genes. The

predominant Na_v α subunit genes were Scn3a ($Na_v1.3$) and Scn9a ($Na_v1.7$); only ~5–6% of neurons expressed one of the remaining 7 Na_v α subunit genes. Based on these results, cells were considered sympathetic neurons if they expressed Dbh, Ntrk1, Slc6a2, as well as Cacna1a, Cacna1b, or both, and either Scn3a, Scn9a, or both, and not Notch1, 2 or 3. This is a conservative estimation, as the expression of one or more of these marker genes were likely below detectable levels in some neurons; these neurons were excluded from my analysis.

The distribution of neurons that expressed Cacna1a, Cacna1b, or both were highly similar between the WT dataset and the α3 KO dataset (±2–4% difference; Figures 7.1A, B). Approximately a quarter expressed Cacna1a without Cacna1b ($Ca_v2.1$ group), ~54–58% expressed Cacna1b without Cacna1a ($Ca_v2.2$ group), and ~18–20% expressed both Cacna1a and Cacna1b ($Ca_v2.1$ and $Ca_v2.2$ group; Figures 7.1A, B).

For each of the three Ca_v groups, I determined which Na_v α subunit genes they expressed and whether there was any relationship between the expression of the Na_v and Ca_v isoforms. The proportions of neurons that expressed Scn3a, Scn9a, or both were similar between the three Ca_v groups, indicating that the expression of one Ca_v isoform is not correlated to any particular Na_v isoform (Figures 7.1A, B).

Interestingly, there were minor differences in the proportions of neurons that expressed Scn3a, Scn9a, or both between the WT and α3 KO subsets. In α3 KO neurons, the proportion of cells that expressed Scn3a without Scn9a ($Na_v1.3$ group) was reduced when compared to WT neurons, particularly in the Cacna1a ($Ca_v2.1$) subset. On the other hand, the proportions of cells that expressed Scn9a without Scn3a ($Na_v1.7$ group) were slightly increased, which, again, was most apparent in the subset that expressed Cacna1a ($Ca_v2.1$).

+	Dbh
+	Ntrk1
+	Slc6a2
+	Cacna1a/Cacna1b
+	Scn3a/Scn9a
–	Notch1,2,3

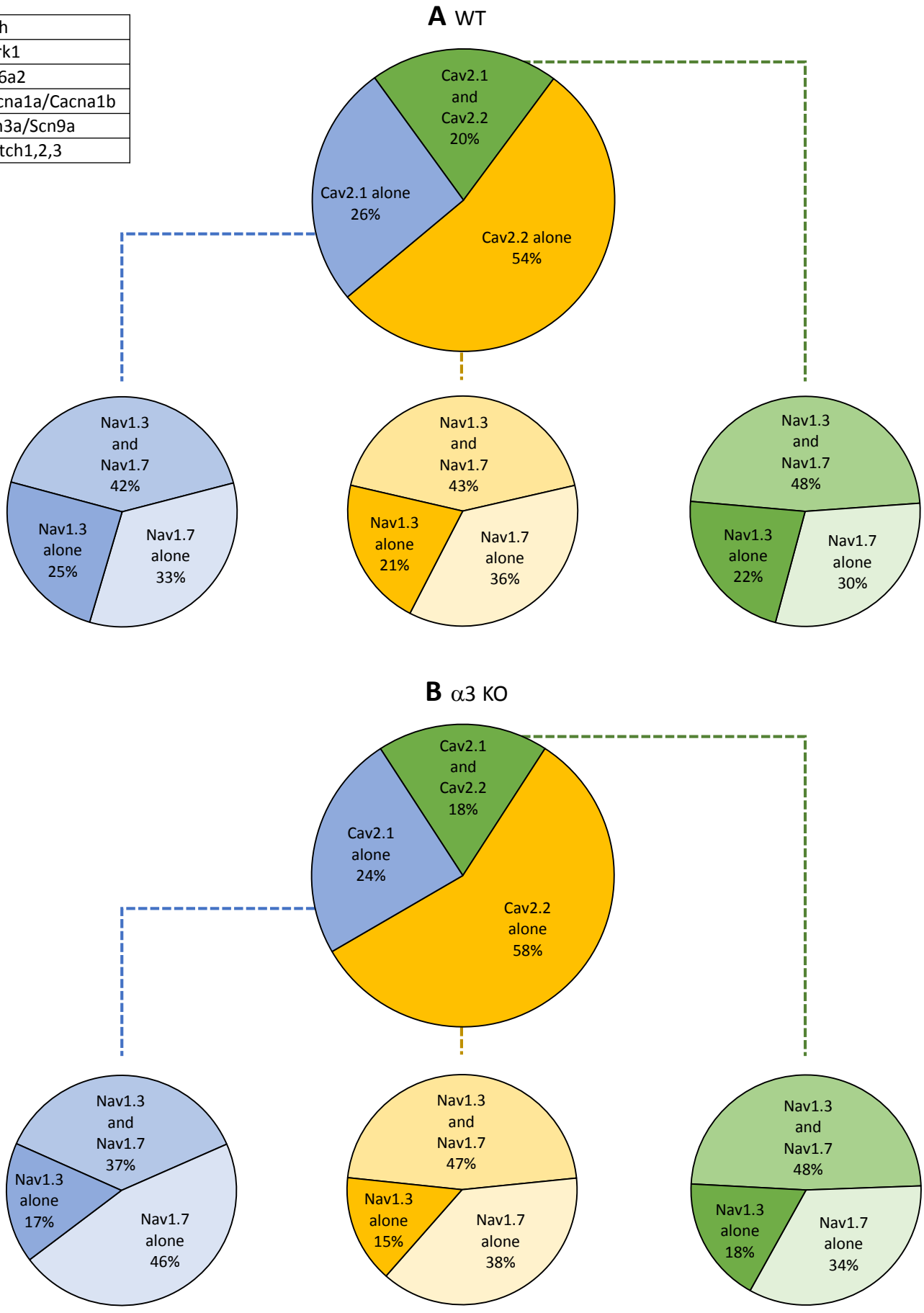

Figure 7.1

Figure 7.1 Expression of α_1 Ca_v subunit and α Na_v subunit genes in WT and α3 KO neurons.

(**A**-**B**) Inset: Selection markers used to identify adrenergic neurons in the dataset.

Top: Distribution of neurons that expressed Cacna1a without Cacna1b ($Ca_v2.1$; blue), Cacna1b without Cacna1a ($Ca_v2.2$; yellow), or both (green) in (**A**) WT SCG and (**B**) α3 KO SCG.

Bottom: Each of the three Ca_v groups were further broken down according to the distribution of neurons that expressed Scn3a without Scn9a ($Na_v1.3$), Scn9a without Scn3a ($Na_v1.7$), or both.

The proportion of cells that expressed both Scn3a and Scn9a ($Na_v1.3$ and $Na_v1.7$ group) were similar (Figures 7.1A, B).

7.3.3 Activity-dependent genes are differentially regulated between WT and α3 KO neurons

To examine activity-dependent changes in transcriptional regulation in sympathetic neurons, I compared the global gene expression profiles between WT and α3 KO neurons. From this, I identified a number of differentially expressed genes that were expressed at significantly different levels between WT neurons and α3 KO neurons (log fold change > ±0.25). The 20 most upregulated and downregulated genes were plotted as a heatmap (Figure 7.2A), and all differentially expressed genes were broadly classified based on their molecular functions and biological processes according to Gene Ontology terms (Figures 7.2B, C; Table 2; Ashburner *et al*., 2000; The Gene Ontology Consortium, 2017).

In comparing the global gene expression profiles between neuronal populations of WT and α3 KO SCG, several important details may be masked. For example, if a gene was upregulated in some neuronal subtypes and downregulated in others, the overall average global gene expression may show little change. In addition, a change in the average global gene expression can reflect either a change in the number of neurons that express the gene, or a change in the level of expression for each neuron that expresses that gene, or both. Therefore, to obtain a more in-depth analysis of the effects of synaptic activity on gene expression in different sympathetic neuronal subtypes, I clustered the neurons into subtypes based on gene expression profiles.

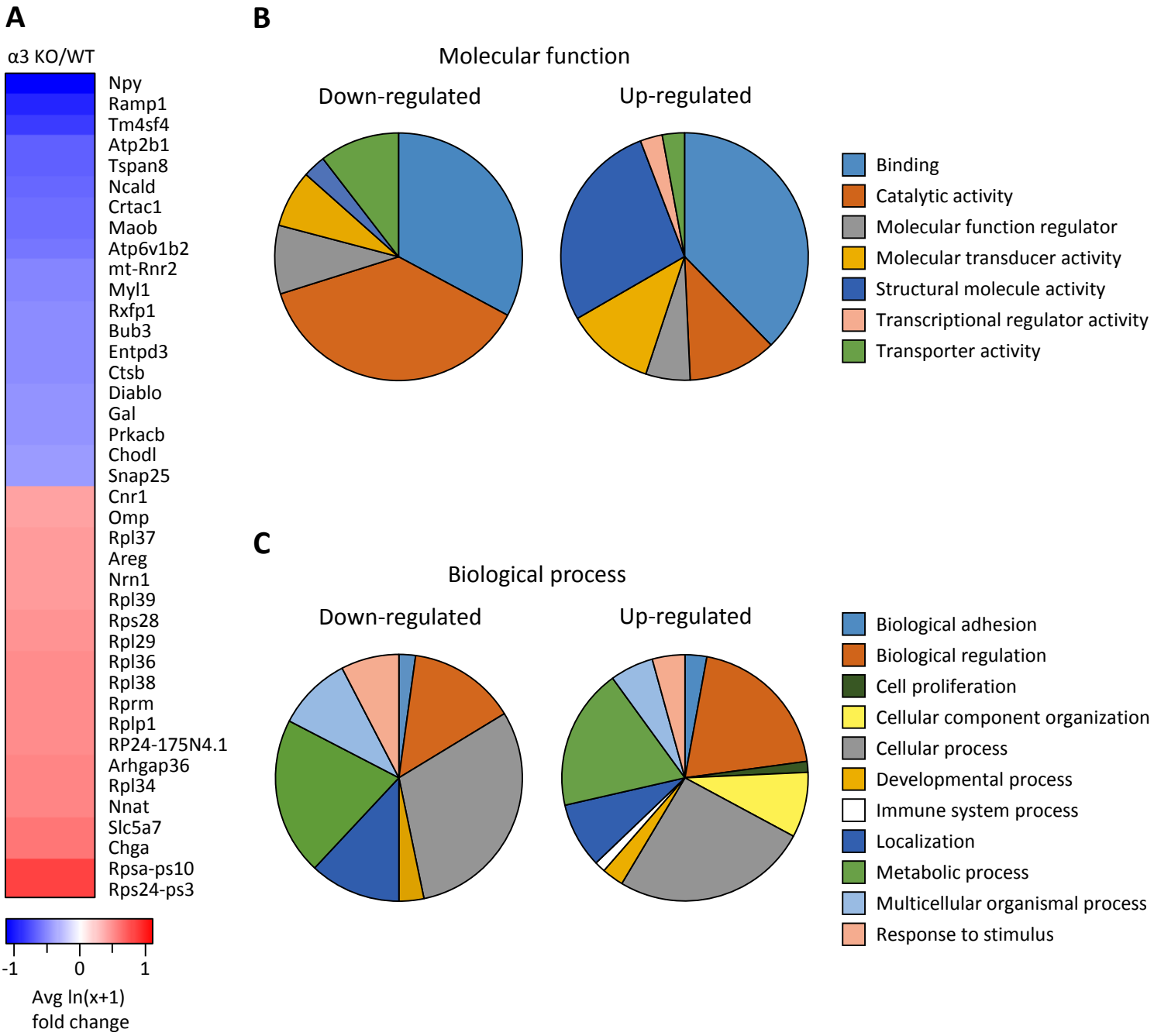

Figure 7.2 Differentially expressed genes between WT and α3 KO neurons.

(**A**) Heatmap showing the average ln(x+1) fold change of the 20 most downregulated (blue) and 20 most upregulated genes (red) in α3 KO SCG neurons compared to WT SCG neurons. Average expression levels of these 40 genes and the remaining differentially expressed genes are listed in Table 2.

(**B-C**) Pie charts showing the classification of 147 globally differentially expressed genes between WT SCG neurons and α3 KO SCG neurons into (**B**) molecular functions, and (**C**) biological processes according to Gene Ontology terms.

Table 2. Differentially expressed genes between WT and α3 KO neurons, see heatmap in Figure 7.2A.

Gene	ln(x+1) fold change α3 KO/WT	Average Expression per Cell	
		WT	α3 KO
Npy	-1.112	28.479	8.697
Ramp1	-0.923	2.468	0.378
Tm4sf4	-0.841	1.428	0.047
Atp2b1	-0.676	4.198	1.643
Tspan8	-0.672	8.233	3.714
Ncald	-0.650	7.685	3.535
Crtac1	-0.629	1.366	0.261
Maob	-0.622	2.886	1.087
Atp6v1b2	-0.577	4.670	2.183
mt-Rnr2	-0.522	29.703	17.225
Myl1	-0.509	1.988	0.796
Rxfp1	-0.506	1.647	0.597
Bub3	-0.500	4.057	2.068
Entpd3	-0.492	0.791	0.095
Ctsb	-0.484	7.762	4.398
Diablo	-0.473	3.602	1.869
Gal	-0.448	12.287	7.487
Prkacb	-0.446	3.179	1.676
Chodl	-0.436	0.621	0.048
Snap25	-0.428	13.340	8.344
Cidea	-0.386	1.170	0.474
mt-Nd2	-0.370	72.582	49.813
Cpe	-0.368	3.660	2.226
Oxct1	-0.367	3.477	2.102
Bmp3	-0.367	0.678	0.163
Clu	-0.361	1.491	0.736
Slc10a4	-0.355	6.529	4.278
Atp1a3	-0.349	1.668	0.881
Tub	-0.348	2.171	1.239
mt-Nd4	-0.345	75.981	53.534
Mapk10	-0.340	2.721	1.648
Lxn	-0.340	5.486	3.617
Slc25a33	-0.338	1.854	1.036
Plcb4	-0.333	4.092	2.648
Serpini1	-0.332	2.067	1.200
Fabp3	-0.330	1.424	0.744
RP23-346N8.2	-0.324	0.931	0.397
Rarres1	-0.323	0.750	0.267
Thy1	-0.323	3.936	2.573
Chchd10	-0.322	5.234	3.520
Th	-0.320	8.631	5.993
Nefh	-0.319	2.020	1.195
Ptprt	-0.315	0.513	0.104
Hpcal1	-0.315	1.399	0.751
Isoc1	-0.314	2.091	1.259
S100a6	-0.313	10.649	7.517
mt-Cytb	-0.311	102.226	74.668
Pcsk1	-0.309	0.648	0.210
Arg1	-0.305	1.469	0.820
Gucy1a3	-0.304	3.155	2.064

Table 2. (continued)

Gene	ln(x+1) fold change α3 KO/WT	Average Expression per Cell	
		WT	α3 KO
Pam	-0.304	2.247	1.395
Mcam	-0.300	4.847	3.332
Syt1	-0.295	27.312	20.075
mt-Nd1	-0.294	52.690	38.997
Dbh	-0.292	26.325	19.396
Hand1	-0.292	3.148	2.099
Efr3a	-0.290	3.868	2.643
Lgmn	-0.285	2.991	2.003
Dner	-0.284	2.277	1.467
Olfm1	-0.283	7.481	5.392
Mgll	-0.282	0.949	0.470
Rgs7bp	-0.282	0.776	0.340
Chgb	-0.281	2.769	1.845
Spock2	-0.280	4.369	3.056
Ntrk3	-0.273	0.754	0.335
Kcnmb4	-0.272	2.085	1.349
Prkg2	-0.270	0.437	0.097
Dlgap1	-0.270	0.599	0.221
Tm4sf1	-0.270	0.921	0.467
Ctsz	-0.266	1.307	0.769
Tacc2	-0.264	0.708	0.312
Gcnt2	-0.262	0.842	0.417
Dnm1	-0.261	2.270	1.519
Fst	-0.257	2.342	1.586
Map7	-0.255	0.559	0.208
RP23-338E5.2	-0.252	2.178	1.470
Ddah1	0.251	5.566	7.441
Ddc	0.252	7.842	10.379
Rpl15	0.254	2.049	2.932
Romo1	0.254	2.050	2.934
Rps7	0.258	3.853	5.280
Atp5e	0.258	5.376	7.253
Rpl23	0.261	11.555	15.301
Synm	0.263	1.045	1.659
Rpl13	0.264	6.695	9.021
Ncam2	0.270	1.333	2.057
Chn2	0.274	0.323	0.740
Rps13	0.276	4.137	5.769
Tshz2	0.276	0.621	1.137
RP24-281K23.1	0.276	0.682	1.217
Tenm4	0.277	0.578	1.082
Phactr1	0.278	0.544	1.038
Ptn	0.283	2.068	3.072
Rps27	0.285	3.102	4.454
RP24-262G23.6	0.286	2.704	3.932
Rpl18	0.287	2.941	4.252
Galnt14	0.291	0.155	0.545
Ubc	0.296	3.983	5.697
Rpl32	0.298	11.380	15.677
Ubb	0.304	15.960	21.982

Table 2. (continued)

Gene	ln(x+1) fold change α3 KO/WT	Average Expression per Cell	
		WT	α3 KO
Pthlh	0.304	0.261	0.709
Rplp2	0.306	5.385	7.670
Nfib	0.308	0.392	0.893
Gnas	0.310	134.209	183.399
Rpl41	0.311	10.472	14.656
Marcksl1	0.313	0.415	0.935
Tmem100	0.318	0.514	1.082
Ifitm2	0.318	0.184	0.628
Rpl22l1	0.319	4.301	6.289
Ptger3	0.319	0.244	0.712
Rps29	0.327	6.388	9.250
Cygb	0.329	2.476	3.831
Arpc1b	0.331	1.386	2.323
Rps18	0.333	5.009	7.380
Rpl36a	0.333	3.126	4.755
Agtr1a	0.337	0.448	1.027
Rpl37a	0.338	5.544	8.175
Slc18a3	0.343	0.032	0.453
Rpl30	0.345	3.308	5.083
Rps15a	0.347	4.154	6.290
Tle1	0.351	0.552	1.206
Rps26	0.352	3.424	5.293
Rps21	0.353	6.221	9.275
Tmsb10	0.360	19.848	28.896
Rpl35	0.384	2.440	4.053
Rpl26	0.389	5.313	8.318
Cnr1	0.398	0.374	1.045
Omp	0.406	2.452	4.180
Rpl37	0.423	6.402	10.295
Areg	0.427	1.036	2.120
Nrn1	0.428	2.008	3.613
Rpl39	0.444	6.394	10.526
Rps28	0.447	1.741	3.287
Rpl29	0.475	1.120	2.408
Rpl36	0.477	3.129	5.654
Rpl38	0.488	4.235	7.525
Rprm	0.494	0.391	1.280
Rplp1	0.495	10.002	17.041
RP24-175N4.1	0.501	0.906	2.145
Arhgap36	0.521	0.198	1.017
Rpl34	0.523	2.089	4.213
Nnat	0.524	2.600	5.078
Slc5a7	0.587	0.245	1.239
Chga	0.600	1.657	3.842
Rpsa-ps10	0.821	0.453	2.302
Rps24-ps3	0.823	0.598	2.638

7.3.4 SCG neurons cluster into 7 subtypes based on gene expression profiles

Based on the highly variable genes in the population, neurons were clustered into subtypes and visualized with a uniform approximation and projection method (UMAP) (Becht *et al*., 2019). I clustered the neurons using two different approaches: in the first, datasets were integrated and treated as one large population of cells, whereas in the second method, the WT dataset was clustered, and used to build a classifier to sort the α3 KO, $X^{\alpha 3}$ and X^{RFP} neurons into the same subtypes that are present in the WT dataset (see section 7.3.7). Here, I will first discuss the results based on the integrated dataset. Within this integrated dataset, 7 subtypes of neurons were identified in the SCG (Figures 7.3A, B). The 20 most significant marker genes that define each subtype are listed in Table 3. The number of neurons that make up each subtype was not equal, indicating that the specification of neuronal identity does not occur randomly.

Next, I determined in two ways whether the cellular identity of SCG neurons was affected by activity. First, I calculated the proportion of WT and α3 KO neurons for each subtype (Figure 7.3C, D). Out of the 7 subtypes, one (#3) had an equal proportion of WT and α3 KO neurons, five subtypes had a moderate change (~ ±30%) in proportion, and for one subtype (#2), the proportion of α3 KO neurons was approximately 2-fold greater than the proportion of WT neurons (Figure 7.3D).

Second, for each subtype, I compared the gene expression profiles between WT neurons and α3 KO neurons. Those subtypes that had little or no differences between the proportion of WT and α3 KO neurons or in gene expression were likely composed of neurons whose identities were not significantly affected by postsynaptic activity. On the

A

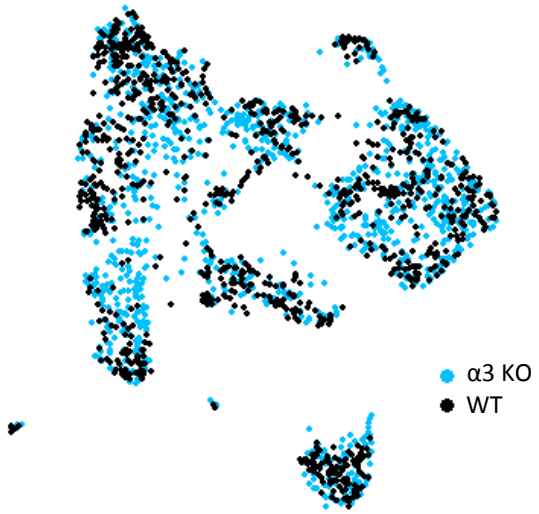

B

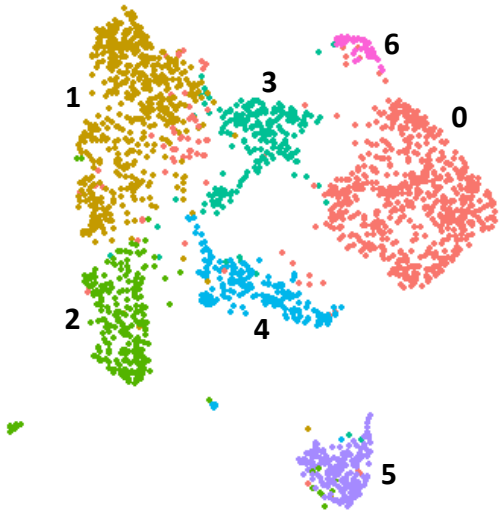

C

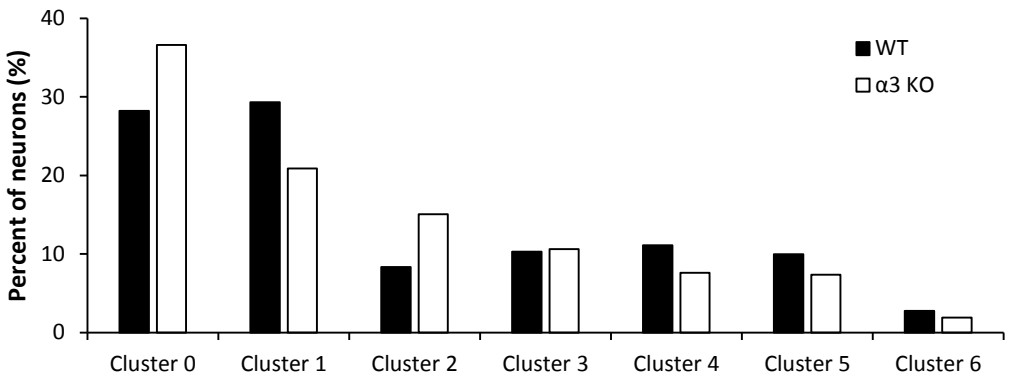

D

	WT	α3 KO	% change	# DE genes
Cluster 0	277 (28%)	428 (37%)	+30%	160
Cluster 1	288 (29%)	244 (21%)	-29%	104
Cluster 2	82 (8%)	176 (15%)	+80%	95
Cluster 3	101 (10%)	124 (11%)	+3%	38
Cluster 4	109 (11%)	89 (8%)	-31%	24
Cluster 5	98 (10%)	86 (7%)	-26%	23
Cluster 6	27 (3%)	22 (2%)	-32%	0
Total	982	1169		

Figure 7.3

Figure 7.3 WT and α3 KO SCG neurons were clustered into 7 subtypes based on gene expression profiles.

(**A**-**B**) SCG neurons were clustered into 7 subtypes and visualized with UMAP, displayed according to (**A**) genotype: WT SCG neurons (black) and α3 KO SCG neurons (blue), and (**B**) subtype identity.

(**C**) The proportion of WT (filled columns) and α3 KO (open columns) SCG neurons categorized into each subtype.

(**D**) The number of WT and α3 KO SCG neurons categorized into each subtype, the % change in proportion for each subtype [(α3 KO–WT)/WT], and the number of differentially expressed genes between WT and α3 KO neurons for each subtype.

Table 3. Twenty of the most significant marker genes that define each cluster. "+" or "–" indicate whether the gene is up-regulated or down-regulated in expression between neurons in this cluster and the remaining neurons in the neuronal subset.

Cluster 0		Cluster 1		Cluster 2		Cluster 3		Cluster 4		Cluster 5		Cluster 6	
Gene		Gene		Gene		Gene		Gene		Gene		Gene	
Fxyd2	+	Npy	+	Slc5a7	+	Crabp1	+	Tmsb4x	–	Fabp7	+	Slc30a3	+
Omp	+	Pcp4	+	Cntn5	+	C1ql1	+	Rps24	–	Plp1	+	C1ql1	+
Ddah1	+	Rxfp1	+	Kctd12	+	Ramp1	+	Rpl9	–	Sparc	+	Agtr1a	+
Edn3	+	Fst	+	Ntrk3	+	Ddah1	–	Tmsb10	–	Gpm6b	+	Agrp	+
Ppp1r1c	+	Gal	+	Htr3a	+	B2m	–	Rps27a	–	Timp3	+	Nbl1	+
Tmsb10	+	Ncald	+	Nnat	+	Htr3a	–	Sepw1	–	Apoe	+	Gap43	+
Fth1.1	+	Sctr	+	Cyb561	–	Ptn	–	Rpl32	–	Cyr61	+	Trnp1	+
Sepw1	+	Bub3	+	Gal	–	Maoa	+	Rps4x	–	Sdc4	+	Fxyd2	+
Areg	+	Gfra3	+	Lhfpl2	+	Ret	–	Rpl3	–	Atp1a2	+	Rgs4	+
Npy	–	S100a6	+	Omp	–	Gda	–	Rps20	–	Cebpd	+	Grina	+
Crip1	–	Epha5	+	Chga	–	H2-D1	–	Rps3a1	–	Lpar1	+	Lsamp	–
Tle1	+	Plcb4	+	Cpne8	+	Prune2	–	Rpl19	–	Vim	+	Npy	–
Ccnd1	–	Fxyd2	–	Rgs4	–	Pcdh17	–	Ppia	–	Zfp36	+	Zbtb20	–
Scg2	–	Ddah1	–	Maoa	–	Mmp2	–	Eef1a1	–	Igfbp4	+	Tpd52l1	+
Sh3bgrl3	+	Edn3	–	Crip1	+	H2-K1	–	Rpl14	–	Gpr37l1	+	Gucy1a3	–
Arhgdig	+	Gda	+	Myl1	+	Cd9	–	Hint1	–	Mal	+	Cadm1	–
Ncam1	–	Htr3a	–	Brinp1	+	Tmem176a	–	Rps3	–	Ptprz1	+	S100a6	–
Chl1	–	Pcdh9	+	Cygb	–	Methig1	–	Rps12	–	Dbi	+	St6galnac5	+
Fxyd7	+	Fth1.1	–	Cidea	+	Necab1	+	Rpl41	–	Ttyh1	+	Scg2	–
Fst	–	Pcdh7	+	Slc31a1	–	Areg	–	Rplp1	–	Egr1	+	Tcf4	–

other hand, the SCG subtypes that had the greatest changes in these parameters were sensitive to changes in postsynaptic activity.

For each subtype, I identified differentially expressed genes that were expressed at significantly different levels between WT neurons and α3 KO neurons (log fold change > ±0.25). Subtype #0 had the largest number of differentially expressed genes; whereas subtype #6 had no genes that were at significantly different levels between WT and α3 KO neurons (Figure 7.3D). Subtype #3 had similar proportions of WT and α3 KO neurons and had a moderate number of genes that were differentially expressed (Figure 7.3D).

The classification of neurons into subtypes allows us to account for cellular heterogeneity by testing for changes in gene expression within subtype categories, and identify differentially expressed genes that were masked in the global neuronal population. Using this type of clustering analysis, I demonstrated that transcriptionally, not all sympathetic adrenergic neurons respond in the same way to changes in activity.

7.3.5 Cholinergic neurons are over-represented in α3 KO SCG

The neurons that make up subtype #2 appeared to be one of the most susceptible to changes in neuronal activity. This subtype had the largest change in the proportion of WT and α3 KO neurons, and a large number of differentially expressed genes between WT and α3 KO neurons.

Among the marker genes for subtype #2 were genes that encode proteins found in cholinergic neurons (Table 3). Moreover, α3 KO neurons that belong to this subtype expressed essential adrenergic genes at significantly lower levels that in WT neurons (Table 4), including the vesicular monoamine transporter (VMAT2/Slc18a2) and tyrosine

Table 4. Differentially expressed genes between WT and α3 KO neurons in Cluster 2

Gene	Average Expression per Cell			Percentage		
	WT	α3 KO	X^{RFP}	WT	α3 KO	X^{RFP}
Aes	11.439	7.888	6.831	0.988	0.943	0.990
Ankrd29	1.190	0.383	0.444	0.524	0.199	0.423
Ano2	0.319	0.024	0.035	0.183	0.017	0.052
Arpc1b	0.913	2.517	2.427	0.415	0.636	0.794
Ass1	0.815	4.197	3.050	0.366	0.739	0.876
Atp1a3	2.614	1.362	1.425	0.744	0.477	0.845
Atp2b1	3.882	1.682	1.952	0.866	0.597	0.835
Atp6v1b2	8.071	2.529	2.515	0.976	0.676	0.856
Bmp3	2.363	0.452	0.619	0.659	0.153	0.464
Bub3	3.499	1.562	1.512	0.744	0.494	0.763
Cartpt	2.409	3.973	1.597	0.012	0.307	0.309
Ccne1	0.564	0.124	0.093	0.305	0.074	0.124
Cd24a	6.630	11.885	9.640	0.963	0.994	1.000
Chchd10	7.419	3.909	3.908	0.976	0.847	0.959
Chn2	0.209	1.460	1.065	0.122	0.466	0.598
Chodl	0.904	0.026	0.060	0.354	0.017	0.093
Cpe	4.251	2.450	2.291	0.927	0.676	0.897
Cpne2	0.702	0.149	0.176	0.402	0.085	0.216
Crtac1	1.269	0.437	0.451	0.500	0.188	0.392
Ctsb	10.295	6.266	5.986	0.963	0.926	0.979
Dbh	24.117	12.312	8.504	1.000	1.000	1.000
Ddah1	5.107	9.148	8.020	0.866	0.926	0.969
Dkk3	1.622	3.581	3.748	0.524	0.795	0.928
Dlgap1	1.239	0.405	0.719	0.537	0.199	0.608
Edn3	0.329	2.227	1.382	0.122	0.500	0.619
Efr3a	5.443	3.250	3.059	0.963	0.750	0.928
Entpd3	0.898	0.302	0.377	0.439	0.142	0.381
Fgf13	0.166	1.334	1.233	0.085	0.369	0.515
Fth1.1	55.620	37.263	37.870	1.000	1.000	1.000
Gal	2.659	0.746	1.044	0.561	0.244	0.577
Gnas	143.960	208.366	188.938	1.000	1.000	1.000
Gng4	0.706	0.173	0.065	0.402	0.080	0.072
Hcfc1r1	5.382	3.318	2.971	0.951	0.807	0.918
Hpcal1	3.211	1.446	1.095	0.793	0.432	0.722
Kcnmb4	1.747	0.436	0.421	0.598	0.193	0.402
Kitl	1.653	0.769	0.635	0.646	0.318	0.515
Laptm4b	0.869	0.270	0.241	0.451	0.148	0.278
Lsamp	3.622	1.487	1.734	0.866	0.517	0.794
Lxn	4.452	2.145	2.370	0.817	0.540	0.856
Maob	3.130	0.651	0.594	0.780	0.239	0.526
mt-Nd1	49.898	37.716	31.592	1.000	1.000	1.000
mt-Nd2	66.272	46.377	51.616	1.000	1.000	1.000
mt-Nd4	72.359	53.413	54.563	1.000	1.000	1.000
Myl1	4.849	2.069	1.855	0.890	0.557	0.845
Ncald	6.369	2.805	3.761	0.927	0.653	0.918
Ndrg4	16.000	11.047	8.367	1.000	0.989	0.979
Ndufa4	11.654	16.426	13.259	0.988	0.994	1.000
Neat1	0.466	1.839	2.284	0.183	0.540	0.608
Nlgn1	0.042	1.055	0.968	0.024	0.403	0.485
Nnat	5.381	11.385	10.675	0.829	0.949	0.990

Table 4. (continued)

Gene	Average Expression per Cell			Percentage		
	WT	α3 KO	X^{RFP}	WT	α3 KO	X^{RFP}
Npy	24.600	4.254	5.411	0.780	0.460	0.670
Nrp2	1.313	0.272	0.301	0.439	0.136	0.309
Nsg2	9.396	6.600	6.427	0.988	0.943	0.990
Ntrk3	4.188	1.318	1.445	0.756	0.438	0.763
Olfm1	8.817	5.484	4.974	0.976	0.903	1.000
Phactr1	0.584	1.863	1.825	0.329	0.591	0.835
Plppr5	0.344	0.029	0.012	0.183	0.017	2.000
Prkacb	3.388	1.500	1.688	0.878	0.562	0.814
Ptma	21.547	28.463	27.263	1.000	1.000	1.000
Ptn	1.696	3.632	3.207	0.610	0.778	0.866
Ptprt	0.818	0.199	0.105	0.451	0.091	0.155
Rab3b	5.967	2.081	1.472	0.939	0.614	0.794
Ramp1	4.208	0.300	0.288	0.890	0.119	0.216
Ret	1.757	3.595	2.297	0.573	0.784	0.845
Rgs7bp	0.825	0.197	0.221	0.427	0.114	0.206
RP23-299D2.2	0.531	0.153	0.141	0.305	0.074	0.134
RP23-83I13.10	4.905	7.595	8.405	0.915	0.955	0.990
Rpl14	12.839	9.482	6.931	0.988	0.972	0.979
Rpl26	5.759	9.381	9.330	0.720	0.972	0.990
Rpl32	12.088	15.997	14.843	1.000	1.000	1.000
Rpl36	2.958	5.729	3.977	0.817	0.926	0.928
Rpl37	6.852	11.491	7.423	0.939	0.994	1.000
Rpl38	4.263	7.724	4.206	0.915	0.966	0.979
Rpl39	7.442	10.856	7.052	0.951	0.983	0.979
Rplp1	11.089	18.800	19.058	0.963	1.000	1.000
Rplp2	5.386	8.301	6.365	0.939	0.989	1.000
Rps18	5.029	7.800	10.094	0.939	0.977	1.000
Rps26	3.298	5.628	5.040	0.841	0.920	0.969
Rps27	3.481	5.442	3.712	0.890	0.915	0.938
Rps4x	10.409	13.786	15.927	1.000	1.000	0.990
Rpsa-ps10	0.533	2.306	5.067	0.293	0.574	0.959
Serpinb6a	3.944	6.859	6.936	0.817	0.955	1.000
Serpini1	2.612	1.076	1.381	0.732	0.460	0.742
Slc18a2	7.758	2.097	2.224	0.939	0.528	0.691
Slc18a3	0.263	2.432	2.140	0.110	0.574	0.536
Slc5a7	1.824	5.947	4.968	0.463	0.903	0.907
Slc6a2	19.187	13.580	12.199	1.000	1.000	1.000
Snap25	14.419	9.585	8.210	0.988	0.960	0.979
Syt1	26.394	16.479	13.909	0.988	0.994	1.000
Th	7.385	2.596	2.408	0.976	0.585	0.814
Tm4sf4	1.178	0.018	0.057	0.500	0.011	0.052
Tmem132c	0.410	0.053	0.138	0.195	0.023	0.155
Tmem176b	3.844	6.422	6.650	0.866	0.926	0.990
Tmem54	0.768	0.124	0.177	0.317	0.074	0.186
Tubb3	32.671	43.006	35.885	1.000	1.000	1.000

hydroxylase (TH). In addition, although Dbh was used as a selection marker, and therefore expressed in all cells, mRNA levels of Dbh in α3 KO neurons of this subtype was half that of WT neurons. Furthermore, monoamine oxidase B (Maob), which oxidizes the noradrenaline precursor, dopamine, is also expressed in fewer α3 KO neurons of this subtype and at lower levels than in WT. On the other hand, these α3 KO neurons expressed several cholinergic genes, including the high-affinity choline transporter, CHT (Slc5a7), and VAChT (Slc18a3) at significantly higher levels than in WT neurons (Figures 7.4A, B, C, D). These data suggest that synaptic activity suppresses a cholinergic phenotype in SCG neurons.

7.3.6 Some differentially expressed genes are restored in X^{RFP} neurons from mosaic mice

Given these differences in gene expression between WT SCG neurons and α3 KO SCG neurons, I asked whether these changes occur in synaptically silent X^{RFP} neurons from mosaic SCG. If gene expression profiles do not change between α3 KO SCG neurons and X^{RFP} neurons, it would indicate that the expression of these genes is regulated primarily by synaptic activity. On the other hand, a difference in gene expression between α3 KO neurons and X^{RFP} neurons would indicate that these particular genes are regulated by external factors, rather than postsynaptic activity.

For the alignment of my datasets, it was necessary to use a custom reference genome. In mosaic mice, the endogenous α3 nAChR subunit gene (Chrna3) on chromosome 9 has a deletion in exon 5. Even though this deletion prevents the formation of functional α3 subunit protein, it was possible that partial mRNA is produced; if so, it would interfere with the classification of neurons from mosaic SCG as α3-expressing ($X^{\alpha3}$) or RFP-

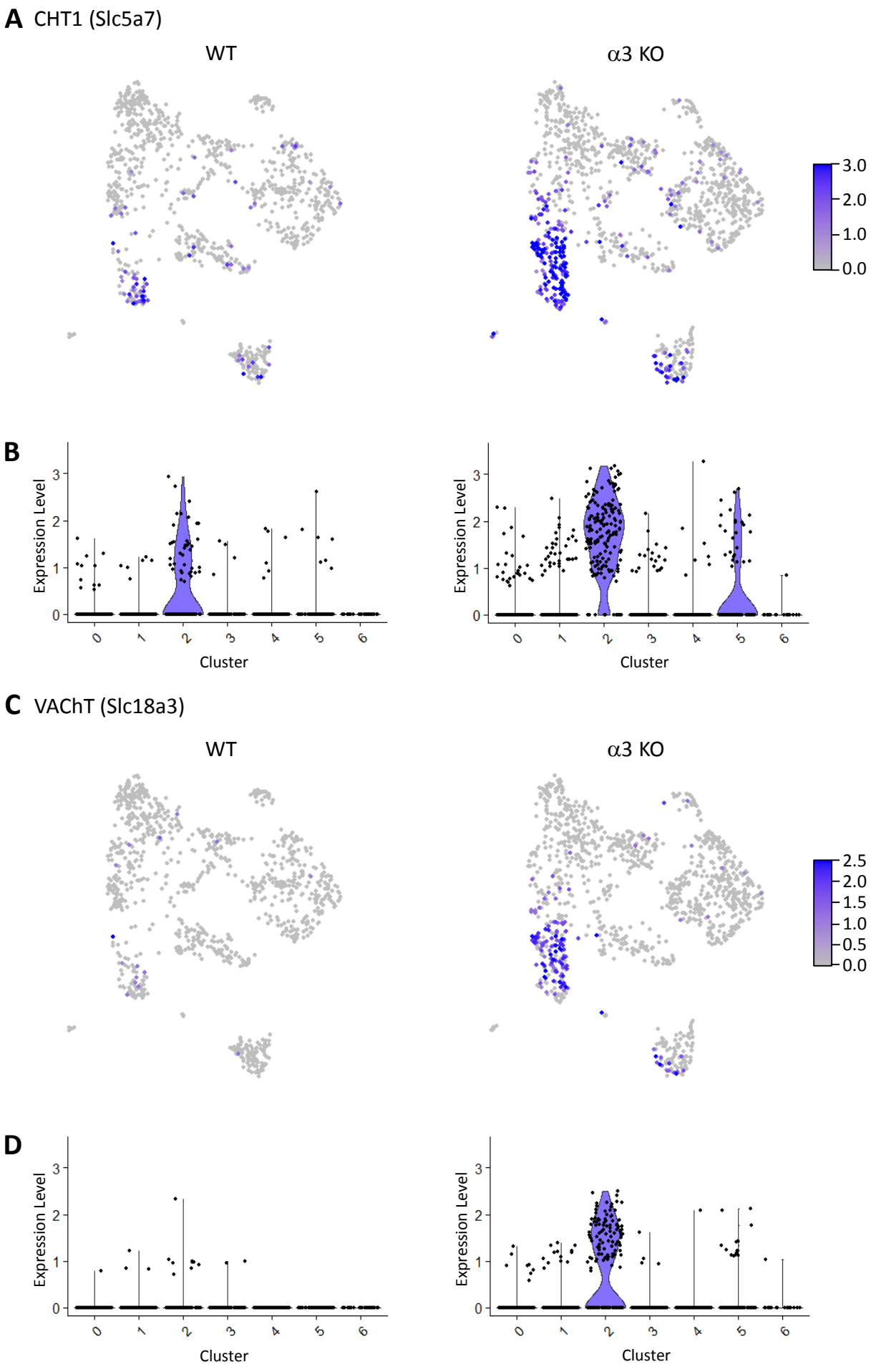
A CHT1 (Slc5a7)
WT
α3 KO
3.0
2.0
1.0
0.0
B
Expression Level
Cluster
C VAChT (Slc18a3)
WT
α3 KO
2.5
2.0
1.5
1.0
0.5
0.0
D
Expression Level
Cluster

Figure 7.4

Figure 7.4 Cholinergic neurons are over-represented in α3 KO SCG.

(**A**) UMAP indicating expression level of CHT1 (Slc5a7) per neuron and their distribution between subtypes (see Figure 7.3B) in WT SCG (left) and α3 KO SCG (right).

(**B**) Violin plots indicating distribution of expression level of CHT1 (Slc5a7) per neuron for each subtype in WT SCG (left) and α3 KO SCG (right).

(**C**) UMAP indicating expression level of VAChT (Slc18a3) per neuron and their distribution between subtypes in WT SCG (left) and α3 KO SCG (right).

(**D**) Violin plots indicating distribution of expression level of VAChT (Slc18a3) per neuron for each subtype (see Figure 7.3B) in WT SCG (left) and α3 KO SCG (right).

expressing (X^{RFP}). Anticipating this possibility, we generated the mosaic mouse model by recombining rat α3 cDNA rather than mouse α3 cDNA into the X chromosome. Minor differences between the mouse and rat α3 sequences allow us to distinguish between partial mRNA transcribed from the endogenous α3 gene on mouse chromosome 9 (present in all SCG neurons in mosaic mice) and mRNA transcribed from the rat α3 cDNA on the X chromosome (present only in $X^{\alpha 3}$ neurons in mosaic mice). Therefore, the read data were aligned to a custom reference package consisting of the mouse genome with the addition of rat α3 and RFP sequences, and transcript count data of the endogenous Chrna3 gene were removed from all datasets for downstream analysis.

In the mosaic dataset, neurons were divided according to their expression of rat α3 and RFP. In some neurons, α3 and RFP expression were below detectable levels, and were not included in my analysis. $X^{\alpha 3}$ and X^{RFP} neurons were categorized into the same 7 subtypes based on their gene expression profiles (Figures 7.5A, B). I calculated the proportions of X^{RFP} neurons for each subtype (Figures 7.5C, D), and identified differentially expressed genes (Figure 7.5C) as above. Interestingly, for some subtypes, X^{RFP} neurons appeared more similar to WT neurons, while for other subtypes, X^{RFP} neurons were more similar to α3 KO neurons. For example, subtype #3 consisted of a stable proportion of neurons between α3 KO and WT datasets, and also contained a similar proportion of X^{RFP} neurons. In subtype #0, the proportions of X^{RFP} neurons were restored to near WT proportions, whereas in subtypes #2 and #5, the proportions of X^{RFP} neurons showed no change from α3 KO neurons. Different still, were subtypes (#1 and #4), in which X^{RFP} neurons were at intermediate levels between WT and α3 KO proportions.

A

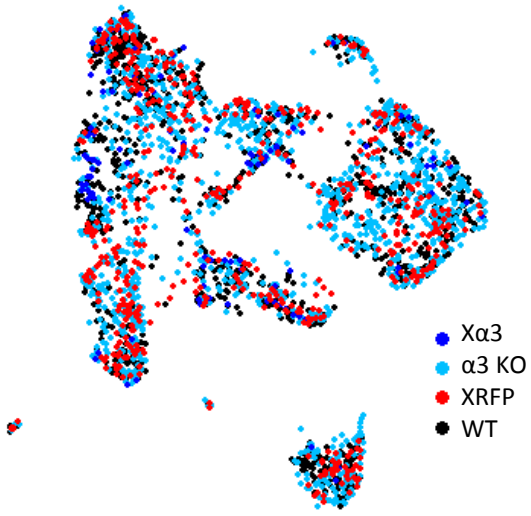

B

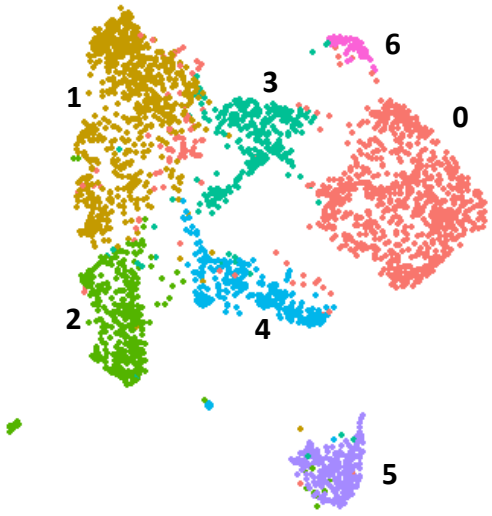

C

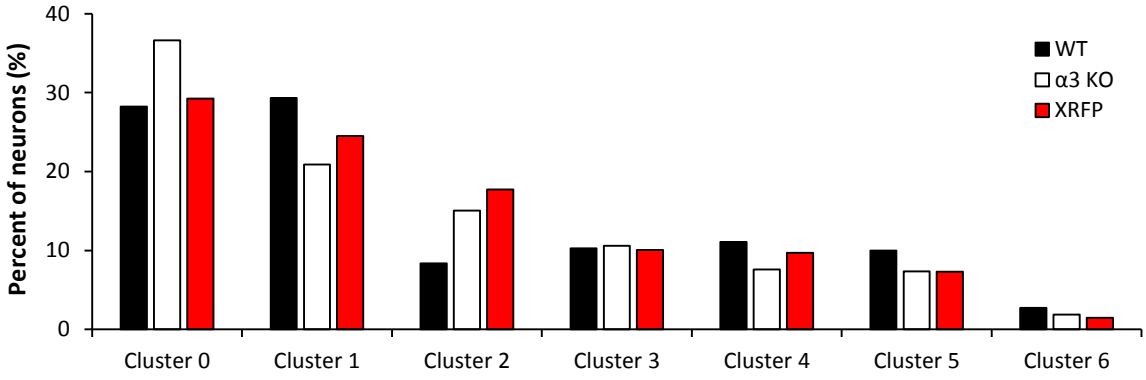

D

	WT	α3 KO	X^{RFP}	# rescued genes
Cluster 0	277 (28%)	428 (37%)	160 (29%)	61
Cluster 1	288 (29%)	244 (21%)	134 (24%)	30
Cluster 2	82 (8%)	176 (15%)	97 (18%)	14
Cluster 3	101 (10%)	124 (11%)	55 (10%)	14
Cluster 4	109 (11%)	89 (8%)	53 (10%)	1
Cluster 5	98 (10%)	86 (7%)	40(7%)	4
Cluster 6	27 (3%)	22 (2%)	8 (1%)	0
Total	982	1169	547	

Figure 7.5

Figure 7.5 X^{RFP} neurons were categorized into the same 7 subtypes based on their gene expression profiles.

(**A**-**B**) X^{RFP} neurons from mosaic SCG were clustered into 7 subtypes and visualized with UMAP, displayed according to (**A**) genotype: X^{RFP} neurons (red) WT SCG neurons (black) and α3 KO SCG neurons (blue), and (**B**) subtype identity. WT and α3 KO data are from Figure 7.3.

(**C**) The proportion of WT (filled columns), α3 KO (open columns) and X^{RFP} (red columns) SCG neurons categorized into each subtype. WT and α3 KO data are from Figure 7.3.

(**D**) The number of WT, α3 KO and X^{RFP} neurons categorized into each subtype, and the number of genes that were differentially expressed between WT and α3 KO SCG neurons and restored to normal levels in X^{RFP} neurons for each subtype.

For each subtype, I identified the genes that were differentially expressed between WT neurons and α3 KO neurons. Then, I determined the expression level of the differentially expressed genes in X^{RFP} neurons of the same subtype. In total, there were 255 unique genes that were identified as differentially expressed between WT neurons and α3 KO neurons for at least one subtype, and 90 of these genes were expressed at levels that were not significantly different between WT neurons and X^{RFP} neurons (Figure 7.6). These changes occurred either in the number of neurons that express a particular gene or by a change in the average expression in the neurons that express that gene, or both.

For subtype #2, the number of X^{RFP} neurons that expressed adrenergic markers Slc18a2 (VMAT2) and TH increased slightly from that expressed by α3 KO neurons (Table 4); however, the average expression level in X^{RFP} neurons did not increase from levels in α3 KO neurons when normalized to the number of neurons that express that gene. On the other hand, there was no change in the number of X^{RFP} that express cholinergic markers, or in the expression level of cholinergic marker genes.

7.3.7 α3 KO and X^{RFP} SCG neurons were sorted into WT subtypes using a classifier

Integrating datasets is useful when correcting for technical variation between samples and to identify shared features and properties between datasets. When the WT, α3 KO, $X^{\alpha 3}$ and X^{RFP} neuronal populations were integrated and collectively clustered into subtypes, gene expression profiles from all four neuronal groups played a role in defining the number and identities of subtypes. As a result, it is conceivable that these clusters were not a true representation of the biological subtypes present in any of these WT, α3 KO, or mosaic mice; rather, they may represent an average of these four populations of neurons

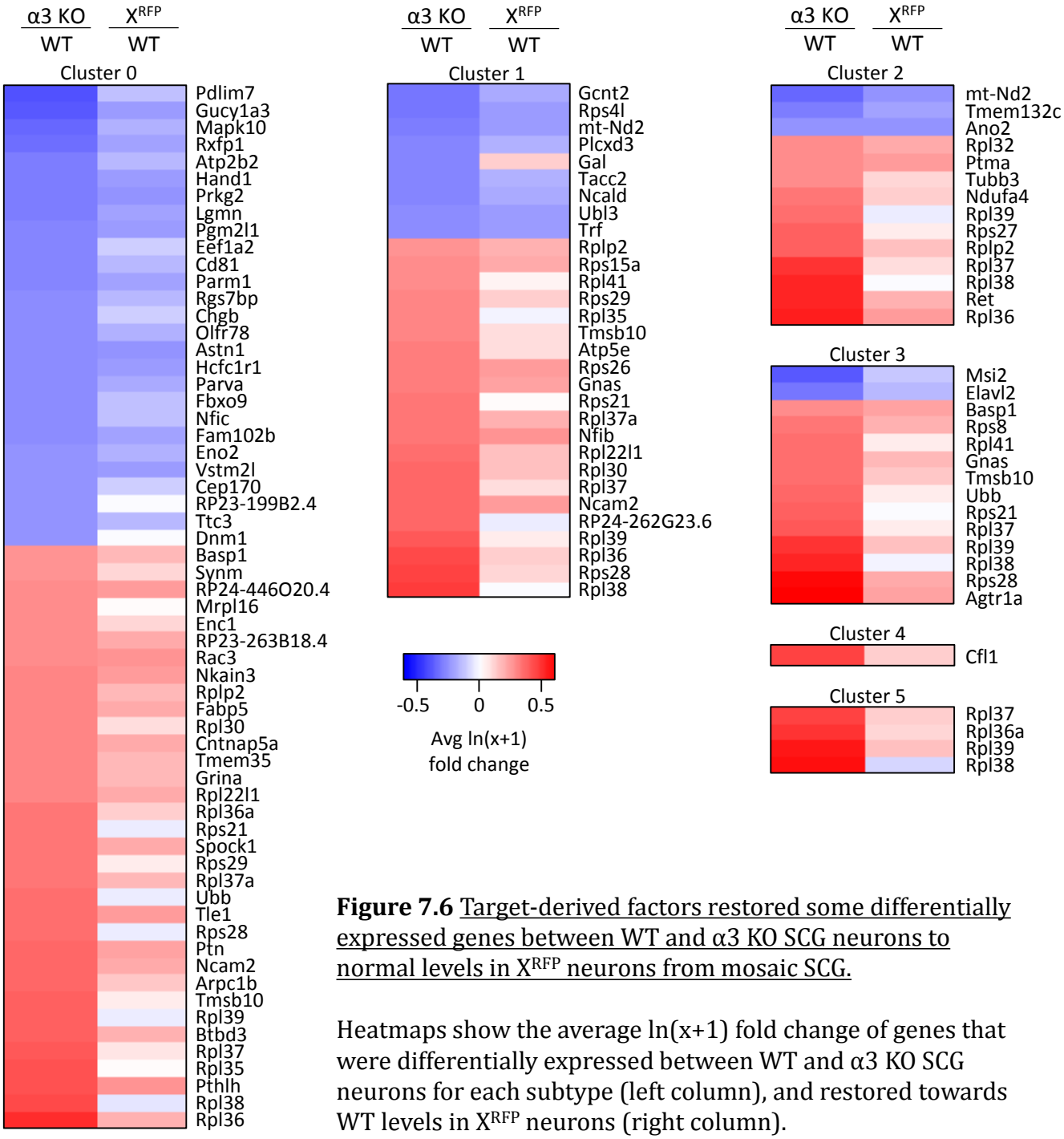

Figure 7.6 Target-derived factors restored some differentially expressed genes between WT and α3 KO SCG neurons to normal levels in X^{RFP} neurons from mosaic SCG.

Heatmaps show the average ln(x+1) fold change of genes that were differentially expressed between WT and α3 KO SCG neurons for each subtype (left column), and restored towards WT levels in X^{RFP} neurons (right column).

and mask differences in gene expression between datasets. A better approach to test how SCG neurons from α3 KO and mosaic mice differ from WT mice is to use the WT neuronal population as a reference and classify the remaining α3 KO, $X^{\alpha3}$ and X^{RFP} neurons into the subtypes present in WT SCG. Therefore, I analyzed these single cell gene expression datasets using a second approach that did not require integrating WT, α3 KO, $X^{\alpha3}$ and X^{RFP} neuronal populations for clustering. First, I identified the highly variable genes in the WT neuronal dataset and clustered WT neurons into subtypes, such that each subtype was comprised of cells with similar gene expression profiles, and was defined by a list of marker genes that were either up- or downregulated. Next, these WT data were used to build a classifier to sort α3 KO, $X^{\alpha3}$ and X^{RFP} neurons into the same subtypes identified in the WT dataset.

The WT population contained 7 subtypes of SCG neurons (Figure 7.7A), the same number as identified previously, however, the marker genes for each subtype from this clustering strategy (Table 5) differed from those that defined subtypes in the integrated dataset. Using the WT distribution as a reference, I compared the proportion of α3 KO neurons classified into each subtype (Figures 7.7B, C, D). A larger proportion of neurons in the α3 KO dataset were classified into subtypes #1 and #5 than in the WT dataset, and there were fewer neurons sorted into subtype #2. This result clearly indicates that postsynaptic activity influences the differentiation of neurons into these subtypes.

Differences in gene expression between WT and α3 KO varied across subtypes: subtype #1 had the greatest number of differentially expressed genes (160 genes), whereas subtype #6 had the lowest number (20 genes). Furthermore, the same gene can be upregulated in one subtype and downregulated in another; for example, the gene encoding

A WT

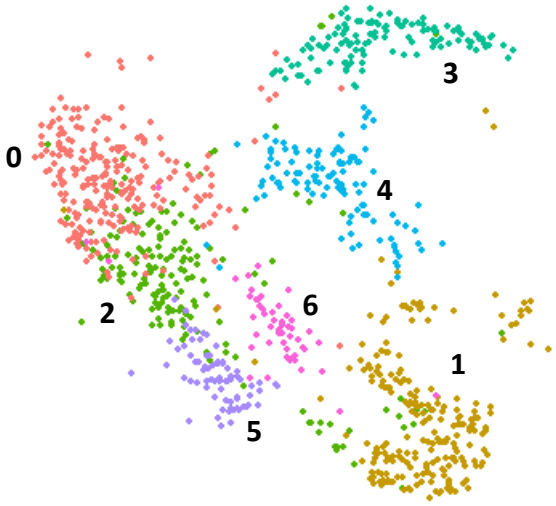

B α3 KO

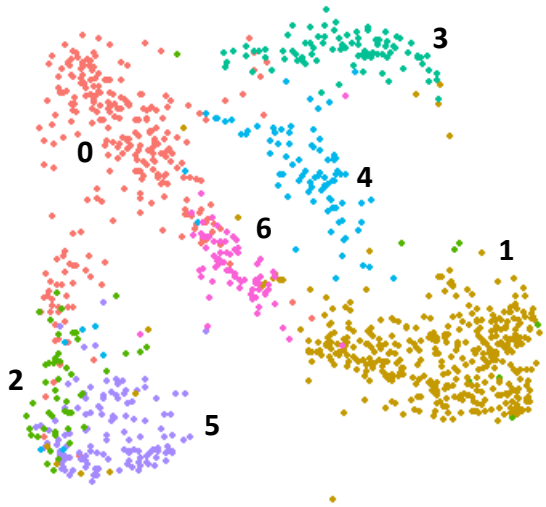

C

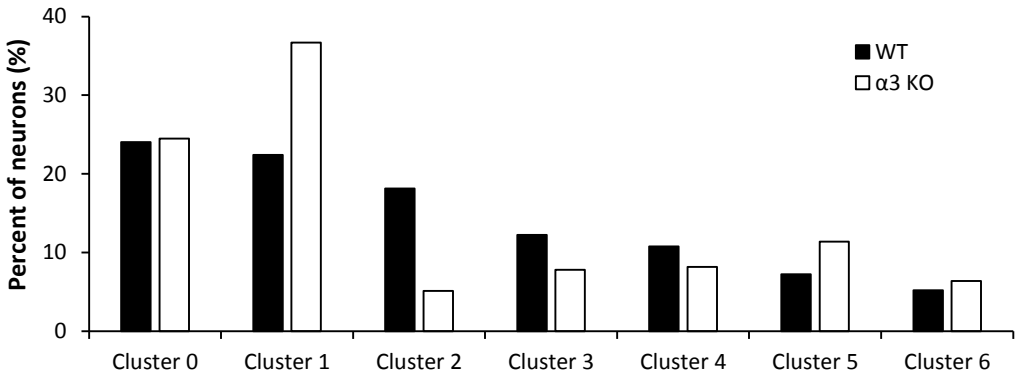

D

	WT	α3 KO	% change	# DE genes
Cluster 0	236 (24.0%)	273 (24.5%)	+1.9%	72
Cluster 1	220 (22.4%)	409 (36.7%)	+63.7%	160
Cluster 2	178 (18.1%)	57 (5.1%)	-71.8%	60
Cluster 3	120 (12.2%)	87 (7.8%)	-36.1%	24
Cluster 4	106 (10.8%)	91 (8.2%)	-24.4%	26
Cluster 5	71 (7.2%)	127 (11.4%)	+57.5%	70
Cluster 6	51 (5.2%)	71 (6.4%)	+22.6%	20
Total	982	1115		

Figure 7.7

Figure 7.7 WT SCG neurons were clustered into 7 subtypes, and a classifier sorted α3 KO SCG neurons into these subtypes.

(**A**-**B**) (**A**) WT and (**B**) α3 KO SCG neurons were clustered into 7 subtypes and visualized with UMAP.

(**C**) The proportion of WT (filled columns) and α3 KO (open columns) SCG neurons categorized into each subtype.

(**D**) The number of WT and α3 KO SCG neurons categorized into each subtype, the % change in proportion for each subtype [(α3 KO–WT)/WT], and the number of differentially expressed genes between WT and α3 KO neurons for each subtype.

Table 5. Twenty of the most significant marker genes that define each cluster. "+" or "–" indicate whether the gene is up-regulated or down-regulated in expression between neurons in this cluster and the remaining neurons in the neuronal subset.

Cluster 0		Cluster 1		Cluster 2		Cluster 3		Cluster 4		Cluster 5		Cluster 6	
Gene		Gene		Gene		Gene		Gene		Gene		Gene	
Sctr	+	Edn3	+	Prkg2	+	Tmsb4x	–	Fabp7	+	Ntrk3	+	Crabp1	+
Htr3a	–	Fxyd2	+	Crtac1	+	mt-Rnr2	+	Sparc	+	Slc5a7	+	Ramp1	+
Npy	+	Ppp1r1c	+	Methig1	+	Tmsb10	–	Plp1	+	Cnr1	+	Necab1	+
Gal	+	Fth1.1	+	Lxn	+	mt-Cytb	+	Gpm6b	+	Hpca	+	Chst15	+
Gda	+	Sepw1	+	Ncald	+	mt-Nd2	+	Timp3	+	Bmp3	+	Tenm4	+
Tubb5	+	Sh3bgrl3	+	Rarres1	+	Rps24	–	Mpz	+	Brinp1	+	Nbl1	+
Tuba1a	+	Ddah1	+	Slc6a4	+	Rpl9	–	Apoe	+	Tspan8	–	C1ql1	+
Plcb4	+	Npy	–	Bmp3	+	Rps27a	–	Igfbp4	+	Nefl	+	Ddah1	–
mt-Cytb	–	Areg	+	Snap25	+	mt-Nd4	+	Sdc4	+	Kctd12	+	Gal	–
Stmn1	+	Arhgdig	+	Atp6v1e1	+	Rps20	–	Cyr61	+	Atp6v1b2	+	Prune2	–
Pcp4	+	Snhg11	–	Phox2a	+	Sepw1	–	Atp1a2	+	Kitl	+	Maoa	+
Fst	+	Gap43	+	Atp2b1	+	Eef1a1	–	Lpar1	+	Myl1	+	Bean1	+
Rxfp1	+	Meg3	–	Bub3	+	Rps4x	–	Sostdc1	+	Gng4	+	Lxn	–
mt-Nd4	–	Prr15	+	Egln3	+	Rpl32	–	Vim	+	Hpcal1	+	Isoc1	+
Epha5	+	Tesc	+	RP23-83I13	+	Rps3	–	Zfp36	+	Cntn5	+	Fst	–
Dgkh	+	Scg2	–	Edn3	–	Rps12	–	Ednrb	+	Nefm	+	Crtac1	–
Syn2	+	Pcdh17	+	Rxfp1	+	Rplp1	–	Sepp1	+	Tmem54	+	Bub3	–
Bub3	+	Cox8a	+	Prkar2b	+	mt-Nd1	+	Dbi	+	Cidea	+	H3f3a	+
S100a6	+	Enc1	+	Slitrk5	+	Tpt1	–	Fos	+	Nsg2	+	Atp1a1	–
Ddah1	–	Agrp	+	Fth1.1	–	Rps11	–	Cebpd	+	Ina	–	Myl1	+

the neuropeptide galanin was expressed at levels ~2.9X greater than WT in subtype #6, yet it was ~0.75X of WT in subtype #0, and ~0.28X of WT in subtype #2 (Figure 7.8, Table 6). These results further support the idea that individual subtypes of neurons respond differently to changes in postsynaptic activity.

Consistent with my previous findings, a greater number of neurons in α3 KO SCG expressed the cholinergic markers CHT1 and VAChT when compared to WT SCG, and did so at significantly higher levels than in WT neurons (Figures 7.9A, B, C, D, E). Together, I identified 243 genes that were differentially expressed between WT and α3 KO neurons in at least one subtype. Of these 243 genes that were identified as differentially expressed, 87 were expressed at levels similar to WT in X^{RFP} neurons (Table 7). This result supports the idea that the expression of these genes was not regulated directly downstream of postsynaptic activity.

7.4 Discussion

In this chapter, I used scRNAseq to generate gene expression profiles from SCG neurons in WT, α3 KO and mosaic mice. These neurons were clustered in two ways: first as an integrated population of neurons, and second, WT neurons were clustered into subtypes, and the sets of marker genes that defined each subtype were used to sort neurons from α3 KO and mosaic mice into these subtypes. Neurons were classified into 7 subtypes based on up- and downregulated genes. The differences in gene expression between WT, α3 KO and mosaic samples were calculated to identify the neuronal subtypes and genes that were more susceptible to changes in postsynaptic activity. Between WT and α3 KO neurons, there were ~250 unique genes that were differentially expressed in at least

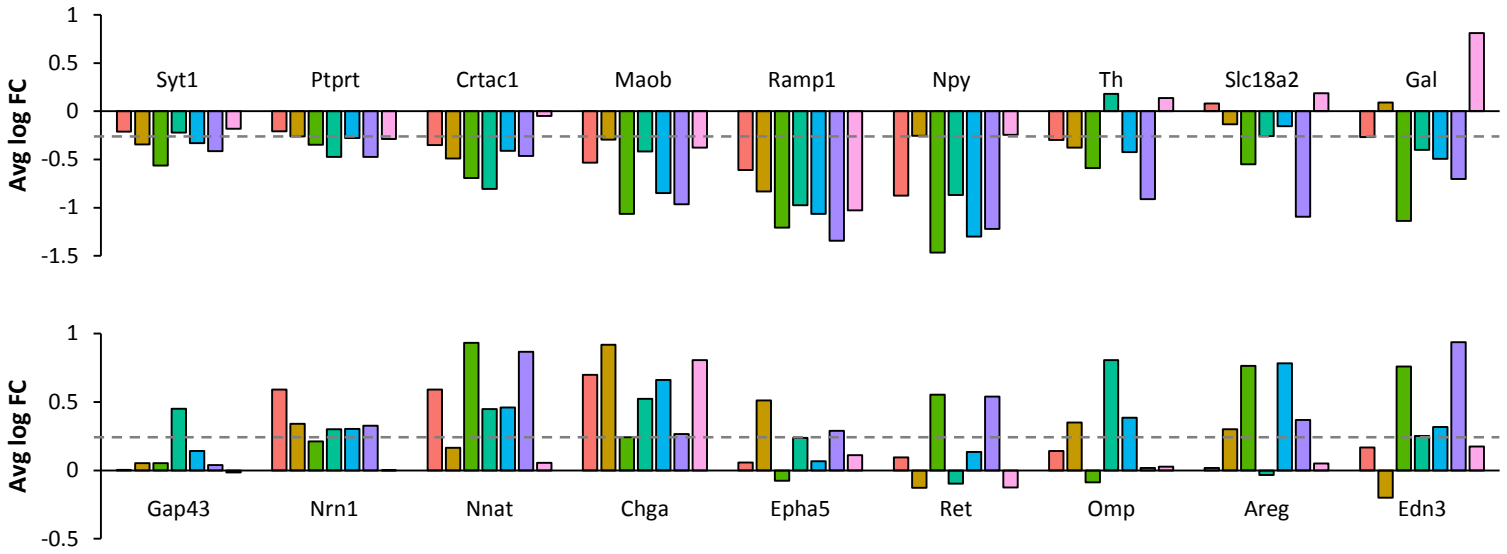

Figure 7.8 Subtypes of SCG neurons respond differently to changes in postsynaptic activity.

Graphs show ln(x+1) fold change (α3 KO/WT) in each subtype for selected genes that were differentially expressed between WT and α3 KO SCG neurons. Negative fold change indicates downregulation in α3 KO neurons. Dashed line indicates Avg log FC of ±0.25. See Table 6 for average expression values.

Table 6. Normalized average expression per cell in each subtype for selected genes that were differentially expressed between WT and α3 KO neuronal subtypes (see Figure 7.8).

Gene	Cluster 0		Cluster 1		Cluster 2		Cluster 3		Cluster 4		Cluster 5		Cluster 6	
	WT	α3 KO	WT	α3 KO	WT	α3 KO	WT	α3 KO	WT	α3 KO	WT	α3 KO	WT	α3 KO
Slc5a7	0.00	0.22	0.09	0.19	0.08	3.26	0.19	0.46	0.41	1.60	1.97	6.69	0.03	0.21
Slc18a3	0.03	0.11	0.01	0.03	0.00	0.95	0.00	0.08	0.02	0.60	0.28	2.68	0.03	0.07
Syt1	28.24	22.70	26.21	18.26	24.19	13.32	28.86	22.92	27.31	19.31	28.13	18.27	33.67	27.95
Ptprt	0.39	0.12	0.35	0.04	0.58	0.11	0.70	0.06	0.46	0.11	0.96	0.22	0.61	0.21
Crtac1	0.76	0.24	0.83	0.12	3.15	1.08	1.63	0.18	1.30	0.52	1.11	0.33	0.08	0.03
Maob	4.21	2.05	1.03	0.51	3.43	0.53	1.34	0.54	3.84	1.07	3.14	0.57	4.15	2.52
Ramp1	1.76	0.50	1.78	0.21	2.63	0.09	1.98	0.13	2.75	0.29	4.64	0.47	5.65	1.38
Npy	59.55	24.25	1.40	0.85	32.88	6.82	16.69	6.41	37.28	9.43	20.84	5.45	6.07	4.53
Th	10.41	7.47	8.45	5.49	9.20	4.65	4.46	5.54	9.07	5.60	7.84	2.55	9.13	10.61
Slc18a2	9.36	10.21	5.64	4.80	8.81	4.66	13.45	10.16	8.26	6.92	8.09	2.04	6.44	7.97
Gal	24.68	18.62	2.95	3.32	14.87	4.09	10.36	6.61	13.55	7.88	2.30	0.63	1.95	5.63
Gap43	18.18	18.26	29.03	30.65	17.81	18.81	13.38	21.56	16.90	19.65	21.18	22.05	24.81	24.47
Nrn1	2.14	4.68	2.83	4.38	1.42	2.00	1.45	2.31	2.16	3.29	0.60	1.21	2.81	2.81
Nnat	1.70	3.89	2.33	2.93	2.61	8.19	1.97	3.66	2.79	5.02	5.14	13.62	5.38	5.74
Chga	3.23	7.52	0.40	2.52	1.06	1.63	3.48	6.57	1.02	2.92	0.26	0.65	0.77	2.96
Epha5	9.27	9.89	2.43	4.71	7.09	6.51	6.01	7.90	6.59	7.12	3.36	4.83	4.23	4.84
Ret	1.05	1.26	3.72	3.16	1.06	2.59	5.14	4.58	1.46	1.82	1.78	3.76	1.04	0.80
Omp	1.97	2.43	4.75	7.16	1.82	1.58	1.82	5.32	1.70	2.96	0.56	0.59	2.65	2.75
Areg	0.01	0.03	3.24	4.73	0.08	1.33	2.21	2.10	0.14	1.49	0.10	0.59	0.00	0.06
Edn3	0.13	0.33	5.17	4.05	0.34	1.88	2.36	3.32	0.79	1.46	0.16	1.95	0.59	0.89

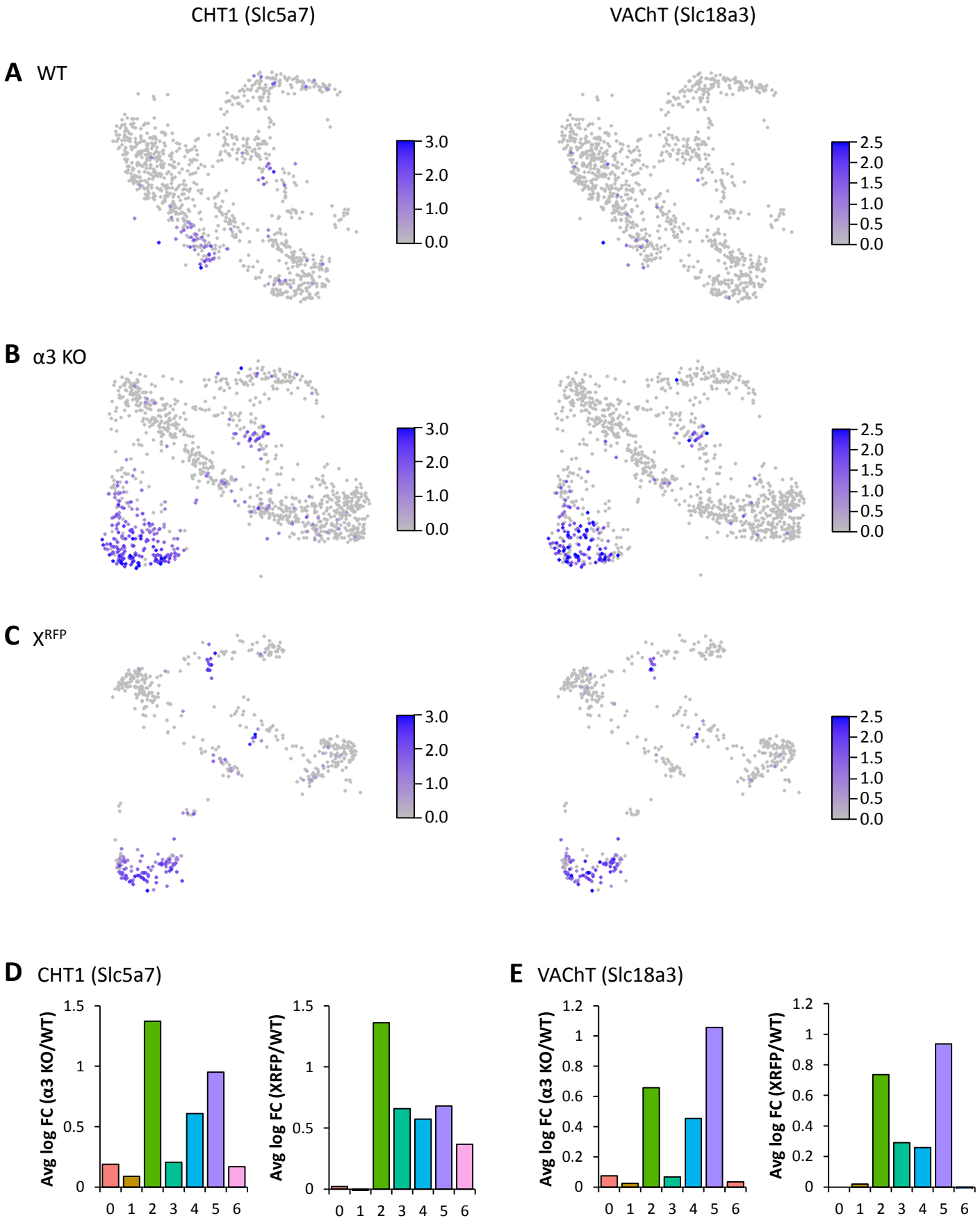
CHT1 (Slc5a7)
VAChT (Slc18a3)
A WT
B α3 KO
C X^RFP
3.0
2.0
1.0
0.0
2.5
2.0
1.5
1.0
0.5
0.0
D CHT1 (Slc5a7)
E VAChT (Slc18a3)
Avg log FC (α3 KO/WT)
Avg log FC (XRFP/WT)
0 1 2 3 4 5 6

Figure 7.9

Figure 7.9 Cholinergic markers are expressed at higher levels in α3 KO and X^{RFP} SCG neurons than in WT SCG neurons.

(**A**-**C**) UMAP indicating expression level of CHT1 (Slc5a7; left) or VAChT (Slc18a3; right) per neuron and their distribution between subtypes in (**A**) WT neurons, (**B**) α3 KO neurons, and (**C**) X^{RFP} neurons.

(**D**) Graphs show ln(x+1) fold change in each subtype for CHT1 (Slc5a7).

(**E**) Graphs show ln(x+1) fold change in each subtype for VAChT (Slc18a3).

Table 7. Average expression per cell of genes that were differentially expressed between WT and α3 KO SCG neurons, and restored towards WT levels in X^{RFP} neurons.

Cluster 0	Average Expression per cell		
Gene	WT	α3 KO	X^{RFP}
Arhgap36	0.588	2.160	1.465
Atp5e	4.983	6.741	5.519
Dnm1	2.411	1.386	1.681
Fabp3	1.112	0.523	0.712
Gal	24.680	18.617	31.286
Gnas	119.372	158.416	137.832
Ifitm2	0.157	0.625	0.169
Nnat	1.704	3.888	1.891
Plcb4	7.305	5.127	6.269
Plcxd3	1.656	0.874	1.170
RP24-262G23.6	2.590	4.097	2.441
Rpl22l1	4.144	5.796	4.916
Rpl30	3.256	5.175	3.959
Rpl36	3.260	5.234	3.663
Rpl37	6.889	10.169	7.768
Rpl37a	5.719	8.102	6.994
Rpl38	4.655	7.426	4.448
Rpl39	6.441	10.035	7.060
Rpl41	9.403	12.784	10.025
Rps15a	4.771	6.490	5.815
Rps21	6.050	8.631	6.112
Rps26	3.844	5.395	4.882
Rps28	1.667	2.998	1.924
Rps29	6.535	8.896	7.191
Rps4l	1.162	0.503	0.809
Rxfp1	3.070	1.931	2.417
Slc25a33	1.711	1.057	1.245
Tmsb10	19.830	25.803	21.777
Cluster 1	Average Expression per cell		
Gene	WT	α3 KO	X^{RFP}
Arpc1b	1.934	2.978	2.028
Atp2b1	3.243	1.453	1.928
Atp2b2	0.934	0.459	0.675
Btbd3	0.149	0.665	0.380
Chgb	2.236	1.343	1.625
Cidea	0.816	0.181	0.344
Diablo	3.374	1.610	2.198
Dnm1	2.226	1.434	2.105
Fbxo9	1.177	0.668	0.896
Gucy1a3	1.987	1.292	1.766
Ifitm2	0.148	0.681	0.465
Isoc1	2.091	1.149	1.490
Maob	1.029	0.509	0.658
Mapk10	2.107	1.291	1.499
Marcksl1	0.040	0.425	0.274
Napb	5.565	3.957	4.467
Ncald	3.472	1.240	1.942
Nkain3	0.182	0.561	0.453

Cluster 1 (cont.)	Average Expression per cell		
Gene	WT	α3 KO	X^{RFP}
Pacsin1	2.031	1.294	1.631
Pdlim7	0.883	0.407	0.795
Phactr1	0.449	0.908	0.769
Prkacb	2.239	1.353	1.656
Prkar2b	0.263	0.664	0.500
Pthlh	0.503	1.212	0.841
Ptn	2.559	3.713	2.974
RP23-263B18.4	1.312	2.022	1.811
Rpl22l1	5.187	7.285	6.600
Rpl30	3.780	5.368	4.274
Rpl35	2.943	4.790	2.891
Rpl36	3.894	6.770	4.744
Rpl36a	3.917	5.347	4.359
Rpl37	7.476	11.229	8.029
Rpl37a	6.005	8.576	7.081
Rpl38	5.180	8.115	4.678
Rpl39	7.975	11.977	7.664
Rps21	7.596	10.374	7.073
Rps26	3.686	5.592	5.240
Rps28	2.211	3.507	2.101
Rps29	6.924	9.972	7.156
Th	8.453	5.489	6.470
Tle1	1.358	2.166	1.903
Tmem100	0.801	1.442	1.050
Tmsb10	27.853	38.119	28.008
Ubb	16.648	24.308	16.189
Vstm2l	1.616	0.966	1.182
Ybx1	1.216	2.341	2.060
Cluster 2	Average Expression per cell		
Gene	WT	α3 KO	X^{RFP}
Areg	0.083	1.326	0.269
Ass1	0.824	4.147	2.493
Cartpt	0.064	11.032	2.483
Cd24a	9.297	13.608	11.855
Crip2	6.376	10.042	7.186
Edn3	0.344	1.875	0.378
Efr3a	4.445	1.992	2.871
Fgf13	0.160	2.682	1.751
Fgf7	0.032	0.526	0.153
Gal	14.867	4.087	7.010
Gnas	131.855	175.088	142.515
Ncald	11.279	4.589	6.956
Ndufa4	12.611	17.281	12.425
Phactr1	0.491	1.879	1.238
Prr15	0.231	1.003	0.473
Ret	1.062	2.588	1.283
Rpl36	3.209	6.269	4.208
Rpl38	4.314	7.575	4.226

Table 7. (continued)

Cluster 2 (cont.)	Average Expression per cell		
Gene	WT	α3 KO	X^{RFP}
Rps28	1.664	3.351	2.403
Spock2	4.724	2.684	3.296
Tmem100	0.685	1.876	0.756
Cluster 3	Average Expression per cell		
Gene	WT	α3 KO	X^{RFP}
Arhgap36	0.041	1.120	0.396
Omp	1.823	5.320	3.796
Rpl39	1.738	4.219	2.704
Rpl41	3.814	7.444	5.991
Cluster 4	Average Expression per cell		
Gene	WT	α3 KO	X^{RFP}
mt-Nd4	61.171	45.361	52.548
Rpl37	7.140	11.438	8.080
Rpl38	4.210	8.112	3.790
Rpl39	6.808	11.706	7.181
Cluster 5	Average Expression per cell		
Gene	WT	α3 KO	X^{RFP}
Ass1	0.735	4.312	3.098
Cd24a	6.894	11.271	8.493
Chn2	0.205	1.347	0.993
Dlgap1	1.329	0.426	0.656
Fth1.1	56.220	38.061	43.509
Ndufa4	12.015	16.829	14.299
Nlgn1	0.089	0.963	0.552
Npy	20.842	5.447	12.351
Rpl34	2.679	4.857	4.060
Rpl36	3.257	6.058	4.337
Rpl37	7.067	11.631	7.549
Rpl38	4.213	8.070	4.147
Rplp2	5.660	8.700	6.880
Rps21	7.016	10.568	6.574
Slc5a7	1.972	6.685	4.867
Tmem132c	0.433	0.060	0.183
Cluster 6	Average Expression per cell		
Gene	WT	α3 KO	X^{RFP}
Fam219a	1.289	0.249	0.571
Fxyd7	9.071	4.215	5.915
Gda	0.046	1.870	0.294
Gnas	161.750	209.194	170.970
Ncald	5.086	1.930	2.926
Rpl34	2.244	4.910	4.000
Rpl38	4.108	8.203	4.497
Rps8	10.590	16.066	13.559
Tmsb10	20.976	29.271	24.240

one subtype, and of these genes, ~90 were restored towards WT levels in X^{RFP} neurons. In addition, α3 KO and X^{RFP} neurons had a greater proportion of cholinergic neurons than WT neurons, and the expression levels of cholinergic genes was significantly greater in α3 KO and X^{RFP} cholinergic neurons than in WT cholinergic neurons. Taken together, I identified a subset of genes that were differentially expressed in the absence of postsynaptic activity and restored toward WT levels when synaptically silent neurons are in mosaic SCG with active neighbouring neurons. Additionally, my results establish a role for postsynaptic activity in regulating the differentiation of adrenergic neurons into cholinergic neurons.

7.4.1 Expression of Na_v α subunit genes in SCG neurons and identifying the neuronal subset

In my preparation of our single cell suspensions, I minimized the contribution of non-neuronal cells by filtering cells by size. Nonetheless, the recovered cells still comprised of a heterogeneous population of neurons and non-neuronal cells. To isolate the neuronal population, I selected cells that expressed several key markers for adrenergic neurons. These markers were Dbh, Ntrk1, Slc6a2, either Scn3a ($Na_v1.3$) or Scn9a ($Na_v1.7$) or both, and either Cacna1a ($Ca_v2.1$) or Cacna1b ($Ca_v2.2$) or both.

Interestingly, there was a slight difference in the expression of the Na_v α subunit genes between the WT subset and the α3 KO subset. My results demonstrate for the first time that a significant proportion of sympathetic neurons (~50%) express the Scn3a ($Na_v1.3$) gene. The proportion of cells that expressed Scn3a without Scn9a ($Na_v1.3$ group) was lower in the α3 KO subset, whereas the proportion of cells that expressed Scn9a without Scn3a ($Na_v1.7$) were slightly increased. This suggests that in the absence of postsynaptic activity, expression of Scn3a may be downregulated in some SCG neurons.

For droplet-based scRNAseq experiments, there exists a balance between the number of recovered cells and the occurrence of doublets, which are two (or more) cells captured in the same droplet. Ideally, the frequency of doublets is minimized while maintaining a large number of recovered cells. I optimized the concentrations of our single cell suspensions to be within the company's (10X Genomics) recommended range, which estimated a doublet rate to be ~5%. Presumably, doublets have a greater number (~2X) of transcript counts than average, however, after using the selection markers to generate the neuronal subset, I did not observe any outliers with a greater number of transcripts. In addition, less than 0.5% of cells from mosaic SCG expressed both rat α3 and RFP. Furthermore, similar numbers of cells were loaded and recovered across my samples and the frequency of doublets in the neuronal subset should not differ between datasets. Nevertheless, the filtering of doublets can be further explored in future iterations.

There are several caveats to using a stringent set of selection markers. Transcript capture rates are estimated to be ~20% (Shalek *et al*., 2014), therefore neurons that expressed any of these genes at a level that were below a detectable threshold were excluded. Smaller neurons often have a lower number of transcripts, and by chance, mRNA generated from the selection markers may not have been captured. Conceivably, inactive α3 KO and X^{RFP} neurons may also have lower levels of total transcript counts. In addition, there may be a subtype of neuron in the α3 KO or X^{RFP} population, in which one or more of these genes was significantly downregulated to levels below a detectable threshold. For example, α3 KO neurons may express Dbh at undetectable levels if they re-specify into neuronal subtypes that do not synthesize noradrenaline. In this instance, this important subpopulation of neurons would be excluded from the neuronal subset and therefore

omitted from my analyses. Although these issues should be considered, it should also be recognized that between WT, α3 KO and mosaic datasets, a proportionally similar number of cells were identified as neurons from the total population of recovered cells, indicating that it is unlikely that I am overlooking a significant population of neurons.

Additionally, expression of rat α3 and RFP from the UbiC promoter appears to be low. There was a significant number of neurons (i.e. express Dbh, Ntrk1, Slc6a2, as well as Cacna1a, Cacna1b, or both, and either Scn3a, Scn9a, or both and not Notch1, 2, or 3) that did not have detectable levels of either rat α3 and RFP. For the analysis of SCG neurons from mosaic mice, I only included neurons with detectable levels of rat α3 and RFP.

7.4.2 Differentially expressed genes between WT and α3 KO neurons

I identified a set of activity-dependent genes that were differentially expressed in the absence of neuronal activity. These differentially expressed genes included those that encode proteins involved in regulating intracellular calcium levels. Some examples include Ramp1, which regulates the activity of the calcitonin receptor, an ATP-driven Ca^{2+} pump (Atp2b1), and olfactory marker protein (Omp), which modulates the activity of a sodium-calcium exchanger in the plasma membrane (Kwon *et al*., 2009). Since these genes are all heavily involved in maintaining calcium homeostasis, they are likely downregulated because α3 KO neurons are at low risk of excitotoxicity and do not require many mechanisms to extrude excess calcium.

Several of the misregulated genes may reflect the phenotypic defects observed in α3 KO neurons. Among these include neurofilament-H (Nefh), which is a structural component of the axonal cytoskeleton, and Crtac1/LOTUS, which appears to indirectly promote axon

growth by antagonizing inhibition mediated by the binding of Nogo to its receptor (Kurihara *et al*., 2014). Nefh and LOTUS are both downregulated in α3 KO neurons, consistent with my results from Chapter 5, in which I find axon innervation of the iris to be reduced. Also supporting these results, the genes encoding the t-SNARE protein Snap25 and the calcium-sensing protein synaptotagmin 1 (Syt1), both involved in vesicle fusion and the exocytosis of neurotransmitters at sympathetic nerve terminals, are also downregulated. This may be because inactive neurons do not receive stimulation and therefore do not release neurotransmitters, or because α3 KO neurons extend less extensive axonal arbours and have fewer nerve terminals. Also in this context, a number of differentially expressed genes, such as those in the tetraspanin family (Tm4sf4, Tspan8) are involved in signalling pathways downstream of growth factor receptors (Charrin *et al*., 2014).

Interestingly, although neuronal activity is conventionally thought of as a stimulus that promotes pathways and enhance transcription, I identified a number of genes whose expression was upregulated in the absence of activity. Possibly, the regulation of these genes was disinhibited, or their expression was enhanced to compensate for the absence of synaptic transmission. Of particular interest is a collection of ribosomal proteins. Given my previous results from Chapter 6, indicating that cap-dependent translation is depressed in α3 KO neurons, I speculate that the production of ribosomal proteins may be upregulated through a compensatory mechanism to elevate translation.

7.4.3 Genes restored to WT levels in X^{RFP} neurons from mosaic mice

Since X^{RFP} neurons differentiated and were innervated normally during postnatal development, genes that were misregulated in α3 KO neurons and restored to WT levels in X^{RFP} neurons may play key roles in coordinating dendritic growth, synaptic targeting and the refinement of connections. Interestingly, genes that have previously been implicated in refinement, such as those involved in the complement cascade and BDNF signalling (Singh *et al*., 2008; Stephan *et al*., 2012), do not appear on this list. Several of the identified genes have roles in regulating intracellular calcium homeostasis, including Marcksl1 and Atp2b2, which encodes an ATP-driven Ca^{2+} pump. Even though synaptic transmission is absent, it is possible that activity-dependent target-derived factors may induce the release of intracellular stores of calcium or promote the influx of extracellular calcium.

Many of the genes that were restored in X^{RFP} neurons are well known to interact with many different intracellular pathways. For example, Rgs10 encodes a protein that operates downstream of GPCR signalling, Arhgap36 encodes a protein that acts on Rho GTPases, and several genes encoding kinases were identified, including Mapk10, Prkg2, and Ret, a receptor tyrosine kinase that binds GDNF. These proteins act on a wide variety of cell signalling pathways, including those that converge to regulate mTOR activity, and influence a diverse set of neuronal properties. On the other hand, the precise functions of many of the genes that were identified are not well established, and whether these genes may play a role in regulating neuronal development remains unclear.

7.4.4 Differentiation of adrenergic neurons into cholinergic neurons

Sympathetic ganglia are known to contain a small subpopulation of cholinergic neurons (Ernsberger and Rohrer, 1999; Schotzinger and Landis, 1990). A proportionally greater number of α3 KO neurons were categorized into the cholinergic subtype than in WT neurons, indicating that a greater proportion of the α3 KO neuronal population expressed markers involved in acetylcholine synthesis or packaging. If the proportion of one subtype changed, then the proportion of at least one other subtype must have changed as well. Whether these cholinergic neurons all originated from one other subtype or whether they differentiated from several other subtypes is unclear.

In addition to a greater number of cholinergic neurons, the expression levels of cholinergic genes in this subtype of neurons in α3 KO SCG was greater than in WT cholinergic neurons. On the other hand, their expression of adrenergic genes, VMAT2 and TH, was decreased when compared WT.

Given this downregulation of adrenergic genes, and the use of Dbh and the Slc6a2 gene, which encodes a noradrenaline transporter, as selection markers for the neuronal subset, I investigated whether there was an omitted subset of neurons in the WT or α3 KO datasets that expressed only cholinergic markers and not adrenergic markers. Interestingly, cholinergic SCG neurons in WT and α3 KO mice continued to express at least some of the markers of adrenergic neurons. Virtually all cells that expressed cholinergic markers also expressed Dbh and Slc6a2, indicating that I did not exclude a population of cholinergic neurons from the neuronal subset.

The proportion of cholinergic neurons and the expression levels of cholinergic genes in X^{RFP} neurons did not regress towards WT values, indicating that the differentiation of

SCG neurons into cholinergic neurons is likely mediated by pathways downstream of postsynaptic activity in a cell-autonomous manner. It appears as if postsynaptic activity suppresses the expression of cholinergic genes, and when synaptic transmission is abolished, as it is in α3 KO and X^{RFP} neurons, this inhibition is lifted and cholinergic genes become upregulated. When placed in culture, SCG neurons from rats have been shown to differentiate into cholinergic neurons (Furshpan *et al*., 1976; Iacovitti *et al*., 1981; Landis, 1990; Reichardt and Patterson, 1977). Consistent with the idea that postsynaptic activity influences the expression of cholinergic genes, several studies indicate that the differentiation of sympathetic neurons into cholinergic neurons *in vitro* can be suppressed by depolarizing neurons with electrical stimulation or with high extracellular potassium (Walicke *et al*., 1977; Wolinsky and Patterson, 1983).

7.4.5 Conclusion

The differentiation of neurons into subtypes during postnatal development of the nervous system is regulated by a complex combination of several factors, some of which are genetically preprogrammed, while others include extracellular signals. In the SCG, each neuronal subtype likely share a unique set of cellular properties that are related to their function, and are different from the other subtypes. One obvious example would be the neurotransmitter that is released (noradrenaline vs. acetylcholine), however, other properties may include neuronal excitability or dendritic and axonal morphology.

It is reasonable for afferent synaptic activity to play a role in specifying how neurons differentiate into each subtype in order to regulate how electrical stimuli are processed and integrated in SCG neurons, and how signals are conducted to control the function of

downstream targets. In the absence of synaptic transmission, neurons may fail to fully differentiate and remain in an immature state, or follow a genetic program that leads to a default identity. My results from α3 KO neurons indicate some defects in differentiation, particularly of those expressing cholinergic genes. Overall, all 7 of the neuronal subtypes found in WT SCG were represented in the α3 KO neuronal subset. However, when examined on a finer scale, there were differences in the proportions of neurons categorized into each subtype. Some of these differences persisted in X^{RFP} neurons, while others regressed towards WT proportions. Clearly, the differentiation of SCG neurons is complex.

Overall, synaptically silent neurons show some degree of differentiation, possibly mediated by a combination of genetically preprogrammed cues and external signals that are independent of neuronal activity, whereas synaptic activity and target-derived factors fine-tune the differentiation process.

Chapter 8: Discussion of findings and conclusions

The primary goal of my doctoral research was to improve our understanding of the mechanisms that regulate the reorganization of neural circuits during early postnatal development. Existing models have persisted since the 1980s (Changeux and Danchin, 1976; Katz and Shatz, 1996; Purves and Lichtman, 1980), and even though there are several studies that contradict their predictions, these new ideas have not been incorporated into revised models, and the classical view remains more or less unchanged.

One of the most widely accepted models for refinement is that presynaptic nerve terminals compete for a retrograde trophic factor, or a "reward" signal, that is secreted by the postsynaptic target cell in limited quantities locally at synaptic sites. The activity of the presynaptic axons confers a competitive advantage by promoting increased release of the "reward" signal from the postsynaptic cell. Ultimately, the terminals that are more active receive a greater quantity of the trophic factor and become stabilized, whereas weaker terminals receive an insufficient amount of the trophic factor and withdraw (Changeux and Danchin, 1976; Katz and Shatz, 1996; Purves and Lichtman, 1980). Furthermore, the model postulates a "punishment" factor that is released by presynaptic nerve terminals of active and stronger axons, and diffuses to nearby synapse to destabilize competing, less active inputs (Jennings, 1994; Lichtman and Colman, 2000). The results from my thesis demonstrate that this model is incomplete because refinement can occur even when presynaptic inputs do not generate postsynaptic responses, and therefore they cannot stimulate the release of "reward" signals. My revised model incorporates retrograde, target-derived factors that play a key role in matching presynaptic inputs to appropriate postsynaptic neurons as connections refine.

As an example, I will use a relatively well-defined circuit that mediates pupil dilation. Pupillary responses are important and non-invasive read-outs of several behavioural and cognitive tests for attention (Eckstein *et al*., 2017; Wang and Munoz, 2015). Briefly, several CNS regions, including the locus coeruleus-norepinephrine system, the superior colliculus, the mesencephalic cuneiform nucleus, the hypothalamus, and a few brainstem nuclei are involved in controlling pupil dilation. The integrated output of these structures excites specific preganglionic neurons located in the lateral horn of the spinal cord that synapse onto sympathetic neurons in the SCG innervating the iris, causing the radial muscles of the iris to contract and dilate the pupil. Of the ~10,000–12,000 sympathetic neurons in the mouse SCG (Deppmann *et al*., 2008; Purves *et al*., 1986), only ~30–40 neurons innervate the iris (less than 0.5% of the total), as I demonstrated in Chapter 5. Therefore, preganglionic neurons carrying signals destined for the iris need to connect specifically onto these ~30–40 SCG neurons.

During embryonic development, preganglionic axons branch and diverge to innervate an excess number of SCG neurons. As I demonstrated in my thesis, at P1–P3, each sympathetic neuron is innervated by 7-8 preganglionic neurons. This allows each preganglionic axon to sample hundreds of sympathetic neurons that project to a variety of different targets. Ultimately, preganglionic axons that receive iris-destined signals from higher CNS regions need to specifically maintain connections onto the ~30–40 sympathetic neurons that project to the iris and withdraw from other sympathetic neurons. Similarly, each of these ~30–40 sympathetic neurons that innervate the iris need to only receive innervation from ~1–3 specific preganglionic neurons that carry signals destined for the iris and eliminate other inputs. This matching of preganglionic neurons and sympathetic

neurons is necessary to establish the appropriate circuit for pupil dilation, in order for pupil dilation to be controlled specifically without inappropriately activating other sympathetic targets.

For this type of matching between connections in a complex circuit, I propose that it is the iris, signalling through retrograde, target-derived factors that instructs each of these ~30–40 iris-specific sympathetic neurons to selectively retain ~1–3 preganglionic neurons and to eliminate others; these connections may then be fine-tuned by their activity. This matching process is necessary at nearly all nodes of a circuit, and through a similar process, the preganglionic neurons that persist in innervating iris-specific sympathetic neurons also become specified to receive innervation from those CNS neurons that mediate pupil dilation.

The results from my thesis provide strong support for many aspects of this model; however, further work is needed to determine whether this model stands up to further scrutiny. Below, I discuss both the evidence that support the model, and propose further experiments to test rigorously some of the components that require further examination.

8.1 Refinement does not depend on local postsynaptic activity

For preganglionic neurons to refine their connections to converge onto the correct subset of SCG neurons that project to the iris, there is no reason that stronger and more active axons should have a competitive advantage over less active inputs, as proposed by the “reward” model.

One of my most exciting findings is that refinement can occur in the absence of postsynaptic activity. I demonstrated this in two mouse models in which (i) cap-dependent

translation is enhanced; and (ii) in mosaic SCG where synaptically silent and synaptically active neurons are intermingled. That refinement can occur in the absence of postsynaptic activity is surprising because of the prevailing idea that synaptic transmission is essential for refinement, as I showed in Chapter 3, and refinement without synaptic activity had never been reported previously.

The results in Chapter 3 showed that preganglionic axons onto SCG neurons undergo developmental refinement during the early postnatal period. However, in the absence of postsynaptic activity (α3 KO mice), connections in SCG do not refine, consistent with the refinement literature. Next, in Chapter 4, I investigated the refinement of connections in mosaic ganglia, which consists of a mixed population of active neurons and inactive neurons. I found that preganglionic inputs onto synaptically inactive neurons in mosaic ganglia refined their connections. This result indicates that refinement of inputs is not regulated locally by postsynaptic neurons; rather it can be driven by external activity-dependent cues. Additionally, enhancing cap-dependent translation by deleting 4E-BP genes from α3 KO mice (α3/4E-BP DKO mice) further demonstrated that synapses can refine even when there is no differential in strength because they are all equally silent (Chapter 6).

Similar to refinement, the dendritic morphology of sympathetic neurons is also regulated by factors that do not include local postsynaptic activity. Numerous studies have previously shown that the growth and extension of dendrites is an activity-dependent process, in which calcium influx mediated by afferent synaptic activity acts on several signalling pathways to promote and stabilize dendritic branching (Cline, 2001; Haas *et al*., 2006; Redmond, 2008; Wong and Ghosh, 2002). While my results showing that SCG

neurons in α3 KO mice have stunted dendritic growth support this idea, synaptically inactive neurons extend large and elaborate dendritic arbours when neighbouring neurons are active as in mosaic SCG.

Furthermore, silent synapses that are mistargeted to the cell soma in α3 KO mice are restored to the dendritic arbour in mosaic SCG. However, it remains unclear whether dendritic growth and synaptic targeting are distinct processes that are regulated independently, or whether defects in synaptic target are secondary to defects in dendritic morphology. When the dendritic arbour is small, dendritic space is limited and may become saturated with synapses, thereby directing all additional synapses to the cell soma. Possibly, with the expansion of the dendritic arbour, there are more opportunities for synaptic innervation, supporting a greater proportion of synapses.

Taken together, my results establish that the refinement of connections, dendritic growth and synaptic targeting can all be regulated by external factors that are not generated by local postsynaptic activity.

8.2 Refinement is regulated by external signals that are likely target-derived

Part of my main strategy to examine the role of postsynaptic activity was to isolate its contribution by generating a novel and unique mosaic mouse model. In sympathetic circuits, manipulation of a single gene for the α3 nAChR subunit controls the postsynaptic activation of sympathetic neurons. Whereas most other neuronal types, such as those that receive glutamatergic inputs, require the deletion of multiple genes, and their excitatory inputs are often compounded by inhibitory inputs.

To my knowledge, only one similar model exists. Lu *et al*. (2013) used a quadruple conditional KO mouse, in which the genes encoding AMPAR subunits GluA1-3 and NMDAR subunit GluN1 were floxed, and a low concentration of an adeno-associated virus expressing GFP-Cre was delivered to the hippocampus at P0. This strategy eliminated excitatory inputs onto a small subset of CA1 pyramidal neurons, while keeping neighbouring neurons synaptically active. Lu *et al*. showed that these synaptically inactive neurons extended normal dendrites. However, the authors did not investigate the refinement of inputs on these neurons.

My results from the mosaic mouse model indicate that the refinement of connections, dendritic growth and synaptic targeting can all be regulated by external factors. These external factors are likely either (a) local diffusible signals released from neighbouring active neurons or (b) activity-dependent retrograde signals secreted by targets such as the iris.

I cannot rule out the possibility that neighbouring neurons or satellite glial cells in the SCG play a role in mediating refinement, however, there is little evidence to support this idea. There are no gap junctions that electrically couple sympathetic neurons in SCG. And, unlike astrocytes that extensively ensheath thousands of retinogeniculate connections in visual circuits (Chung *et al*., 2013), satellite glial cells in the SCG envelop individual neurons with minimal interaction with neighbouring cells.

Neural-glial interactions in the SCG have not been well characterized, however there is no evidence to suggest that synaptic transmission or activity of sympathetic neurons influences the properties of glial cells. As I described in Chapter 7, I generated cell single gene expression datasets from SCG. For my thesis, I focused on the neuronal population

(discussed below), however, these datasets also contain gene expression profiles of non-neuronal cells, including satellite glial cells. With these data, I can examine whether there are any differences in gene expression between glial cells in WT, α3 KO, and mosaic SCG; the absence of differentially expressed genes in non-neuronal cells between these mouse models would make it unlikely that active neurons modulate the development of inactive neurons in mosaic SCG by signalling through glial cells.

On the other hand, I provide evidence that target innervation plays a role in the differentiation and innervation of SCG neurons, likely through the release of activity-dependent factors that act on SCG neurons. The fundamental difference between sympathetic neurons in α3 KO SCG and mosaic SCG is the functional innervation of their targets. Targets of SCG neurons α3 KO mice are not functionally innervated and do not receive adrenergic stimulation. In mosaic mice, ~50% of the SCG neurons are active and provide functional innervation to common targets, stimulating the release of activity-dependent, target-derived factors.

Although I did not quantify the activity of the targets of the SCG, which include the iris, pineal gland, bone marrow, blood vessels and various other tissues in the head and neck, it is evident that they do not function in α3 KO mice and are functionally innervated in mosaic mice. In α3 KO mice, severe defects in autonomic function are observed (Campanucci *et al*., 2010; Xu *et al*., 1999), whereas mosaic mice are healthy and fertile, and do not exhibit any signs of dysautonomia.

For synaptically inactive neurons in the SCG to be regulated by target-derived factors in a retrograde manner, their axons need to be present at the target to receive these signals. Using the innervation of the iris as an example (Chapter 5), I found that active

sympathetic targets in WT and mosaic mice are innervated by a higher density of axons and by more nerve terminals than inactive targets in α3 KO mice. Given that the same number of SCG neurons project to the iris regardless of their activity, a reduced innervation density in α3 KO mice indicates that each neuron has fewer nerve terminal sites to endocytose retrograde growth factors. Endocytosis may also be defective in inactive neurons, possibly due to a reduction in vesicle docking; however, this seems unlikely because inactive neurons in mosaic SCG develop normally, and retrograde labeling experiments with CTB-488 do not appear to depend on activity.

The low density of innervation on inactive targets also suggests a positive feedback loop, in which functionally innervated targets release factors that promote their innervation by sympathetic axons, further enhancing their uptake of such activity-dependent, target-derived factors. On the other hand, SCG neurons in α3 KO mice (i) do not stimulate their targets to release activity-dependent signals, and (ii) form significantly fewer nerve terminals at the target: both factors could result in insufficient uptake of retrograde factors.

Collectively, my results show a strong correlation between the refinement of inputs, morphology of SCG neurons, and the functional innervation of targets, providing strong support that these properties are co-regulated by common processes; the most likely are those involving activity-dependent, target-derived factors. While my findings do not firmly establish a role for target activation in refinement, there are several approaches that could be used to address this component of my model.

One critical test is to determine whether specifically activating sympathetic targets in α3 KO mice would induce preganglionic axons to refine without postsynaptic activity.

Because all sympathetic neurons in α3 KO mice are synaptically silent, this experiment would rule out the possibility that the external signals that direct refinement in mosaic SCG are generated by neighbouring neurons.

There are several methods that can be used to carry out this experiment. One strategy would be to use channelrhodopsin (ChR2) expression and light stimulation to specifically activate SCG targets. For example, a smooth muscle SM22-Cre driver mouse line (Kühbandner *et al*., 2000) crossed to a LSL-ChR2 reporter line on an α3 KO background would abolish synaptic transmission in the SCG, and express ChR2 in the iris. Since the iris is easily accessible, it would be relatively straightforward to stimulate with blue light without surgeries or implanting light guides. Additionally, the SCG neurons that do not project to the iris would not receive retrograde signals. And, according to my model, their preganglionic inputs should not refine, serving as internal negative controls. However, the main challenge of using this strategy in identifying and recording from the SCG neurons that project to the iris. As demonstrated by my CTB-488 retrograde labelling experiments in Chapter 5, a relatively low number of neurons project to the iris, and those neurons may not be accessible for intracellular recordings.

Alternatively, pharmacological agonists such as epinephrine would have the benefit of activating many targets, eliminating the challenge of identifying and recording from a very specific subset of SCG neurons that innervate the iris. On the other hand, pharmacological agonists lack the specificity that ChR2-mediated stimulation would provide as it would likely activate a number of non-specific targets outside of this circuit, and complicate the interpretation of the results.

To determine whether activity-dependent, target-derived factors work in parallel with cell-autonomous signals generated by postsynaptic activity, one could functionally block the activation of target in WT mice. If target-derived factors alone direct refinement, then preganglionic inputs onto sympathetic neurons should not refine even if they are synaptically active.

In addition, to learn more about the identity of the retrograde factors that are upregulated by target organs in response to sympathetic stimulation, one could conduct gene expression profiles of sympathetic target tissues in WT, α3 KO and mosaic mice. Since targets in mosaic mice and in WT mice are both functionally innervated, their gene expression profiles are expected to be similar. Therefore, by identifying genes that are differentially expressed between functionally innervated targets of WT and mosaic mice and inactive targets of α3 KO mice, one could identify the signaling pathways that are regulated by stimulation and identify the activity-dependent, target-derived factors that act on SCG neurons.

8.3 Molecular mechanisms downstream of external factors

Because the regulation of refinement is a complex process, the underlying molecular mechanisms likely involve several signaling pathways that involve a combination of gene transcription, translation and post-translational modifications. To learn more about the signaling pathways that external factors may act on to regulate neuronal development, I investigated the role of cap-dependent translation, as well as the activity-dependent changes in gene transcription.

8.3.1 Cap-dependent translation

Enhancing cap-dependent translation in α3 KO mice rescued their defects in refinement and in dendritic growth (Chapter 6). One might argue that enhancing cap-dependent translation promotes dendritic growth through pathways that are independent of activity. However, enhancing cap-dependent translation in active neurons did not produce any excessive dendritic growth or branching.

Proteomic profiling identified several proteins whose levels were decreased in α3 KO mice and restored by enhancing cap-dependent translation. Since the levels of these proteins correlated with the rescue of dendritic growth, synaptic targeting and refinement, these proteins likely underlie, in part, these developmental properties.

Cap-dependent translation is regulated in large part by mTOR activity. Since many intracellular signalling pathways converge on mTOR, including those activated by the binding of growth factors, it is reasonable to hypothesize that retrograde factors from sympathetic targets elevate mTOR activity and enhance cap-dependent translation in SCG neurons to regulate their development. In support of this idea, levels of P-4E-BP are depressed in synaptically inactive neurons in α3 KO mice and normal in synaptically inactive in mosaic SCG. This indicates that cap-dependent translation can be mediated by external signals.

My interpretation of the results from 4E-BP KO mice are based heavily on the assumption that developmental defects in sympathetic neurons were rescued due to the enhancement of cap-dependent translation in SCG neurons, as is demonstrated by our proteomic profiling data. However, it is also possible that enhancing cap-dependent translation rescues developmental defects through a target-based mechanism. Since 4E-BP

genes are deleted globally, cap-dependent translation is likely elevated in sympathetic targets as well. According to my model, in the absence of functional innervation, targets downregulate the production of activity-dependent, target-derived factors. As a result, synaptically inactive neurons in α3 KO mice receive insufficient quantities of these factors and have defects in development. However, if cap-dependent translation is enhanced, then such factors may be over-produced in inactive targets. If so, then target-derived factors would be present at higher levels and promote normal development of synaptically inactive neurons.

8.3.2 Gene transcription

To gain further insight into the identity of molecules that are differentially regulated by postsynaptic activity and by external factors, I conducted single cell gene expression profiling experiments on SCG from WT, α3 KO and mosaic mice (Chapter 7). I identified a collection of genes that were downregulated in synaptically inactive neurons in α3 KO SCG and restored to normal levels in mosaic SCG, indicating that these genes are regulated by external signals rather than by local postsynaptic activity. Many of the genes that are restored encode proteins that are known to function in a number of different intracellular pathways, including several that converge onto mTOR to regulate its activity. In addition, there are several genes that have not been shown previously to be expressed in sympathetic neurons. The precise functions of many of these genes in sympathetic nerve function are not clear, and it will be interesting to explore whether some of these genes are involved in neuronal differentiation, or in the regulation of synaptic refinement.

8.4 Conclusion

The idea that distal targets such as the iris regulate the refinement of upstream connections from preganglionic neurons onto sympathetic neurons is a compelling model. Intuitively, it is reasonable that a circuit-wide approach involving long-range bidirectional signalling of anterograde cues and retrograde feedback from target organs is necessary for connections to refine in such a way that circuits function with specificity and precision.

One issue that has not yet been addressed is the relative order in which upstream and downstream connections are refined. Possibly, all connections at different nodes of a circuit refine simultaneously; or refinement occurs in either an anterograde direction, in which preganglionic neurons in the spinal cord determine how SCG neurons innervate their targets; or in a retrograde direction, such that sympathetic targets govern which preganglionic inputs are maintained on SCG neurons. My proposed model involving activity-dependent, target-derived factors suggests a sort of coordination between both ends of the circuit: the iris sends retrograde signals that allow preganglionic inputs identify the iris-specific SCG neurons, and higher order CNS structures somehow instruct preganglionic neurons that their signals are destined for the iris.

These ideas can be explored using trans-synaptic labelling techniques to trace connections between multiple nodes of sympathetic circuits. In addition, even though synaptic refinement occurs in the absence of postsynaptic activity when cap-dependent translation is enhanced, or when the targets of synaptically silent neurons receive functional innervation, I am curious to know whether the refinement of silent connections retains the specificity that is present in active circuits. If specific circuits are appropriately formed in the absence of postsynaptic activity, then this result would provide very strong

support for the model that downstream targets regulate the refinement of upstream connections.

Lastly, my findings may have implications on how diffuse and unorganized circuits of overlapping connections become highly specific neural circuits that function with precision. My results demonstrate that synaptic transmission at individual connections is not essential for their refinement, rather, the collective activity within the circuit has a much stronger influence on its connectivity. Therefore, it is conceivable that many synapses remain silent and synaptically inactive neurons continue to develop normally with little influence on circuit function. Unsilencing of these neurons could be involved in mechanisms to strengthen certain connections through processes involved in learning and memory, or in the event that circuits become disrupted, compensatory mechanisms can activate these silent connections to restore circuit function.

References

Andersen, C.L., Jensen, J.L., and Ørntoft, T.F. (2004). Normalization of real-time quantitative reverse transcription-PCR data: a model-based variance estimation approach to identify genes suited for normalization, applied to bladder and colon cancer data sets. Cancer Research *64*, 5245–5250.

Andjus, P.R., Zhu, L., Cesa, R., Carulli, D., and Strata, P. (2003). A change in the pattern of activity affects the developmental regression of the Purkinje cell polyinnervation by climbing fibers in the rat cerebellum. Neuroscience *121*, 563–572.

Ashburner, M., Ball, C.A., Blake, J.A., Botstein, D., Butler, H., Cherry, J.M., Davis, A.P., Dolinski, K., Dwight, S.S., Eppig, J.T., et al. (2000). Gene Ontology: tool for the unification of biology. Nat Genet *25*, 25–29.

Balice-Gordon, R.J., and Lichtman, J.W. (1994). Long-term synapse loss induced by focal blockade of postsynaptic receptors. Nature *372*.

Banko, J.L., Poulin, F., Hou, L., DeMaria, C.T., Sonenberg, N., and Klann, E. (2005). The Translation Repressor 4E-BP2 Is Critical for eIF4F Complex Formation, Synaptic Plasticity, and Memory in the Hippocampus. Journal of Neuroscience *25*, 9581–9590.

Becht, E., McInnes, L., Healy, J., Dutertre, C.-A., Kwok, I.W.H., Ng, L.G., Ginhoux, F., and Newell, E.W. (2019). Dimensionality reduction for visualizing single-cell data using UMAP. Nat Biotechnol *37*, 38–44.

Benarroch, E.E. (1994). Neuropeptides in the sympathetic system: Presence, plasticity, modulation, and implications. Ann Neurol. *36*, 6–13.

Bialas, A.R., and Stevens, B. (2013). TGF-β signaling regulates neuronal C1q expression and developmental synaptic refinement. Nature Neuroscience *16*, 1773–1782.

Bramham, C.R., and Wells, D.G. (2007). Dendritic mRNA: transport, translation and function. Nature Reviews Neuroscience *8*, 776–789.

Bruderer, R., Bernhardt, O.M., Gandhi, T., and Reiter, L. (2016). High-precision iRT prediction in the targeted analysis of data-independent acquisition and its impact on identification and quantitation. Proteomics *16*, 2246–2256.

Buffelli, M., Burgess, R.W., Feng, G., Lobe, C.G., Lichtman, J.W., and Sanes, J.R. (2003). Genetic evidence that relative synaptic efficacy biases the outcome of synaptic competition. Nature *424*, 430–434.

Bustin, S.A., Benes, V., Garson, J.A., Hellemans, J., Huggett, J., Kubista, M., Mueller, R., Nolan, T., Pfaffl, M.W., Shipley, G.L., et al. (2009). The MIQE Guidelines: Minimum Information for Publication of Quantitative Real-Time PCR Experiments. Clinical Chemistry *55*, 611–622.

Butler, A., Hoffman, P., Smibert, P., Papalexi, E., and Satija, R. (2018). Integrating single-cell transcriptomic data across different conditions, technologies, and species. Nat Biotechnol *36*, 411–420.

Campanucci, V., Krishnaswamy, A., and Cooper, E. (2010). Diabetes Depresses Synaptic Transmission in Sympathetic Ganglia by Inactivating nAChRs through a Conserved Intracellular Cysteine Residue. Neuron *66*, 827–834.

Cao, L., Dhilla, A., Mukai, J., Blazeski, R., Lodovichi, C., Mason, C.A., and Gogos, J.A. (2007). Genetic modulation of BDNF signaling affects the outcome of axonal competition in vivo. Current Biology *17*, 911–921.

Changeux, J.-P., and Danchin, A. (1976). Selective stabilisation of developing synapses as a mechanism for the specification of neuronal networks. Nature *264*, 705.

Charrin, S., Jouannet, S., Boucheix, C., and Rubinstein, E. (2014). Tetraspanins at a glance. Journal of Cell Science *127*, 3641–3648.

Chong, Y., Saviuk, N., Pie, B., Basisty, N., Quinn, R.K., Schilling, B., Sonenberg, N., Cooper, E., and Haghighi, A.P. (2018). Removing 4E-BP Enables Synapses to Refine without Postsynaptic Activity. Cell Reports *23*, 11–22.

Chung, W.-S., Clarke, L.E., Wang, G.X., Stafford, B.K., Sher, A., Chakraborty, C., Joung, J., Foo, L.C., Thompson, A., Chen, C., et al. (2013). Astrocytes mediate synapse elimination through MEGF10 and MERTK pathways. Nature *504*, 394–400.

Cline, H.T. (2001). Dendritic arbor development and synaptogenesis. Current Opinion in Neurobiology *11*, 118–126.

Cline, H., and Haas, K. (2008). The regulation of dendritic arbor development and plasticity by glutamatergic synaptic input: a review of the synaptotrophic hypothesis: The synaptotrophic hypothesis. The Journal of Physiology *586*, 1509–1517.

Cohen-Cory, S. (2002). The developing synapse: construction and modulation of synaptic structures and circuits. Science *298*, 770–776.

Cohen-Cory, S., Kidane, A.H., Shirkey, N.J., and Marshak, S. (2010). Brain-derived neurotrophic factor and the development of structural neuronal connectivity. Developmental Neurobiology *70*, 271–288.

Colman, H., Nabekura, J., and Lichtman, J.W. (1997). Alterations in Synaptic Strength Preceding Axon Withdrawal. Science *275*, 356–361.

Deppmann, C.D., Mihalas, S., Sharma, N., Lonze, B.E., Niebur, E., and Ginty, D.D. (2008). A Model for Neuronal Competition During Development. Science *320*, 369–373.

Eckstein, M.K., Guerra-Carrillo, B., Miller Singley, A.T., and Bunge, S.A. (2017). Beyond eye gaze: What else can eyetracking reveal about cognition and cognitive development? Developmental Cognitive Neuroscience *25*, 69–91.

Emmenlauer, M., Ronneberger, O., Ponti, A., Schwarb, P., Griffa, A., Filippi, A., Nitschke, R., Driever, W., and Burkhardt, H. (2009). XuvTools: free, fast and reliable stitching of large 3D datasets. Journal of Microscopy *233*, 42–60.

Ernsberger, U., and Rohrer, H. (1999). Development of the cholinergic neurotransmitter phenotype in postganglionic sympathetic neurons. Cell and Tissue Research *297*, 339–361.

Favero, M., Busetto, G., and Cangiano, A. (2012). Spike timing plays a key role in synapse elimination at the neuromuscular junction. Proceedings of the National Academy of Sciences *109*, E1667–E1675.

Forehand, C.J. (1985). Density of somatic innervation on mammalian autonomic ganglion cells is inversely related to dendritic complexity and preganglionic convergence. The Journal of Neuroscience *5*, 3403–3408.

Furshpan, E.J., MacLeish, P.R., O'Lague, P.H., and Potter, D.D. (1976). Chemical transmission between rat sympathetic neurons and cardiac myocytes developing in microcultures: evidence for cholinergic, adrenergic, and dual-function neurons. Proceedings of the National Academy of Sciences *73*, 4225–4229.

Ganguly, K., and Poo, M. (2013). Activity-Dependent Neural Plasticity from Bench to Bedside. Neuron *80*, 729–741.

Gillet, L.C., Navarro, P., Tate, S., Reiter, L., Bonner, R., and Aebersold, R. (2012). Targeted Data Extraction of the MS/MS Spectra Generated by Data-independent Acquisition: A New Concept for Consistent and Accurate Proteome Analysis*□S. Molecular & Cellular Proteomics *11*.

Gingras, A.-C., Gygi, S.P., Raught, B., Polakiewicz, R.D., Abraham, R.T., Hoekstra, M.F., Aebersold, R., and Sonenberg, N. (1999). Regulation of 4E-BP1 phosphorylation: a novel two-step mechanism. Genes & Development *13*, 1422–1437.

Ginty, D., and Segal, R.A. (2002). Retrograde neurotrophin signaling: Trk-ing along the axon. Current Opinion in Neurobiology *12*, 268–274.

Gkogkas, C.G., Khoutorsky, A., Ran, I., Rampakakis, E., Nevarko, T., Weatherill, D.B., Vasuta, C., Yee, S., Truitt, M., Dallaire, P., et al. (2013). Autism-related deficits via dysregulated eIF4E-dependent translational control. Nature *493*, 371–377.

Glebova, N.O., and Ginty, D.D. (2005). Growth and survival signals controlling sympathetic nervous system development. Annu. Rev. Neurosci. *28*, 191–222.

Guillery, R.W. (1972). Binocular competition in the control of geniculate cell growth. Journal of Comparative Neurology *144*, 117–129.

Haas, K., Li, J., and Cline, H.T. (2006). AMPA receptors regulate experience-dependent dendritic arbor growth invivo. Proceedings of the National Academy of Sciences *103*, 12127–12131.

Hashimoto, K., and Kano, M. (2003). Functional differentiation of multiple climbing fiber inputs during synapse elimination in the developing cerebellum. Neuron *38*, 785–796.

Hashimoto, K., Ichikawa, R., Kitamura, K., Watanabe, M., and Kano, M. (2009). Translocation of a "Winner" Climbing Fiber to the Purkinje Cell Dendrite and Subsequent Elimination of "Losers" from the Soma in Developing Cerebellum. Neuron *63*, 106–118.

Hashimoto, K., Tsujita, M., Miyazaki, T., Kitamura, K., Yamazaki, M., Shin, H.-S., Watanabe, M., Sakimura, K., and Kano, M. (2011). Postsynaptic P/Q-type Ca2+ channel in Purkinje cell mediates synaptic competition and elimination in developing cerebellum. Proceedings of the National Academy of Sciences *108*, 9987–9992.

He, T.-C., Zhou, S., Da Costa, L.T., Yu, J., Kinzler, K.W., and Vogelstein, B. (1998). A simplified system for generating recombinant adenoviruses. Proceedings of the National Academy of Sciences *95*, 2509–2514.

Hong, Y.K., and Chen, C. (2011). Wiring and rewiring of the retinogeniculate synapse. Current Opinion in Neurobiology *21*, 228–237.

Huberman, A.D., Murray, K.D., Warland, D.K., Feldheim, D.A., and Chapman, B. (2005). Ephrin-As mediate targeting of eye-specific projections to the lateral geniculate nucleus. Nat Neurosci *8*, 1013–1021.

Huberman, A.D., Feller, M.B., and Chapman, B. (2008). Mechanisms Underlying Development of Visual Maps and Receptive Fields. Annual Review of Neuroscience *31*, 479–509.

Iacovitti, L., Joh, T.H., Park, D.H., and Bunge, R.P. (1981). Dual expression of neurotransmitter synthesis in cultured autonomic neurons. Journal of Neuroscience *1*, 685–690.

Je, H.S., Yang, F., Ji, Y., Nagappan, G., Hempstead, B.L., and Lu, B. (2012). Role of pro-brain-derived neurotrophic factor (proBDNF) to mature BDNF conversion in activity-dependent competition at developing neuromuscular synapses. Proceedings of the National Academy of Sciences *109*, 15924–15929.

Je, H.S., Yang, F., Ji, Y., Potluri, S., Fu, X.-Q., Luo, Z.-G., Nagappan, G., Chan, J.P., Hempstead, B., Son, Y.-J., et al. (2013). ProBDNF and Mature BDNF as Punishment and Reward Signals for Synapse Elimination at Mouse Neuromuscular Junctions. Journal of Neuroscience *33*, 9957–9962.

Jennings, C. (1994). Death of a synapse. Nature *372*, 498–499.

Jung, H., Yoon, B.C., and Holt, C.E. (2012). Axonal mRNA localization and local protein synthesis in nervous system assembly, maintenance and repair. Nature Reviews Neuroscience.

Kano, M., and Hashimoto, K. (2009). Synapse elimination in the central nervous system. Current Opinion in Neurobiology *19*, 154–161.

Katz, and Shatz (1996). Synaptic activity and the construction of cortical circuits. Science.

Kawata, S., Miyazaki, T., Yamazaki, M., Mikuni, T., Yamasaki, M., Hashimoto, K., Watanabe, M., Sakimura, K., and Kano, M. (2014). Global Scaling Down of Excitatory Postsynaptic Responses in Cerebellar Purkinje Cells Impairs Developmental Synapse Elimination. Cell Reports *8*, 1119–1129.

Kolodkin, A.L., and Tessier-Lavigne, M. (2011). Mechanisms and Molecules of Neuronal Wiring: A Primer. Cold Spring Harbor Perspectives in Biology *3*, a001727–a001727.

Krishnaswamy, A., and Cooper, E. (2009). An Activity-Dependent Retrograde Signal Induces the Expression of the High-Affinity Choline Transporter in Cholinergic Neurons. Neuron *61*, 272–286.

Kuczewski, N., Porcher, C., Ferrand, N., Fiorentino, H., Pellegrino, C., Kolarow, R., Lessmann, V., Medina, I., and Gaiarsa, J.-L. (2008). Backpropagating action potentials trigger dendritic release of BDNF during spontaneous network activity. Journal of Neuroscience *28*, 7013–7023.

Kühbandner, S., Brummer, S., Metzger, D., Chambon, P., Hofmann, F., and Feil, R. (2000). Temporally controlled somatic mutagenesis in smooth muscle. Genesis *28*, 15–22.

Kumer, S.C., and Vrana, K.E. (1996). Intricate Regulation of Tyrosine Hydroxylase Activity and Gene Expression. Journal of Neurochemistry *67*, 443–462.

Kurihara, Y., Iketani, M., Ito, H., Nishiyama, K., Sakakibara, Y., Goshima, Y., and Takei, K. (2014). LOTUS suppresses axon growth inhibition by blocking interaction between Nogo receptor-1 and all four types of its ligand. Molecular and Cellular Neuroscience *61*, 211–218.

Kwon, H.J., Koo, J.H., Zufall, F., Leinders-Zufall, T., and Margolis, F.L. (2009). Ca2+ Extrusion by NCX Is Compromised in Olfactory Sensory Neurons of OMP−/− Mice. PLoS ONE *4*, e4260.

Landis, S.C. (1990). Target regulation of neurotransmitter phenotype. Trends in Neurosciences *13*, 344–350.

Le Vay, S., Wiesel, T.N., and Hubel, D.H. (1980). The development of ocular dominance columns in normal and visually deprived monkeys. Journal of Comparative Neurology *191*, 1–51.

Lee, H., Brott, B.K., Kirkby, L.A., Adelson, J.D., Cheng, S., Feller, M.B., Datwani, A., and Shatz, C.J. (2014). Synapse elimination and learning rules co-regulated by MHC class I H2-Db. Nature *509*, 195–200.

Lefebvre, J.L., Sanes, J.R., and Kay, J.N. (2015). Development of dendritic form and function. Annual Review of Cell and Developmental Biology *31*, 741–777.

Levi-Montalcini, R. (1987). The nerve growth factor 35 years later. Science *237*, 1154–1162.

Lichtman, J.W., and Colman, H. (2000). Synapse elimination and indelible memory. Neuron *25*, 269–278.

Lin, T.V., Hsieh, L., Kimura, T., Malone, T.J., and Bordey, A. (2016). Normalizing translation through 4E-BP prevents mTOR-driven cortical mislamination and ameliorates aberrant neuron integration. Proc Natl Acad Sci USA *113*, 11330–11335.

Listerud, M., Brussaard, A., Devay, P., Colman, D., and Role, L. (1991). Functional contribution of neuronal AChR subunits revealed by antisense oligonucleotides. Science *254*, 1518–1521.

Longair, M.H., Baker, D.A., and Armstrong, J.D. (2011). Simple Neurite Tracer: open source software for reconstruction, visualization and analysis of neuronal processes. Bioinformatics *27*, 2453–2454.

Lorenzetto, E., Caselli, L., Feng, G., Yuan, W., Nerbonne, J.M., Sanes, J.R., and Buffelli, M. (2009). Genetic perturbation of postsynaptic activity regulates synapse elimination in developing cerebellum. Proceedings of the National Academy of Sciences *106*, 16475–16480.

Lu, B., Pang, P.T., and Woo, N.H. (2005). The yin and yang of neurotrophin action. Nature Reviews Neuroscience *6*, 603.

Lu, W., Bushong, E.A., Shih, T.P., Ellisman, M.H., and Nicoll, R.A. (2013). The Cell-Autonomous Role of Excitatory Synaptic Transmission in the Regulation of Neuronal Structure and Function. Neuron *78*, 433–439.

Luebke, J.I., and Wright, L.L. (1992). Characterization of superior cervical ganglion neurons that project to the submandibular glands, the eyes, and the pineal gland in rats. Brain Research *589*, 1–14.

Ma, X.M., and Blenis, J. (2009). Molecular mechanisms of mTOR-mediated translational control. Nature Reviews Molecular Cell Biology *10*, 307–318.

Masliukov, P.M., Konovalov, V.V., Emanuilov, A.I., and Nozdrachev, A.D. (2012). Development of neuropeptide Y-containing neurons in sympathetic ganglia of rats. Neuropeptides *46*, 345–352.

Matsumoto, T., Rauskolb, S., Polack, M., Klose, J., Kolbeck, R., Korte, M., and Barde, Y.-A. (2008). Biosynthesis and processing of endogenous BDNF: CNS neurons store and secrete BDNF, not pro-BDNF. Nature Neuroscience *11*, 131–133.

McDonough, J., and Deneris, E. (1997). β43′: an enhancer displaying neural-restricted activity is located in the 3′-untranslated exon of the rat nicotinic acetylcholine receptor β4 gene. The Journal of Neuroscience *17*, 2273–2283.

Munz, M., Gobert, D., Schohl, A., Poquerusse, J., Podgorski, K., Spratt, P., and Ruthazer, E.S. (2014). Rapid Hebbian axonal remodeling mediated by visual stimulation. Science *344*, 901–904.

Niell, C., Meyer, M.P., and Smith, S.J. (2004). In vivo imaging of synapse formation on a growing dendritic arbor. Nature Neuroscience.

Nja, A., and Purves, D. (1977). Specific innervation of guinea-pig superior cervical ganglion cells by preganglionic fibres arising from different levels of the spinal cord. The Journal of Physiology *264*, 565–583.

Parker, M.J., Zhao, S., Bredt, D.S., Sanes, J.R., and Feng, G. (2004). PSD93 regulates synaptic stability at neuronal cholinergic synapses. Journal of Neuroscience *24*, 378–388.

Pfeiffenberger, C., Cutforth, T., Woods, G., Yamada, J., Rentería, R.C., Copenhagen, D.R., Flanagan, J.G., and Feldheim, D.A. (2005). Ephrin-As and neural activity are required for eye-specific patterning during retinogeniculate mapping. Nat Neurosci *8*, 1022–1027.

Purves, D., and Lichtman, J. (1980). Elimination of Synapses in the Developing Nervous System. Science.

Purves, D., Rubin, E., Snider, W.D., and Lichtman, J. (1986). Relation of animal size to convergence, divergence, and neuronal number in peripheral sympathetic pathways. The Journal of Neuroscience *6*, 158–163.

Purves, D., Snider, W.D., and Voyvodic, J.T. (1988). Trophic regulation of nerve cell morphology and innervation in the autonomic nervous system. Nature.

Quach, D.H., Oliveira-Fernandes, M., Gruner, K.A., and Tourtellotte, W.G. (2013). A Sympathetic Neuron Autonomous Role for Egr3-Mediated Gene Regulation in Dendrite Morphogenesis and Target Tissue Innervation. Journal of Neuroscience *33*, 4570–4583.

Rassadi, S., Krishnaswamy, A., Pie, B., McConnell, R., Jacob, M., and Cooper, E. (2005). A Null Mutation for the 3 Nicotinic Acetylcholine (ACh) Receptor Gene Abolishes Fast Synaptic Activity in Sympathetic Ganglia and Reveals That ACh Output from Developing

Preganglionic Terminals Is Regulated in an Activity-Dependent Retrograde Manner. Journal of Neuroscience *25*, 8555–8566.

Redmond, L. (2008). Translating Neuronal Activity into Dendrite Elaboration: Signaling to the Nucleus. Neurosignals *16*, 194–208.

R Core Team (2013). R: A language and environment for statistical computing. R Foundation for Statistical Computing, Vienna, Austria. URL http://www.R-project.org/.

Redmond, L., and Ghosh, A. (2005). Regulation of dendritic development by calcium signaling. Cell Calcium *37*, 411–416.

Reichardt, L.F., and Patterson, P.H. (1977). Neurotransmitter synthesis and uptake by isolated sympathetic neurones in microcultures. Nature *270*, 147–151.

Richter, J.D., and Sonenberg, N. (2005). Regulation of cap-dependent translation by eIF4E inhibitory proteins. Nature *433*, 477–480.

RStudio Team (2015). RStudio: Integrated Development for R. RStudio, Inc., Boston, MA URL http://www.rstudio.com/.

Rubin, E. (1985a). Development of the rat superior cervical ganglion: ganglion cell maturation. The Journal of Neuroscience *5*, 673–684.

Rubin, E. (1985b). Development of the rat superior cervical ganglion: ingrowth of preganglionic axons. The Journal of Neuroscience *5*, 685–696.

Rubin, E. (1985c). Development of the rat superior cervical ganglion: initial stages of synapse formation. The Journal of Neuroscience *5*, 697–704.

Schafer, D.P., Lehrman, E.K., Kautzman, A.G., Koyama, R., Mardinly, A.R., Yamasaki, R., Ransohoff, R.M., Greenberg, M.E., Barres, B.A., and Stevens, B. (2012). Microglia Sculpt Postnatal Neural Circuits in an Activity and Complement-Dependent Manner. Neuron *74*, 691–705.

Schilling, B., Gibson, B.W., and Hunter, C.L. (2017). Generation of high-quality SWATH® acquisition data for label-free quantitative proteomics studies using TripleTOF® mass spectrometers. In Proteomics, (Springer), pp. 223–233.

Schorpp, M., Jäger, R., Schellander, K., Schenkel, J., Wagner, E.F., Weiher, H., and Angel, P. (1996). The human ubiquitin C promoter directs high ubiquitous expression of transgenes in mice. Nucleic Acids Research *24*, 1787–1788.

Schotzinger, R.J., and Landis, S.C. (1990). Acquisition of cholinergic and peptidergic properties by sympathetic innervation of rat sweat glands requires interaction with normal target. Neuron *5*, 91–100.

Shalek, A.K., Satija, R., Shuga, J., Trombetta, J.J., Gennert, D., Lu, D., Chen, P., Gertner, R.S., Gaublomme, J.T., Yosef, N., et al. (2014). Single-cell RNA-seq reveals dynamic paracrine control of cellular variation. Nature *510*, 363–369.

Shelton, D.L., and Reichardt, L.F. (1986). Studies on the regulation of beta-nerve growth factor gene expression in the rat iris: the level of mRNA-encoding nerve growth factor is increased in irises placed in explant cultures in vitro, but not in irises deprived of sensory or sympathetic innervation in vivo. The Journal of Cell Biology *102*, 1940–1948.

Shilov, I.V., Seymour, S.L., Patel, A.A., Loboda, A., Tang, W.H., Keating, S.P., Hunter, C.L., Nuwaysir, L.M., and Schaeffer, D.A. (2007). The Paragon Algorithm, a next generation search engine that uses sequence temperature values and feature probabilities to identify peptides from tandem mass spectra. Molecular & Cellular Proteomics *6*, 1638–1655.

Sin, W.C., Haas, K., Ruthazer, E.S., and Cline, H. (2002). Dendrite growth increased by visual activity requires NMDA receptor and Rho GTPases. Nature.

Singh, K.K., Park, K.J., Hong, E.J., Kramer, B.M., Greenberg, M.E., Kaplan, D.R., and Miller, F.D. (2008). Developmental axon pruning mediated by BDNF-p75NTR–dependent axon degeneration. Nature Neuroscience *11*, 649–658.

Smolen, A., and Raisman, G. (1980). Synapse formation in the rat superior cervical ganglion during normal development and after neonatal deafferentation. Brain Research *181*, 315–323.

Snider, W.D. (1988). Nerve growth factor enhances dendritic arborization of sympathetic ganglion cells in developing mammals. The Journal of Neuroscience *8*, 2628–2634.

Sonenberg, N., and Hinnebusch, A.G. (2007). New Modes of Translational Control in Development, Behavior, and Disease. Molecular Cell *28*, 721–729.

Sonenberg, N., and Hinnebusch, A.G. (2009). Regulation of Translation Initiation in Eukaryotes: Mechanisms and Biological Targets. Cell *136*, 731–745.

Stephan, A.H., Barres, B.A., and Stevens, B. (2012). The Complement System: An Unexpected Role in Synaptic Pruning During Development and Disease. Annual Review of Neuroscience *35*, 369–389.

Stevens, B., Allen, N.J., Vazquez, L.E., Howell, G.R., Christopherson, K.S., Nouri, N., Micheva, K.D., Mehalow, A.K., Huberman, A.D., Stafford, B., et al. (2007). The Classical Complement Cascade Mediates CNS Synapse Elimination. Cell *131*, 1164–1178.

Stuart, T., Butler, A., Hoffman, P., Hafemeister, C., Papalexi, E., Mauck, W.M., Hao, Y., Stoeckius, M., Smibert, P., and Satija, R. (2019). Comprehensive Integration of Single-Cell Data. Cell *177*, 1888-1902.e21.

Tao, X., West, A.E., Chen, W.G., Corfas, G., and Greenberg, M.E. (2002). A calcium-responsive transcription factor, CaRF, that regulates neuronal activity-dependent expression of BDNF. Neuron *33*, 383–395.

Taylor, S., Wakem, M., Dijkman, G., Alsarraj, M., and Nguyen, M. (2010). A practical approach to RT-qPCR—publishing data that conform to the MIQE guidelines. Methods *50*, S1–S5.

The Gene Ontology Consortium (2017). Expansion of the Gene Ontology knowledgebase and resources. Nucleic Acids Res *45*, D331–D338.

Thompson, W., Kuffler, D.P., and Jansen, J.K.S. (1979). The effect of prolonged, reversible block of nerve impulses on the elimination of polyneuronal innervation of new-born rat skeletal muscle fibers. Neuroscience *4*, 271–281.

Thoreen, C.C., Chantranupong, L., Keys, H.R., Wang, T., Gray, N.S., and Sabatini, D.M. (2012). A unifying model for mTORC1-mediated regulation of mRNA translation. Nature *485*, 109–113.

Truitt, M.L., Conn, C.S., Shi, Z., Pang, X., Tokuyasu, T., Coady, A.M., Seo, Y., Barna, M., and Ruggero, D. (2015). Differential Requirements for eIF4E Dose in Normal Development and Cancer. Cell *162*, 59–71.

Tsukiyama-Kohara, K., Poulin, F., Kohara, M., DeMaria, C.T., Cheng, A., Wu, Z., Gingras, A.-C., Katsume, A., Elchebly, M., Spiegelman, B.M., et al. (2001). Adipose tissue reduction in mice lacking the translational inhibitor 4E-BP1. Nature Medicine *7*, 1128–1132.

Uesaka, N., Uchigashima, M., Mikuni, T., Nakazawa, T., Nakao, H., Hirai, H., Aiba, A., Watanabe, M., and Kano, M. (2014). Retrograde semaphorin signaling regulates synapse elimination in the developing mouse brain. Science *344*, 1020–1023.

Voyvodic, J.T. (1987). Development and regulation of dendrites in the rat superior cervical ganglion. The Journal of Neuroscience *7*, 904–912.

Voyvodic, J.T. (1989). Peripheral target regulation of dendritic geometry in the rat superior cervical ganglion. Journal of Neuroscience *9*, 1997–2010.

Walicke, P.A., Campenot, R.B., and Patterson, P.H. (1977). Determination of transmitter function by neuronal activity. Proceedings of the National Academy of Sciences *74*, 5767–5771.

Walsh, M.K., and Lichtman, J.W. (2003). In vivo time-lapse imaging of synaptic takeover associated with naturally occurring synapse elimination. Neuron *37*, 67–73.

Wang, C.-A., and Munoz, D.P. (2015). A circuit for pupil orienting responses: implications for cognitive modulation of pupil size. Current Opinion in Neurobiology *33*, 134–140.

Wang, D.O., Martin, K.C., and Zukin, R.S. (2010). Spatially restricting gene expression by local translation at synapses. Trends in Neurosciences *33*, 173–182.

Wang, J.-Y., Chen, F., Fu, X.-Q., Ding, C.-S., Zhou, L., Zhang, X.-H., and Luo, Z.-G. (2014). Caspase-3 Cleavage of Dishevelled Induces Elimination of Postsynaptic Structures. Developmental Cell *28*, 670–684.

Wiesel, T.N., and Hubel, D.H. (1963a). Effects of visual deprivation on morphology and physiology of cells in the cat's lateral geniculate body. Journal of Neurophysiology *26*, 978–993.

Wiesel, T.N., and Hubel, D.H. (1963b). Single-cell responses in striate cortex of kittens deprived of vision in one eye. Journal of Neurophysiology *26*, 1003–1017.

Wiesel, T.N., and Hubel, D.H. (1965). Comparison of the effects of unilateral and bilateral eye closure on cortical unit responses in kittens. Journal of Neurophysiology *28*, 1029–1040.

Wolinsky, E., and Patterson, P. (1983). Tyrosine hydroxylase activity decreases with induction of cholinergic properties in cultured sympathetic neurons. J. Neurosci. *3*, 1495–1500.

Wong, R.O.L., and Ghosh, A. (2002). Activity-dependent regulation of dendritic growth and patterning. Nature Reviews Neuroscience *3*, 803–812.

Xu, W., Gelber, S., Orr-Urtreger, A., Armstrong, D., Lewis, R.A., Ou, C.-N., Patrick, J., Role, L., De Biasi, M., and Beaudet, A.L. (1999). Megacystis, mydriasis, and ion channel defect in mice lacking the α3 neuronal nicotinic acetylcholine receptor. Proceedings of the National Academy of Sciences *96*, 5746–5751.

Young, H.M., Anderson, R.B., and Anderson, C.R. (2004). Guidance cues involved in the development of the peripheral autonomic nervous system. Autonomic Neuroscience *112*, 1–14.

Yurchenko, E., Friedman, H., Hay, V., Peterson, A., and Piccirillo, C.A. (2007). Ubiquitous expression of mRFP-1 in vivo by site-directed transgenesis. Transgenic Research *16*, 29–40.

Zhang, J., Ackman, J.B., Xu, H.-P., and Crair, M.C. (2011). Visual map development depends on the temporal pattern of binocular activity in mice. Nature Neuroscience *15*, 298–307.

Zhang, X., Li, T., Liu, F., Chen, Y., Yao, J., Li, Z., Huang, Y., and Wang, J. (2019). Comparative Analysis of Droplet-Based Ultra-High-Throughput Single-Cell RNA-Seq Systems. Molecular Cell *73*, 130-142.

Zou, D.-J., and Cline, H.T. (1996). Expression of Constitutively Active CaMKII in Target Tissue Modifies Presynaptic Axon Arbor Growth. Neuron *16*, 529–539.